CHROMIUM (VI) REDUCTION IN A MICROBIAL FUEL CELL USING BIOGENIC PALLADIUM NANOPARTICLES AND MODEL DEVELOPMENT

Submitted By

MPUMELELO THOMAS MATSENA

A dissertation submitted in partial fulfilment of the requirements for the degree of

DOCTOR OF PHILOSOPHY
(CHEMICAL ENGINEERING)

In the

FACULTY OF ENGINEERING, BUILT ENVIRONMENT AND INFORMATION TECHNOLOGY

DEPARTMENT OF CHEMICAL ENGINEERING

UNIVERSITY OF PRETORIA

2022

ABSTRACT

Title:	**Chromium (VI) Reduction in a Microbial Fuel Cell using Biogenic Palladium Nanoparticles and Model Development**
Author:	Mpumelelo Thomas Matsena
Supervisor:	Prof. Evans Martin Nkhalambayausi Chirwa
Department:	Chemical Engineering
University:	University of Pretoria
Degree:	Doctor of Philosophy (Chemical Engineering)

Microbial fuel cell (MFC) architectural modification is increasingly becoming an important area of research due to the need to improve energy recovery. In this study, we present a simple low-cost modification method of the anode that does not require pre-treatment-step involving hazardous chemicals to improve performance. The modification step involves deposition of granular activated carbon (GAC) which is highly conductive and provides a high specific surface area inside a carbon cloth that acts as an anode and as a supporting material. The GAC particle size of 0.6-1.1 mm led to an increase in air-cathode MFC performance due to both an increase in the available surface area of 879.5 m^2 g^{-1} for cell attachment based on Brunauer, Emmett, and Teller (BET) results, and an increase in relevant surface for cell attachment which was rough based on the scanning electron microscope (SEM) results. This study also showed that there is an economic benefit in modifying carbon cloth with GAC.

The second part of the study explored an environmentally friendly process for the treatment of Cr(VI) with a codeposition of biologically synthesized zero-valent palladium nanoparticles on the anode electrode of a dual chambered microbial fuel cell (MFC). The MFC featured a granular activated carbon (GAC) anode modified with biogenic palladium nanoparticles (Bio-

PdNPs). Temperature, pH, and initial Cr(VI) concentration were first optimized to 38 °C, pH 4, and 100 mg L^{-1} Cr(VI), respectively. Thereafter, the GAC average particle size was successfully optimized to 0.6-1.1 mm. The results from the study showed that GAC can be successfully modified using Bio-PdNPs to improve the performance of Cr(VI)-reducing MFC with Bio-PdNPs loading of 6 mg Bio-PdNPs g^{-1} GAC resulting in peak output potential difference of 393.1 mV, maximum power density of 1965.4 mW m^{-3}, and complete removal of 100 mg L^{-1} Cr(VI) in 25 h.

The third part of the study was to develop a dynamic computational model for Cr(VI) reduction in MFC. The model incorporated Monod kinetics with Butler-Volmer equation. Accuracy of the parameter estimation and capacity of prediction of the model was validated with usage of two independent data sets. The results of the normalized root mean squared errors for both reduction of Cr(VI) and output voltage were less than 0.2, which indicated that the model fit for the experimental data was acceptable. The model was then used to demonstrate the effect of both the primary microbial cell and substrate concentration on Cr(VI)-reducing MFC performance. An increase in primary microbial cell and substrate concentration improved the reduction rate of Cr(VI) in the cathode chamber. Lastly, the model was used for the optimization of both concentrations. The time it takes to achieve maximum power output was minimized by using a primary microbial cell concentration of 25 mg L^{-1} as opposed to a value of 45 mg L^{-1}. In addition, the substrate concentration was optimized to 60 mmol L^{-1} as opposed to a value of 120 mmol L^{-1}. Overall, the model provided an initial step into determining optimal MFC operational conditions without doing much lab-work.

Keywords: Electrocatalysis; biogenic palladium; Cr(VI) reduction; energy recovery; dynamic model.

DECLARATION

I **Mpumelelo Thomas Matsena**, declare that this thesis which I hereby submit for the degree of Doctor of Philosophy in Chemical Engineering at the University of Pretoria, is my own work and has not been previously submitted by me or any other party for any degree at this or other institutions.

Mpumelelo Thomas Matsena

Date

DEDICATION

This dissertation is dedicated to

My family

My father Rufus Lemoko Matsena for the unconditional love, support and sacrifices.

My late mother Martha Mamsi Matsena for the unconditional love, prayers, encouragement, and raising me to be the person that I am today.

My grandmother, Moloko Filia Matsena for the support and unconditional love displayed throughout my life.

I extend my thanks to my sibling Lebogang Matsena. I extend my gratitude to Mpho Sharon Mthimunye for the support during this time of my research. Also, to all my family and friends, I am grateful for the support.

ACKNOWLEDGEMENTS

To God the Almighty, I thank Him for the wisdom and the strength that He has given me to successfully complete my research and for the abundant blessings throughout the journey of my life.

I would like to extend my profound gratitude to Prof. Evans M.N. Chirwa and would like to thank him for giving me the opportunity to conduct research under his supervision, for providing guidance, sponsorship and resources for the successful completion of the research. His active participation and support allowed me the opportunity to achieve the objectives to the best of my ability, and his continuous motivation and attitude towards research inspired me to reach my full potential. I would also like to thank Dr. Shepherd M. Tichapondwa for his valuable inputs.

I am extremely grateful to my father Rufus Lemoko Matsena for the unconditional love, support and sacrifices towards my education and preparing me for the future. I am also giving special thanks and great appreciation to my late mother Martha Mamsi Matsena for the unconditional love, prayers, encouragement, and raising me to be the person that I am today. To my grandmother, Moloko Filia Matsena, I extend my gratitude for the support and unconditional love displayed throughout my life. I extend my thanks to my sibling Lebogang Matsena. I extend my gratitude to Mpho Sharon Mthimunye for the support during this time of my research. Also, to all my family and friends, I am grateful for the support.

I would like to thank Mrs. Alette Devega and Mrs. Elmarie Otto for the laboratory and administrative help, and would like to thank the Water Utilisation and Environmental Engineering Division members for the assistance with my several experiments.

Technical assistance:

- Prof. Fanus Venter at University of Pretoria for helping with microbial characterization.
- Mrs. Erna van Wilpe for assistance with SEM/EDS analysis.
- Mrs Wiebke Grote for assistance with XRD analysis.

- Mr. Noble Zhonga for assistance with BET analysis.

Funding:

- National Research Foundation (NRF) for Rated Researchers (IFRR) Grant No. IFR170214222643 awarded to Prof. Evans M. N. Chirwa.
- SASOL Postgraduate Bursary.

TABLE OF CONTENTS

LIST OF FIGURES

LIST OF TABLES

LIST OF ABBREVIATIONS AND ACRONYMS

ACNQ	2-amino-3-carboxy-1,4-naphthoquinone
ADP	Adenosine diphosphate
AEM	Anion exchange membrane
AFM	Atomic force microscopy
AHQDS	Anthrahydroquinone-2,6-disulfonate
ANME	Anaerobic methanotrophic archaea
AOM	Anaerobic oxidation of methane
AQDS	Anthraquinone-2,6-disulfonate
ATP	Adenosine triphosphate
Bio-PdNPs	Biogenic palladium nanoparticles
BPM	Bipolar membrane
CCS	Carbon capture and storage
CE	Coulombic efficiency
CEM	Cation exchange membrane
CNT	Carbon nanotubes
COD	Chemical oxygen demand
Cr(VI)	Hexavalent chromium
Cr(III)	Trivalent chromium
DET	Direct electron transfer
DIET	Direct interspecies electron transfer
DO	Dissolved oxygen
EAB	Electrochemically active bacteria
EDS	Electron dispersive spectroscopy
EET	Extracellular electron transfer
FO	Forward osmosis
FO-MFC	Forward-osmosis microbial fuel cell
GAC	Granular activated carbon
HA	Humic acid
MDC	Microbial desalination cell
MEC	Microbial electrolysis cell

MEC-MFC	Microbial electrolysis cell-Microbial fuel cell
MET	Mediated electron transfer
MFC	Microbial fuel cell
MWCNT	Multi-walled carbon nanotubes
NADPH	Reduced nicotinamide adenine dinucleotide phosphate
$NADP^+$	Nicotinamide adenine dinucleotide phosphate
NASA	National Aeronautics and Space Administration
NRMSE	Normalized root mean squared error
PAH	Polycyclic aromatic hydrocarbons
PCB	Polychlorinated biphenyl
Pd	Palladium
Pd(II)	Palladium (II)
PdNPs	Chemically synthesized palladium nanoparticles
PEM	Proton exchange membrane
RMSE	Root mean squared error
SEM	Scanning electron microscope
SWCNT	Single walled carbon nanotubes
UMFC	Upflow microbial fuel cell
UPBR	Upflow packed bed reactor
UPBR-UMFC	Upflow packed bed reactor-Upflow microbial fuel cell
XRD	X-ray diffraction

NOMENCLATURE

Symbols	**Description (units)**
A	Area (m^2)
C	Concentration (mmol L^{-1})
$C_{Cr(VI)o}$	Concentration of Cr(VI) initially (mg L^{-1})
$C_{Cr(VI)}$	Concentration of Cr(VI) at any time (mg L^{-1})
F	Faraday's constant (A s mol^{-1})
E	Cell potential (V)
I	Current output (A)
Io	Exchange current (A)
j	Current density (A m^{-2})
k	Rate constant (s^{-1})
k_1	First order equation rate constant (h^{-1})
k_2	Second order equation rate constant (L mg^{-1} h^{-1})
kd	Cell decay rate (s^{-1})
K	Monod half-saturation constant (mmol L^{-1})
l	Number of times that the rate determining step must take place for the overall reaction to occur once (-)
MM	Molar mass (g mol^{-1})
n	Number of moles of electrons transferred per mole reaction (mol mol^{-1})
na	Number of electrons being transferred after the rate determining step (-)
nb	Number of electrons being transferred before the rate determining step (-)
no	Number of electrons being transferred in the overall reaction (-)
P	Power density (W m^{-2})
q	Reaction rate (mmol L^{-1} s^{-1})
r	Resistance (Ω)
R	Gas constant (Pa m^3 mol^{-1} K^{-1})
t	time (s)
t_d	Time delay before the model fits the kinetics (h)
T	Temperature (K)
v	Chamber volume (L)

ΔV	Output potential difference (V)
$Y_{MR/s}$	Yield of reducing agent intracellular mediator to substrate (mg mg^{-1})
$Y_{Xpr/s}$	Yield of primary cells to subtrate (mg mg^{-1})
$Y_{Xse/s}$	Yield of secondaty cells to substrate (mg mg^{-1})
z	Number of data points (-)

Species	**Description (units)**
$[Cr_2O_7^{2-}]$	Dichromate concentration (mmol L^{-1})
$[Cr(VI)]$	Cr(VI) concentration (mmol L^{-1})
$[Cr(III)]$	Cr(III) concentration (mmol L^{-1})
M_O	Oxidising agent intracellular mediator concentration (NAD$^+$) (mmol L^{-1})
M_R	Reducing agent intracellular mediator concentration (NADH) (mmol L^{-1})
M_T	Total intracellular mediator concentration (mmol L^{-1})
p	Product concentration (mmol L^{-1})
$[O]$	Oxidising agent concentration (mmol L^{-1})
$[R]$	Reducing agent concentration (mmol L^{-1})
S	Substrate concentration (mmol L^{-1})
X	Microbial cell concentration (mg L^{-1})

Greek	**Description (units)**
α	Transfer coefficient (-)
β	Geometry symmetry factor (-)
ε	Residual (-)
ϵ	Constant that removes discontinuity (-)
η	Overpotential (V)
μ	Growth rate (s^{-1})
μmax	Maximum growth rate (s^{-1})
$\overline{\omega}$	Mean of the measured values
$\theta_{X_{pr}}$	Primary cells steepness constant (L mg^{-1})
$\theta_{Cr(VI)}$	Cr(VI) steepness constant (L mmol^{-1})
θ_S	Substrate steepness constant (L mmol^{-1})

Subscripts	**Description**

act	Activation
c	Cathode
conc	Concentration
$Cr_2O_7^{2-}$	Dichromate
a	Anode
b	Backward reaction
ct	Charge transfer
e	Equilibrium
exp	Experimental
ext	External
f	Forward reaction
int	Internal
M_R	Reducing agent intracellular mediator (NADH)
M_O	Oxidising agent intracellular mediator (NAD$^+$)
max	Maximum
min	Minimum
MFC	Microbial fuel cell
net	Total change in the variabe
ohmic	Ohmic
pr	Primary
red	Reduction
rev	Reversible
S	Substrate
se	Secondary
sim	Simulation

Superscripts	**Description**
o	At standard conditions

RESEARCH PORTFOLIO: BOOK CHAPTERS, JOURNAL ARTICLES, AND CONFERENCE PROCEEDINGS

PEER-REVIEWED BOOK CHAPTERS

1. **Matsena, M.T.,** Chirwa, E.M.N., **2022**. Advances in microbial fuel cell technology for zero-emission energy generation from waste. In: Gurunathan, B., Sahadevan, R., Zakaria, Z.A. (Eds.), Biofuels and Bioenergy: Opportunities and Challenges. Elsevier, Amsterdam. doi:10.1016/B978-0-323-85269-2.00013-7 (**Adapted from chapter 2 of the thesis**)

PEER-REVIEWED JOURNAL ARTICLES

2. **Matsena, M.T.,** Chirwa, E.M.N., **2022**. Hexavalent chromium-reducing microbial fuel cell modeling using integrated Monod kinetics and Butler-Volmer equation. **Fuel**, 312, 122834. doi:10.1016/j.fuel.2021.122834 (**Impact factor: 6.609; adapted from chapter 6 of the thesis**)

3. **Matsena, M.T.,** Tichapondwa, S.M., Chirwa, E.M.N., **2021**. Improved chromium (VI) reduction performance by bacteria in a biogenic palladium nanoparticle enhanced microbial fuel cell. **Electrochimica Acta**, 368, 137640. doi:10.1016/j.electacta.2020.137640 (**Impact factor: 6.901; adapted from chapter 5 of the thesis**)

4. **Matsena, M.T.,** Mabuse, M., Tichapondwa, S.M., Chirwa, E.M.N., **2021**. Improved performance and cost efficiency by surface area optimization of granular activated carbon in air-cathode microbial fuel cell. **Chemosphere**, 281, 130941. doi:10.1016/j.chemosphere.2021.130941 (**Impact factor: 7.086; adapted from chapter 4 of the thesis**)

5. **Matsena, M.T.,** Chirwa, E.M.N., **2021**. Comparative analysis of biological versus chemical synthesis of palladium nanoparticles for catalysis of chromium (VI) reduction. **Scientific Reports**, 11, 16674. doi:10.1038/s41598-021-96024-0 (**Impact factor: 4.379**)

6. Kholisa, B., **Matsena, M.T.,** Chirwa, E.M.N., **2021**. Evaluation of Cr(VI) reduction using indigenous bacterial consortium isolated from a municipal wastewater sludge:

batch and kinetic studies. **Catalysts**, 11(9), 1100. doi:10.3390/catal11091100 (**Impact factor: 4.146**)

7. **Matsena, M.T.,** Tichapondwa, S.M., Chirwa, E.M.N., **2020**. Synthesis of biogenic palladium nanoparticles using Citrobacter sp. for application as anode electrocatalyst in a microbial fuel cell. **Catalysts**, 10(8), 838. doi:10.3390/catal10080838 (**Impact factor: 4.146**)

8. Igboamalu T.E., Nyakale A., **Matsena M.T.,** Chirwa E.M.N., **2020**. Effect of oxidation reduction potential (Eh) on the biocatalytic oxidation of as 3^+ to as 5^+ in a mixed culture of chemoautotrophic bacteria. **Chemical Engineering Transactions**, 79, 301-306. doi:10.3303/CET2079051

9. Igboamalu T.E., Bezuidenhout, N., **Matsena M.T.,** Chirwa E.M.N., **2019**. Microbial fuel cell power output and growth: effect of substrate pH on anaerobic microbe consortium. **Chemical Engineering Transactions**, 76, 1381-1386. doi:10.3303/CET1976231

10. Igboamalu T.E., Needham-Clark, B., **Matsena M.T.,** Chirwa E.M.N., **2019**. Energy output from a dual chamber anoxic biofilm microbial fuel cell subjected to variation in substrate concentration. **Chemical Engineering Transactions**, 76, 1387-1392. doi:10.3303/CET1976232

11. **Matsena M.T.,** Igboamalu T.E., Chirwa E.M.N., **2018**. Phenol degrading and chromium (VI) reducing biofilm system: effect of shock-loading. **Chemical Engineering Transactions**, 70, 1237-1242. doi:10.3303/CET1870207

PEER-REVIEWED CONFERENCE PROCEEDINGS

12. Presented in Agios Nikolaos, Crete, Greece, at 22nd Conference on Process Integration for Energy Saving and Pollution Reduction – PRES 2019, 20-23 October 2019.

13. Presented in Prague, Czech Republic, at 21st Conference on Process Integration for Energy Saving and Pollution Reduction – PRES 2018, 25-29 August 2018.

GRAPHICAL ABSTRACT

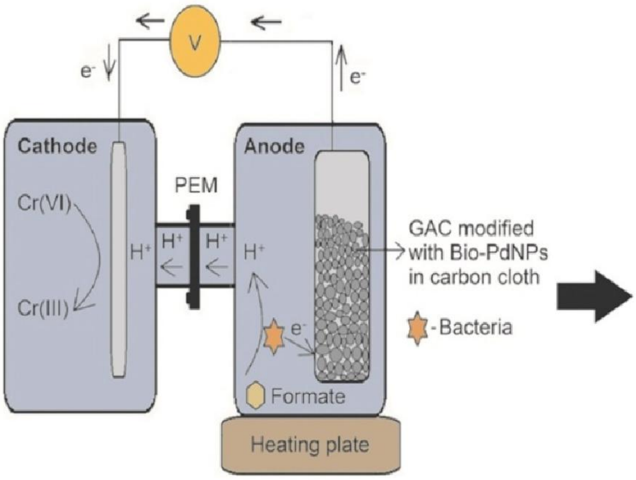

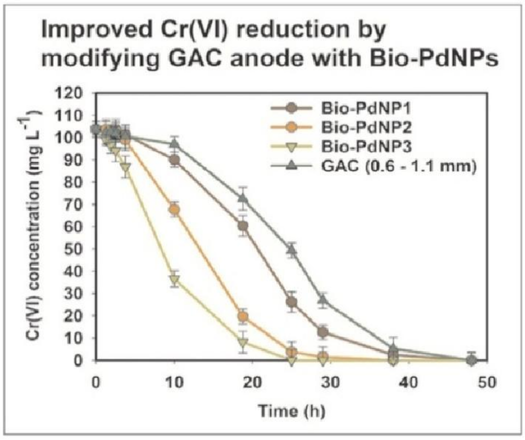

Cathode:
$Cr_2O_7^{2-} + 14H^+ + 6e^- \leftrightarrow 2Cr^{3+} + 7H_2O$
$E^o = 1.33$ V vs. SHE

Anode:
$3HCOO^- \leftrightarrow 3CO_2 + 3H^+ + 6e^-$
$E^o = -0.43$ V vs. SHE

From Experimental Data to Model Development

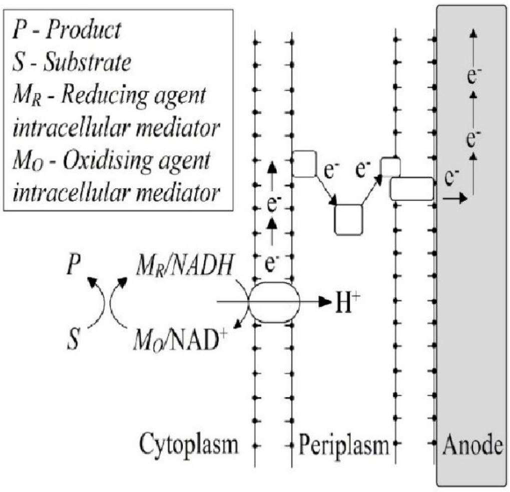

Electrons generated within the electrogens transferred to the anode

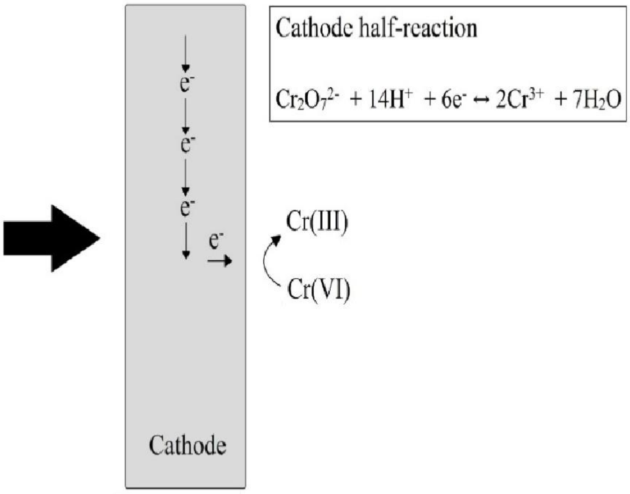

Electrons from the anode transferred to the cathode and used to reduce Cr(VI)

CHAPTER 1: INTRODUCTION

1.1 Background

Wastewater bearing hexavalent chromium [Cr(VI)] is discharged from industrial activities such as electroplating, textile production, leather tanning, paint manufacturing and wood processing to the environment and that leads to heavy metal pollution (Matsena et al., 2018). The discharged Cr(VI) gives rise to negative health effects in humans as it is known to be carcinogenic and mutagenic at high concentrations and acutely toxic at lower concentrations (Occupational Safety and Health Administration., 2006). Studies have shown heightened cases of skin, lung, bladder and liver cancer in populations with prolonged exposure to Cr(VI) (De Flora, 2000). These deleterious effects necessitate the careful treatment of effluents containing Cr(VI) before releasing them to the environment.

Several technologies have been proposed for the reduction of Cr(VI) into the more benign, less mobile trivalent chromium [Cr(III)] oxidation state (Tichapondwa et al., 2018). These include chemical reduction (Kang et al., 2017), biological reduction (Chirwa and Molokwane, 2011) and electrochemical reduction (Sriram et al., 2018). Chemical induced reduction methods have several drawbacks which include high operational costs, the need for toxic reducing agents and high energy input (Song et al., 2016). Biological reduction is therefore an attractive alternative process due to its low operating costs, however, its efficiency is limited by Cr(VI) toxicity to Cr(VI) reducing microorganisms (Chirwa and Molokwane, 2011). Recently, the use of bioelectrochemical systems such as dual chambered microbial fuel cells (MFCs) as an alternative method to treat wastewaters containing Cr(VI) has been receiving considerable attention (Li et al., 2018; Song et al., 2016; Sophia and Saikant, 2016). In this method, the Cr(VI) is used as an electron acceptor in the cathode chamber. Not only is this method cost effective, it also generates energy that can be used in other sections of the process. In addition, dual chambered MFCs have been shown to have high tolerance to Cr(VI) toxicity (Li et al., 2008).

The standard reduction potential of Cr(VI) is 1.33 V higher than 1.23 V for O_2 (Li et al., 2008). This implies that Cr(VI) can theoretically act as a better electron acceptor in the cathode chamber as compared to O_2. In addition, when formate ($HCOO^-$) is used as an electron donor (-0.43 V) (Zhang et al., 2018), Cr(VI) reduction using dual chambered microbial fuel cell (MFC) is theoretically possible due to a positive overall cell potential (E^{o}_{cell}), where E^{o}_{cell}=1.76 V.

The anodic surface area and electrocatalytic activity play a crucial role in the performance of the MFC. In order to improve the surface area and electrocatalytic activity of the anode electrode, dispersed material and palladium can be used. Dispersed materials are mostly inexpensive, durable and have high surface area (Jiang and Li, 2009). Usage of dispersed materials can improve performance of MFCs as shown in studies that used activated carbon granules in titanium mesh (Liu et al., 2014), graphite in titanium mesh (Zhang et al., 2013), anode activated carbon granular bed (Jiang and Li, 2009), and biochar in carbon cloth (Wang et al., 2018). This is because these materials provide high surface area for cell attachment when using the same amount of mass as one would use in a solid material such as a carbon rod.

To the best of our knowledge, no study has reported the use of dispersed anode material modified with biogenic palladium nanoparticles (Bio-PdNPs) to improve the performance of a Cr(VI)-reducing MFC. Therefore, one the purposes of this research is to help provide more knowledge in that regards by conducting a simple modification of the carbon cloth anode by the disposition of granular activated carbon.

Another problem addressed in this research involves the modelling of Cr(VI)-reducing MFC. Most of Cr(VI)-reducing MFC studies are lab-based and the contributions of different parameters including bacterial concentration, bacterial kinetics, mass transport phenomena, and temperature cannot all be studied either independently or in combination at the lab. This is due to time constraints and the costs involved. Therefore, modelling techniques have to be developed in order to model metal reduction and energy production of not only Cr(VI)-reducing MFCs but all metal-reducing MFCs. Models are valuable in studying parameters because not only do they reduce the time and costs involved, but they also provide the ability to simulate and adjust the configurations and operating conditions without conducting much of lab-work.

Since the first model development by Zhang and Halme (1995), which was simplistic in its form and provided a stepping stone into the advanced modelling of MFCs, MFC modelling has now been expanded to different applications such as modelling different electron transfer mechanisms using Nernst-Monod (Kato Marcus et al., 2007; Torres et al., 2008) and Butler-Volmer-Monod (Hamelers et al., 2011) models. These electron transfer mechanisms include direct electron transfer (DET), solid-conductive matrix, and mediated electron transfer (MET). DET mechanism occurs via physical contact between the outer membrane and the anode (Cao et al., 2019). Solid-conductive matrix refers to the microorganism using a pilus-like structure called a nanowire instead of using an outer membrane to attach to the electrode (Santoro et al., 2017). Lastly, MET mechanism involves electron transfer that occurs with the help of low molecule, soluble mediator that eliminates the requirement of direct contact between the microorganism and the anode (Cao et al., 2019).

To further elaborate, the Nernst-Monod model was successfully used to study the effect of substrate and anode potential on the performance of MFC considering the electron transfer was through a solid-conductive matrix (Kato Marcus et al., 2007; Renslow et al., 2013; Torres et al., 2008), and Butler-Volmer-Monod model was shown to have success in modelling MET mechanism via internal redox components of the microbial cell (Hamelers et al., 2011). Picioreanu et al. (2007) also developed a multidimensional mathematical model for MET mechanism and used the Butler-Volmer equation to understand the effect of parameters such as the external resistance, concentration of the mediator, suspended to biofilm cells ratio and initial substrate on the MFC performance. The problem with the multidimensional mathematical model was the level of computation required to solve the equations, and Gadkari et al. (2019) solved the problem by introducing a simple fast converging model with the ability to provide a detailed parametric analysis over a range of parameters through using a simple mathematical formulation that incorporated Butler-Volmer equations and sufficiently described the important processes of MFCs with their governing equations for bio-electrochemical kinetics and charge transfer without being computationally intensive.

Recent studies have expanded on both Nernst-Monod and Butler-Volmer-Monod models to MFC applications such as nitrogen oxides removal (Su et al., 2018), phenol removal (Hejazi et al., 2019), and biosensor for monitoring water quality (Radeef and Ismail, 2019). Hence in this study, Butler-Volmer-Monod is used as a basis to model metal-reducing MFCs.

1.2 Problem Statement

Palladium (Pd) has been used to increase the electrocatalytic activity of MFCs. This is due to Pd having an excellent electrocatalytic oxidation of various organic molecules such as formate (Quan et al., 2015) and ethanol (Wang et al., 2013) which are the metabolites from the metabolic processes of electrogens in the anode in order to improve MFC performance. In addition, Pd is abundant (Fang et al., 2020) and has been shown to favour direct pathway in the oxidation of various organic molecules which avoids the surface of the electrocatalyst being poisoned by carbon monoxide (Pramanick et al., 2020). However, drawbacks exist in chemically synthesized Pd nanoparticles as they are mostly fabricated using a variety of toxic chemical reagents under harsh conditions (Moon et al., 2014).

Biological synthesis of Pd, which is a more environmentally friendly process, eliminates these drawbacks since it requires less chemical reagents and occurs under gentle conditions. Biologically synthesized Pd nanoparticles have been used to improve the electrocatalytic activity of the anode in previous studies (Matsena et al., 2020; Quan et al., 2018b) and are therefore used in this study to improve the performance of the Cr(VI)-reducing MFC.

Solid material such as a carbon rod has a low surface area as compared to dispersed material such as GAC when using the same amount of mass. Therefore, GAC is a viable replacement to solid material anode electrodes which is used in this study in order to improve MFC performance since the anode surface area plays a crucial role in the performance of MFCs.

With respect to the modelling of Cr(VI)-reducing MFC, models have been used by previous studies to provide an initial step in modelling Cr(VI) reduction in both microbial and plant fuel cells (Habibul et al., 2016; Song et al., 2016), however, the models did not include modelling the bio-anode processes and the electrochemical properties of the Cr(VI)-reducing MFC. Therefore, this study addresses the development of a mechanistic model which provides an initial step of modelling metal reducing MFCs and includes bio-anode processes and the electrochemical properties of MFCs.

1.3 Scope of the Study

In this study, a series of experiments to enhance the performance of Cr(VI)-reducing MFC were conducted. In addition, a mechanistic model was developed to provide an initial step in the simulation of Cr(VI) reduction in MFCs. This study is comprised of two major parts:

- To conduct MFC experiments for energy generation and Cr(VI) reduction in a dual chambered MFC.
- To develop a simplistic mechanistic model for ease of implementation in dual chambered Cr(VI)-reducing MFC.

1.4 Research Hypothesis

In the current research, it is hypothesized that biologically synthesized palladium nanoparticles and GAC will enhance the performance of Cr(VI)-reducing MFC. It is additionally hypothesized that the mechanistic model that incorporates Monod kinetics with Butler-Volmer equation should be able to represent the performance of the dual chambered Cr(VI)-reducing MFC.

1.5 The Objectives of the Present Research

1.5.1 General objectives

To evaluate the potential of the Bio-PdNPs and GAC on improving the performance of Cr(VI)-reducing MFC. In addition, model the Cr(VI)-reducing MFC.

1.5.2 Specific objectives

- o optimize various parameters such as cathode pH, Cr(VI) concentration, and anode temperature for the dual chambered Cr(VI)-reducing MFC.
- To perform experiments to evaluate the effect of GAC on the performance of the dual chambered Cr(VI)-reducing MFC in order to evaluate its impact on anode surface area.
- To conduct morphology analysis on the GAC using the scanning electron microscope (SEM) in order to evaluate the smoothness or roughness of the surface.
- To evaluate the effect of using Bio-PdNPs on the performance of dual chambered Cr(VI)-reducing MFC as a way of improving the anode electrode catalytic activity.

- To develop a mechanistic model for the Cr(VI)-reducing MFC using the Monod kinetics and Butler-Volmer equation, evaluate its predictive capacity and conduct various simulations.

1.6 Thesis Outline

This dissertation is composed of eight chapters.

Chapter 1. This chapter contains the introduction, problem statement, the objectives and the scope of this research, and the outline of the thesis.

Chapter 2. Reviews previous work and developments in the area of MFCs, their history and the emergence, the science behind MFCs, the various electrochemically active bacteria that are used in MFC applications, the effect of physical/structural parameters on the performance of MFCs, the effect of chemical and biochemical parameters on the MFC performance, and various MFC applications.

Chapter 3. This chapter is the materials and methods section and it includes the details of the chemicals used, methods on the inoculation of the anode chamber, isolation and enrichment methods of microorganisms for Bio-PdNPs production, the fabrication of the anode using GAC and Bio-PdNPs, the Cr(VI)-reducing MFC experimental setup, and the analytical methods and instruments used in this study.

Chapter 4. This chapter includes the results and discussion on the anode modification with GAC in order to enhance energy recovery in an air-cathode MFC.

Chapter 5. This chapter includes the results and discussion on the anode modification with Bio-PdNPs and GAC in order to enhance energy recovery and Cr(VI) reduction in MFC.

Chapter 6. This chapter details the results and discussion on the modelling of dual chambered Cr(VI)-reducing MFC using the Monod kinetics and Butler-Volmer equation.

Chapter 7. The conclusions from this study and recommendations are presented.

Chapter 8. The appendices are attached in this chapter.

CHAPTER 2: LITERATURE REVIEW

2.1 Background

2.1.1 The history and emergence of microbial fuel cells

The researcher who first conducted work on microbial fuel cells was a professor of botany at the University of Durham, Michael Cresse Potter. In 1910, when he was researching on how microbes degrade organic compounds, he observed that microorganisms actually have the ability to generate a potential difference and deliver current (Potter, 1910). In 1911, he continued on the work and used platinum wires as electrodes and microbial cultures of *Escherichia coli* and *Saccharomyces cerevisiae* to further demonstrate the ability of microbes to generate electricity (Potter, 1911). This work led to the discovery of the first microbial fuel cell (MFC) which was further explored by Barnett Cohen, a biochemist at Cambridge University. Cohen connected these MFCs in series and demonstrated in 1931 how this type of connection can improve energy generation (Cohen, 1931).

It was not until the 1960s that MFCs took part of a program that was launched by the National Aeronautics and Space Administration (NASA) as an opportunity to recycle waste into electrical energy during a space flight (Liengen et al., 2014). This never attracted much attention up until 1983 when Bennetto et al. (1983) and Stirling et al. (1983) at Kings College put emphasis on the usage of redox mediators in MFCs to improve energy generation. In addition, the interest increased in 1999 when it was demonstrated by the Byung Hong Kim group at the Korean Institute of Science and Technology that electrochemically active bacterial species in MFCs did not require mediators for electron transport (Kim et al., 1999). Since the beginning of the 21st century, the research in MFCs has exponentially increased with notable advances being made in the improvement of energy recovery. Table 2.1 shows the summary of the history and emergence of MFCs.

Table 2.1 Summary of the history and the emergence of MFCs.

Scientist	Year	Contribution	Ref.
Galvani, L. (University of Bologna)	1791	Reported the first observations of bioelectricity.	(Kipnis, 1987)
Volta, A. (Pavia University)	1800	Discovered a 'Voltaic pile' which was the first non-rechargeable power source.	(Volta, 1800)
Davy, H. (Royal Institution)	1800	Recognised the relationship between chemical and electrical effects.	(Dicks and Rand, 2018)
Schönbein, C.F. (Basel University)	1839	The first demonstration of the principle of a fuel cell effect.	(Schönbein, 1839)
Grove, W.R. (Royal Institution)	1839	Demonstrated a more efficient voltaic cell called the 'Grove cell'.	(Wisniak, 2015)
Grove, W.R. (Royal Institution)	1842	Developed the first working prototype of a fuel cell.	(Grove, 1842)
Ostwald, F.W. (Leipzig University)	1893	Described the interconnections between several components of the fuel cell.	(Flimban et al., 2019)
Potter, M.C. (University of Durham)	1910	Observed that microorganisms actually have an ability to generate a potential difference.	(Potter, 1910)
Potter, M.C. (University of Durham)	1911	Used *Escherichia coli* and *Saccharomyces cerevisiae* for electricity generation.	(Potter, 1911)
Cohen, B. (Cambridge University)	1931	Connected microbial fuel cells in series to improve energy generation.	(Cohen, 1931)
Bernetto et al. (Kings College)	1983	Put emphasis on the usage of redox mediators in MFCs to improve energy generation.	(Bennetto et al., 1983)
Kim et al. (Korean Institute of Science and Technology)	1999	Demonstrated that no mediators for electron transport are required for electrogens.	(Kim et al., 1999)

2.1.2 Advances and limitations

From the time when Luigi Galvani reported the first observations of bioelectricity in the 18th century, to the time when Michael Cresse Potter discovered the first MFC in the 20th century, the technology has grown and has attracted an increasing number of researchers in recent years as shown in Figure 2.1.

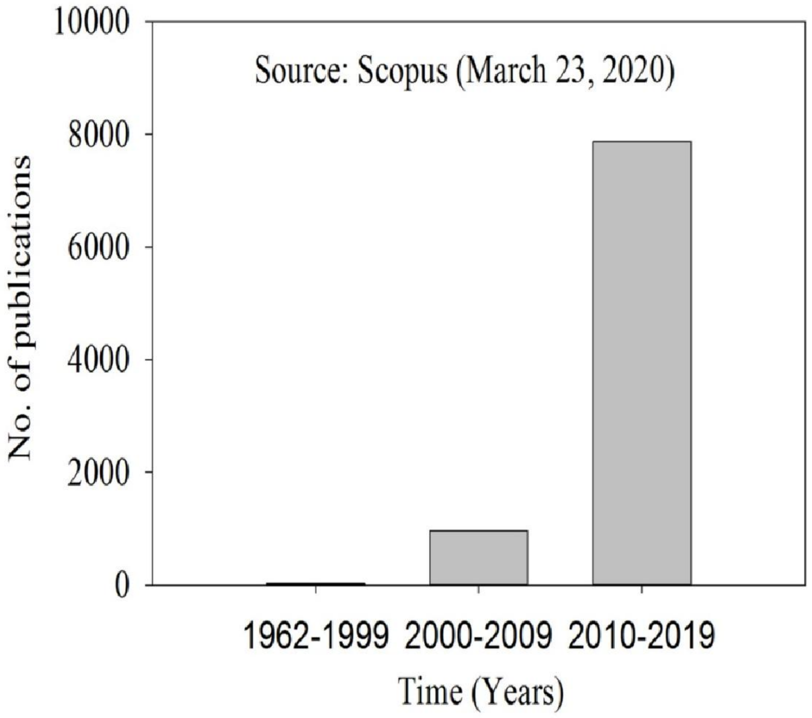

Figure 2.1 The total number of publications in the years of 1962-1999, 2000-2009 and 2010-2019. The data is based on the number of articles mentioning ‘microbial fuel cell’ in Scopus till March 23, 2020.

The first major research on MFCs was published in 1910 to 1931, which includes research by Potter (1910, 1911) and Cohen (1931) on the demonstration of MFC and how series connection improves performance. Between 1962 and 1999, only 29 papers on the research based on MFCs were published according to Scopus. These include the work done by Bennetto et al. (1983) and Stirling et al. (1983) on the mediator and Kim et al. (1999) on the mediatorless MFC. It is not up until the years between 2000 and 2009 that the number began to increase. During this time, 965 papers where published (Figure 2.1). The most prominent publications that were most cited based on Scopus were the work done by Chaudhuri and Lovley (2003) and Rabaey et al. (2004) which confirmed a mediatorless MFC, Liu and Logan (2004) which presented a single chamber MFC, and Gorby et al. (2006) which expanded on the knowledge of electrically conductive bacterial nanowires.

A spike in the number of publications was experienced in the years between 2010 and 2019 with 7866 publications. This is because MFCs do not only provide solutions to today’s environmental problems but they can also be applied over a wide-range of applications. These applications presented in the years 2010 to 2019 include the simultaneous nitrification, denitrification and carbon removal (Virdis et al., 2010); salt removal in a continuously operated upflow microbial desalination cell with an air cathode (Jacobson et al., 2011); and self-powered supercapacitive microbial fuel cell that uses high-power operation of an internal supercapacitor (Santoro et al., 2016). From Figure 2.2, it can also be seen that in the last ten years, the MFC research has been growing meaning in the future, there exists a potential for new applications on MFCs to be developed.

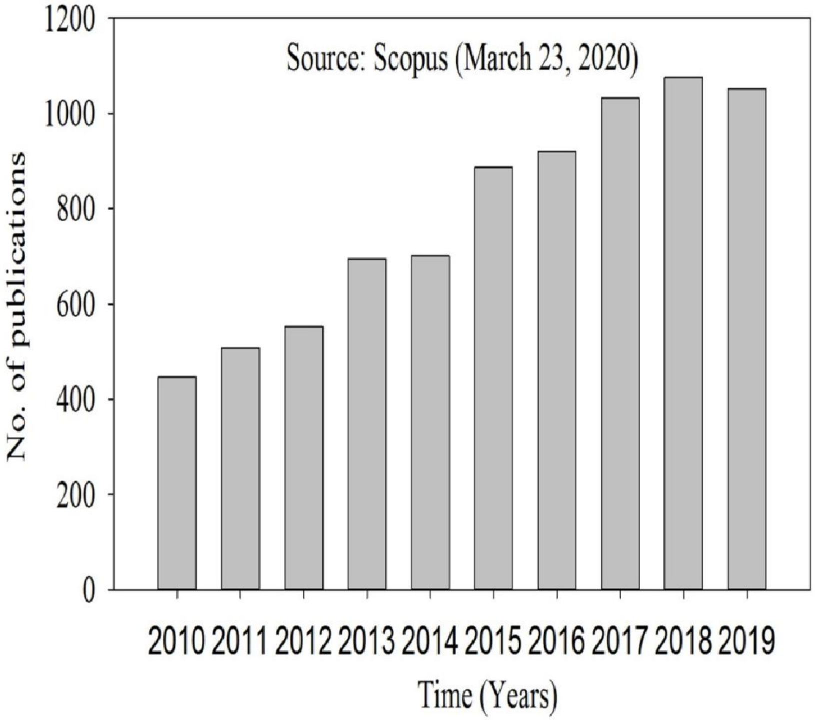

Figure 2.2 The total number of publications in each year from 2010 to 2019. The data is based on the number of articles mentioning 'microbial fuel cell' in Scopus till March 23, 2020.

2.1.3 *Implication to the energy industry – water/energy nexus*

Figure 2.3 shows the rise in global electricity consumption from 1999 to 2019 (Enerdata, 2020).

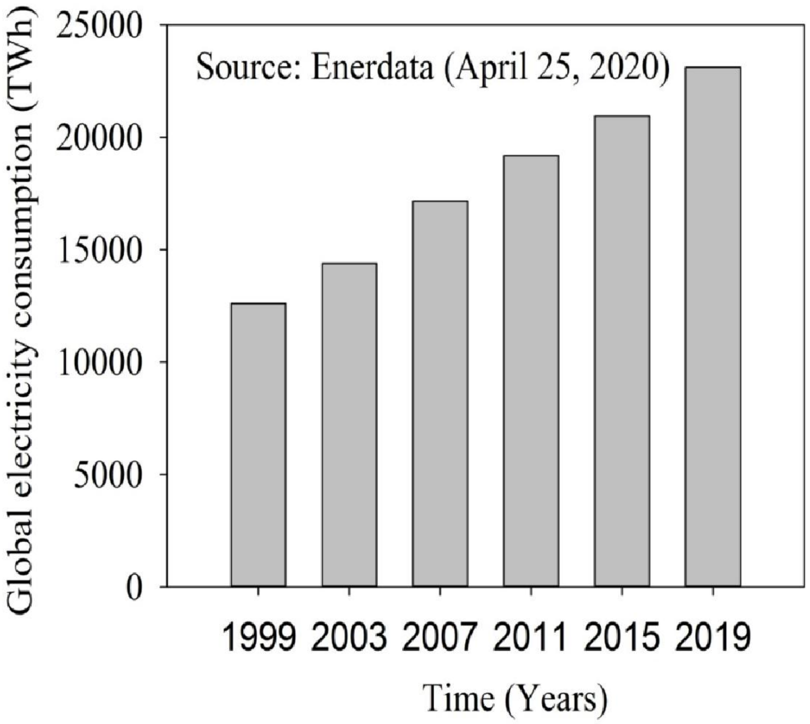

Figure 2.3 Global electricity consumption (Enerdata, 2020).

It is projected that energy-related water consumption is set to increase by 60% in the year 2040 due to several energy technologies which can have high water demands such as biofuels production, nuclear power, and carbon capture and storage (CCS) (IEA, 2017). In addition, although it is estimated that the global electricity consumption by the supply, treatment and desalination of water will remain at about 4%, the increase in electricity consumption due to water-related issues in the Middle East is set to increase from 9% in 2015 to 16% by 2040 (IEA, 2017). This is actually something that will mostly be experienced by countries which rely on nuclear and coal-fired power plants such as China, India, and South Africa, many of which are located in areas that are experiencing water shortages. As such, making the efforts to find new technologies which can reduce both water-use and energy consumption necessary.

A technology that currently provides such capability is MFC. Although it is still in the laboratory stages, it is a promising technology that can address the challenges of treating wastewater whilst generating renewable energy. It functions independent of the sun or the wind, and it provides additional ways in which electricity can be generated by converting organic matter to energy by the use of microorganisms. It should be noted that MFCs should never be thought of as a technology that can be a major energy supplier, however, it should be thought of as a new approach in solving global water-energy problems which can be integrated into already existing clean and renewable energy solutions such as wind and solar power.

2.2 The Science of Microbial Fuel Cells

2.2.1 Electrochemistry and thermodynamic feasibility

Intense amount of research has gone into the successful implementation of different constructions of MFCs. Most of these constructs are adapted from the already existing technologies such as the fuel cell and packed bed reactors. MFCs are comprised of the anode and cathode compartments which are separated by a proton exchange membrane (PEM). Furthermore, the general electrochemical reactions that occur in each compartment are oxidation at the anode and reduction at the cathode which are given by Equations (2.1) and (2.2):

$$\text{Substrate} \leftrightarrow \text{Oxidized product} + H^{+} + e^{-} \qquad (2.1)$$

$$\text{Oxidant} + H^{+} + e^{-} \leftrightarrow \text{Reduced oxidant} \qquad (2.2)$$

The electrons produced by oxidising the substrate or organic matter using the electrochemically active bacteria move from the anode to the cathode to reduce the oxidant. In addition, the charge balance is maintained by the movement of hydrogen ions (H^+) through the PEM from the anode to the cathode. For the electrochemical reactions in MFC to be thermodynamically feasible, an overall positive standard reduction potential should be obtained. This will be illustrated by using glucose ($C_6H_{12}O_6$) as a substrate and oxygen (O_2) as an oxidant. This is the most widely used MFC. The redox half-reactions are given in Equations (2.3) and (2.4) (Sharma and Li, 2010):

$$C_6H_{12}O_6 + 6H_2O \leftrightarrow 6CO_2 + 24H^{+} + 24e^{-} \quad E^{o}_{red,anode} = -0.42\,V \qquad (2.3)$$

$$6O_2 + 24H^{+} + 24e^{-} \leftrightarrow 12H_2O \quad E^{o}_{red,cathode} = 0.82\,V \qquad (2.4)$$

where, $E^o_{red,anode}$ and $E^o_{red,cathode}$ represent the standard reduction potentials of the anode and cathode, respectively. To compute the overall standard reduction potential, the difference between $E^o_{red,cathode}$ and $E^o_{red,anode}$ is calculated, which gives a positive value of 1.24 V indicating that this type of MFC is thermodynamically feasible.

2.2.2 *Cr(VI) reduction in microbial fuel cells*

The main redox reactions occurring in the Cr(VI)-reducing MFC include formate ($HCOO^-$) oxidation at the anode, where electrons generated are consumed in the cathode chamber by Cr(VI) in the form of dichromate ($Cr_2O_7^{2-}$) to form trivalent chromium (Cr^{3+}). Equations (2.5) and (2.6) represent the half reactions with their standard reduction potentials defined for the anode ($E^o_{red,anode}$) and cathode ($E^o_{red,cathode}$), respectively:

Anode chamber:

$$3HCOO^- \leftrightarrow 3CO_2 + 3H^+ + 6e^- \qquad E^o_{red,anode} = -0.43 V \tag{2.5}$$

Cathode chamber:

$$Cr_2O_7^{2-} + 14H^+ + 6e^- \leftrightarrow 2Cr^{3+} + 7H_2O \qquad E^o_{red,cathode} = 1.33 V \tag{2.6}$$

The standard reduction potential of Cr(VI) is 1.33 V higher than 1.23 V for O_2 (Li et al., 2008). This implies that Cr(VI) can theoretically act as a better electron acceptor in the cathode chamber as compared to O_2. In addition, when formate ($HCOO^-$) is used as an electron donor (-0.43 V) (Zhang et al., 2018), Cr(VI) reduction using dual chambered microbial fuel cell (MFC) is theoretically possible due to a positive overall cell potential (E^o_{cell}), where E^o_{cell}=1.76 V. Based on this information, Cr(VI) reduction using MFCs is one of the methods that offers opportunities for treatment of Cr(VI) contaminated wastewater.

2.2.3 *The construct of a microbial fuel cell*

2.2.3.1 Dual-chamber microbial fuel cell

The schematic of the dual-chambered MFC is shown in Figure 2.4.

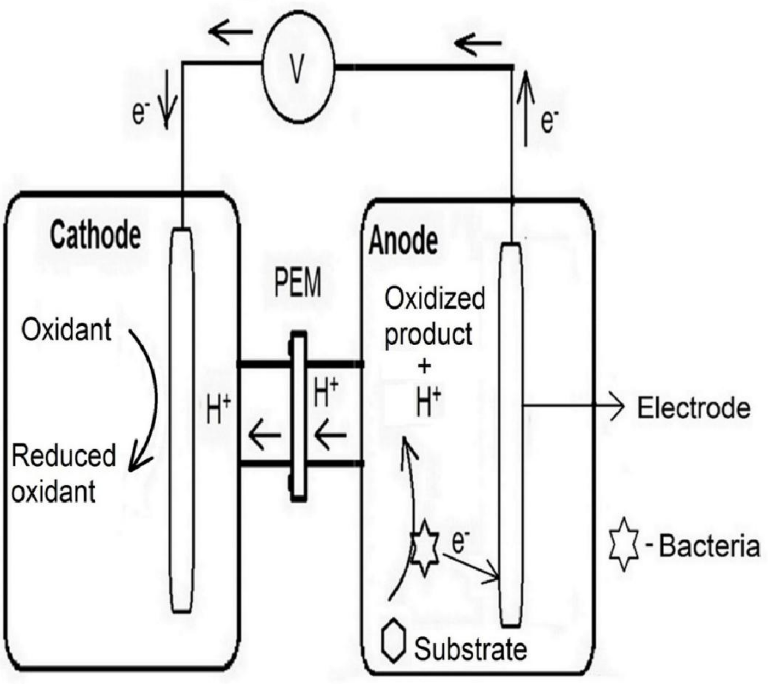

Figure 2.4 Schematic of a dual-chambered MFC.

In addition to the generation of energy, dual-chambered MFCs are known for their dual functionality for the treatment of wastewaters containing organic pollutants and for the recovery and treatment of wastewaters containing heavy metals. This is because they contain two compartments, namely the anode with the ability to breakdown organic waste, and the cathode with the ability for metal recovery or reduction to less toxic forms. In addition, this is the reason why this construct is highly favoured in the treatment of waste in general due to its versatility in its applications. The organic pollutants that have been treated in previous studies include phenol (Luo et al., 2009), polycyclic aromatic hydrocarbons (PAHs) (Gambino et al., 2017) and polychlorinated biphenyl (PCBs) (Xu et al., 2015). Also, the heavy metals that have been recovered using this construct include vanadium (Zhang et al., 2012), copper (Heijne et al., 2010), silver (Choi and Cui, 2012) and chromium (Sophia and Sai, 2016).

2.2.3.2 Single-chamber microbial fuel cell

The schematic of the single-chambered MFC is shown in Figure 2.5.

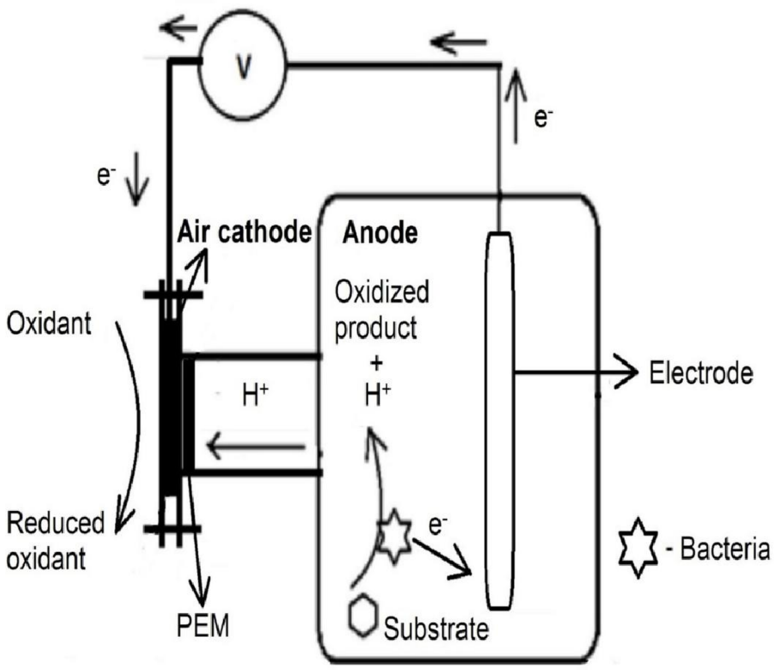

Figure 2.5 Schematic of a single chambered MFC.

Single-chambered MFCs can only be implemented in the treatment of organic waste without the functionality of metal recovery. This is because the only oxidant that they can utilize is the available oxygen in air and hence they are also known as air-cathode MFCs. The introduction of single-chambered MFCs was due to the problems that were experienced in the mass transfer of dissolved oxygen to the cathode electrode in dual chambered MFCs. This led to the removal of the cathode compartment and the implementation of air-cathodes which can be easily modified to improve the mass transfer of oxygen and MFC performance. Some of the modification of air-cathodes to improve MFC performance which have been implemented include using nitrogenous mesoporous carbon air cathode coated with cobalt and copper nanoparticles (Liang et al., 2020), diffusion-layer-free air cathode based on ionic conductive hydrogel (Li et al., 2020), activated carbon-supported Fe-Ag-N multi-doped graphene (Lv et al., 2019), and manganese dioxide on carbon Vulcan air-cathode (Majidi et al., 2019).

2.2.3.3 Upflow microbial fuel cell

In the treatment processes, biofilm systems are known to offer an opportunity for the bacterial community to survive under high concentrations of either organic or metallic pollutants. This is achieved by presenting an environment with a variable survivability range due to the biofilm thickness forming a dynamic concentration gradient (Matsena et al., 2018). Therefore, under high loading concentrations of pollutants, the mass transport resistance leads to zones in the biofilm where the concentration is low enough to allow for the survival of detoxifying microbial agents. An example of such a biofilm system is an upflow packed bed reactor (UPBR). To reduce the energy requirements of such systems, He et al. (2005; 2006) developed and demonstrated that a UPBR can be integrated with an upflow MFC (UMFC) to realize a continuously operated MFC with improved performance (Figure 2.6).

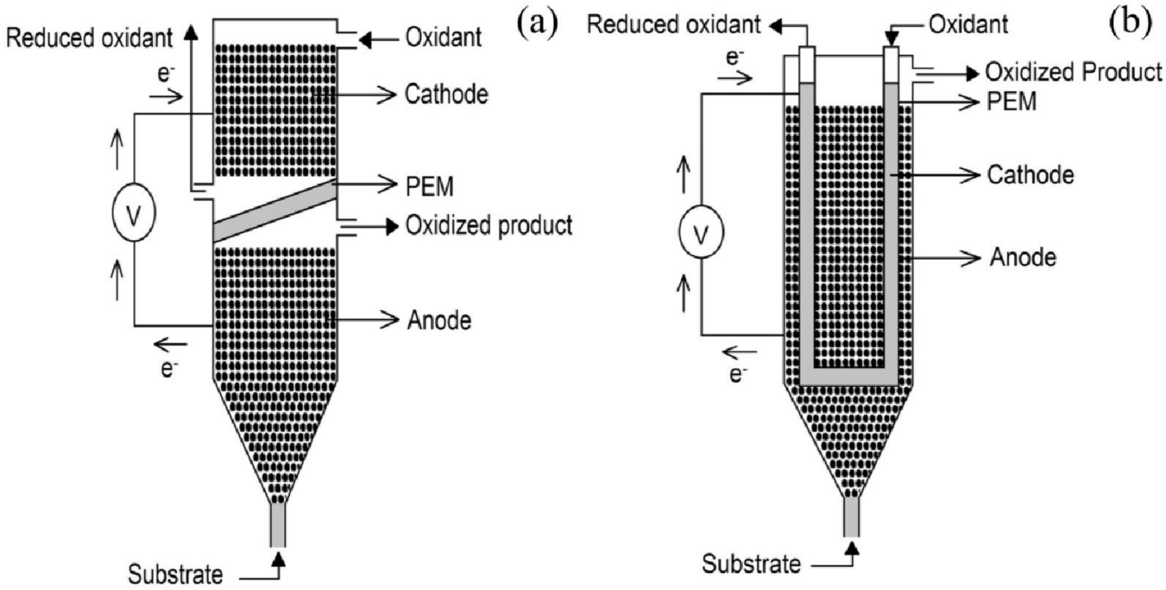

Figure 2.6 Schematic of (a) an upflow MFC, and (b) an annular upflow MFC with interior PEM.

Since then, UPBR-UMFC systems have been used in studies such as thermophilic microbial communities fed with acetate (Dessì et al., 2019), an anaerobic aged sludge fuelled with a synthetic acetate-based and actual domestic wastewater (Ismail and Jaeel, 2016), development of double-layer-capacitor-materials modified anodes (Chen et al., 2018), and evaluation of electrochemical performance of a photosynthetic UMFC (Zheng et al., 2017).

2.2.3.4 Stacked microbial fuel cells

Due to the fact that the output potential difference of an individually operated construct of MFC can never be above a theoretical value, even when neglecting losses and limitations, this leads to finding other means in order to enhance the performance of MFCs. One of the solutions is to use a stacked MFC which can be classified into three groups, namely, series, parallel and hybrid (Figure 2.7).

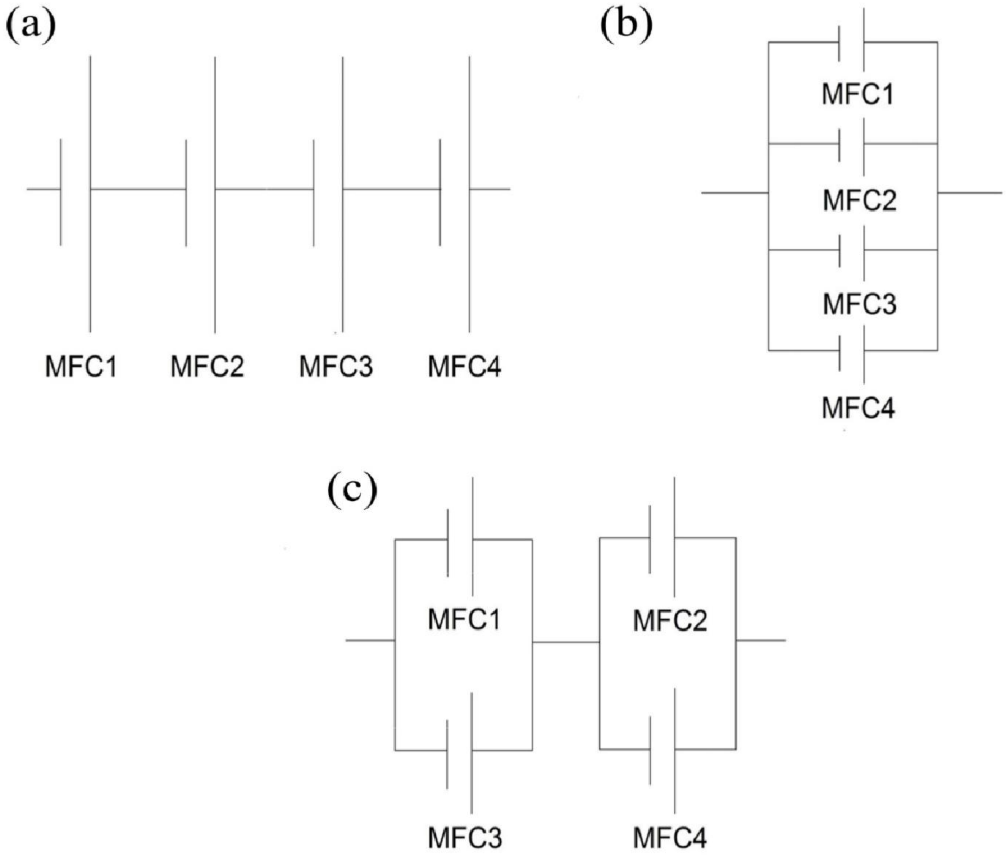

Figure 2.7 Schematic of different stacked MFC configurations such as (a) series MFC connection, (b) parallel MFC connection, and (c) hybrid MFC connection.

The usage of stacked MFCs was demonstrated by Aelterman et al. (2006) in which it was shown that stacked MFCs of either series or parallel connections have the ability to produce high power densities. Zhang et al. (2017) then showed that these two work in different ways in order to achieve maximum power densities. A series connection improves operational output potential difference and on the other hand, a parallel connection improves operational current output. Due to this trade-off between operational output potential difference and current output, Zhang et al. (2017) demonstrated that a hybrid configuration can be used for stacked MFCs in order to improve both current output and output potential difference, although the power density will be lower as compared to parallel and series connections.

2.2.4 Factors affecting performance

Figure 2.8 shows typical polarization curve and output potential difference losses in MFC.

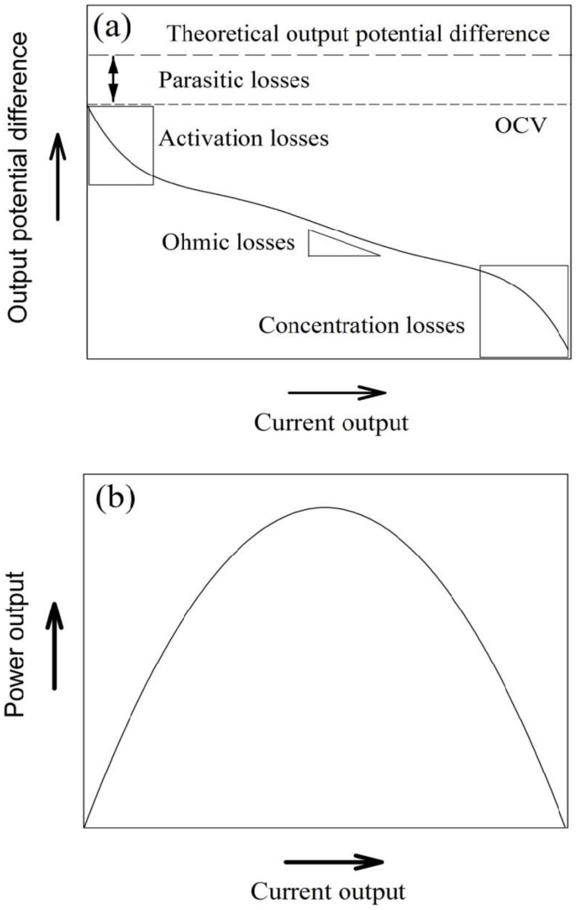

Figure 2.8 (a) A typical polarization curve and output potential difference losses in MFC, and (b) a typical power output curve.

The performance of MFCs is affected by various losses which limit the attainment of theoretical output potential difference under open circuit conditions. This is due to irreversible losses that occur in the MFC which are also known as overpotentials. These three main irreversible losses are identified as activation losses, ohmic losses and concentration losses as shown in Figure 2.8a. These losses occur due to the thermodynamic requirement to activate the electrochemical reactions, resistance to charge flow and mass transfer limitations. Other losses which affect the performance of MFC are parasitic losses which are mainly caused by the crossover of substrate and unwanted side reactions. The level of magnitude of these losses varies from system to system. A typical power density curve is shown Figure 2.8b.

2.2.4.1 Activation losses

The performance of MFC depends on the kinetics of the electrochemical reactions which take place at the cathode and anode. The kinetics are limited by the activation energy of each reaction and are mostly dominant at low current densities/output as shown in Figure 2.8a (Fu et al., 2010). Various steps can be taken to reduce the activation losses. These include increasing the porosity and surface area of the anode, introduction of soluble mediators to improve the anode-bacteria interaction or using microbes that use conducting pili to attach to the electrode, increasing the operating temperature of the anode, and establishing an enriched biofilm on the anode electrode (Kundu and Dutta, 2018).

2.2.4.2 Ohmic losses

MFC performance is also restricted by the ohmic losses. These are the losses caused by the resistance to the flow of electrons through the interconnections, electrodes, catholyte and anolyte. This loss is located on the linear region of the polarization curve as shown in Figure 2.8a and can be calculated using Ohm’s law in which the magnitude of the gradient represents the internal resistance (Kundu and Dutta, 2018). There are several ways which can be employed to reduce this type of loss, namely by minimizing the spacing of the cathode and anode electrode, reducing the electron travel distance within the electrodes, and using low resistive electrodes. It should be noted that the internal resistance is dominated by ionic resistance due to the electrolyte, and in addition, the electronic resistance is mostly negligible.

2.2.4.3 Concentration losses

The process of supplying substrates and oxidants at the electrode and the removal of the oxidized products and reduced oxidants is governed by mass transfer. When there is insufficient mass transfer, this leads to low oxidant or substrate concentration at the surface of the electrode. This in turn results in a loss of output potential difference which is caused by a decrease in reaction rate at the electrode surface. These losses normally occur at high current densities and increase as the current density increases as shown in Figure 2.8a. In order to reduce this type of loss, one can modify the electrode design such as porosity, composition, thickness, and specific surface area (Rismani-Yazdi et al., 2008). Ideally this should improve mass transfer and prevent product accumulation. Employing continuous flow MFCs such as UMFC can improve the flux of substrate or oxidant to the electrode. This has been reported in a previous study by Jong et al. (2006) in which the reduction of retention time from 2.7 min to 0.7 min increased the performance of the MFC.

2.2.4.4 Parasitic losses

Additional losses to the three main losses are known as parasitic losses. These losses occur due to substrate crossover and unwanted reactions which have been reported in previous studies (Elangovan and Dharmalingam, 2016, 2017; Kim et al., 2016). Ideally, the substrate should not pass through the membrane but due to molecular diffusion and electro-osmosis (Jiang and Chu, 2003), there is some form of substrate crossover that occurs. This results in the lowering of MFC performance due to the decrease in coulombic efficiency since less substrate is consumed at the anode. Furthermore, the substrate and its oxidized products may lead to the poisoning of the cathode surface. Therefore, this means that a careful consideration on both the material and thickness of the membrane needs to be looked at so that parasitic losses are reduced.

2.3 Electrochemically Active Bacteria

2.3.1 Classification of electrochemically active bacteria

Electrochemically active bacteria (EAB) can be classified as either electrogenic bacteria or electrotrophic bacteria. Electrogenic bacteria are microorganisms that have the ability to transfer electrons outside of the bacterial cell to extracellular electron acceptors. They are used in the anode as biocatalysts in order to generate electrons from the substrate and improve MFC performance. The examples of electrogens that have been identified in previous studies include *Geobacter sulfurreducens* (Bond and Lovley, 2003), *Shewanella oneidensis* MR-1 (Bretschger et al., 2007) and *Shewanella putrefaciens* (Yang et al., 2017). In addition, weak electrogens which produce low current densities that have been identified include *Bacillus subtilis* and *Klebsiella aerogenes* (Logan et al., 2019). The other type of EAB includes electrotrophic bacteria which are microorganisms that have the ability to transfer electrons into the bacterial cell from extracellular electron donors. They can be used in cathode as biocatalysts in order to consume electrons and enhance the performance of the MFC. Microorganisms that have been identified as electrotrophs include *Geobacter metallireducens* (Gregory et al., 2004), *Klebsiella pneumoniae* (Rhoads et al., 2005) and *Acidithiobacillus ferrooxidans* (Ishii et al., 2015).

Recently, it has been shown that EAB are not limited to mesophilic conditions or typical ranges of pH and salinity. This is because several EAB can be classified as extremophiles, which are electrochemically active bacteria that can survive extreme environmental conditions. These include acidophiles, alkaliphiles, halophiles and thermophiles. An example of an acidophile EAB which survived an acidic MFC environment includes *Acidiphilium* sp. (Malki et al., 2008), and an alkaliphile EAB which survived an alkaline MFC environment includes *Geoalkalibacter* spp. (Badalamenti et al., 2013). Both also improved MFC performance. Furthermore, halophilic and thermophilic EAB which improved MFC performance are *Geoalkalibacter* (Luo et al., 2017) and *Calditerrivibrio nitroreducens* (Fu et al., 2013). The usage of extremophilic EAB demonstrates that there are no limitations in the generation of current under extreme conditions. Also, the usage of extreme conditions such as high temperatures can provide advantages such as reduced contamination and fast electrochemical reaction rates in the MFC.

2.3.2 Types of electron transfer mechanisms

Electron transfer to and from the EAB is one of the most important factor which plays a role in the performance of the MFC. Also, numerous studies have been performed in order to understand the mechanisms involved in the transfer of electrons. This is due to the fact that the knowledge acquired from these studies will be able to help researchers to better select the microorganisms suitable for MFC application through correct classification of the EAB and identification of the mechanisms involved in the electron transfer. The extracellular electron transfer (EET) mechanisms can be classified into two main categories, namely direct electron transfer (DET) and mediated electron transfer (MET). Furthermore, electron transfer through conductive pili of EAB can be used to represent an extension of DET. Figure 2.9 illustrates the schematic representation of the mechanisms.

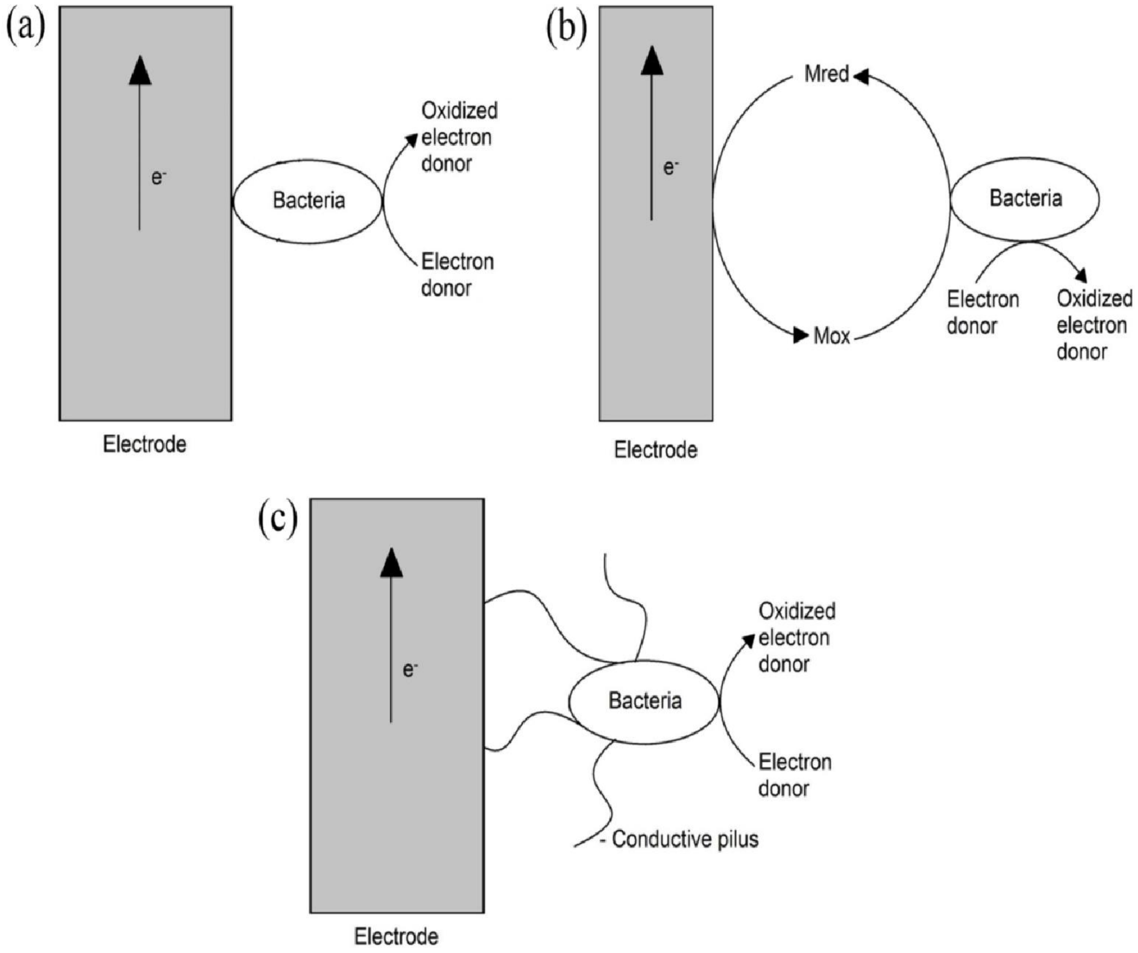

Figure 2.9 Electron transfer mechanisms that exists between anode and the electrochemically active bacteria: (a) direct electron transfer, (b) mediated electron transfer, and (c) via conductive pili.

2.3.2.1 Direct electron transfer

DET is related to the transfer of electrons through the adherence of bacterial cells on the electrode without exogenous mediators (Figure 2.9a). Most of the bacterial cells that use this type of mechanism belong to the *Geobacteraceae* family. Although it must be mentioned that the first genus to demonstrate the transfer of electrons without exogenous mediators through possibly DET was *Shewanella* (Kim et al., 1999). Furthermore, *Geobacter* sp. was confirmed to transfer electrons through possibly DET (Basséguy et al., 2014). DET is known to use membrane-bound redox proteins which require a direct contact between the surface of the bacteria and the electrode. This was demonstrated in a study by Holmes et al. (2006) who showed that these redox proteins are c-cytochromes. C-cytochromes were oxidized and reduced by losing and gaining electrons from the iron atom located in the heme of the bacteria. Some of the c-type cytochromes used for DET that exist on the surface of the bacterial cells include OmcS, OmcE and OmcB.

2.3.2.2 Mediated electron transfer

MET can occur via two types of mediators: exogenous mediator and endogenous mediator. MET via exogenous mediator involves an electron transfer between bacteria and the electrode using an external soluble mediator (Figure 2.9b). The oxidized form of this mediator enters the bacteria and gets reduced, and upon its release into the electrolyte solution, it gets re-oxidized and transfers electrons to the electrode. Various compounds have been tested in the past as exogenous mediators. Quinine, phenoxazine, phenozine, and phenothiazine are one of the compounds tested and with thionine being the most widely used artificial mediator (Basséguy et al., 2014). However, due to the fact that the bacteria are dependent on the external mediator to transfer electrons, most of these MFCs which use exogenous mediators contain bacteria which are not intrinsically electroactive. Also, the mediators produce low current densities and coulombic efficiencies i.e., 54% of the consumed glucose leads to energy generation in MFC (Schröder, 2007). Additional disadvantages include constant addition of the mediator when using a continuous MFC and the mediators are toxic to humans and cannot be used in an environment that is open. Therefore, in order to avoid having to use exogenous mediators, one has to consider possibly using EAB which employ MET via endogenous mediator.

Previous studies have shown that bacteria have the ability to transfer electrons using endogenous mediators (Xin et al., 2020; Zou et al., 2017). The endogenous mediators are naturally derived from the bacterial cell and include flavinic compounds from *S. oneidensis* MR-1 (Yang et al., 2015) and 2-amino-3-carboxy-1,4-naphthoquinone (ACNQ) secreted by *Shewanella putrefaciensare* (Freguia et al., 2010). They are excreted from the cells in reduced forms and are oxidized to transfer electrons at the electrode. Most bacteria that generate electricity in MFC without exogenous mediators are electroactive. In addition, the bacteria produce their own mediators and eliminate the requirement of a constant mediator addition during continuous operation of the MFC. Since most of the mediators naturally produced by bacteria are non-toxic, this enables the MFC to be easily handled by humans without being detrimental to their health.

2.3.2.3 Electron transfer via conductive pili

From the earliest to present studies, the investigations on DET have focused on the c-type cytochromes which are located in the periplams and outer membrane (Shi et al., 2016). However, in order to explain the improvement of MFC due to thicker biofilms, a hypothesis was presented which described the long distance electron transfer in mediator-less MFCs. This involved a pilus acting as a conductive nanowire produced by the bacterial cells as a possible explanation (Figure 2.9c). Many studies used *Geobacter* as a model species. One of the first studies to report on conductive nanowire was a study done by Childers et al. (2002). This study found that when *Geobacter metallireducens* was grown on insoluble Fe(III) oxides as an electron acceptor, it expressed pili and led to the detection of gene transcripts for the putative pilin monomer, PilA. A similar study done by Reguera et al. (2005) also observed the same pili expression during the growth of *Geobacter sulfurreducens* on Fe(III) oxide, but not with soluble Fe(III) and determined the diameter of the conductive nanowires to be 3 nm. In addition, there was no filament development and reduction in Fe(III) oxide observed when the PilA pilin monomer gene was deleted from the wild-type *G. sulfurreducens*. This meant that *G. sulfurreducens* depended on PilA pilin monomer for the development of pili and reduction of Fe(III) oxide.

Reguera et al. (2005) found that in addition to using Fe(III) oxide for pili growth in *G. sulfurreducens*, fumerate can also be used as an electron acceptor substitute. Moreover, they observed that when adding poorly crystalline Fe(III) oxide to *G. sulfurreducens* grown using fumerate, the nanoparticles attached to the pili. To determine if the pili were conductive, Reguera et al. (2005) used conductive-tip atomic force microscopy (AFM) which revealed that the pili were conductive. This finding coupled with the observation that pilA-deficient *G. sulfurreducens* could not reduce Fe(III) oxide, led to the discovery that there is a long-distance electron transfer mechanism involved in addition to the DET mechanism through direct membrane attachment. This was further demonstrated for biolectrochemical systems, which suggested that *G. sulfurreducens* nanowires played an important role in the long-distance electron transfer to the electrode (Reguera et al., 2006). To avoid confusion with other conductive structures such as flagella, pilin-based microbial nanowires are now referred to as e-pili (Lovley, 2017).

It should be noted that there is still more work that needs to be done. This is because it has been demonstrated that the *G. sulfurreducens* outer surface *c*-type cytochrome known as OmcS can form filaments (Wang et al., 2019). Which introduces the question that was the e-pili detected not OmcS filaments? One recent study even makes such an interesting claim that previous studies on *G. sulfurreducens* e-pili had made a mistake, and were in fact studying filaments of OmcS (Wang et al., 2019). However, due to the evidence that exists in some studies, that the filaments were retaining the diameter of an e-pili, and differing greatly in conductivity depending on the density of aromatic amino acids in the pilin monomer (Lovley and Walker, 2019), it is difficult to accept such a claim. Provided that the filaments are OmcS, how could the aromatic density of the PilA monomer influence the OmcS filament conductivity? Maybe the two coexisted. That is still a question that needs to be answered which makes the study of conductive nanowires intriguing.

2.4 Other Organisms Used in Microbial Fuel Cells

2.4.1 Humus powered fuel cell

The soil has several layers which are named horizons in which the arrangement of these layers is called soil profile. These horizons can be easily identified due to their different textures, structure and colour (Upton and de Groot, 2008). The nature of the horizons can then be used to classify different soil types to help provide information about the ground that is most suitable for a specific application such as farming and construction. A soil profile generally contains the following horizons: humus, topsoil, subsoil, weathered rock fragments and bedrock. The schematic is shown in Figure 2.10.

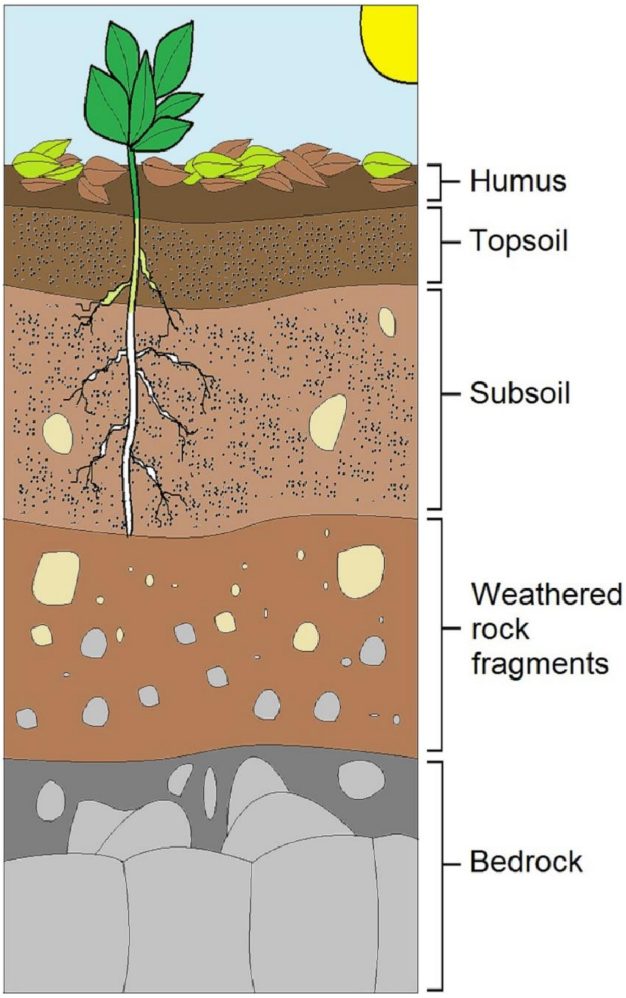

Figure 2.10 Schematic showing the soil profile.

Humus, which contains a variety of organic compounds that are chemically heterogeneous is distributed on both land and aquatic environments. Furthermore, humus is also a stable organic material that accumulates on top of the soil when plant and animal matter decay. It is considered to be a product of phenol polymerization and the phenols are derived from both fungal breakdown of lignin and as secondary metabolites in plants and bacteria. In addition, the polymerization occurs due to oxidative coupling which is catalyzed by oxidative enzymes such as phenol oxidase and laccases (Martinez et al., 2013). During oxidative coupling, amino acids are also copolymerized into the polymers (Field, 2001). Although humus is not easily biodegradable, it is very useful in providing humic substances which can be utilized as redox mediators, electron donors and electron acceptors.

Humic substances contain several redox-active moieties such as (hydro)quinone, sulfhydy, carboxylic, and phenolic functional groups which can be utilized by bacteria (Lipczynska-Kochany, 2018). They are utilized by bacteria by functioning as electron sinks, and can also function as electron sources in the form of reduced-humic substances. The first demonstration of humic substances as electron sinks or acceptors was done by Lovley et al. (1996). They showed that *Geobacter metallireducens* and *Shewanella alga* can use humic acid (HA) as a terminal electron acceptor and oxidize acetate. On the other hand, it was shown by Coates et al. (2002) that reduced-humic substances can act as electron sources or donors for the reduction of NO_3^- using anaerobes. Since humus contains quinone moieties, it has also been shown that they have the potential of acting as redox mediators. This was done by using humic hydroquinone model compound, anthrahydroquinone-2,6-disulfonate (AHQDS) and humic quinone model compound, anthraquinone-2,6-disulfonate (AQDS) (Lovley et al., 1999; Scott et al., 1998).

Due to the reason that humus can act as an electron donor, electron acceptor, and redox mediator, its use was expanded to MFCs. One of the studies which showed that the introduction of humic substances in the anode can promote the reduction of azo dye and enhance the MFC performance was done by Sun et al. (2013). Also, it was shown by another study that humus can act as a sole carbon source for an enriched microbial inoculum in the anode and effectively improve the performance of the MFC (Adekunle et al., 2017). Various studies have successfully used *M. acetivorans* and *Geobacter* sp. species such as *Geobacter sulfurreducens* (McAnulty et al., 2017; Yamasaki et al., 2018). This process is still at its developing stage, however, it introduces an interesting application into the generation of clean energy.

2.5 Physical/Structural Parameters

2.5.1 H^+ transport systems

One of the most important steps in MFC operation is the transfer of protons, mainly hydrogen ions, from the anode to the cathode chamber. This step neutralizes the build up of hydrogen ions generated in the anode. In addition, it ensures that the electrons generated from the anode are consumed at the cathode in order to complete the cell. Several ways can be employed to improve the transfer of hydrogen ions to the cathode such as the usage of salt bridge, ion selecting membranes and forward osmosis membranes.

2.5.1.1 Salt bridges

During the early stages of MFC research, salt bridges were widely used to ensure a complete MFC connection and neutralization of hydrogen build up in the anode. Most of the studies used agar salt bridges (Khan et al., 2012; Kumar et al., 2012; Sevda and Sreekrishnan, 2012). Agar would come in the form of a powder, which when dissolved in water and heated, it would form a gelatinous substance upon cooling. By adding agar and various salts in water, an agar salt bridge could then be prepared. In addition, the salts would mainly consist of potassium chloride (KCl), sodium chloride (NaCl), and potassium nitrate (KNO_3). However, almost all of the studies reported low power densities. This was attributed to high internal resistance and substrate cross-over caused by the salt bridge during operation (Min et al., 2005). Recently, various researchers are trying to minimise the internal resistance and substrate cross-over caused by salt bridge. Sarma et al. (2019) used the Taguchi method in the optimisation of salt bridge parameters. Hernández-Flores et al. (2019) synthesized and implemented characterization methods for both proton transfer and oxygen permeability which gave detailed information on how various changes affect performance. Therefore, although salt bridge is an old concept, continuous research dedicated to successful utilization of salt bridges in MFCs is still relevant today because they are less expensive and their success in improving MFC performance can help in the development of large-scale MFCs.

2.5.1.2 Ion-selective membranes

A useful characteristic that a MFC chamber separator should have is the ability to select the type of ions which permeate through it in addition to not allowing substrate or oxygen cross-over. There are various ion-selective separators that are available which can be used in MFCs. These include cation exchange membranes (CEMs) which allow positively charged ions to permeate and anion exchange membranes (AEMs) which allow negatively charged ions to permeate. Other ion-selective separators that can be used include bipolar membranes (BPMs) which allow the permeation of both the anions and cations. The schematic of the ion-selective membranes is shown in Figure 2.11.

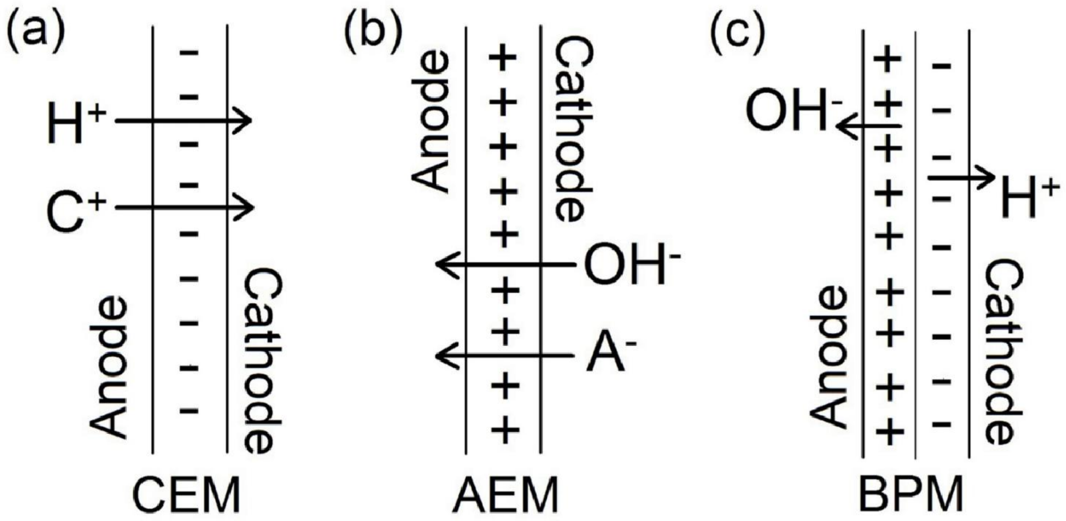

Figure 2.11 Charge transport in ion-selective membranes, namely (a) cation exchange membrane (CEM), (b) anion exchange membrane (AEM) and (c) bipolar membrane (BPM). Cations (C^+) and anions (A^-).

Membranes which allow the permeation of positively charged ions, mainly protons, are also known as proton exchange membranes (PEMs). PEMs which are commonly used in MFCs are normally made from a Nafion. Nafion is a perfluorosulphuric acid with a backbone of hydrophobic fluorocarbons ($-CF_2-CF_2-$) to which the negatively charged sulphonated groups (SO_3^-) are attached. The presence of SO_3^- is what allows the Nafion to bring into effect proton conductivity or permeation. However, pH splitting is a problem when operating MFCs with Nafion. The splitting of pH occurs due to a decrease in the anode pH as hydrogen ions are generated and an increase in the cathode pH as hydrogen ions are consumed. This leads to an increase in internal resistance and decreased MFC performance (Rahimnejad et al., 2015). Kim et al. (2007) found that this can be solved by using an AEM. Reason being that since phosphate is normally used as a buffer in MFCs, orthophosphate anions (HPO_4^{2-} and $H_2PO_4^-$) could help buffer the pH drop in the anode chamber while maintaining charge balance in both chambers. Therefore, Kim et al. (2007) used an AEM and showed an enhanced MFC performance as compared to using a Nafion. Koók et al. (2020) also demonstrated a better performance when using an AEM. The usage of BPM was shown by a previous study (ter Heijne et al., 2006), however, in comparison to both PEM and AEM, it leads to the lowest MFC performance (Harnisch et al., 2008).

It has to be noted that ion-selective membranes do have disadvantages. In addition to them being expensive, during operation they can undergo fouling. Igboamalu et al. (2019a) demonstrated that PEM is susceptible to fouling which can affect both proton transfer and performance. Therefore, finding ways to reduce membrane fouling will be beneficial when considering ion-selective membranes.

2.5.1.3 Forward osmosis membrane systems

Forward osmosis (FO) has been used to draw clean water from wastewater. FO is used to promote the flow of water from a high water potential to a low water potential area. The driving force in the process is the concentrated solution called a draw solution on the permeate side of the membrane, which has high osmotic efficiency and can be easily separated from the solution to produce portable water (Zhang et al., 2011). The advantage of using FO is that it leads to low fouling, has high rejection for a large range of contaminants, and uses low hydraulic pressure.

FO can be integrated in the operation of MFCs. In forward-osmosis microbial fuel cells (FO-MFCs), the construction of a dual chambered MFC is coupled with an installation of FO membrane instead of an ion-selective membrane (Kim et al., 2015). The wastewater and microbes are in the anode, and an oxidant and the draw solution (NaCl solution or seawater) are used in the cathode. This enables both water permeation through the FO-membrane due to the difference in osmotic pressure between the cathode and the anode chamber, and promotes energy generation. FO-MFC operation was demonstrated by Zhang et al. (2011) who successfully achieved wastewater treatment, water extraction and seawater desalination. The same study also showed that FO membranes can improve proton/ion transport.

FO membranes integrated in MFCs can perform better than AEMs or CEMs and improve MFCs power output. This is attributed to the FO membranes having a low internal resistance. One study even showed that the FO membrane can achieve an internal resistance as low as 54 Ω when compared to the 63 Ω and 73 Ω of AEM and CEM, respectively (Werner et al., 2013). In the same study, the FO membrane’s low internal resistance was consistent with ease of transport of protons and water permeation through the membrane.

2.5.2 Electrode compositions

2.5.2.1 Material

The role played by an electrode material on MFC performance is important. This is attributed to the fact that different materials have different characteristics which can affect MFC performance, and of the most important one between them all being electrical conductivity. This explains why most research in MFCs is conducted using carbon as the prime material for the electrode. Carbon is not only chemically inert under ambient conditions but it is also highly conductive. Different types of carbon materials have been used to enhance MFC performance such as graphite (Li et al., 2019), carbon cloth (Tran et al., 2019) and carbon paper (Quaglio et al., 2019). However, research is still underway in developing novel materials for application to MFCs such as carbon nanotubes (CNT). CNTs are cylindrical molecules which are made of rolled-up sheets of single-layer carbon atoms (graphene). A diameter between 0.4 nm and 6 nm represents a single-walled CNT (SWCNT) (Shi et al., 2015). A multi-walled CNT (MWCNT) consists of concentric interlinked nanotubes with diameters reaching more than 100 nm. In comparison to the widely used carbon cloth, paper or graphite, CNTs are recently receiving attention in their possible applications to MFCs. Erbay et al. (2015) reported that electrogens grown over CNTs result in excellent electron transfer due to π-π stacking between the carbon atoms and the pili of electrogenic bacteria. Also, it was reported in the same study that the spaces between CNTs provide openings for microbial growth. Furthermore, forming a highly conductive anode with a large surface area by coating CNTs over carbon cloth led to an increase in maximum power density by 250 percent when compared to non-modified carbon cloth (Tsai et al., 2009). Therefore, CNTs provide an alternative to widely used electrode materials in order to improve both conductivity and surface area.

2.5.2.2 Surface area

The surface area of an electrode has an influence on the performance of MFC. When increased, more electrogenic bacteria are able to attach which improves electron transfer by DET. Also, more reaction sites become available for oxidant reduction on the cathode electrode. Therefore, surface area optimization of the electrode provides an approach to enhance MFC performance. This was demonstrated by Oh and Logan (2006) who increased power output by only changing the cathode surface area from 2 cm^2 to 22.5 cm^2. Similar results have been reported by previous studies (Bian et al., 2018; Penteado et al., 2018). UMFCs which provide high surface area to volume ratios have also been reported (Dessì et al., 2019; Subha et al., 2019). In addition, the UMFC scalable characteristic makes them suitable for developing large scale MFCs.

2.5.3 Anode temperature

An optimal MFC anode temperature depends on the type of electrogens used in the cell. This is because electrogens can be classified based on their optimal growth temperature range such as: psychrophiles (-5°C to 20°C), mesophiles (20°C to 45°C), and thermophiles (above 45°C). Most studies performed in MFC research optimized temperatures in the mesophilic range (Li et al., 2013; Song et al., 2017), however, the limits are endless. A study done Larrosa-Guerrero et al. (2010) obtained the highest coulombic efficiency using a temperature as low as 4°C, and a study by Fu et al. (2015) optimized MFC performance to a temperature as high as 95°C. This means that MFCs can be operated at a wide range of temperatures. It all depends on the electrogens used. It must be mentioned that although MFC performance depends on the temperature where the optimal growth for the electrogens is achieved, high optimal temperatures are favoured due to high MFC power densities as compared to low optimal temperatures. This is due to an increased rate of bioelectrochemical reaction when the temperature is increased (Zhang et al., 2019).

2.6 Chemical and Biochemical Parameters

2.6.1 Carbon sources

A carbon source simply refers to any molecule which consists of a carbon that a microorganism uses to build biomass. It can be inorganic or organic. Microorganisms which can produce their own carbon source from carbon fixation in the Calvin cycle are known as autotrophs. Those that cannot are known as heterotrophs. Heterotrophs can directly utilize organic carbon sources or use inorganic compounds as sources of energy, and autotrophs only need inorganic carbon (carbon dioxide) as shown in Table 2.2.

Table 2.2 Types of heterotrophs and autotrophs.

Description	Type	Source	Examples
Heterotrophs	Chemoorganoheterotroph	Organic carbon	Fungi, non-photosynthetic bacteria
	Chemolithoheterotroph	Inorganic compound	Nitrifying bacteria
	Photoheterotroph	Organic carbon	Non-sulphur bacteria
Autotrophs	Chemoautotroph	Carbon dioxide	Methanogens
	Photoautotroph	Carbon dioxide	Green algae, cyanobacteria

Examples of electrogenic heterotrophs and autotrophs used in MFC applications are shown in Table 2.3. Heterotrophs, specifically chemoorganoheterotrophs, are most widely used.

Table 2.3 Electrogenic heterotrophs and the carbon sources utilized in MFC applications.

Name	Type	Carbon source	Construct	Maximum power density	Ref.
Rhodobacter sphaeroides	Photoheterotroph	Sodium acetate	Dual chamber	408.06 mW/m^2	(Cadirci, 2018)
Shewanella putrefaciens	Chemoorgano-heterotroph	Lactate	Dual chamber	928 mW/m^2	(Zhao et al., 2020)
Geobacter sp.	Chemoorgano-heterotroph	Sodium acetate	Single chamber	329 mW/m^2	(Kondaveeti et al., 2020)
Chlorella vulgaris	Photoautotroph	CO_2	Dual chamber	248 mW/m^2	(Aiyer, 2021)

2.6.2 Nutrient sources

For microorganisms to be able to build biomass, not only are carbon sources required, but also other nutrient sources such as nitrogen, phosphate and sulphur are essential. Microorganisms are able to utilize both organic and inorganic nitrogen sources. Although one might be preferred over the other. Organic nitrogen sources include whey, tryptone, peptone and yeast extract, however, it should be noted that these contain other growth sources. A preference of one type of organic nitrogen source over the other indicates that the microorganism favours one type of amino acid or vitamin. This is due to the fact that different organic nitrogen sources contain different amino acids or vitamins. Inorganic nitrogen sources are comprised of NH_4^+, NO_2^- and NO_3^-. Amino acids and vitamins can be added separately when using inorganic nitrogen sources. NO_2^- and NO_3^- are notably used for anaerobic respiration. When considering phosphate, potassium salts such as KH_2PO_4 and K_2HPO_4 and sodium salts such as NaH_2PO_4, and Na_2HPO_4 can be added. To add both nitrogen and phosphate, NH_4PO_4 can be used. Phosphates are important in offering buffering capacity to ensure proper functioning of the microorganism. Since some bacteria require sulphur for growth, the addition of Na_2SO_4 can help in maintaining growth, especially for sulphate reducing bacteria. Table 2.4 details nutrient sources that have worked in previous studies and their respective concentrations.

Table 2.4 Preferred nutrient source used by Matsena et al. (2020) and Igboamalu et al. (2020) (Basal mineral medium).

Inorganic nitrogen source (concentration)	phosphate source (concentration)	sulphur source (concentration)
NH_4Cl (10 mM)	KH_2PO_4 (20 mM)	Na_2SO_4 (0.8 mM)
	Na_2HPO_4 (30 mM)	$MgSO_4$ (0.2 mM)

2.6.3 Limiting micronutrients

Traces of other elements such as Fe, Mn, Mo, Cu, Co, Mg and K are required for the functioning and growth of a microorganism. This is because these can be limiting to microbial growth even though they are in trace concentrations. For example, Mn functions as an enzyme cofactor and used in Mn-containing ribonucleotide reductase, Fe functions as an electron source or sink during electron transfer, Co functions as an enzyme cofactor and Cu functions as an electron carrier (Merchant and Helmann, 2012). Table 2.5 shows the micronutrients that can be used.

Table 2.5 Preferred micronutrients used by Matsena et al. (2020) and Igboamalu et al. (2020) (Basal mineral medium).

	Element									
	Ca	Fe	Zn	Cu	Br	Mo	Mn	K	B	Co
Chemical compound	$CaCl_2$	$FeSO_4$	$ZnCl_2$	$CuCl_2$	NaBr	Na_2MoO_2	$MnCl_2$	KI	H_3BO_3	$CoCl_2$
Concentration (µM)	50	25	0.1	0.2	0.1	0.05	0.1	0.1	0.2	0.1

2.6.4 Redox potential and anode pH

Redox potential measures the reducing or oxidizing potential of a substrate or oxidant, respectively. It can be used to determine a suitable electron acceptor or donor. A more positive redox potential indicates a better electron acceptor, and a more negative redox potential indicates a better electron donor. The operational pH of the anode is specific to the intended application and the electrogens utilized. For example, some electrogens are acidophilic such as *Acidiphilium* sp. (Malki et al., 2008), some are alkaliphilic such as *Geoalkalibacter* spp. (Badalamenti et al., 2013). Hence what is normally suggested is to conduct lab experiments to optimize the pH provided the electrogen utilized is not known. For example, Vélez-Pérez et al. (2020) conducted MFC experiments under acidic anode conditions when performing the co-treatment of industrial acid mine drainage and municipal wastewater. Also, Geng et al. (2020) conducted experiments under alkaline anode conditions to improve performance of MFC. Provided that there are methanogens which hinder the performance of MFC, the pH can be optimized in order to reduce their impact and improve performance (Igboamalu et al., 2019a).

2.7 Applications of Biogenic Nanoparticles in MFCs

2.7.1 Biogenic palladium nanoparticles anode

The anode material properties can greatly affect the transfer of electrons between electrogens and the anode electrode, as a result, the enhancement of anode material properties is a crucial step in improving the efficiency of MFC. Palladium (Pd) which is a metal closely related to platinum (Pt), has been previously used to modify the anode and improve its electrocatalytic activity. This is due to Pd having an excellent electrocatalytic oxidation of various organic molecules such as formate (Quan et al., 2015) and ethanol (Wang et al., 2013) which are the metabolites from the metabolic processes of electrogens in the anode in order to improve MFC performance. For example, Formate can be oxidized by Pd nanoparticles via a direct reaction pathway (Equation (2.7)-(2.9)) (Wang et al., 2020):

$$\mathrm{HCOO^{-}{}_{ad}} \rightarrow \mathrm{H_{ad}} + \mathrm{COO^{-}{}_{ad}} \qquad (2.7)$$

$$\mathrm{H_{ad}} + \mathrm{OH^{-}} \rightarrow \mathrm{H_2O} + \mathrm{e^{-}} \qquad (2.8)$$

$$\mathrm{COO^-}_{ad} \rightarrow \mathrm{CO}_2 + e^- \tag{2.9}$$

This pathway is important since it avoids carbon monoxide (CO) poisoning during formate oxidation on Pd nanoparticles (Pramanick et al., 2020; Yu and Manthiram, 2015). Then each of the reactions of the desorption of hydrogen (Equation (2.8)) and oxidation of adsorbed $\mathrm{COO^-}$ (Equation (2.9)) can contribute one electron charge transfer which can improve the performance of MFC during formate oxidation on the anode.

However, due to the chemical synthesis of Pd nanoparticles (PdNPs) involving toxic chemicals under severe conditions, a biological synthesis has been proposed as an alternative synthesis method. This is due to the utilization of less chemical agents under less harsh conditions during biological synthesis. Previous studies which have reported on improving the anode electrocatalytic activity using biogenic palladium nanoparticles (Bio-PdNPs) include studies by both Matsena et al. (2020) and Quan et al. (2015). They utilized the ability of Pd-reducing bacteria to reduce Pd(II) to elemental Pd [Pd(0)] to synthesize Bio-PdNPs. This is achieved by Pd(II) crossing the outer membrane, reduction taking place via the periplasmic hydrogenase, and re-deposition of Pd(0) on the cells outer surface as shown in Figure 2.12 (Lloyd et al., 1998; Malunga and Chirwa, 2019). Further applications of Bio-PdNPs in MFC include evans blue removal (Quan et al., 2018b), and iohexol degradation (Quan et al., 2018a).

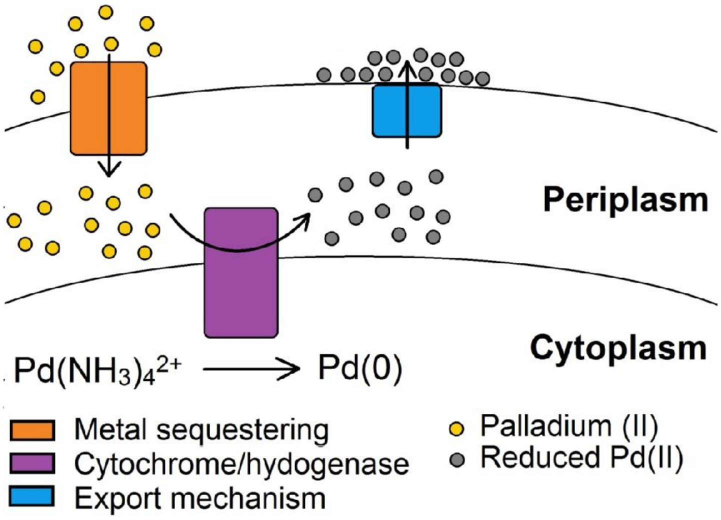

Figure 2.12 Pd(II) reduction and re-deposition of reduced Pd on Pd-reducing bacteria.

CHAPTER 3: MATERIALS AND METHODS

3.1 Bacterial Culture

3.1.1 Sources of Pd(II) reducing bacteria

The microbial culture consortium was from the sand drying beds at the Brits Wastewater Treatment Works (North West Province, South Africa). The samples were collected in sterile containers and stored at 4 °C in the refrigerator until used.

3.1.2 Culture Isolation

Bacteria cultures were isolated from the samples from sand drying beds at Wastewater treatment plant using the enrichment culture technique. A grain (0.2 g) of sludge was inoculated in the sterilized media (100 mL, Luria-Bertani (LB) broth amended with 70 mg L^{-1} initial concentration of Pd(II)) for culturing. The inoculum was incubated for 74 h at 35 ± 2 °C under shaking at 120 rpm in a Rotary Environmental Shaker (Labotec, Gauteng, South Africa). Aerobic cultures were grown in cotton plugged 250 mL Erlenmeyer flasks whereas anaerobic cultures were grown in 100 mL serum bottles purged with pure nitrogen (N_2) gas (99 % pure grade) and sealed with silicon rubber stoppers and aluminium seals prior to incubation. After 74 h enriched bacteria strains were isolated by serial dilution of the cultivated culture (Mtimunye, 2011).

Pure cultures were prepared by depositing 1 mL of serially diluted sample from the 7th to the 10th tube in the petri dishes containing LB agar using the spread method. The plates were then incubated for 24-48 h at 30 ± 2 °C to develop separate identifiable colonies. Individual colonies based on their colour and morphology were transferred into 100 mL sterile LB broth amended with 100 mg L^{-1} of Pd(II) using a heat sterile wire loop. Cells were allowed to grow for 24 h. Then again, 1 mL of culture grown for 24 h was serially diluted and 1 mL from the 7th to the 10th tube was deposited into a LB agar plate and incubated for 24-48 h at 30 ± 2 °C. The persistent colonies from the third isolation of 200 mg L^{-1} Pd(II) were used for detailed Pd(II) reduction experiments (Mtimunye, 2011).

3.2 Culture Storage

To 80 mL of bacterial culture, 20 mL of sterile glycerol was added (final glycerol concentration: 20 %, v/v). The culture was then vortexed to ensure that the glycerol was evenly dispersed and then transferred into a screw cap tube, labelled and stored at –70 °C. In order to utilize the pure stored bacterial isolates, the frozen cultures were allowed to melt at room temperature for approximately 10-15 min. The cultures were then streaked onto the surface of an LB agar plate using a sterile inoculating loop. The labelled LB plates were then incubated for 18-24 h at 30 ± 2 °C.

3.3 Culture Characterization

The phylogenetic characterization of cells was performed on isolated individual colonies of bacteria from the 7th to the 10th tube in the serial dilution preparation. In preparation for the 16S rRNA (16 Svedburg unit ribosomal Ribo-Nucleic-Acid) fingerprint method which is used to obtain DNA sequences of pure isolated cultures, the colonies were first classified based on morphology. Three different morphologies labelled (B1, B2, B3) were identified in anaerobic conditions and four different morphologies labelled (B4, B5, B6, B7) were identified for the aerobic cultures. These cultures were streaked on LB agar plates followed by incubating at 30 ± 2 °C for 18 h.

Genomic DNA was extracted from the pure cultures using a DNeasy tissue kit (QIAGEN Ltd, West Sussex, UK). The 16S rRNA genes of isolates were amplified by a reverse transcriptase-polymerase chain reaction (RT-PCR) using primers pA and pH1 (Primer pA corresponds to position 8-27; Primer pH to position 1541-1522 of the 16S gene. An internal primer pD was used for sequencing (corresponding to position 519 - 536 of the 16S gene). The resulting sequences were deposited in the GenBank to be compared to known bacteria using a basic BLAST tool search of the National Centre for Biotechnology Information (NCBI, Bethesda, MD).

3.4 Growth Media

3.4.1 Basal mineral media

Basal Mineral Medium (BMM) was prepared by dissolving: 10 mM NH_4Cl, 30 mM Na_2HPO_4, 20 mM KH_2PO_4, 0.8 mM Na_2SO_4, 0.2 mM $MgSO_4$, 50 µM $CaCl_2$, 25 µM $FeSO_4$, 0.1 µM $ZnCl_2$, 0.2 µM $CuCl_2$, 0.1 µM NaBr, 0.05 µM Na_2MoO_2, 0.1 µM $MnCl_2$, 0.1 µM KI, 0.2 µM H_3BO_3, 0.1 µM $CoCl_2$, and 0.1 µM $NiCl_2$ into 1 L of distilled water. The prepared medium was sterilized before use by autoclaving at 121 °C at 115 kg cm^{-2} for 15 min.

3.4.2 Commercial broth and agar

The first three media, LB broth, LB agar, and Plate count (PC) agar (Merck, Johannesburg, South Africa) was prepared by respectively dissolving 25 g, 45 g, and 23 g in 1000 mL of distilled water. The LB and PC agar media were cooled at room temperature after sterilization at 121 °C at 115 kg cm^{-2} for 15 min and then dispensed into petri dishes to form agar plates for colony development.

3.5 Reagents

3.5.1 Standard and stock solutions

3.5.1.1 Pd(II) standard and stock solution

Pd(II) stock solution (1000 mg L^{-1}) was prepared by dissolving 2.48 g of 99 % pure $Pd(NH_3)_4Cl_2{\bullet}H_2O$ (analytical grade) in 1 L deionised water. This stock solution was used throughout the experiments to serve as Pd(II) source. The standard solutions used in calibration of Atomic Absorption Spectroscopy (AAS) for total Pd(II) measurement were prepared from the Pd(II) AAS standard solution in 5 % nitric acid stock solution in a 50 mL volumetric flask by diluting certain volume of Pd(II) AAS standard solution with distilled water to give desirable final concentrations: 1 mg L^{-1}, 2.5 mg L^{-1}, 5 mg L^{-1}. From these data points a linear graph/calibration curve with the regression of 99 % was obtained.

3.5.1.2 Cr(VI) standard and stock solution

Cr(VI) stock solution (1000 mg L^{-1}) was prepared by dissolving 3.74 g of 99 % pure K_2CrO_4 (Analytical grade) in 1 L deionised water. This stock solution was used throughout the experiments to serve as Cr(VI) source. The standard solutions of Cr(VI) were prepared from the Cr(VI) stock solutions in a 10 mL volumetric flask by diluting certain volume of Cr(VI) stock solution with distilled water to give desirable final concentrations ranging from 0-100 mg L^{-1}. From these data points (absorbance against concentration) a linear graph/calibration curve with the regression of 99 % was obtained (Mtimunye, 2011).

3.5.2 Sodium formate stock solution

The 20 000 mg L^{-1} stock solution was prepared by adding 20 g of sodium formate (Sigma Aldrich) in 1 L bottle.

3.5.3 DPC solution

1,5-diphenylcarbazide (DPC) (Merck, South Africa) solution was prepared for Cr(VI) reduction analysis by dissolving 0.5 g of 1,5-diphenylcarbazide in 100 mL of HPLC grade acetone and was stored in a brown bottle covered with a foil.

3.5.4 Sodium chloride solution

Sodium chloride solution (0.85 % NaCl) was prepared by dissolving 1.85 g of sodium chloride salt in 100 mL distilled water and sterilized by autoclaving at 121 °C for 15 min.

3.6 Anaerobic Bio-PdNPs Synthesis

Pd(II) stock solution described in Section 3.5.1.1 was used throughout the experiments to serve as Pd(II) source. *Citrobacter* sp. which was isolated by Matsena et al. (2020) capable of Bio-PdNPs production was used during synthesis. *Citrobacter* sp. was grown anaerobically in a 1 L Erlenmeyer flask containing 400 mL LB broth for a period of 24 h at 28 °C. Cells were then collected under anaerobic conditions by centrifuging at 6000 rpm (2820 g) at 4 °C for 10 min. The supernatant was decanted and the remaining pellet was washed three times in a sterile saline solution (0.85 % NaCl) under an anaerobic glove bag purged with 99 % N_2 gas.

Bio-PdNPs production was conducted in 100 mL serum bottles by adding Pd(II) and sodium formate stock solution into the BMM to give the optimum final Pd(II) concentration of 100 mg L^{-1} at optimized pH of 6 and temperature of 30 °C as determined by Matsena et al.

(2020). Sodium formate with a concentration of 5 g L^{-1} was used as an electron donor. Prior to inoculating the serum bottles with the harvested cells under anaerobic conditions, 4 mL of a sample was withdrawn from each serum bottle at various Pd(II) concentration to determine the Pd(II) concentration before inoculating the bottles with viable cells. The cells were then transferred into 100 mL experimental serum bottles under an anaerobic glove bag purged with 99 % N_2 gas. The experimental serum bottles were then directly purged with 99 % N_2 gas for about 10 min to expel any oxygen gas before sealing with silicon rubber stopper and aluminium seals. The experimental serum bottles were then incubated at 30 ± 2 °C with continuous shaking on a lateral shaker (Labotec, Gauteng, South Africa) at 120 rpm.

Pd(II) reduction was monitored by withdrawing 4 mL of the sample at regular time intervals using a sterile syringe. Then the withdrawn samples were then centrifuged using a 2 mL Eppendorf tube at 6000 rpm (2820 g) for 10 min in a Minispin® Microcentrifuge (Eppendorf, Hamburg, Germany) in order to remove suspended cells before Pd(II) concentration analysis. The microbial cells after Bio-PdNPs formation and complete removal of Pd(II) were then collected through centrifugation at 6000 rpm for 15 min, cleaned with distilled water, and dried in an oven at 105 °C.

3.7 Single chamber (air-cathode) MFC Studies

3.7.1 Anode chamber inoculation

The microbial culture consortium collected from Brits was grown in 2 days incubation time at a temperature of 30 ± 1 °C at 150 rpm anaerobically in Erlenmeyer flasks containing 1 L of LB broth and 1 g dried sludge. Cells were harvested by centrifuging at 6,000 rpm at 4 °C for 10 minutes, the supernatant was discarded, and the pellet was washed three times in a sterile solution of 0.85 % of NaCl whilst centrifuging. Experiments were conducted in 250 mL anode chamber by adding glucose (5 g L^{-1}) in BMM, and the harvested cells were added in anode chamber which was then purged with nitrogen gas for 12 minutes before each experiment. Anode chamber was tightly sealed to prevent air from entering.

3.7.2 Air-cathode MFC construction

Air-cathode MFC was constructed as shown in Figure 3.1, Figure 8.1 and Figure 8.2.

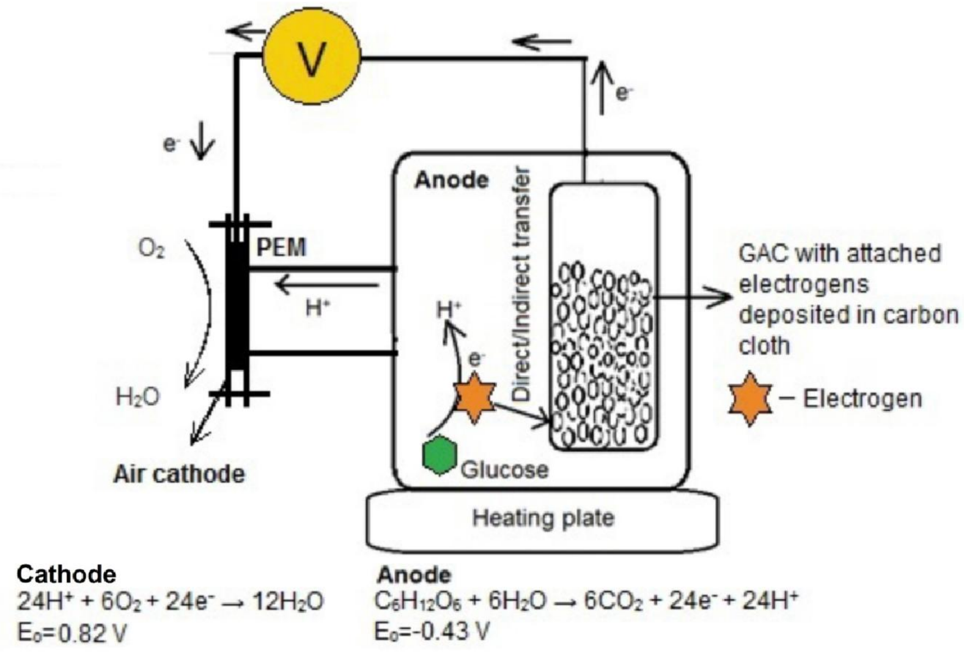

Figure 3.1 Air-cathode MFC set-up.

Air-cathode MFCs operate similarly to fuel cells with the addition of bacteria acting as biocatalysts (Debabov, 2008). Under anaerobic conditions, the substrate is consumed at the anode and the bacteria attached on the anode electrode release electrons and hydrogen ions (Sharma and Li, 2010). The oxygen at the cathode then accepts the electrons and also leads to the consumption of hydrogen ions. This process leads to the generation of current due to the electrons which travel to the external circuit and hydrogen ions which travel through the membrane (Lal, 2013). Essentially, the substrate acts as an electron donor while oxygen acts as an electron acceptor and thus leads to a bioelectrochemical reaction which generates energy. The process can be described by using the electrochemical reactions for glucose as a reductant with bacteria acting as biocatalysts and oxygen as an oxidant as shown by Equations (3.1)-(3.3) (Sharma and Li, 2010):

At the anode:

$$C_6H_{12}O_6 + 6H_2O \leftrightarrow 6CO_2 + 24H^+ + 24e^- \quad E^{o}_{red,anode} = -0.43V \tag{3.1}$$

At the cathode:

$$6O_2 + 24H^+ + 24e^- \leftrightarrow 12H_2O \quad E^o_{red,cathode} = 0.82V \tag{3.2}$$

The overall redox reaction:

$$C_6H_{12}O_6 + 6O_2 \leftrightarrow 6CO_2 + 6H_2O \quad E^o_{red,cathode} - E^o_{red,anode} = 1.25V \tag{3.3}$$

where, $E^o_{red,anode}$ and $E^o_{red,cathode}$ represent the standard reduction potentials of the anode and cathode, respectively. To compute the overall standard reduction potential, the difference between $E^o_{red,cathode}$ and $E^o_{red,anode}$ is calculated, which gives a positive value of 1.25 V indicating that this type of MFC is thermodynamically feasible.

Each chamber of the air-cathode MFC had an effective reactor volume of 200 mL. The anode and cathode chambers were separated by a salt bridge with 1 M potassium chloride and 10 wt % nutrient agar composition (Sigma-Aldrich Pty. Ltd., Modderfontein, South Africa) for the salt bridge experiments, and Nafion 117 (Fuel Cell Store, Texas, USA) for the proton exchange membrane (PEM) experiments. A heating plate was used to adjust the temperature of the anode chamber.

A Polyvinylidenefluoride (PVDF) cathode was constructed by binding PVDF paste to 35 x 40 mm carbon cloth. Initially a 10 wt % PVDF solution was formed by stirring PVDF powder in 10 mL N,N-dimethylacetamide (DMAc) at room temperature. The PVDF solution was then mixed with 300 mg of activated carbon powder (ACP) and 30 mg of carbon black (CB) to form a 10:30:3 ratio of PVDF solution:ACP:CB (Yang et al., 2014). The mixture yielded a paste that was spread evenly on the carbon cloth (Aerontec Pty. Ltd., Cape town, South Africa) as shown in Figure 8.3. Thereafter, the cathode was placed in demineralized water for fifteen minutes then left to dry in a fume-hood for eight hours. For the anode, different particle sizes of 7 g of GAC (Sigma-Aldrich Pty. Ltd., Modderfontein, South Africa) were placed in 49 cm^2 carbon cloth as shown in Figure 8.4. This was done by cutting the carbon cloth to size, depositing the GAC inside the carbon cloth, and using a sewing thread to form an enclosure and to ensure that the activated carbon granules do not fall out. The air-cathode MFC was operated in a batch mode with a fixed external resistance of 1 kΩ.

3.8 Dual chamber MFC Studies

3.8.1 GAC anode modified with Bio-PdNPs preparation

The GAC anode assemblage constituted of Bio-PdNPs dispersion in a 7 mL 5 % Nafion binder solution (Fuel Cell Store, Texas, USA) using a vortex mixer for 5 min. The mixture was then coated on to the surface of GAC and left to dry under room temperature for 24 h. 5 g of GAC (Sigma-Aldrich Pty. Ltd., Modderfontein, South Africa) was then placed inside a carbon cloth with an area of 49 cm^2 as shown in Figure 8.5 (Aerontec Pty. Ltd., Cape Town, South Africa). Electrodes with different Bio-PdNPs loading were fabricated, i.e. anode electrodes loaded with Bio-PdNP1: 2 mg Bio-PdNPs g^{-1} GAC, Bio-PdNP2: 4 mg Bio-PdNPs g^{-1} GAC, Bio-PdNP3: 6 mg Bio-PdNPs g^{-1} GAC, and an unmodified GAC.

3.8.2 Proton exchange membrane

Nafion 117 (Fuel Cell Store, Texas, USA) was used to separate anode and cathode chambers.

3.8.3 Dual chamber MFC construction

A dual chambered MFC was constructed and used in the MFC experiments. The schematic of the MFC is shown in Figure 3.2.

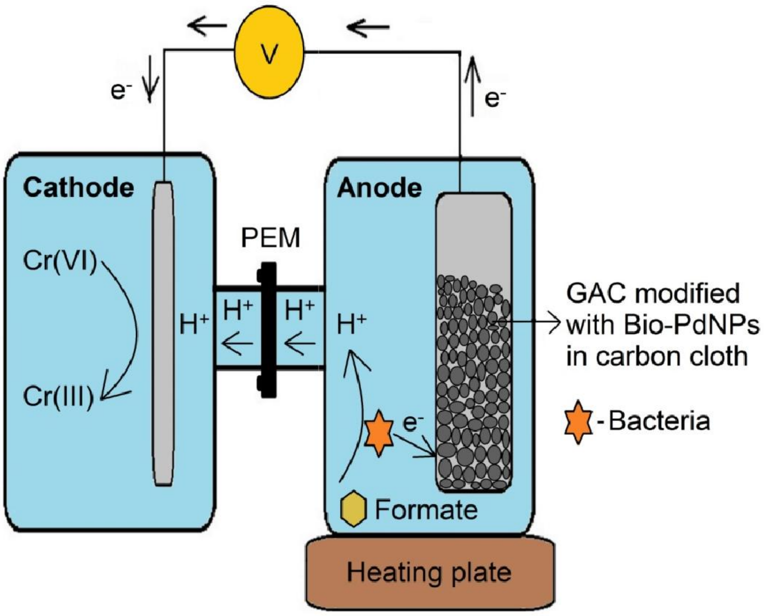

Figure 3.2 Dual chambered Cr(VI)-reducing MFC schematic.

Each chamber had a reactor volume of 250 mL. A heating plate was used to adjust the temperature of the anode chamber. During the temperature, pH and initial Cr(VI) concentration experiments, a carbon cloth without the GAC that is modified with Bio-PdNPs with an area of 49 cm^2 was used as an anode. In addition, carbon cloth with an area of 49 cm^2 was used as a cathode for all experiments as shown in Figure 8.5. The visual representation of the MFC is shown in Figure 8.6 and Figure 8.7.

The main redox reactions occurring in the Cr(VI)-reducing MFC include formate ($HCOO^-$) oxidation at the anode, where electrons generated are consumed in the cathode chamber by Cr(VI) in the form of dichromate ($Cr_2O_7^{2-}$) to form trivalent chromium (Cr^{3+}). Equations (3.4) and (3.5) represent the half reactions with their standard reduction potentials defined for the anode ($E^o_{red,anode}$) and cathode ($E^o_{red,cathode}$), respectively:

Anode chamber:

$$3HCOO^- \leftrightarrow 3CO_2 + 3H^+ + 6e^- \qquad E^o_{red,anode} = -0.43V \tag{3.4}$$

Cathode chamber:

$$Cr_2O_7^{2-} + 14H^+ + 6e^- \leftrightarrow 2Cr^{3+} + 7H_2O \qquad E^o_{red,cathode} = 1.33V \tag{3.5}$$

3.8.4 Start-up culture

The anode chambers were inoculated with sludge obtained from Brits Wastewater Treatment Plant in South Africa. Before usage in the MFC, 2 g of the microbial culture consortium from Brits sludge was first enriched 1 L Erlenmeyer flask containing 400 mL of Luria-Bertani (LB) medium for 24 h at 28 °C under anaerobic conditions with continuous shaking on a lateral shaker (Labotec, Gauteng, South Africa) at 120 rpm. After enrichment the microbial cells were then collected under anaerobic conditions by centrifuging at 6000 rpm (2820 g) at 4 °C for 10 min to be used in MFC experiments.

3.8.5 Reactor start-up

Prior to the experimental run, the pH of the BMM containing a carbon source of sodium formate (5 g L^{-1}) was adjusted to pH of 7. The microbial cells were then added to the BMM and fed to the anode chamber. After that, the anode was purged with N_2 for 5 min. Phosphate buffer solution (PBS) was used to regulate pH of the cathode.

3.8.6 Reactor operation

The MFC was operated in a batch mode with a fixed external resistance of 1000 Ω and at a desired temperature. After each experiment, a polarization curve was constructed. Three sets of experiments were performed. For all sets, BMM composition was constant. For the first set, the temperature, pH and initial Cr(VI) concentration were optimized and a carbon cloth without the GAC that is modified with Bio-PdNPs with an area of 49 cm^2 was used as an anode. For the second set, the effect of GAC on the Cr(VI)-reducing MFC performance was evaluated. The last set involved using the Bio-PdNPs to improve Cr(VI)-reducing MFC performance.

3.9 Analytical Methods

3.9.1 Pd(II) concentration analysis (AAS)

An AAnalyst 400 Atomic Absorption Spectrometry (AAS) fitted with a S/N 201S8070301 Auto sampler Model 510 was used to determine the Pd(II) concentration. All tests were carried out using a Perkin-Elmer Lumina Pd lamp at a wavelength of 244.79 nm.

3.9.2 Cr(VI), total Cr and Cr(III) concentration analysis (UV/Vis spectrophotometer and AAS)

Cr(VI) concentration was determined colorimetrically using UV/Vis spectrophotometry (WPA, Light Wave II, and Labotech, South Africa) and the 1,5-diphenylcarbazide (DPC) method (American Public Health Association, 2005). Total chromium (Cr) was determined using a AAnalyst 400, S/N 201S8070301 atomic absorption spectrometer fitted with a model Model 510 auto sampler. The analysis was conducted using a 3 mA chromium hollow cathode lamp at a wavelength of 359.9 nm. Calibration curves were constructed for both Cr(VI) concentration and total Cr analysis using standard solutions prior to determination of the sample concentrations. Total Cr measures the sum of aqueous Cr(VI) and Cr(III) concentrations. Therefore, Cr(III) in the solution was determined as a difference between total Cr and Cr(VI) (Huang et al., 2010).

3.9.3 Morphology analysis (SEM)

The morphologies of the GAC were determined using a Zeiss Ultra Plus field emission scanning electron microscope (FE-SEM) (Zeiss, Germany) at 2 kV. The samples were allowed to air dry and pieces of each sample were mounted with adhesive carbon tape on aluminium stubs in the upright position.

3.9.4 Surface area analysis (BET)

The surface area of the GAC was determined using nitrogen adsorption and desorption isotherms measured at 77.3 K using Micromeritics TriStar analyzer (TriStar II 3020 V3.02). The samples were degassed in vacuum at 100 °C for at least 8 h. The surface area is derived according to the Brunauer, Emmett, and Teller (BET) method.

3.9.5 Electrochemical analysis and calculations

The output potential difference of the MFC was monitored using a computer-based data acquisition system connected to a UNIT-TREND UT61A multimeter (UNI-TREND TECHNOLOGY Limited, Kowloon, Hong Kong) and UT61 software (UNI-TREND TECHNOLOGY Limited, Kowloon, Hong Kong). Polarization curves were constructed by varying the external resistance (2.7 Ω - 1.2 MΩ) at 15-min time interval, starting from open circuit voltages (OCV). The current density was determined using Equation (3.7):

$$j = \frac{\Delta \mathrm{Voltage}}{R_{ext} v} \tag{3.7}$$

where j denotes current density in mA m^{-3}, ΔVoltage is the measured output potential difference in mV, v is the effective anode volume in m^3 and R_{ext} is the external resistance in Ω. The power density was determined using Equation (3.8):

$$P = \frac{j\Delta V}{1000} \tag{3.8}$$

where P is power density in mW m^{-3}. The coulombic efficiency (CE) was obtained by determining the ratio between the current generated to the theoretical current output as per Equation (3.9):

$$CE = \frac{M \int_0^t I dt}{nFv\Delta C_{cr}} x100 \tag{3.9}$$

where I is current output (A), M is molecular weight of chromium (52 g mol^{-1}), v is the working volume of the cathodic chamber (L), n is the number of electrons exchanged per mole of Cr(VI)=3, F is Faraday's constant (96485 A s mol^{-1}), ΔC_{cr} is the concentration of Cr(VI) (g L^{-1}). To get the volume-specific internal resistance, the slopes of the polarization plots as a function of current density were fitted to a linear equation as shown in Equation (3.10) (Liu et al., 2017):

$$\Delta \text{Voltage} = mj + c \tag{3.10}$$

where j is the current density (mA m^{-3}), m is the absolute value defined as the volume-specific internal resistance (Ω m^3), c is the open circuit voltage (mV). To get the internal resistance, the volume-specific internal resistance was divided by the volume of the anode chamber.

3.10 Polarization Curve and Power Output Simulation when Modelling

During output potential difference vs. time curve, the MFC simulation was done until a maximum output potential difference was obtained. Then, the polarization curve was simulated by varying the external resistance (2.7 Ω - 1.2 MΩ) and calculating the output potential difference since external resistance affects output potential difference as shown by Igboamalu et al. (2019a). Then to be able to plot the polarization curve, which is essentially an output potential difference vs. current density curve, the current density was determined using Equation (3.11):

$$j_A = \frac{\Delta V_{MFC}}{r_{ext} A_{anode}} \tag{3.11}$$

where j_A denotes current density in A m^{-2}, ΔV_{MFC} is the predicted MFC output potential difference in V, A_{anode} is the effective anode area in m^2 and r_{ext} is the external resistance in Ω. The power density was calculated using Equation (3.12) so that a power density curve which is a power density vs. current density can be plotted:

$$P_A = j_A \Delta V_{MFC} \tag{3.12}$$

where P_A is power density in W m^{-2}.

CHAPTER 4: IMPROVED PERFORMANCE AND COST EFFICIENCY BY SURFACE AREA OPTIMIZATION OF GRANULAR ACTIVATED CARBON IN AIR-CATHODE MICROBIAL FUEL CELL

4.1 The Effect of Temperature on Air-Cathode MFC

Temperature variation based experiments were initially conducted using a carbon cloth without GAC at pH 6 and by using a salt bridge as a separator (Figure 4.1).

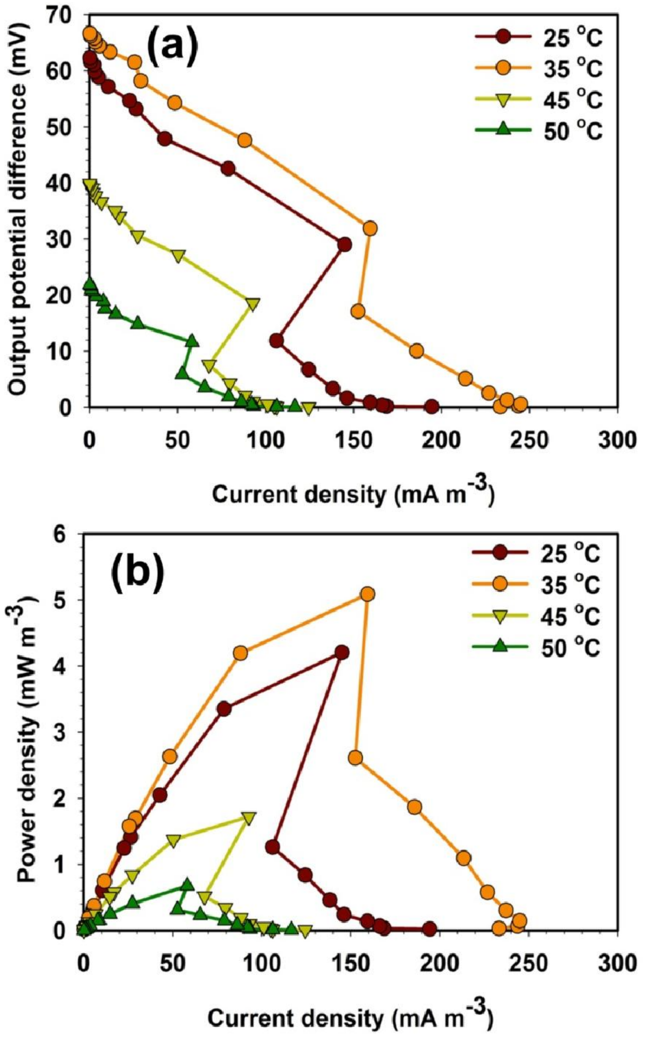

Figure 4.1 The effect of anode temperature (25 °C, 35 °C, 45 °C, 50 °C) on (a) output potential difference (polarization curve), (b) power density of an air-cathode microbial fuel cell.

The results in Figure 4.2 which were adapted from polarization and power density curves in Figure 4.1 will be used to explain the effect of pH on air-cathode MFC performance. The results represent the output potential difference and current density observed at maximum achieved power density (Figure 4.2). The temperature increase from 25 °C to 35 °C led to an increase in achieved output potential difference (from 29.1 mV to 31.9 mV), current density (from 145.2 mA m^{-3} to 159.5 mA m^{-3}) and maximum power density (from 4.2 mW m^{-3} to 5.1 mW m^{-3}). However, a further increase to a temperature of 45 °C and above led to a steep decrease in achieved output potential difference, current density and maximum power density to final values of 11.6 mV, 58.1 mA m^{-3} and 0.7 mW m^{-3} respectively.

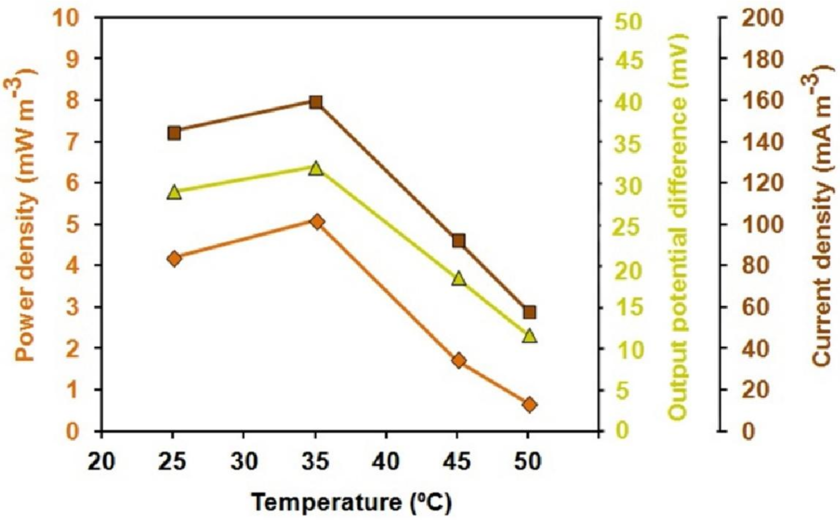

Figure 4.2 The effect of anode temperature on current density and output potential difference at maximum achieved power density.

This can be explained by the consideration of the fact that microorganisms can be categorized by their optimum growth temperature: (i) the temperature range of -5 °C and 20 °C is best for the growth of psychrophiles, (ii) the temperature range of 20 °C and 45 °C is best for the growth of mesophiles, and (iii) the temperatures above 45 °C are best for the growth of thermophiles. As a result, this means that the reason for the differences in air-cathode performance at different temperatures can be related to microbial growth. Just glancing at the results in Figure 4.2, it can be seen that the optimum temperature for the performance of air-cathode MFC was 35 °C. This meant that the bacteria contained in the Brits sludge better grew under mesophilic temperatures. This was ascertained by monitoring the optical density

(OD) of the microorganisms during the experimental runs. As it can be seen in Figure 4.3, the temperature of 35 °C had the highest microbial growth which means that it is the optimal growth temperature for the Brits microbial consortium. The microbial growth was measured in optical density (OD) at wavelength of 600 nm using a UV/Vis spectrophotometer.

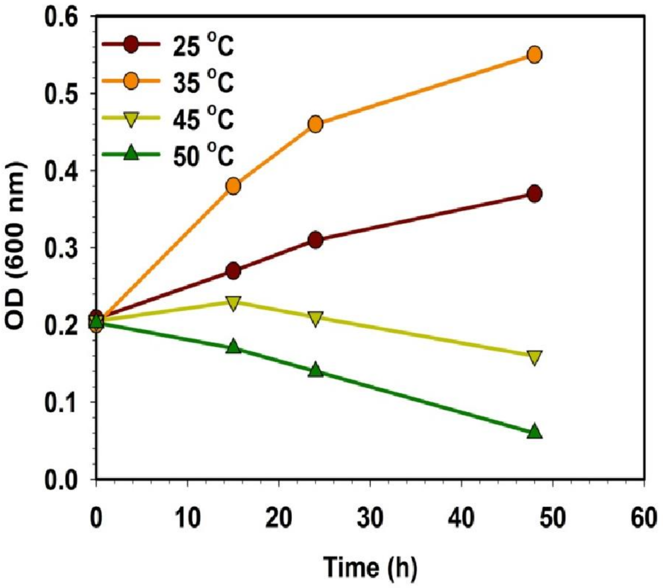

Figure 4.3 The effect of anode temperature on microbial growth.

The reason the temperature led to the deterioration of air-cathode MFC performance was due to two reasons: (i) the decay of the electrogens or (ii) the slow growth rate of the electrogens. To further elaborate, the temperatures of 45 °C and 50 °C displayed a decay in the microorganisms (Figure 4.3) and this is related to the denaturation of proteins which affects the survival of the electrogens at thermophilic temperatures (Behera et al., 2018; Schiraldi and De Rosa, 2014). In addition, it can be seen in Figure 4.3 that at 25 °C, low temperatures lead to slow growth rates (Michie et al., 2011). This is because low temperatures slow down the enzymatic activity and decrease metabolic activity within the microbial cells (Liao et al., 2019). Considering the decay of microorganisms at high temperatures (45 °C and 50 °C), and a slow growth rate at a low temperature (25 °C), this explains the reason for the decrease in performance of the air-cathode MFC.

4.2 The Effect of pH on Air-Cathode MFC

The effect of anode pH on the performance of MFC was evaluated using a carbon cloth without GAC at a temperature of 35 °C and by using a salt bridge as a separator. The results in Figure 4.5 were adapted from polarization and power density curves in Figure 4.4.

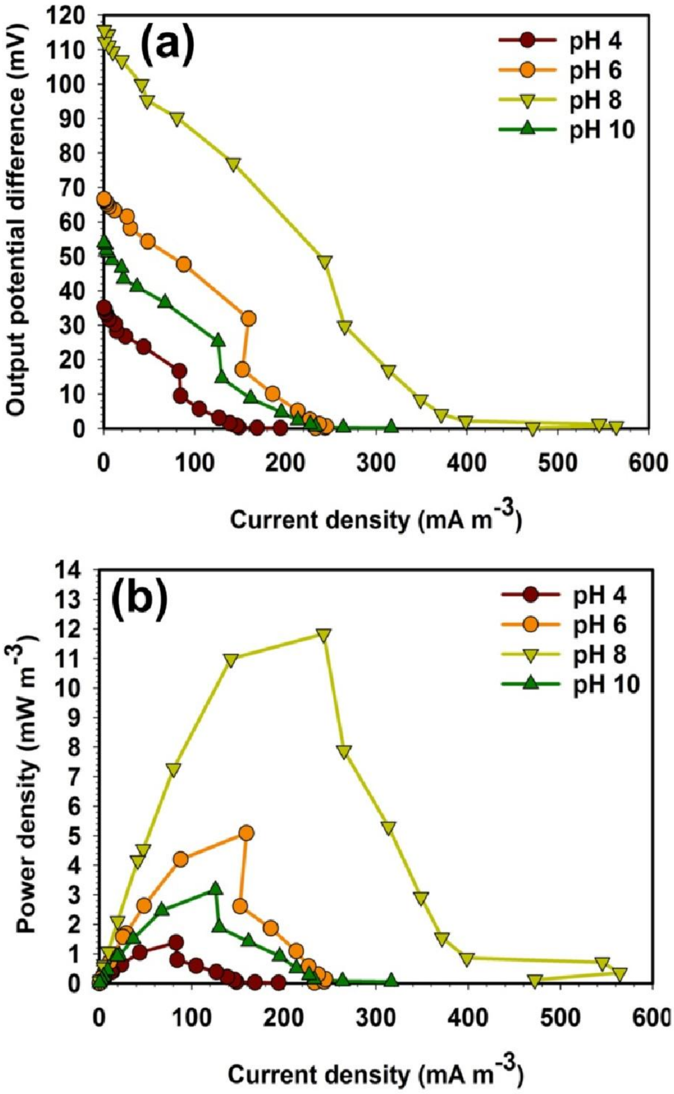

Figure 4.4 The effect of anode pH (4, 6, 8, 10) on (a) output potential difference (polarization curve), (b) power density of an air-cathode microbial fuel cell.

The results in Figure 4.5 represent the output potential difference and current density observed at maximum achieved power density during pH variation experiments. The increase in pH from a value of 4 to 8 led to an increase in achieved output potential difference (from

16.6 mV to 48.6 mV), current density (from 83.1 mA m^{-3} to 243.2 mA m^{-3}) and maximum power density (from 1.4 mW m^{-3} to 11.8 mW m^{-3}). A further increase to a pH of a value of 10 led to a decrease in achieved output potential difference, current density and maximum power density to final values of 25.1 mV, 125.9 mA m^{-3} and 3.2 mW m^{-3} respectively.

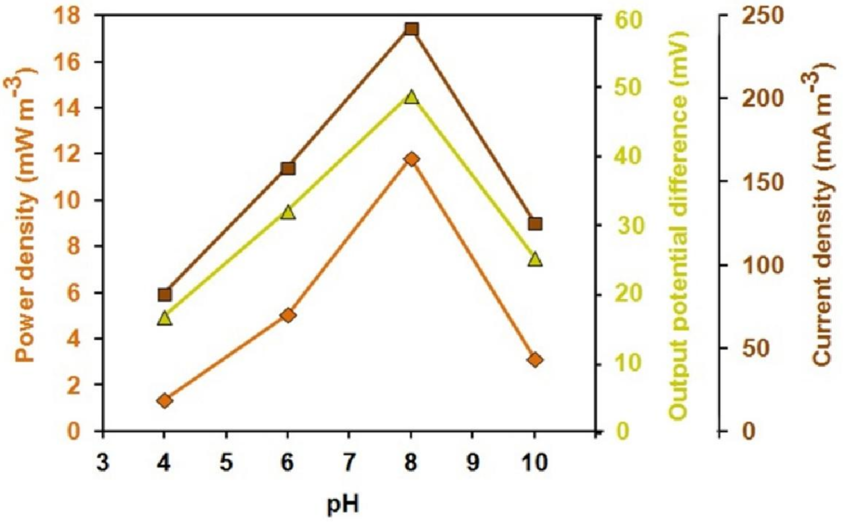

Figure 4.5 The effect of anode pH on current density and output potential difference at maximum achieved power density.

In order to explain the differences in the performance of the air-cathode MFC at varied anode pH, the microbial growth was monitored. In Figure 4.6, it can be seen that the microbial consortium from the Brits sludge preferred an alkaline pH of 8 which explains the reason for the high air-cathode MFC performance. This is due to different microorganisms having a different tolerance to the change in pH. Some microorganisms prefer an acidic environment and others prefer a basic environment. An example of an acidophile electrogen which survives an acidic MFC environment includes *Acidiphilium* sp. (Malki et al., 2008), and an alkaliphile electrogen which survives an alkaline MFC environment includes *Geoalkalibacter* spp. (Badalamenti et al., 2013). However, it should be noted that the high alkaline pH of 10 reduced MFC performance as shown in Figure 4.5 due to low growth rate (Figure 4.6). Hence, what is normally suggested is to conduct lab experiments to optimize the pH provided the electrogens utilized are not known. Although in general, the operational anode pH normally ranges between pH of 7 to 9 (Puig et al., 2010). Provided that there are methanogens which hinder the performance of MFC, the pH can be optimized in order to reduce their impact and improve performance (Igboamalu et al., 2019a).

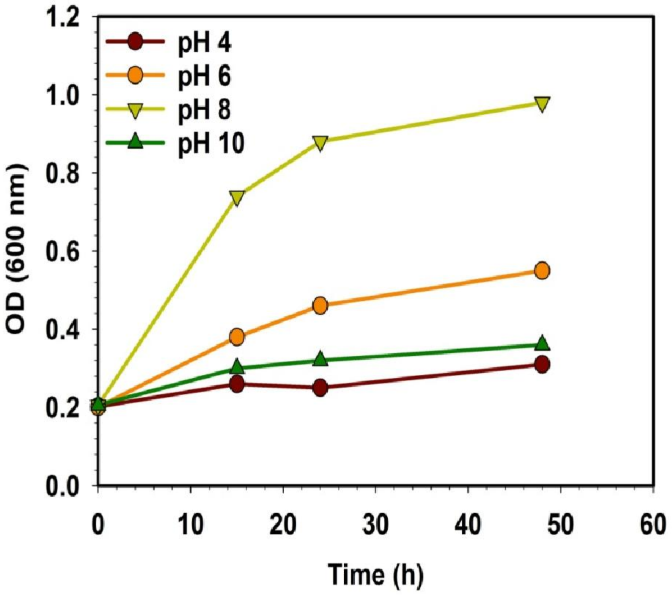

Figure 4.6 The effect of anode pH on microbial growth.

4.3 The Effect of H^+ Transport Systems on Air-Cathode MFC

During the early stages of MFC research, salt bridges were widely used ensure a complete MFC connection and neutralization of hydrogen build up in the anode. Most of the studies used agar salt bridges (Khan et al., 2012; Kumar et al., 2012; Sevda and Sreekrishnan, 2012). Agar would come in the form of a powder, which when dissolved in water and heated, it would form a gelatinous substance upon cooling. By adding agar and various salts in water, an agar salt bridge could then be prepared. In addition, the salts would mainly consist of potassium chloride (KCl), sodium chloride (NaCl), and potassium nitrate (KNO_3). However, almost all of the studies reported low power densities. This is consistent with our observations as shown in Figure 4.7 with salt bridge only achieving an output potential difference of 48.6 mV and maximum power density of 11.8 mW m^{-3} at a current density of 243.2 mA m^{-3}.

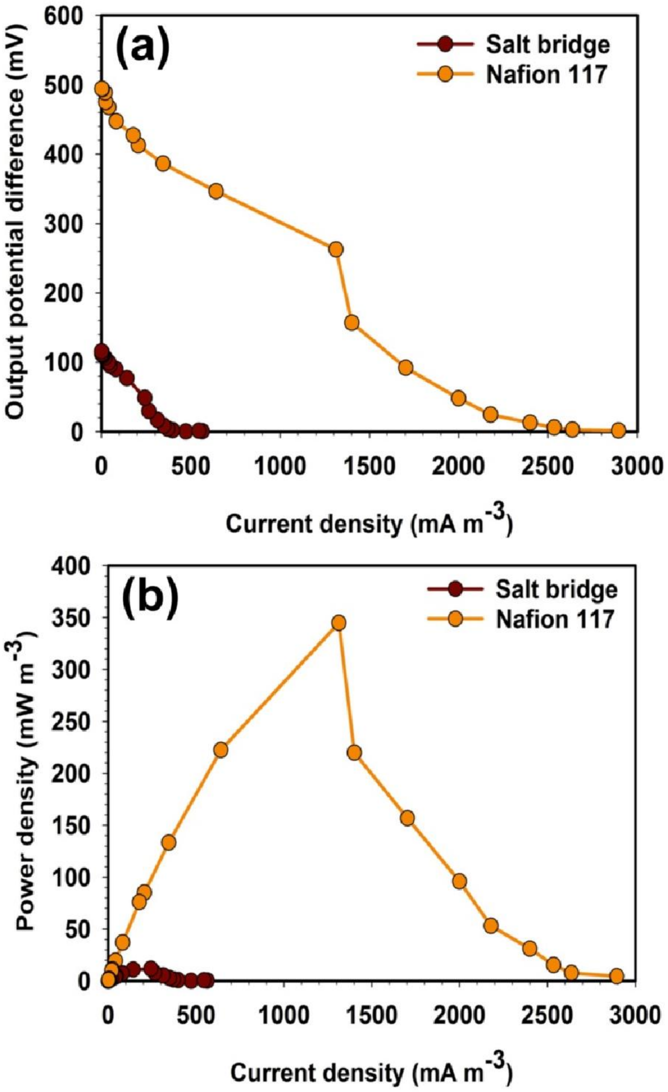

Figure 4.7 The effect of the type of H^+ transport system on (a) output potential difference (polarization curve) and (b) power density of an air-cathode MFC.

A useful characteristic that can be introduced in air-cathode MFC separator to improve performance is the ability of the separator to select the type of ions which permeate through it in addition to not allowing substrate or oxygen cross-over. There are various ion-selective separators that are available which can be used in MFCs. These include cation exchange membranes (CEMs) which allow positively charged ions to permeate and anion exchange membranes (AEMs) which allow negatively charged ions to permeate. Other ion-selective separators that can be used include bipolar membranes (BPMs) which allow the permeation of both the anions and cations.

Membranes which allow the permeation of positively charged ions, mainly protons, are also known as proton exchange membranes (PEMs). PEMs which are commonly used in MFCs are normally made from a Nafion. Nafion is a perfluorosulphuric acid with a backbone of hydrophobic fluorocarbons (-CF_2-CF_2-) to which the negatively charged sulphonated groups (SO_3^-) are attached. The presence of SO_3^- is what allows the Nafion to bring into effect proton conductivity or permeation. Due to the advantageous characteristic of the Nafion membrane in only allowing protons to permeate and not allowing substrate or oxygen cross-over, this explains the reason Nafion 117 performed better than the salt bridge as shown in Figure 4.7. Nafion 117 achieved an output potential difference of 262.6 mV and maximum power density of 344.9 mW m^{-3} at a current density of 1313.1 mA m^{-3}.

This significant increase can also be explained when the internal resistance of the air-cathode MFC is considered. The volume-specific internal resistance in Table 4.1 was calculated using Equation (3.10) and the polarization curves in Figure 4.7a, where the linear ohmic loss region slopes which occurred before and after maximum power point (MPP) represented the volume-specific internal resistance. Salt bridge showed an elevated internal resistance of 1320 Ω and 1215 Ω for before and after MPP (Table 4.1), respectively, due to lack of ion-selectivity and its susceptibility to substrate or oxygen cross-over. The internal resistance of Nafion 117 was minimal for before and after MPP with results of 875 Ω and 730 Ω, respectively, because of only allowing protons to permeate and not allowing oxygen cross-over.

Table 4.1 The effect of the type of H^+ transport system on both the volume-specific internal resistance and internal resistance of the air-cathode MFC.

	Volume-specific internal resistance (Ω m^3)		Internal resistance (Ω)	
Type	Before MPP	After MPP	Before MPP	After MPP
Nafion	0.175	0.146	875	730
Salt bridge	0.264	0.243	1320	1215

4.4 Influence of Carbon Cloth Modification with GAC on Air-Cathode MFC

The effect GAC on the performance of the air-cathode MFC was studied in order to determine whether deposited carbon material can help improve the performance of the carbon cloth anode (Figure 4.8).

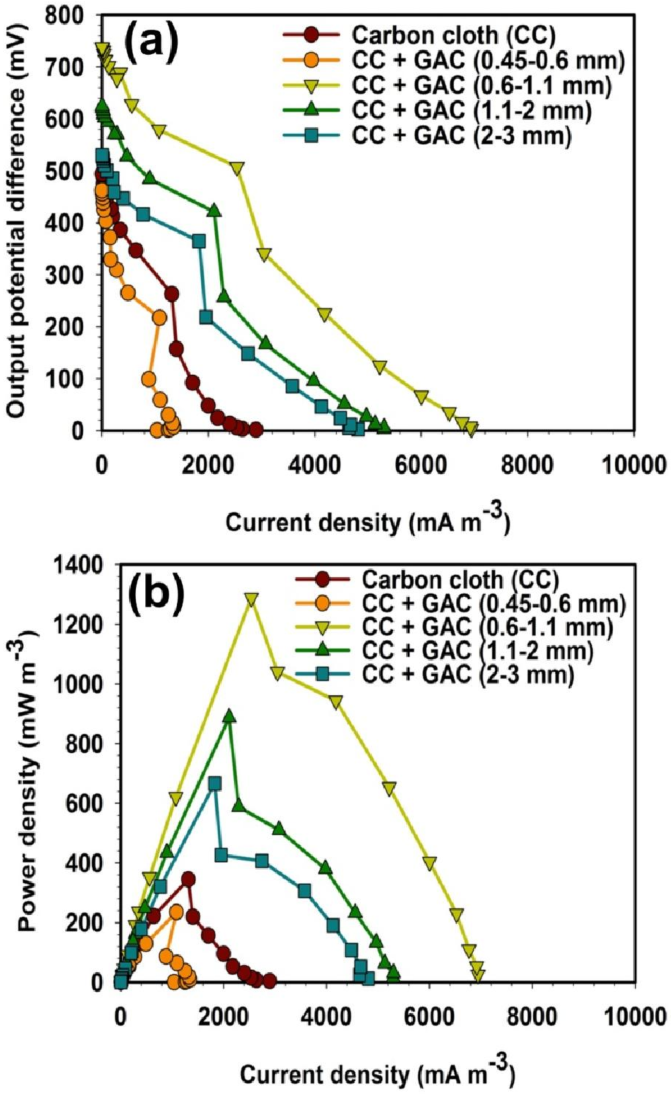

Figure 4.8 The effect carbon cloth modification using GAC with different average particle size (0.45-0.6 mm, 0.6-1.1 mm, 1.1-2 mm, 2-3 mm) on (a) output potential difference (polarization curve), (b) power density of an air-cathode MFC.

This was motivated by previous studies which observed that changing the particle size and surface area can help improve the attachment of electrogenic bacteria (Ahmed et al., 2015; Yang et al., 2018). Average particle size variation experiments were conducted in order to obtain the optimal size range for the improvement of air-cathode MFC performance. The results in Figure 4.8a and Figure 4.8b show that the carbon cloth modified with an average particle size in the range of 0.6-1.1 mm produced an output potential difference of 507.5 mV and maximum power density of 1287.7 mW m^{-3} at a current density of 2537.5 mA m^{-3}. However, the decrease in the average particle size to 0.45-0.6 mm led to a decrease in MFC performance of an output potential difference of 217.1 mV and maximum power density of 235.4 mW m^{-3} at a current density of 1085.2 mA m^{-3}. In addition, when the average particle size was increased above the 0.6-1.1 mm range, a decrease in performance was also observed. The observations in Figure 4.8 can be explained when the morphology of the GAC and the bacterial attachment is considered in Figure 4.9.

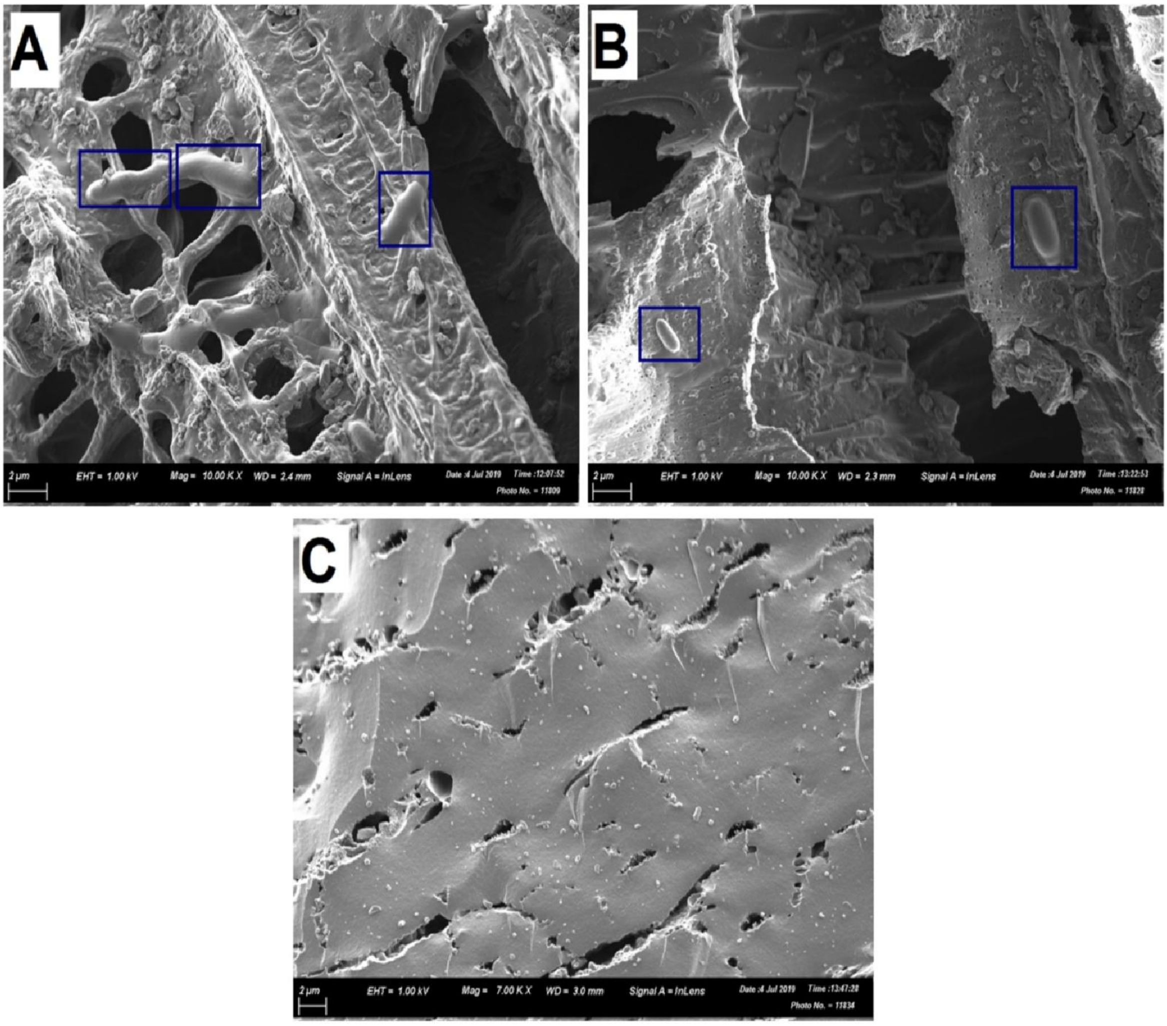

Figure 4.9 Morphology observation of GAC using SEM analysis at different average particle sizes of (a) 2-3 mm, (b) 0.6-1.1 mm, and (c) 0.45-0.6 mm.

The unique morphological structures and cell attachment for the GAC with varying average particle sizes were revealed by the scanning electron micrographs. The GAC with an average particle size of 2-3 mm had a skeletal-type morphology as shown in Figure 4.9a. The skeletal structure then began to disappear as the particle size decreased as shown in Figure 4.9b and Figure 4.9c. The attachment of the bacteria is highlighted in the blue squares depicted in the micrograms in Figure 4.9a and Figure 4.9b. However, as it can be seen in Figure 4.9c, there was no effective bacterial attachment that was observed in the lowest average particle size of 0.45-0.6 mm.

The attachment and the retention of bacteria better occurs on a rough and irregular surface as compared to a smooth and regular surface (Feng et al., 2015; Shelobolina et al., 2018). Furthermore, the reason there was no observation of bacterial attachment in the lowest average particle size of 0.45-0.6 mm is because there is significant reduction in bacterial attachment due to lack of porosity (Santoro et al., 2014). This was consistent with our observations as the smooth 0.45-0.6 mm GAC showed lack of cell attachment as compared to the skeletal surface of 2-3 mm GAC and a rough surface of 0.6-1.1 mm GAC. Due to the lack of cell attachment leading to low output potential difference and power density (Cao et al., 2019), this therefore explains the reason behind the decreased air-cathode MFC performance when using the average particle size of 0.45-0.6 mm of the GAC in carbon cloth. It should also be noted that the output potential difference and maximum power density for the control experiment with carbon cloth only were higher than the ones for experiment with 0.45-0.6 mm GAC deposited in carbon cloth (Figure 4.8). This was due to the introduction of 0.45-0.6 mm GAC in carbon cloth which lacked cell attachment and this led to the deterioration of the performance of the carbon cloth itself.

The surface area normally decreases with an increase in average particle size of the GAC (Li and DiGiano, 1983). Due to that fact, this explains the reason behind a decrease in air-cathode MFC performance when average particle size was increased above 0.6-1.1 mm. This is due to the fact that even though cell attachment was not hindered at high average particle sizes, the available surface area for cell attachment decreased with an increase in particle size. This was ascertained by the Brunauer, Emmett, and Teller (BET) results shown in Table 4.2 which show that an increase in average particle size decreases the available surface area for cell attachment of the GAC. Although an equal amount of GAC of 7 g was used in this study, GAC amount increases surface area which has the ability to improve MFC performance. However, there is an optimum value since increasing GAC amount above the optimum can hinder performance as shown by Fazli et al. (2019).

Table 4.2 The BET results showing the effect of increasing average particle size on the surface area of the GAC.

Type	Surface area (m^2 g^{-1})
GAC (0.45-0.6 mm)	1425.3
GAC (0.6-1.1 mm)	879.5
GAC (1.1-2.0 mm)	870.8
GAC (2.0-3.0 mm)	845.4

The stability of an air-cathode MFC was tested at different GAC particle sizes by monitoring the profile of the output potential difference (Figure 4.10).

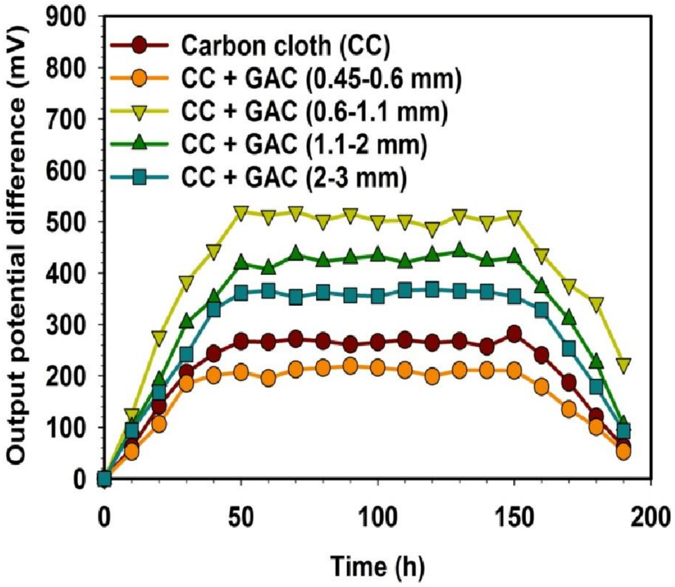

Figure 4.10 Profile of an air-cathode MFC output voltage using GAC with varying average sizes of particles (0.45-0.6 mm, 0.6-1.1 mm, 1.1-2 mm, 2-3 mm).

As it can be seen in Figure 4.10, for all the experiments of different GAC particle sizes, there was an increasing trend in output potential difference up until the 2nd day of inoculation and remained relatively stable at maximum output potential difference until the 6th day of operation. A decrease in output potential difference was observed after the 6th day of operation and this is caused by reduced bacterial growth and decay of electrogens (Choudhury et al., 2021).

4.5 The Economic Benefit of Carbon Cloth Modification with GAC

A carbon cloth is a popular material as of recent due to its excellent properties such as high electrical and thermal conductivity, good chemical and thermal stability, resistance to creep and an exceptional specific tensile strength and tensile modulus (Huang, 2009; Nunna et al., 2017). It is utilized in various fields such as automobiles, aerospace and renewable energy (Nunna et al., 2019). However, the high cost of the material detailed in Table 4.3 makes it challenging to apply it in field-scale applications. Therefore, it is essential to find ways to reduce the cost of using a carbon cloth especially in renewable energy applications such as MFCs. One of the ways identified in this study is to modify the carbon cloth with GAC.

Table 4.3 Material cost for the carbon cloth and the GAC.

Material	Material cost range	Material average cost	Reference
Carbon Cloth	--	5 \$ m^{-2}	(Yazdi et al., 2015)
GAC	1-2 \$ kg^{-1}	1.5 \$ kg^{-1}	(Liu et al., 2019)

It should be noted that the costs in Table 4.3 were updated using the recent chemical engineering plant cost index (CEPCI) to consider the price fluctuations (inflation or deflation) as described in Equation (4.1):

$$C_2 = \frac{C_1 I_2}{I_1} \tag{4.1}$$

where I is the cost index (CEPCI) and C is the cost of material. The updated material average costs for carbon cloth and GAC are 6 \$ m^{-2} and 1.53 \$ kg^{-1} using 2015 CEPCI of 556.8 (Ascher et al., 2020), 2019 CEPCI of 652.9 (Yao et al., 2021) and recent 2020 CEPCI of 668.0 (Yao et al., 2021).

GAC generally ranges between 0.2 mm to 5 mm in particle size and the common manufacturing steps include grinding, blending and agglomeration of coal which is then followed by carbonization and activation (Huggins et al., 2016). It is widely used in wastewater treatment, deodorization and as a solid support matrix for microbial biofilm development. Due to the cost of GAC which is relatively low as shown in Table 4.3, it makes it a suitable candidate for the modification of carbon cloth in order to improve air-cathode MFC performance while reducing the total cost spent on the anode material per energy generated. In order to ascertain that there is an economic benefit in the modification of carbon cloth with GAC, the cost of the individual materials used in the experiments was initially calculated and the results are shown in Table 4.4.

Table 4.4 The individual costs of the carbon cloth and the GAC with different particle sizes used in our experiments.

Description	Carbon cloth (CC) only	GAC (0.45-0.6 mm)	GAC (0.6-1.1 mm)	GAC (1.1-2.0 mm)	GAC (2.0-3.0 mm)
Mass used per experiment (g)	--	7	7	7	7
Area used per experiment (m^2)	4.9×10^{-3}	--	--	--	--
Effective reactor volume (m^3)	2×10^{-4}	2×10^{-4}	2×10^{-4}	2×10^{-4}	2×10^{-4}
Mass used per effective reactor volume ($g\ m^{-3}$)	--	3.5×10^{4}	3.5×10^{4}	3.5×10^{4}	3.5×10^{4}
Area used per effective reactor volume ($m^2\ m^{-3}$)	24.5	--	--	--	--
Material average cost ($\$\ g^{-1}$)	--	1.53×10^{-3}	1.53×10^{-3}	1.53×10^{-3}	1.53×10^{-3}
Material average cost ($\$\ m^{-2}$)	6	--	--	--	--
Cost per reactor volume ($\$\ m^{-3}$)	147.0	53.55	53.55	53.55	53.55

The cost of GAC per reactor volume remained the same at a value of 53.55 $\$\ m^{-3}$ with varying average particle size. This is attributed to the mass used per experiment, effective reactor volume and the material average cost remaining the same with varying GAC average particle size. It should be noted from Table 4.4 that the cost of the carbon cloth per reactor volume was high at a value of 147.0 \$ m^{-3}. The total cost spent on the anode material per energy generated was calculated and the results are shown in Table 4.5. Since the MFC was shown to provide a stable maximum power output for 4 days in Figure 4.10, that information was used to convert power output to energy output in Table 4.5.

Table 4.5 Total cost spent on the anode material per power generated in the air-cathode MFC.

Description	CC (Control)	CC + GAC (0.45-0.6 mm)	CC + GAC (0.6-1.1 mm)	CC + GAC (1.1-2.0 mm)	CC + GAC (2.0-3.0 mm)
Max power density (mW m^{-3})	344.9	235.4	1287.8	887.5	666.1
Energy output (mWh m^{-3})	3.31×10^4	2.26×10^4	12.36×10^4	8.52×10^4	6.39×10^4
Cost per reactor volume (\$ m^{-3})	147.0	200.6	200.6	200.6	200.6
Cost per energy generated (\$ mWh^{-1})	4.44×10^{-3}	8.87×10^{-3}	1.62×10^{-3}	2.35×10^{-3}	3.14×10^{-3}
Cost per energy generated (\$ Wh^{-1})	4.44	8.87	1.62	2.35	3.14

The total costs were calculated on the cost of carbon cloth only as an anode for the control experiment, and the sum of the carbon cloth and GAC for the anode with the combination of both. As it can be seen in Table 4.5, the total cost spent on the carbon cloth only anode per energy generated of a value of 4.44 \$ Wh^{-1} was 2.74 times as much as the one for the carbon cloth modified with optimized GAC average particle size of 0.6-1.1 mm of a value of 1.62 \$ Wh^{-1}. This means that the addition of GAC with an optimized particle size not only improved the performance of the air-cathode MFC but it also had an economic benefit.

However, it should be highlighted that an introduction of a GAC with a particle size of 0.45-0.6 mm that lacks cell attachment not only hinders air-cathode MFC performance but it also leads to total cost spent on the anode material per energy generated of a value of 8.87 \$ Wh^{-1} which is almost 2 times as much as the carbon cloth only. This means that it is necessary to optimize the particle size of the GAC when applying it in the modification of carbon cloth so that the performance does not deteriorate and the anode costs do not escalate to high values.

CHAPTER 5: IMPROVED CHROMIUM (VI) REDUCTION PERFORMANCE BY BACTERIA IN A BIOGENIC PALLADIUM NANOPARTICLE ENHANCED MICROBIAL FUEL CELL

5.1 Optimization of Abiotic Factors for Cr(VI)-Reducing MFC

5.1.1 Influence of anode temperature on Cr(VI)-reducing MFC

The performance of Cr(VI)-reducing MFC was first evaluated under different anode temperatures using a carbon cloth without the GAC that is modified with Bio-PdNPs at both pH 7 and 40 mg L^{-1} initial Cr(VI) concentration. An increase in temperature from 25 °C to 50 °C led to an optimized temperature of 38 °C with a maximum output potential difference of 40.3 mV (Figure 5.1a). Increasing or decreasing the temperature above and below 38 °C led to a decrease in maximum output potential difference for each experiment with 25 °C, 32 °C and 50 °C leading to 29.5 mV, 35.9 mV and 3.21 mV, respectively (Figure 5.1a).

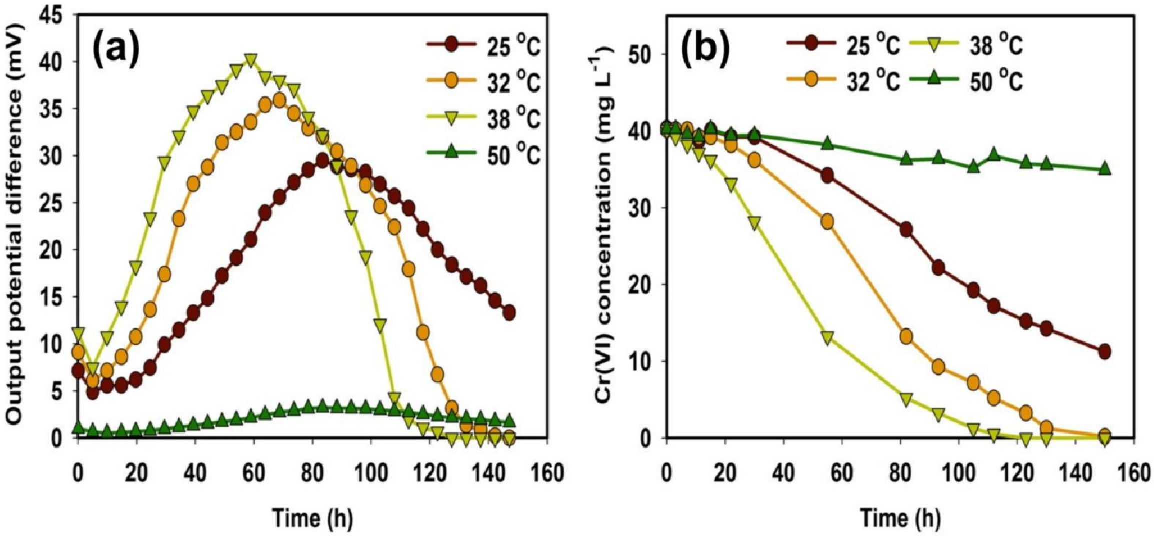

Figure 5.1 The effect of anode temperature on (a) output potential difference and (b) Cr(VI) reduction over a period of 150 h in a Cr(VI)-reducing MFC.

Organisms can be classified according to their optimum growth temperature: (i) psychrophiles grow best between -5 °C and 20 °C, (ii) mesophiles grow best between 20 °C and 45 °C, and (iii) thermophiles grow best at temperatures above 45 °C. In the present experiments, it was observed that the Brits sludge contained mostly mesophiles as electrogenic bacteria since the Cr(VI)-reducing MFC obtained the highest maximum output potential difference at 38 °C. In addition, the reason why temperature affected the output potential difference of the MFC might have been due to the decay or slow growth rate of the mesophiles. This is because temperatures above 39 °C limit the growth of mesophiles due to protein denaturation (Behera et al., 2018; Schiraldi and De Rosa, 2014), and low temperatures lead to slow growth rates (Michie et al., 2011).

Similar temperature effect trends were observed for Cr(VI) reduction in the cathode, where the optimised anode temperature of 38 °C led to a fastest rate of Cr(VI) removal (Figure 5.1b). It should be noted that even though the rate of Cr(VI) reduction was different for both 32 °C and 38 °C experiments, both achieved complete Cr(VI) reduction by 112 h and 150 h, respectively. Incomplete Cr(VI) reduction was observed at both 50 °C and 25 °C, which achieved Cr(VI) reduction of 71.9 % and 12.6 % after 150 h, respectively (Figure 5.1b). This was likely related to the death of cells at high temperatures above 38 °C (Wu et al., 2017). Temperatures lower than 38 °C were also not ideal due to slow growth rates of microbial cells (Michie et al., 2011).

The Cr(VI) removal profile in the MFC displayed a lag in Cr(VI) removal at the start of the experiments (between 0 – 15 h) (Figure 5.1b). It was postulated to be a result of the time required for the cells to adapt to the MFC anode and electrical conditions. This observation has been reported by other researchers who perceive the delay of MFCs caused by adaptation of electrogenic bacteria to the electrical conditions as one of the problems in MFCs that can be solved by bioaugmentation (Pandit et al., 2015; Raghavulu et al., 2013).

The increase in Cr(VI) removal rate after the lag was due to substrate consumption by electrogenic bacteria in which the generated electrons from the anode chamber contribute to the reduction of Cr(VI) in the cathode chamber leading to an increase in output potential difference (Sophia and Saikant, 2016). Also, the gradual increase in the rate of Cr(VI) reduction was caused by the development of biofilm during the experiments (Baranitharan et al., 2015). The decrease in the rate of Cr(VI) removal at the end of each experiment was attributed to mass transfer losses caused by decreasing bulk Cr(VI) concentration in the cathode chamber available to accept the electrons from the anode chamber (Scott, 2016a). It should be noted that the inflection point of Cr(VI) removal profiles (Figure 5.1b) was located at about the time maximum output potential difference was achieved (Figure 5.1a).

5.1.2 Influence of cathode pH on Cr(VI)-reducing MFC

The performance of Cr(VI)-reducing MFC was affected by cathode pH change when using a carbon cloth without the GAC that is modified with Bio-PdNPs. An optimum of pH 4 led to the highest maximum output potential difference of 55.2 mV (Figure 5.2a). On the other hand, an increase in pH above pH 4 led to a decrease in maximum output potential difference of 41.8 mV and 9.91 mV at pH 7 and pH 9, respectively (Figure 5.2a).

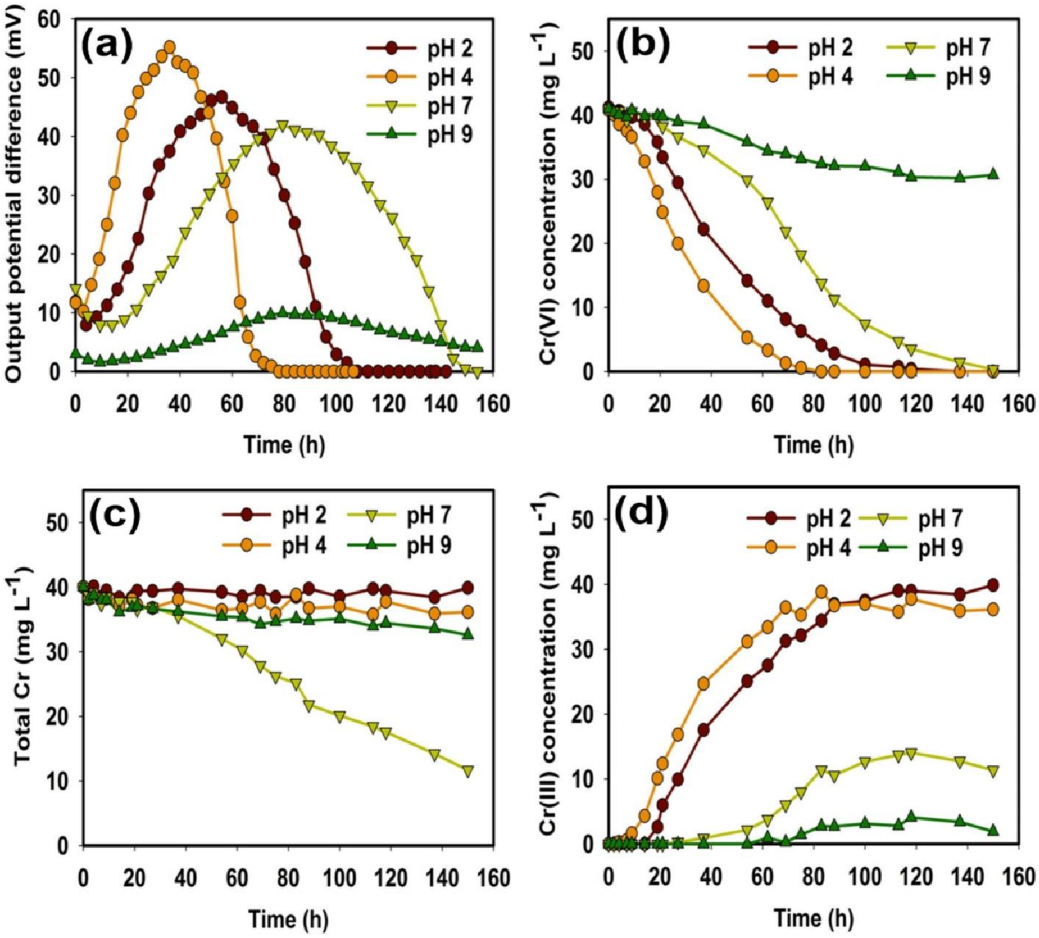

Figure 5.2 The effect of cathode chamber pH on (a) output potential difference, (b) Cr(VI) reduction, (c) total Cr, and (d) Cr(III) concentration over a period of 150 h in a Cr(VI)-reducing MFC.

The observation of a decrease in output potential difference when increasing pH above pH 4 can be explained using the Le Chatelier's principle, where an increase in the cathode pH would result in a decrease in hydrogen ions (H^+) and favour the reverse reaction in the overall redox reaction shown in Equation (5.1):

$$Cr_2O_7^{2-} + 3HCOO^- + 11H^+ \leftrightarrow 3CO_2 + 2Cr^{3+} + 7H_2O \quad E^{o}_{cell} = 176V \qquad (5.1)$$

Due to the reverse reaction not being thermodynamically favoured and requiring energy input, the resulting effect of increasing cathode chamber pH above pH 4 would then result in a decrease in the output potential difference. Decreasing the pH below pH 4 also led to a decrease in maximum output potential difference to a value of 46.7 mV as observed at pH 2 (Figure 5.2a). This was due to reverse proton transfer in which the concentration of the H^+ ions in the cathode chamber diffused to the anode chamber through the proton exchange membrane. To further elaborate, at cathode pH 2, the final cathode pH increased (Figure 5.3a) whilst the final anode pH decreased (Figure 5.3b). Also, the extent of the final pH decrease in the anode at cathode pH 2 experiment was more than the decrease at other cathode pH experiments as shown in Figure 5.3b.

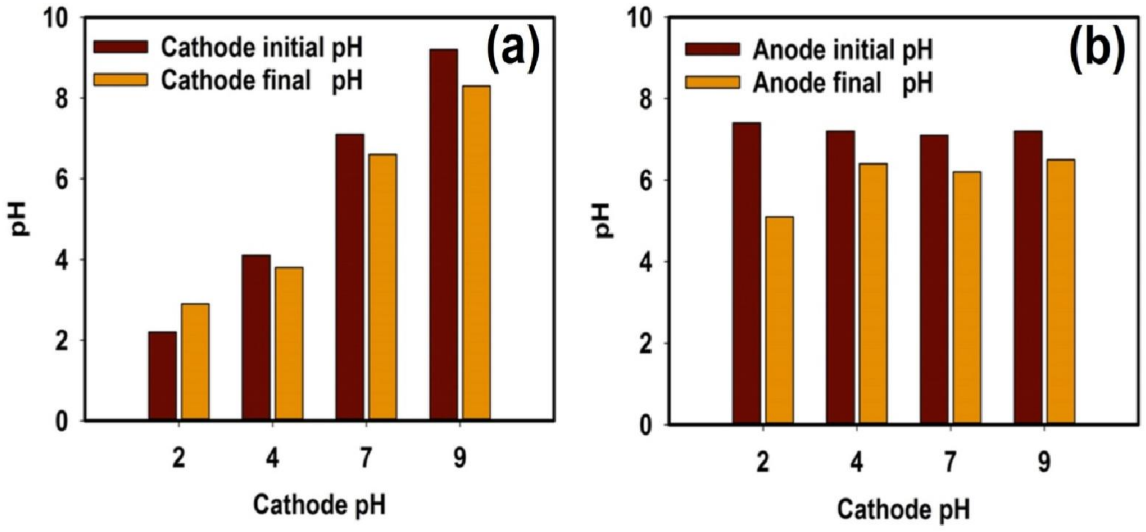

Figure 5.3 The effect of cathode chamber pH on (a) final cathode pH, and (b) final anode pH.

It should also be added that the reason the final cathode pH decreased in cathode pH 4, pH 7 and pH 9 experiments except pH 2 was due to the fact that protons produced in the anode were transferred in the cathode without the proton transfer being reversed. In addition, the final anode pH always decreased due to the production of H^+ ions by the bacteria.

It can be thought that the reduction of Cr(VI) was the reason for a high increase in the final cathode pH at cathode pH 2 experiment (Figure 5.3e) due to the consumption of protons, however, when we observed the extent at which the final anode pH had decreased at cathode pH 2 experiment as compared to the other cathode pH experiments (Figure 5.3f), it was concluded that protons had actually reversed. These observations ascertained reverse proton which is capable of affecting the microbial communities and reduce MFC performance (Kim et al., 2017).

Cr(VI) reduction was related to the output potential difference, and it also achieved an optimum of pH 4 leading to the highest rate of Cr(VI) removal. Complete removal was observed at pH 2, 4, and 7, however, incomplete removal of 23.3 % over a period of 150 h was seen at pH 9 (Figure 5.2b). The reason why pH also affected Cr(VI) removal in addition to it affecting output potential difference in the MFC was because an output potential difference is an indication of how efficient electrons and hydrogen ions are transferred in the MFC. Therefore, a decrease in output potential difference caused by the reverse proton transfer at low pH, or a high pH that favoured the reverse overall redox reaction, impacted the amount of electrons that can be accepted by Cr(VI) in the cathode chamber. This observation was also made by Li et al. (2018) who found that the pH of the cathode chamber affects Cr(VI) removal.

A total chromium (Cr) decrease of 70.7 % in the cathode chamber was seen at pH 7 (Figure 5.2c). However not much of a change in total Cr during pH 2, pH 4, and pH 9 occurred, resulting in only 0.32 %, 9.7 %, 20.25 % of total Cr decrease, respectively (Figure 5.2c). This is because at low range of pH 2 to 6, dichromate ($Cr_2O_7^{2-}$) would be the predominant Cr(VI) species in solution (Guertin et al., 2004) and is reduced in the cathode chamber. It then forms soluble Cr(III) species which do not precipitate below pH 4.5 but are present as $CrOH^{2+}$ ions (Guertin et al., 2004). On the other hand, at pH values above 6, Cr(III) precipitation in the cathode chamber would occur after Cr(VI) reduction according to Equation (5.2) (Guertin et al., 2004):

$$2Cr^{3+} + 6OH^{-} \leftrightarrow 2Cr(OH)_{3(s)} \quad \text{pH range} \quad = 6 \text{ to } 12 \qquad (5.2)$$

It should be noted that the main reason behind the low total Cr decrease observed at pH 9 was mainly due to a low reduction rate of Cr(VI) as seen in Figure 5.2b. This resulted in a low Cr(III) concentration available to form chromium hydroxide [$Cr(OH)_3$] as seen in Figure 5.2d.

5.1.3 Influence of initial Cr(VI) concentration

Increasing the initial concentration of Cr(VI) in the MFC operated at 38 °C and pH 4 using a carbon cloth without the GAC that is modified with Bio-PdNPs led to an increase in the performance of the MFC with 40 mg L^{-1}, 60 mg L^{-1} and 100 mg L^{-1} initial Cr(VI) concentrations generating maximum output potential difference of 239.2 mV, 333.4 mV, and 374.6 mV, respectively (Figure 5.4a).

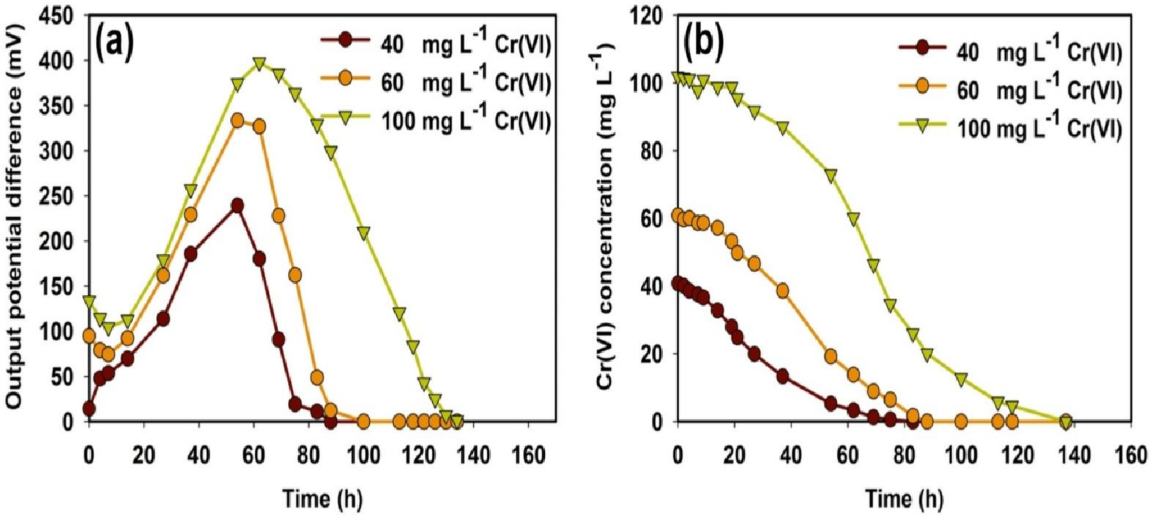

Figure 5.4 The effect of initial Cr(VI) concentration on the (a) output potential difference and, (b) Cr(VI) reduction over a period of 140 h in a Cr(VI)-reducing MFC.

The effect of the initial Cr(VI) concentration on the output potential difference can be explained by considering the equation used to calculate output potential difference in MFC as shown in Equation (5.3) (Niya and Hoorfar, 2014):

$$\Delta V = \Delta V_{rev} - \eta_{act} - \eta_{conc} - \eta_{ohmic} \tag{5.3}$$

The ohmic losses (η_{ohmic}) are caused by resistances to ion and electron flows, activation overpotentials (η_{act}) are losses related to the activation energy of the redox reaction that the MFC needs to overcome, and concentration overpotentials (η_{conc}) are caused by losses due to the concentration gradient between the surface and bulk concentrations (Wang et al., 2015).

Provided that these losses are small, the output potential difference (ΔV) is only related to the reversible output potential difference (ΔV_{rev}). This can be calculated using the Nernst equation for the overall redox reaction in Equation (5.1) as shown by Equation (5.4):

$$\Delta V = \Delta V_{rev} = E^{o}_{cell} + \frac{RT}{6F} ln\left(\frac{[Cr_2O_7{}^{2-}][H^{+}]^{11}[HCOO^{-}]^{3}}{[Cr^{3+}]^{2}[CO_2]^{3}}\right) \tag{5.4}$$

where E^{o}_{cell} is the cell standard reduction potential in V, R is the gas constant (8.314 Pa m^3 mol^{-1} K^{-1}), T is the temperature in K, and F is Faraday's constant (96485 A s mol^{-1}). As it can be seen from Equation (5.4), the initial concentration of Cr(VI) in the form of $Cr_2O_7{}^{2-}$ concentration plays a role in the output potential difference of the MFC, and by increasing the initial concentration of Cr(VI), the overall output potential difference increases (Li et al., 2018; Wang et al., 2008). However, the reason behind the increase in MFC performance with increased Cr(VI) initial concentration can also be attributed to the fact that when initial Cr(VI) concentration is increased, the amount of Cr(VI) available to accept the electrons from the anode chamber also increases. This not only leads to an increase in output potential difference, but it also enhances Cr(VI) removal rate.

Figure 5.4b shows that the initial concentration of Cr(VI) affected rate at which Cr(VI) was removed in the cathode chamber. An increase in initial concentration from 40 mg L^{-1} to 100 mg L^{-1} led to a complete Cr(VI) removal in less than double the time required to remove 40 mg L^{-1} of Cr(VI). This improvement in the rate of removal shows that the amount of Cr(VI) available to accept electrons from the anode chamber has an impact on not only the output potential difference, but also the rate of Cr(VI) removal.

The coulombic efficiency (CE) can further be used to explain the reason behind the facilitation of electron transfer by an increase in Cr(VI) initial concentration which increases the amount of Cr(VI) available to accept the electrons in the cathode chamber. CE describes the charge efficiency in which electrons are being transferred in the Cr(VI)-reducing MFC and further information on its calculation is provided in Equation (3.9) (Huang et al., 2010). Figure 5.5 shows that an increase in initial Cr(VI) concentration increased the CE, which means the efficiency in which the electrons were being transferred in the MFC in order to be accepted by Cr(VI) in the cathode chamber was related to the amount of Cr(VI) available to accept the electrons (Huang et al., 2010; Wang et al., 2008).

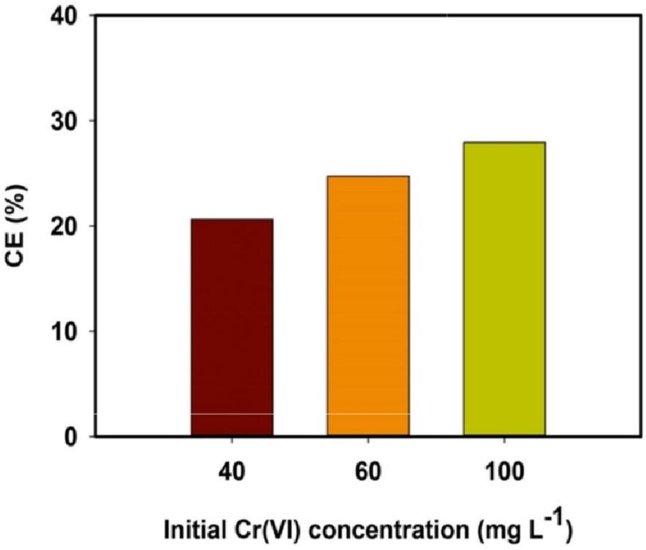

Figure 5.5 The change of coulombic efficiency (CE) with initial Cr(VI) concentration (40, 60, and 100 mg L^{-1}).

5.1.4 Influence of microbial growth on Cr(VI)-reducing MFC

In order to determine whether the low output potential difference when complete Cr(V) reduction was achieved was due to Cr(VI) concentration and not the lack of survival of the microorganisms, the optical density (OD) was monitored. The microbial growth was measured in optical density (OD) at wavelength of 600 nm using a UV/Vis spectrophotometer. Three phases were observed in Figure 5.6 when considering the OD (600 nm) response: (i) lag time in the first 15 h in the increase of the microorganisms, (ii) fast increase in microorganisms, and (iii) a gradual decrease in the microorganisms. Due to the presence of microorganisms even after the complete Cr(VI) reduction was achieved as shown in Figure 5.6, this indicated that the low output potential difference at complete Cr(VI) reduction was due to low Cr(VI) concentration and not the lack of microorganisms.

In Figure 5.6, we can see that the lag time in the Cr(VI) reduction was caused by the lag in the growth of microorganism and this was associated with the time required for the electrogens to adapt to the MFC anode and electrical conditions (Song et al., 2016).

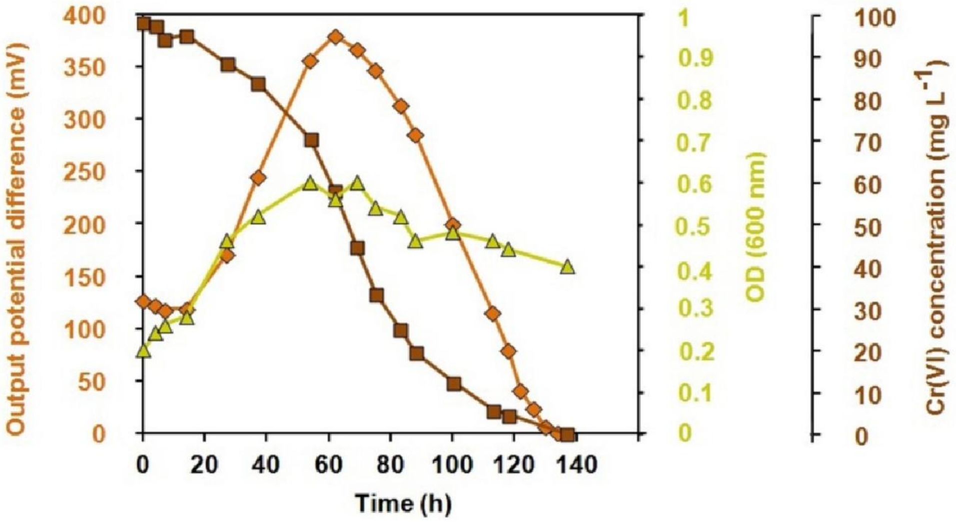

Figure 5.6 The change in OD (600 nm) to monitor the microbial growth in the anode chamber as the output potential difference and Cr(VI) concentration changes over a period of 140 h in a Cr(VI)-reducing MFC.

5.2 Influence of Anode Modified with GAC on Cr(VI)-Reducing MFC

5.2.1 The effect of GAC particle size on Cr(VI)-reducing MFC performance

In order to increase the efficiency of the MFC under investigation, the effect of anode modification was investigated through the addition of GAC into the carbon cloth (Figure 5.7). This was motivated by previous studies that have shown that changing the particle size and surface area plays a significant role in the attachment of electrogenic bacteria (Ahmed et al., 2015; Yang et al., 2018).

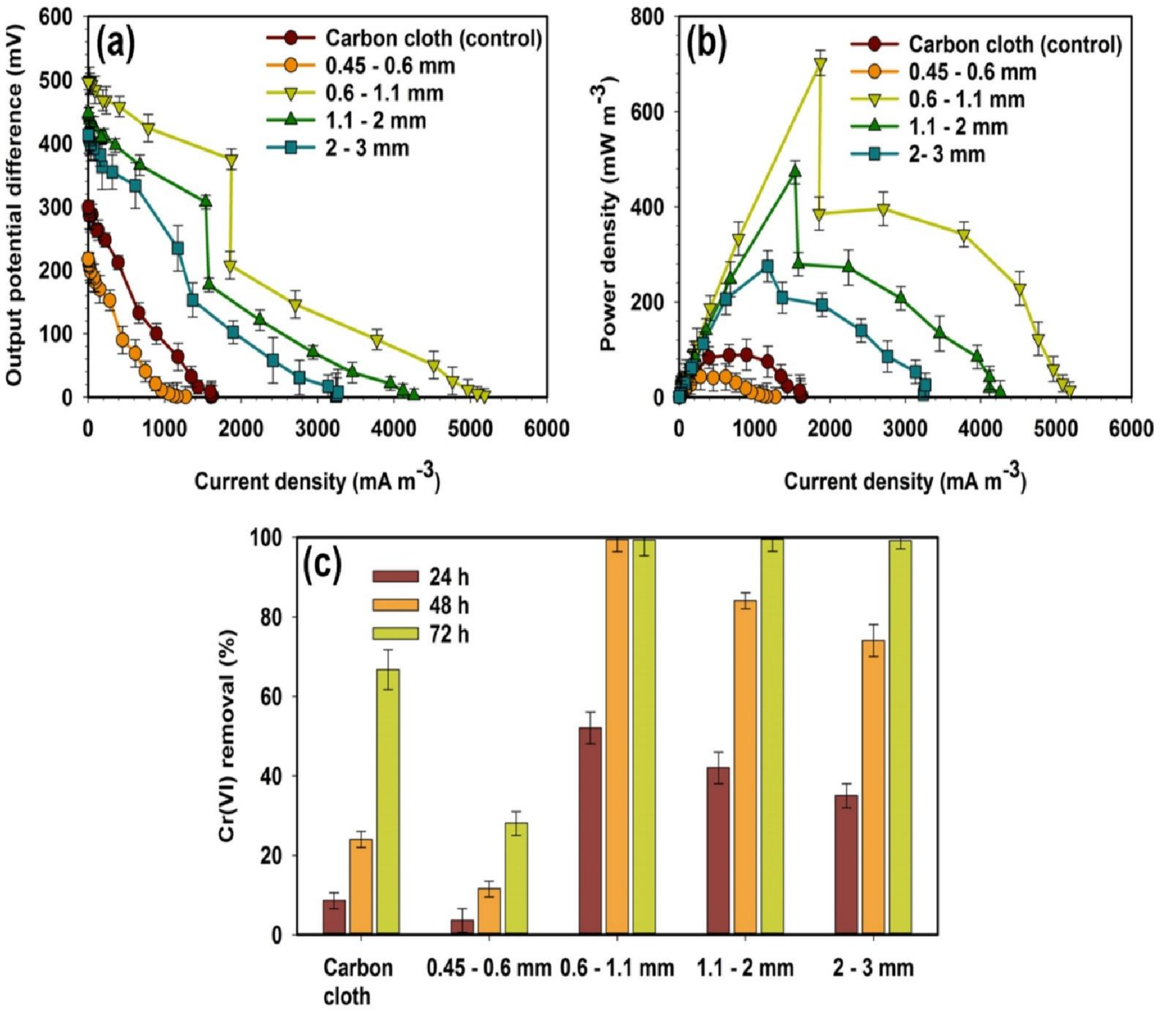

Figure 5.7 The effect of GAC with different average particle size (0.45-0.6 mm, 0.6-1.1 mm, 1.1-2 mm, 2-3 mm) on (a) output potential difference (polarization curve), (b) power density, and (c) Cr(VI) removal.

The average particle size of the GAC was varied so as to determine the optimal size range. Figure 5.7a and Figure 5.7b show that GAC with an average particle size in the range 0.6-1.1 mm produced both the peak output potential difference and maximum power density of 374.8 mV and 702.3 mW m^{-3}, including complete Cr(VI) removal which was observed after 48 h as shown in Figure 5.7c. However, when the average particle size was decreased to 0.45-0.6 mm, both the peak output potential difference and maximum power density achieved their lowest values of 90.2 mV and 45.5 mW m^{-3} and 11.5 % Cr(VI) removal was observed after 48 h. An increase in the average particle size above the 0.6-1.1 mm range also resulted in decreased performance.

5.2.2 The effect of GAC particle size on morphology

The trends noted in Figure 5.7 can be explained by considering the differences in the morphology of the GAC particles (Figure 5.8) together with the accompanying bacterial attachment. The scanning electron micrographs revealed unique morphological structures and cell attachment for the different average particle sizes. GAC with average particle size of 2-3 mm had a skeletal-like morphology (Figure 5.8a), as the particle size decreased, the skeletal structure in the GAC disappeared as depicted in Figure 5.8b and Figure 5.8c. Bacterial attachment was highlighted in the black squares presented in the micrograms in Figure 5.8a and Figure 5.8b. No successful bacterial attachment was observed in the lowest average particle size of 0.45-0.6 mm (Figure 5.8c).

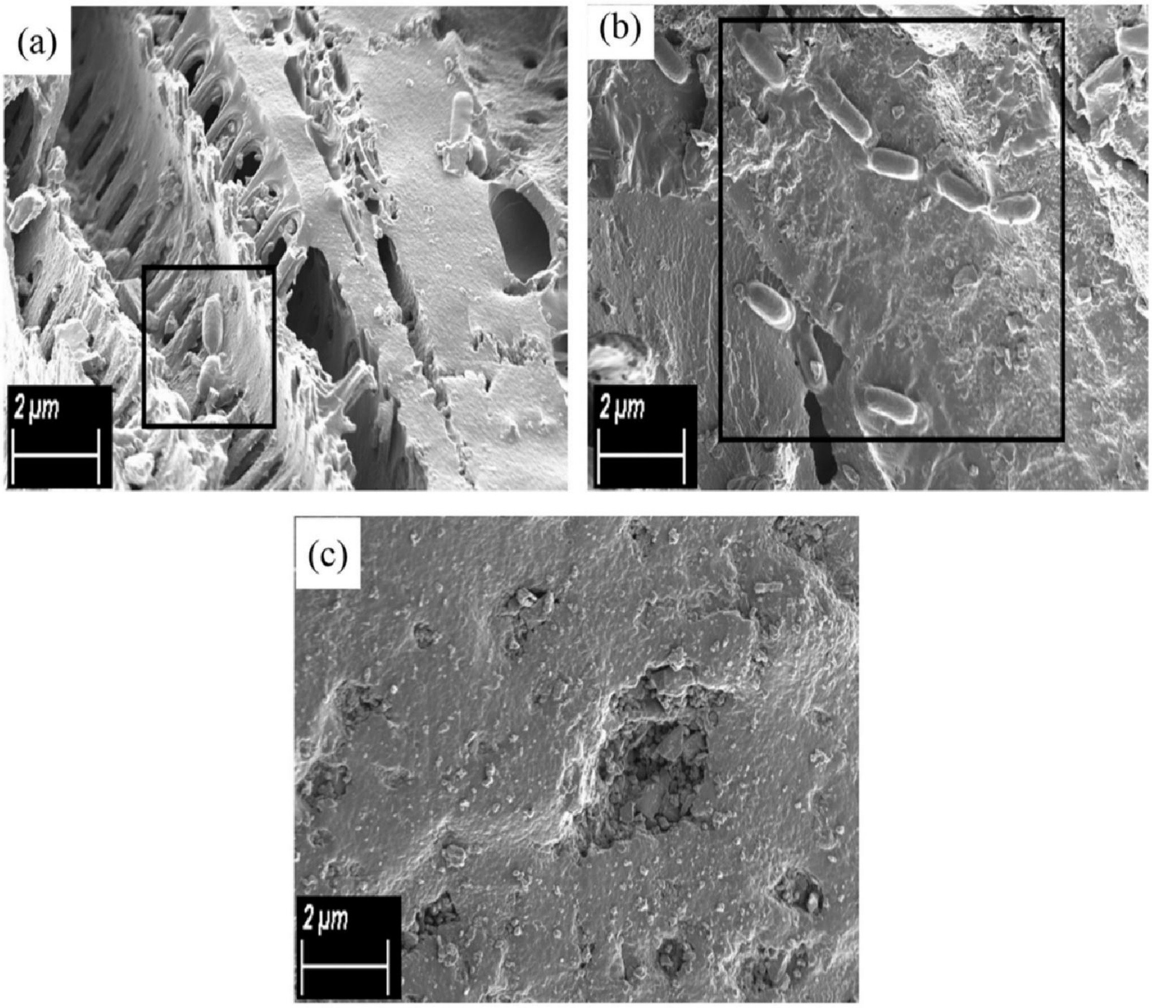

Figure 5.8 SEM morphology observations of GAC at different average particle sizes of (a) 2-3 mm, (b) 0.6-1.1 mm, and (c) 0.45-0.6 mm under 2 µm magnification.

It is postulated that microorganisms generally attach and are retained better on irregular, rough surfaces compared to regular and smooth surfaces (Feng et al., 2015; Shelobolina et al., 2018). In addition, the reason no bacterial attachment was observed is because lack of porosity in a smooth surface significantly reduces bacterial attachment (Santoro et al., 2014). This is consistent with our observation with the smooth 0.45-0.6 mm GAC showing lack of cell attachment as compared to the skeletal and rough surface of both 2-3 mm GAC and 0.6-1.1 mm GAC respectively. Considering that lack of cell attachment leads to low output potential difference (Cao et al., 2019), this explains the reason the average particle size of 0.45-0.6 mm performed the lowest. Since the surface area normally decreases with an increase in average particle size for GAC (Li and DiGiano, 1983), the reason behind a decrease in MFC performance when the average particle size was increased above 0.6-1.1 mm was attributed to a decrease in surface area available for cell attachment. This is due to the fact that even though cell attachment was not hindered at high average particle sizes, the available surface area decreased with an increase in particle size.

5.2.3 The effect of GAC particle size on internal resistance

Internal resistance dependency on the GAC average particle size is shown in Table 5.1.

Table 5.1 The effect of GAC average particle size on both the volume-specific internal resistance and internal resistance of the Cr(VI)-reducing MFC.

	Volume-specific internal resistance (Ω m^3)		Internal resistance (Ω)	
Type	Before MPP	After MPP	Before MPP	After MPP
Carbon cloth (control)	0.23	0.22	1150	1100
0.45 - 0.6 mm	0.26	0.24	1300	1200
0.6 - 1.1 mm	0.066	0.058	330	290
1.1 - 2 mm	0.089	0.073	445	365
2.0 - 3 mm	0.092	0.087	460	435

This dependency is due to the average particle size having an impact on the extent of cell attachment on the GAC surface which in turn influences the internal resistance of the Cr(VI)-reducing MFC. The volume-specific internal resistance in Table 5.1 was calculated using Equation (3.10) and the polarization curves in Figure 5.7a, where the linear ohmic loss region slopes which occurred before and after maximum power point (MPP) represented the volume-specific internal resistance. GAC with an average particle size of 0.45-0.6 mm showed high volume-specific internal resistance of 0.26 Ω m^3 and 0.24 Ω m^3 for both before and after MPP, respectively, due to lack in cell attachment (Table 5.1). The volume-specific internal resistance at 0.6-1.1 mm was the lowest for both before and after MPP with values of 0.066 Ω m^3 and 0.058 Ω m^3, respectively, due to increased cell attachment. Further increase to 2-3 mm resulted in an increase in volume-specific internal resistance (Table 5.1). This was due to the fact that even though cell attachment was not hindered at high average particle sizes, the available surface area decreased with increase in particle size. This observation was also made by a previous study where unmodified graphite anode (GA) with low available surface area had high internal resistance (Liu et al., 2017).

It should be noted that the values of output potential difference, maximum power density, and Cr(VI) removal for the control experiment with carbon cloth only were higher than the ones for experiment with 0.45-0.6 mm GAC dispersed in carbon cloth (Figure 5.7). This was due to the introduction of 0.45-0.6 mm GAC in carbon cloth which lacked cell attachment and led to an increase in internal resistance as shown in Table 5.1.

5.3 Influence of Bio-PdNPs on Cr(VI)-Reducing MFC

5.3.1 Influence of Bio-PdNPs on output potential difference and power output

In order to improve the electrocatalytic performance of the anode, the effect of addition of Bio-PdNPs onto the GAC was investigated. This was because elemental palladium has been shown to have the capability to improve the electrocatalytic activity of the anode (Moon et al., 2014). The results on the biological synthesis, characterization of the Bio-PdNPs and improved electrocatalytic activity of the anode used in this study were reported by Matsena et al. (2020). In this study, we focus more on their impact on the performance of Cr(VI)-reducing MFC. The results are shown in Figure 5.9.

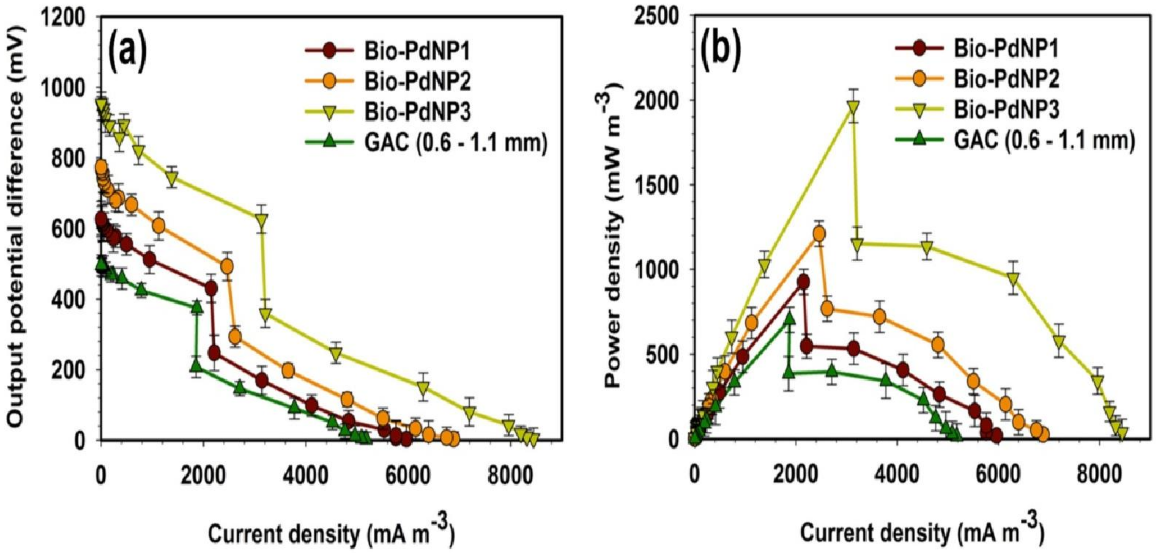

Figure 5.9 The results of (a) output potential difference (polarization curve), and (b) power density in Cr(VI)-reducing MFC containing the GAC anode placed in carbon cloth and modified with Bio-PdNP1 (2 mg Bio-PdNPs g^{-1} GAC), Bio-PdNP2 (4 mg Bio-PdNPs g^{-1} GAC), Bio-PdNP3 (6 mg Bio-PdNPs g^{-1} GAC), and an unmodified 0.6-1.1 mm GAC.

The addition of the Bio-PdNPs to the unmodified GAC resulted in improved performance as both the output potential difference and maximum power output increased with increasing Bio-PdNPs loading. Peak output potential difference of 185.2 mV, 242.3 mV, and 393.1 mV were obtained for Bio-PdNP1, Bio-PdNP2, and Bio-PdNP3, respectively (Figure 5.9a). In addition, Bio-PdNP3 led to a maximum power density of 1965.4 mW m^{-3} as compared to 926.2 mW m^{-3} and 1211.3 mW m^{-3} for Bio-PdNP1 and Bio-PdNP2, respectively (Figure 5.9b). Besides the presence of microbes in the Brits sludge oxidizing formate (Deplanche et al., 2010), further improvement in Cr(VI)-reducing MFC performance in the presence of Bio-PdNPs was attributed to enhanced catalyzation of formate oxidation by Bio-PdNPs (Yong et al., 2002), and an increase in active sites with increased Bio-PdNPs loading.

The enzyme oxidation of formate by microbes (Deplanche et al., 2010) and the catalytic oxidation of formate by palladium nanoparticles (Yong et al., 2002) has previously been reported. Anode modification using Bio-PdNPs has also been demonstrated in applications such as power generation (Matsena et al., 2020; Quan et al., 2015), evans blue removal (Quan et al., 2018b), and iohexol degradation in MFCs (Quan et al., 2018a). However, the present study not only investigates the usage of Bio-PdNPs as a means of enhancing GAC based anodes, but it also explores whether the presence of the palladium nanoparticles influences Cr(VI) removal in the MFC.

5.3.2 Influence of Bio-PdNPs on Cr(VI) reduction

Figure 5.10 shows increased Cr(VI) removal in the MFC upon addition of Bio-PdNPs. While all experimental conditions tested attained complete Cr(VI) removal from a 100 mg L^{-1} initial concentration within 50 h, the Bio-PdNP3 had the fastest rate of Cr(VI) removal and achieved complete Cr(VI) removal in 25 h. This observation was attributed to the fact that Bio-PdNP3 led to both the highest output potential difference (Figure 5.9a) and power density (Figure 5.9b). Since both parameters represent the extent at which electrons are generated and transferred within the MFC, this meant that the Bio-PdNP3 increased the amount of electrons available for Cr(VI) reduction in the cathode chamber. A more elaborate explanation can be related to the fact the Bio-PdNP3 led to the highest formate oxidation catalyzation (Yong et al., 2002) which enhanced the amount of electrons generated (Haan and Masel, 2009) and led to an increased amount of electrons available for Cr(VI) reduction.

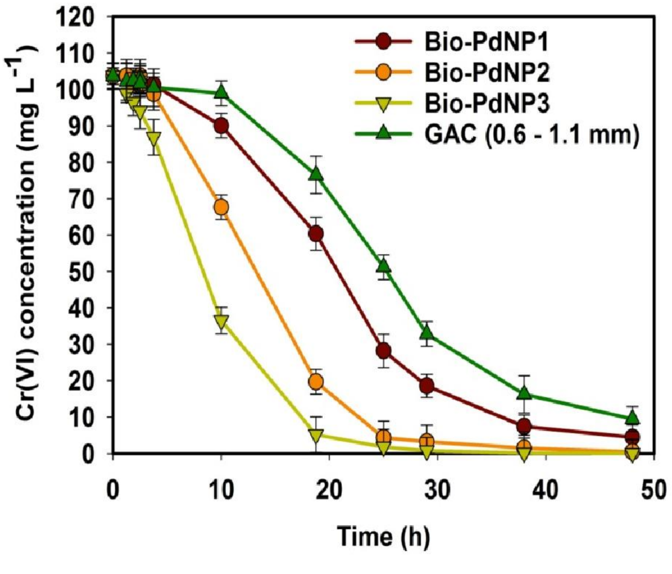

Figure 5.10 Cr(VI) removal in Cr(VI)-reducing MFC containing the GAC anode placed in carbon cloth and modified with Bio-PdNP1 (2 mg Bio-PdNPs g^{-1} GAC), Bio-PdNP2 (4 mg Bio-PdNPs g^{-1} GAC), Bio-PdNP3 (6 mg Bio-PdNPs g^{-1} GAC), and an unmodified 0.6-1.1 mm GAC.

5.3.3 Preliminary Cr(VI)-reducing MFC model

In order to explicitly define the effect of Bio-PdNPs on the performance of Cr(VI)-reducing MFC, the first order and second order models were used. Due to the lag phase that was observed in the reduction of Cr(VI) which is a result of the time required for the electrogens to adapt to the MFC anode and electrical conditions (Song et al., 2016), the time delay was incorporated in both the first order and second order models as shown in Equation (5.5) and Equation (5.6).

The removal kinetics of Cr (VI) were regressed using the first order and the second order rate equations. The first order rate equation with time delay is given by Equation (5.5):

$$-\ln\frac{C_{Cr(VI)}}{C_{Cr(VI)0}} = \begin{cases} 0, & t < t_d \\ k_1(t - t_d), & t \geq t_d \end{cases} \tag{5.5}$$

where $C_{Cr(VI)0}$ and $C_{Cr(VI)}$ are the concentration of Cr(VI) (mg L^{-1}) initially and at any time (t), k_1 is the rate constant for Cr(VI) reduction (h^{-1}), and t_d is the time delay before the model fits the kinetics (h). The plot of $-\ln\frac{C_{Cr(VI)}}{C_{Cr(VI)0}}$ vs. t gives a slope which represents the rate constant, k_1. The second order rate equation with time delay is given by Equation (5.6):

$$\frac{1}{C_{Cr(VI)}} - \frac{1}{C_{Cr(VI)0}} = \begin{cases} 0, & t < t_d \\ k_2(t - t_d), & t \geq t_d \end{cases} \tag{5.6}$$

where k_2 is the rate constant for Cr(VI) reduction (L mg^{-1} h^{-1}). The plot of $\frac{1}{C_{Cr(VI)}} - \frac{1}{C_{Cr(VI)0}}$ vs. t gives a slope which represents the rate constant, k_2. The constants k_1, k_2, and t_d were simply determined by using Solver in Excel and minimizing the sum of squared errors.

The parameters for the first order model were determined for Bio-PdNP1 (k_1 = 0.085 h^{-1}, t_d = 9.6 h, R^2 = 0.99), Bio-PdNP2 (k_1 = 0.13 h^{-1}, t_d = 4.3 h, R^2 = 0.987), Bio-PdNP3 (k_1 = 0.16 h^{-1}, t_d = 1.7 h, R^2 = 0.989) and unmodified 0.6-1.1 mm GAC (k_1 = 0.073 h^{-1}, t_d = 14.3 h, R^2 = 0.995). Figure 5.11a shows the model results during parameter estimation. As it can be seen, Bio-PdNP3 had the lowest time delay and the highest rate constant, hence it performed better. The determined first order model parameters were then used to plot the Cr(VI) profile in Figure 5.11b which is in agreement with the experimental data and shows that the model correctly predicted the time delays.

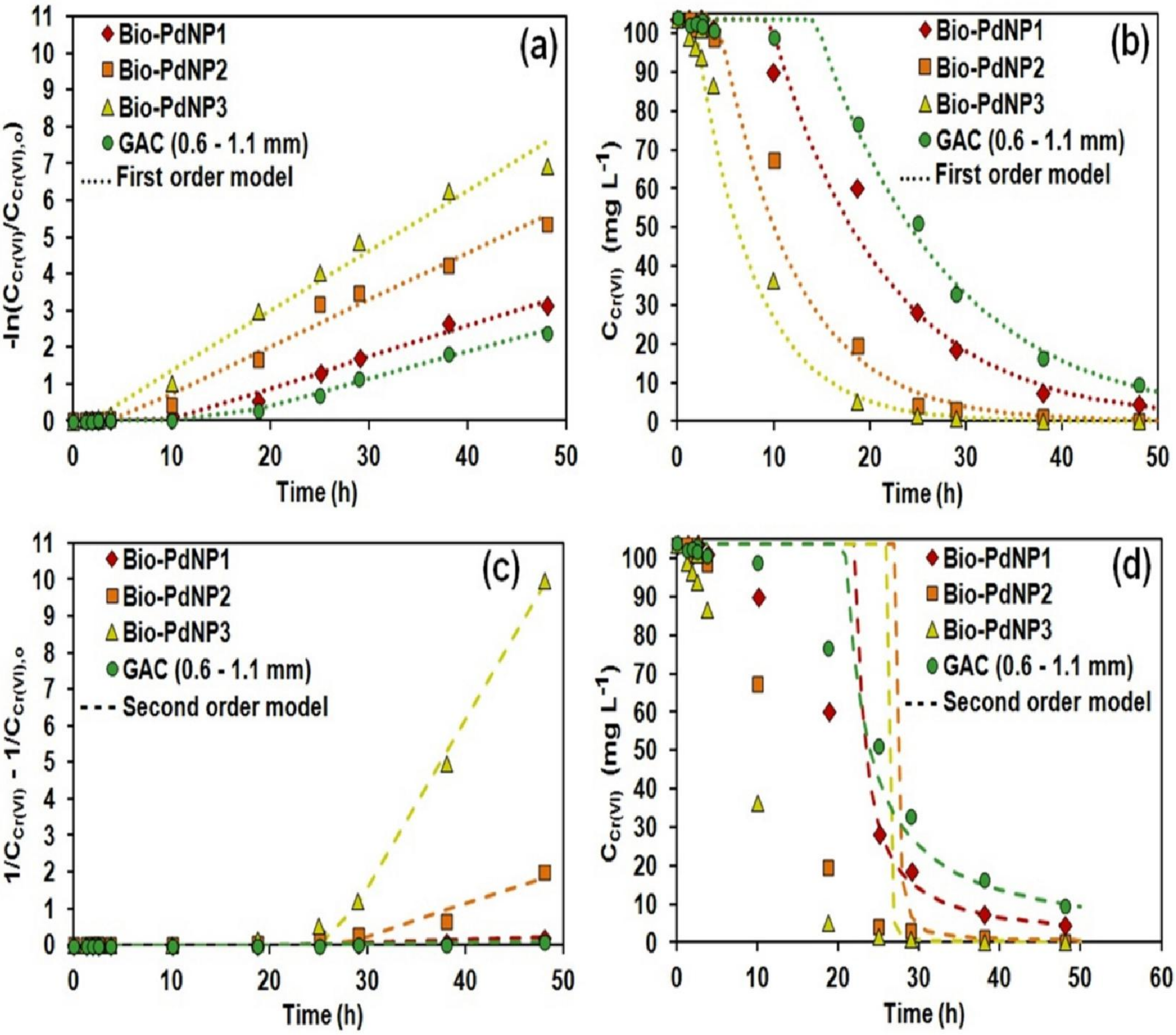

Figure 5.11 (a) Cr(VI) reduction kinetics using the first order kinetic equation with time delay, (b) the Cr(VI) experimental profile plotted against Cr(VI) profile calculated using the parameters determined from the first order kinetic equation with time delay, (c) Cr(VI) reduction kinetics using the second order kinetic equation with time delay, (d) the Cr(VI) experimental profile plotted against Cr(VI) profile calculated using the parameters determined from the second order kinetic equation with time delay.

The parameters for the second order model were determined for Bio-PdNP1 (k_2 = 0.0081 L mg^{-1} h^{-1}, t_d = 22.2 h, R^2 = 0.996), Bio-PdNP2 (k_2 = 0.089 L mg^{-1} h^{-1}, t_d = 27.4 h, R^2 =

0.951), Bio-PdNP3 (k_2 = 0.46 L mg^{-1} h^{-1}, t_d = 26.6 h, R^2 = 0.996) and unmodified 0.6-1.1 mm GAC (k_2 = 0.0033 L mg^{-1} h^{-1}, t_d = 20.9 h, R^2 = 0.988). Figure 5.11c shows the model results during parameter estimation. The second order model was able to determine the rate constants however, it overestimated the time delays. This can be shown by the plot of Cr(VI) profile in Figure 5.11d that was determined by using the second order model parameters. As it can be seen, due to the overestimation of the time delays, the Cr(VI) reduction kinetics were not correctly predicted. This shows that the estimation of time delay is a critical step in the kinetic modelling of systems with lag time.

CHAPTER 6: CHROMIUM (VI)-REDUCING MICROBIAL FUEL CELL MODELING USING INTEGRATED MONOD KINETICS AND BUTLER-VOLMER EQUATION

6.1 Model Description

A mechanistic Cr(VI)-reducing MFC model is developed on a two population microbial model in which the primary microbes represent the microorganisms that are able to utilise substrate (*S*) for energy generation and the secondary ones represent those that utilize the substrate but do not release free electrons to be used for electricity generation in MFC (Figure 6.1) (Gadkari et al., 2019).

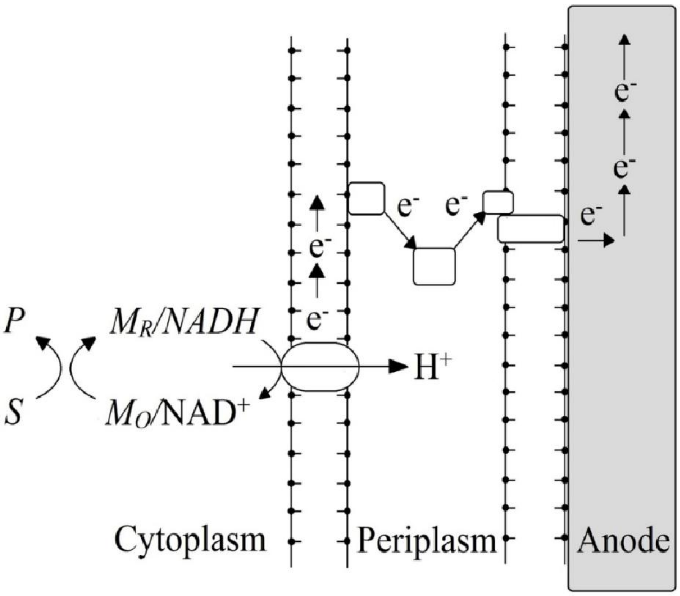

Figure 6.1 Schematic of the bioanode where the primary cells utilize substrate (*S*) which is converted to products (*P*), and where the primary cells in the cytoplasm convert the oxidising agent intracellular mediator (M_O) to the reducing agent intracellular mediator (M_R), which is then transported to the mitochondrial matrix of the primary cells where it oxidises back to M_O and leads to electron transfer.

The electrons generated from the anode chamber are assumed to be transferred via physical contact between the outer membrane of primary cells and the anode using intracellular mediators, i.e., NAD$^+$/NADH, since they are the principal electron shuttle in formate oxidation (Dan Pfenninger-Li and Dimroth, 1992). The electrons are then accepted in the cathode chamber by Cr(VI) which is reduced to trivalent chromium [Cr(III)]. The schematic of electron transport from the cell to the anode is represented by Figure 6.1, where the primary cells utilise the substrate (*S*) to form products (*P*), and during this process, the primary cells in the cytoplasm convert the oxidising agent intracellular mediator (M_O) (i.e., NAD$^+$) to the reducing agent intracellular mediator (M_R) (i.e., NADH), then M_R is transported to the mitochondrial matrix of the primary cells where it oxidises back to M_O and leads to electron generation (Gadkari et al., 2019; Stein and Imai, 2012).

The important assumptions made in the model include:

- The MFC operates under pH conditions where the formed Cr(III) does not precipitate.
- Any gas formation formed such as CO_2 and H_2 remain dissolved in the chamber of anode bulk solution.
- Temperature of both anode and the cathode chamber are assumed constant, and pH change is assumed to be negligible.
- The MFC is operated under batch conditions.
- Electrons are transferred to the anode electrode by direct attachment of electrogens which utilize intracellular redox mediators which transform between oxidized and reduced forms.
- The electrons are accepted in the cathode chamber by Cr(VI) only, and during the experiment, there is no entry of O_2 or any other oxidizing agent in the cathode chamber.
- There is no Cr(VI) crossover to the anode chamber.

6.1.1 Butler-Volmer equation

A reaction in electrochemistry involves the transfer of electrons during the oxidation and reduction of chemical species which can be expressed as a reversible reaction as shown in Equation (6.1):

$$\mathrm{O} + ne^{-} \leftrightarrow \mathrm{R} \tag{6.1}$$

where O is the oxidising agent, R is the reducing agent, and n is the number of moles of electrons transferred per mole reaction. As a consequence, an electric current due to the transfer of electrons is produced and can be determined by using a quantitative proportional relationship that the current itself has with the transferred charges and the net reaction rate which is given by Faraday's law as shown in Equation (6.2) (Seeber et al., 2015):

$$I = \frac{nFv\ q_{net}}{1000} \tag{6.2}$$

where I is the current output, F is the Faraday's constant (96845 A s mol^{-1}), v is the volume of the respective chamber, and q_{net} is the net reaction rate. Due to the reversibility of the reaction in Equation (6.1), the net reaction rate can be expressed as Equation (6.3):

$$q_{net} = k_f[O] - k_b[R] \tag{6.3}$$

where k_f and k_b are the reaction rate constants of both the forward and backward reactions, respectively, with $[O]$ and $[R]$ being the concentrations of the oxidising and reducing agents, respectively. By substituting Equation (6.3) to Equation (6.1), the current output for the net reaction can then be expressed in terms of the concentrations of both oxidising and reducing agents as shown in Equation (6.4):

$$I = \frac{nFv}{1000}\left(k_f[O] - k_b[R]\right) \tag{6.4}$$

Equation (6.4) forms a fundamental basis of the relationship between the concentration and electric current, however, the rate constants are actually dependent on the cell potential and are expressed in terms of an Arrhenius-type equation, in which the activation energy is assumed to be proportional to the cell potential (E) as shown in Equations (6.5) and (6.6) (Scott, 2016b):

$$k_f = k^0{}_f \exp\left(\frac{-\alpha nFE}{RT}\right) \tag{6.5}$$

$$k_b = k^0{}_b \exp\left(\frac{(1-\alpha)nFE}{RT}\right) \tag{6.6}$$

where $k^o{}_f$ and $k^o{}_b$ are reaction rate constants of the forward and backward reactions at standard conditions, respectively, α is the transfer coefficient, R is the gas constant (8.314 Pa m^3 mol^{-1} K^{-1}), and T is the temperature. The relationship between α and the geometry symmetry factor (β) is given by Equations (6.7) and (6.8) (Mann et al., 2006):

$$\alpha = \frac{\beta(no - nb - na) + nb}{l} \tag{6.7}$$

$$1 - \alpha = \frac{(1 - \beta)(no - nb - na) + nb}{l} \tag{6.8}$$

where no is the number of electrons being transferred in the overall reaction, nb is the number of electrons being transferred before the rate determining step (rds), na is the number of electrons being transferred after the rds, and l is stoichiometric coefficient (the number of times that the rds must take place for the overall reaction to occur once). α signifies the fraction of the interfacial potential at an electrode-electrolyte interface that helps in lowering the free energy barrier for the electrochemical reaction, and from Equations (6.7) and (6.8), it can be seen that α should not be confused with β which has the same meaning as α but only applies for a single-step reaction and its value is between 0 and 1 (Bockris and Nagy, 1973; Mann et al., 2006). In a single-step process, when na and nb are 0 and l is equal to 1, the value of α is equal to β and also ranges between 0 and 1. However, in a multi-step process that is not the case. Therefore, care and caution should be taken when applying these two. In our model, we will applyα for a general model. It should be noted that Equations (6.7) and (6.8) only apply when the steps before the rds are in pseudo-equilibrium (Mann et al., 2006).

Substitution of Equations (6.5) and (6.6) to Equation (6.4) leads to an equation that describes the explicit relationship between the current output and both the cell potential and concentrations as shown in Equation (6.9):

$$I = \frac{nFv}{1000}\left(k^o{}_f \exp\left(\frac{-\alpha nFE}{RT}\right)[O] - k^o{}_b \exp\left(\frac{(1-\alpha)nFE}{RT}\right)[R]\right) \tag{6.9}$$

At equilibrium conditions, when the forward rate is equal to the backward rate, $I = 0$ in Equation (6.9). This is because there is an electric current between the forward and the backward reactions which is equal in magnitude but opposite in sign. This current output at equilibrium conditions is known as exchange current (Io) and is described by Equations (6.10) and (6.11):

$$Io = Io_f = \frac{nFv}{1000} k^o{}_f \exp\left(\frac{-\alpha nFE_e}{RT}\right)[O]_e \tag{6.10}$$

$$Io = Io_b = \frac{nFv}{1000} k^o{}_b \exp\left(\frac{(1-\alpha)nFE_e}{RT}\right)[R]_e \tag{6.11}$$

where $[O]_e$ and $[R]_e$ are the equilibrium concentrations of both the oxidising and reducing agents, respectively, and Io_f and Io_b are the exchange currents of both the forward and backward reactions, respectively.

The difference between the actual and equilibrium cell potential (E_e) is called overpotential (η) (Equation (6.12)) and expresses the added amount of thermodynamic force that the MFC must overcome in order to drive the redox reaction. Overpotentials are responsible for the MFC operating at output potential difference values lower than the theoretical/reversible output potential difference.

$$\eta = E - E_e \tag{6.12}$$

By substituting Equation (6.12) to Equation (6.9), and using the definitions of exchange current described in Equations (6.10) and (6.11), we find a more familiar Butler-Volmer type expression which is given by Equation (6.13) (Bard and Faulkner, 2000):

$$\frac{I}{Io} = \left(\frac{[O]}{[O]_e}\exp\left(\frac{-\alpha nF\eta}{RT}\right) - \frac{[R]}{[R]_e}\exp\left(\frac{(1-\alpha)nF\eta}{RT}\right)\right) \tag{6.13}$$

This equation forms one of the most fundamental electrochemical relationships by defining the kinetics of a unimolecular redox reaction using the relationship between electrical current, and both the cell potential and the concentrations of the reducing and oxidising agents, and will therefore be used to further define overpotentials for the Cr(VI)-reducing MFC.

6.1.2 Cr(VI)-reducing MFC overpotential

In electrochemical reactions, there is a thermodynamic requirement which is essential to drive the redox reactions at a certain rate, this requirement is known as overpotential (η) (Bard and Faulkner, 2000). From Equation (6.12), η was defined as the difference between the actual and equilibrium cell potential, and was further shown that it forms part of the Butler-Volmer type equation in Equation (6.13). Therefore, provided that there is no concentration gradient between the equilibrium surface concentration and surface concentration for both O and R in Equation (6.13), then the resulting Butler-Volmer equation can be expressed as Equation (6.14):

$$I = Io\left(\exp\left(\frac{-\alpha nF\eta}{RT}\right) - \exp\left(\frac{(1-\alpha)nF\eta}{RT}\right)\right) \tag{6.14}$$

Equation (6.14) assumes that the overpotential of the MFC can be expressed as activation overpotential with concentration overpotential being negligible. The cause of activation overpotential is due to the losses related to the activation energy of the redox reaction that the MFC needs to overcome (Wang et al., 2015). The concentration overpotential is caused by losses due to the concentration gradient between the surface and equilibrium surface concentration (bulk concentration) (Wang et al., 2015).

When the activation overpotential of the MFC is sufficiently small, according to Taylor polynomial expansion, Equation (6.14) can be approximated as Equation (6.15) (Menictas et al., 2014):

$$I = Io\frac{nF\eta}{RT} \tag{6.15}$$

In which Equation (6.15) will be used to define the overpotentials of the Cr(VI)-reducing MFC. The charge transfer resistance (r_{ct}) which is given by Equation (6.16) can be derived from Equation (6.15):

$$r_{ct} = \frac{1}{Io}\frac{RT}{nF} \tag{6.16}$$

where r_{ct} is a reflection of how facile an electrochemical reaction is in MFC. The lower the r_{ct}, the faster the electrochemical reaction.

6.1.3 Anode chamber equations

In the anode chamber, the substrate (S) is consumed by both primary cells (X_{pr}) and secondary cells (X_{se}), and during this process, the primary cells in the cytoplasm convert the oxidising agent intracellular mediator (M_O) (i.e., NAD$^+$) to the reducing agent intracellular mediator (M_R) (i.e., NADH), then M_R is transported to the mitochondrial matrix of the primary cells where oxidation leads to electron generation (Gadkari et al., 2019; Stein and Imai, 2012). The secondary cells utilize substrate but do not release free electrons to be used for electricity generation in MFC.

The primary cells growth rate (μ_{pr}) is double limited by both S and M_O in the monod expression given in Equation (6.17) (Kato Marcus et al., 2007), and the secondary cells growth rate (μ_{se}) is only dependent on S (Equation (6.18)):

$$\mu_{pr} = \mu_{maxpr}\left(\frac{S}{K_{Spr} + S}\right)\left(\frac{M_O}{K_{M_Opr} + M_O}\right) \tag{6.17}$$

$$\mu_{se} = \mu_{maxse}\left(\frac{S}{K_{Sse} + S}\right) \tag{6.18}$$

where μ_{maxpr} and μ_{maxse} are the maximum growth rates of primary cells and secondary cells, respectively, K_{Spr} and K_{M_Opr} are the half-saturation constants of substrate and oxidising intracellular mediator for primary cells, respectively, and K_{Sse} is the half-saturation constant of substrate for secondary cells. The anode species mass balances are represented by the following equations:

$$\frac{dS}{dt} = -\frac{1}{Y_{Xpr/s}MM_s}\mu_{pr}X_{pr} - \frac{1}{Y_{Xse/s}MM_s}\mu_{se}X_{se} \tag{6.19}$$

$$\frac{dX_{pr}}{dt} = \mu_{pr}X_{pr} - k_{dpr}X_{pr} \tag{6.20}$$

$$\frac{dX_{se}}{dt} = \mu_{se}X_{se} - k_{dse}X_{se} \tag{6.21}$$

where $Y_{Xpr/s}$ and $Y_{Xse/s}$ are the yields of the primary and secondary cells to substrate, respectively, k_{dpr} and k_{dse} are the decay rate constants of the primary and secondary cells, respectively, and MM_s is the molar mass of substrate. In addition, the mass balance of the reducing agent intracellular mediator is given by Equation (6.22):

$$\frac{dM_R}{dt} = \frac{Y_{M_R/s}}{Y_{Xpr/s} MM_{M_R}} \mu_{pr} X_{pr} - \frac{1000 I_{MFC}}{2F v_a} \tag{6.22}$$

where $Y_{M_R/s}$ is the yield of the reducing agent intracellular mediator to substrate, and MM_{M_R} is the molar mass of the reducing agent intracellular mediator. The first term in Equation (6.22) is related to NADH formation in the cytoplasm due to cell growth, and the second term is related to NADH oxidation in the mitochondrial matrix for electron generation (Stein and Imai, 2012). The second term is in the form of the rate equation derived in Equation (6.2) which relates the reaction rate to current output by using Faraday's law due to the reversible reaction between M_O (i.e., NAD$^+$) and M_R (i.e., NADH) shown in Equation (6.23).

$$M_O + \mathrm{H}^+ + 2\mathrm{e}^- \leftrightarrow M_R \qquad E_a^O = -0.32V \tag{6.23}$$

It should be noted that the standard cell potential of the anode (-0.32 V vs. SHE) (Jay et al., 2020) is related to the intracellular mediators and not the substrate because the reaction expressed in Equation (6.23) is the principal reaction involved in electron transport and electron generation during substrate/formate oxidation (Dan Pfenninger-Li and Dimroth, 1992). The total mass of the intracellular mediator (M_T) is given by Equation (6.24):

$$M_T = M_R + M_O \tag{6.24}$$

Provided that M_T is a constant, the mass balance of M_O is given by Equation (6.25):

$$\frac{dM_O}{dt} = -\frac{dM_R}{dt} \tag{6.25}$$

To derive the Cr(VI)-reducing MFC anode overpotential, Equation (6.15) is used. The resulting equation is shown in Equation (6.26):

$$\eta_{aMFC} = \frac{I_{MFC}}{Io_a} \frac{RT_a}{2F} \tag{6.26}$$

where η_{aMFC} , T_a and Io_a are the Cr(VI)-reducing MFC anode overpotential, temperature, and exchange current, respectively. Io_a is assumed to be constant. In addition, the charge transfer resistance of the anode (r_{cta}) is expressed by Equation (6.27):

$$r_{cta} = \frac{1}{Io_a} \frac{RT_a}{2F} \tag{6.27}$$

6.1.4 Cathode chamber equations

In the cathode chamber, Cr(VI) in the form of dichromate is reduced to Cr(III) by gaining the electrons from the anode chamber. The Cr(VI)-reducing MFC is assumed to be operating at low pH values where no Cr(III) precipitation is observed. The reversible reaction of dichromate ($Cr_2O_7^{2-}$) to Cr(III) is represented by Equation (6.28):

$$\mathrm{Cr_2O_7}^{2-} + 14\mathrm{H}^+ + 6\mathrm{e}^- \leftrightarrow 2\mathrm{Cr}^{3+} + 7\mathrm{H_2O} \qquad E_c^o = 133\mathrm{V} \tag{6.28}$$

With the forward reaction in Equation (6.28) favoured, the mass balance of $Cr_2O_7^{2-}$ in the cathode is expressed by Equation (6.29) which is derived from Equation (6.2):

$$\frac{d[Cr_2O_7{}^{2-}]}{dt} = -\frac{1000 I_{MFC}}{6Fv_c} \tag{6.29}$$

where $[Cr_2O_7{}^{2-}]$ is the concentration of dichromate and v_c is the volume of cathode chamber. Since there are 2 mol of Cr(VI) per mol of $Cr_2O_7^{2-}$ in Equation (6.28), the mass balance of Cr(VI) in the cathode chamber is expressed by Equation (6.30):

$$\frac{d[Cr(VI)]}{dt} = 2\frac{d[Cr_2O_7{}^{2-}]}{dt} \tag{6.30}$$

where $[Cr(VI)]$ is the concentration of Cr(VI). Equation (6.31) is used to calculate Cr(III) concentration ($[Cr(III)]$):

$$\frac{d[Cr(III)]}{dt} = 2\frac{1000\,I_{MFC}}{6Fv_c} \tag{6.31}$$

To derive the Cr(VI)-reducing MFC cathode overpotential, Equation (6.15) is used and the resulting equation is shown in Equation (6.32):

$$\eta_{cMFC} = \frac{I_{MFC}}{Io_c}\frac{RT_c}{6F} \tag{6.32}$$

where η_{cMFC} , T_c and Io_c are the Cr(VI)-reducing MFC cathode overpotential, temperature and exchange current, respectively. Io_c is assumed to be a constant. In addition, the charge transfer resistance of the cathode (r_{ctc}) is given by Equation (6.33):

$$r_{ctc} = \frac{1}{Io_c}\frac{RT_c}{6F} \tag{6.33}$$

6.1.5 *Ohmic losses*

Ohmic losses (η_{ohmic}) are caused by the resistance to electron flow within the cell and can be expressed by Equation (6.34):

$$\eta_{ohmic} = I_{MFC}r_{int} \tag{6.34}$$

where r_{int} is the internal resistance. Following an approach suggested by Pinto et al. (2010), the r_{int} can be calculated using Equation (6.35):

$$r_{int} = r_{min} + (r_{max} - r_{min})e^{-\left(\theta_{X_{pr}r_{int}}X_{pr} + \theta_{Cr(VI)r_{int}}Cr(VI) + \theta_{Sr_{int}}S\right)} \tag{6.35}$$

where r_{min} and r_{max} are the minimum and maximum observed internal resistance, respectively, and $\theta_{X_{pr}r_{int}}$, $\theta_{Cr(VI)r_{int}}$ and $\theta_{Sr_{int}}$ are the primary cells, Cr(VI) and substrate constants which determine the internal resistance steepness of the curve, respectively. The usage of Equation (6.35) to represent the Cr(VI)-reducing MFC internal resistance is supported by the fact that the concentration of microbial cells, Cr(VI) and substrate have an impact on the internal resistance of the MFC. Equation (6.35) also improves the modelling accuracy of the start-up phase in MFCs (Pinto et al., 2010).

6.1.6 *Output potential difference*

The reversible output potential difference (ΔV_{rev}) of the Cr(VI)-reducing MFC is calculated using Equation (6.36):

$$\Delta V_{rev} = E_{min} + (E_{max} - E_{min})e^{-\left(\frac{1}{\theta_{X_{pr},\Delta V_{rev}} X_{pr}} + \frac{1}{\theta_{Cr(VI)\Delta V_{rev}} Cr(VI) + \varepsilon} + \frac{1}{\theta_{S\Delta V_{rev}} S + \varepsilon}\right)} \quad (6.36)$$

where ϵ is a constant which is approximately equal to zero ($\epsilon \sim 0$), E_{min} and E_{max} are the minimum and maximum observed open circuit voltages (OCV), respectively, and $\theta_{X_{pr}\Delta V_{rev}}$, $\theta_{Cr(VI)\Delta V_{rev}}$ and $\theta_{S\Delta V_{rev}}$ are the primary cells, Cr(VI) and substrate constants which determine the output potential difference steepness of the curve, respectively. The inclusion of a constant ϵ in Equation (6.36) is because the concentration of Cr(VI) and substrate can reach a value of zero and make the equation discontinuous, therefore ϵ serves to remove the discontinuity during simulation. Equation (6.36) is used because of the dependence of ΔV_{rev} on the concentration of microbial cells, Cr(VI) and substrate. In addition, it improves the modelling accuracy of the start-up phase in MFCs (Pinto et al., 2010). The output potential difference (ΔV_{MFC}) in Equation (6.37) is calculated as the difference between ΔV_{rev} and the Cr(VI)-reducing MFC overpotentials (which includes the ohmic losses derived in Equations (6.34) and (6.35)):

$$\Delta V_{MFC} = \Delta V_{rev} - \eta_{c,MFC} - \eta_{a,MFC} - \eta_{ohmic} \quad (6.37)$$

In addition, I_{MFC} can be expressed using Equation (6.38):

$$I_{MFC} = \frac{\Delta V_{rev}}{r_{ext} + r_{int} + r_{ct,c} + r_{ct,a}} \left(\frac{Cr(VI)}{Cr(VI) + \epsilon}\right)\left(\frac{S}{S + \epsilon}\right) \quad (6.38)$$

where r_{ext} is the external resistance. The terms in brackets are included so that the current is equal to zero when there is no Cr(VI) in the cathode chamber and substrate in the anode chamber. As mentioned, ϵ is a constant which is approximately equal to zero ($\epsilon \sim 0$).

6.1.7 Solution strategy

The Cr(VI)-reducing MFC anode chamber equations (Equations (6.17)-(6.22), Equations (6.25)-(6.27)), cathode chamber equations (Equations (6.29)-(6.33)), ohmic loss equations (Equations (6.34)-(6.35)) and overall output potential difference equations (Equations (6.36)-(6.38)) are coupled together and solved using an open source Python-based odeint() function which can be found from the Python-based scipy.integrate module. Odeint() is a built-in function in Python that allows one to numerically solve ordinary differential equations. The model should be expressed in the form of Equations (6.39)–(6.40) in Python:

$$\dot{x}(t) = f(x(t), t, p) \quad t \in [t_o, t_f] \tag{6.39}$$

$$s.t. \quad x(t_o) = \bar{x}_o \tag{6.40}$$

where x and p are differential variables and parameters, respectively, and f are the explicit ordinary differential equations. Equation (6.40) represents the initial conditions for the differential variables.

To determine the parameters, a Python-based minimize() function from the scipy.optimize Python module was used. Minimize() function contains a Sequential Least SQuares Programming (SLSQP) method which determines the non-linear Cr(VI)-reducing MFC model parameters by minimizing the specified normalized root mean squared error shown in Equation (6.41):

$$\min \frac{\sqrt{\dfrac{\sum_{t=t_o}^{t_f} \varepsilon_{Cr(VI)(t)}^{\;2}}{z_{Cr(VI)}}}}{\overline{\omega}_{Cr(VI)}} + \frac{\sqrt{\dfrac{\sum_{t=t_o}^{t_f} \varepsilon_{\Delta V_{MFC}(t)}^{\;2}}{z_{\Delta V_{MFC}}}}}{\overline{\omega}_{\Delta V_{MFC}}} \tag{6.41}$$

where $z_{Cr(VI)}$ and $z_{\Delta V_{MFC}}$ are the number of data points for Cr(VI) reduction and output potential difference, respectively; $\overline{\omega}_{Cr(VI)}$ and $\overline{\omega}_{\Delta V_{MFC}}$ are the mean of the measured values of Cr(VI) concentration and output potential difference, respectively; and the residuals of both Cr(VI) ($\varepsilon_{Cr(VI)(t)}$) and output potential difference ($\varepsilon_{\Delta V_{MFC}(t)}$) are given by Equations (6.42) and (6.43):

$$\varepsilon_{Cr(VI)(t)} = Cr(VI)_{exp(t)} - Cr(VI)_{sim(t)} \tag{6.42}$$

$$\varepsilon_{\Delta V_{MFC}(t)} = \Delta V_{MFC\,exp(t)} - \Delta V_{MFC\,sim(t)} \tag{6.43}$$

where $Cr(VI)_{exp(t)}$ and $Cr(VI)_{sim(t)}$ are the experimental and simulated results for Cr(VI) concentration, respectively; and $\Delta V_{MFC\,exp(t)}$ and $\Delta V_{MFC\,sim(t)}$ are the experimental and simulated results for output potential difference, respectively.

To determine if the Cr(VI)-reducing MFC model is correctly specified and can be solved by odeint() function, the total number of differential variables (DV) and algebraic variables (AV) are determined. Table 6.1 shows the results.

Table 6.1 The number of differential variables and algebraic variables.

Differential Variables (DV)	Algebraic Variables (AV)
S	μ_{pr}
X_{pr}	μ_{se}
X_{se}	η_{aMFC}
M_R	η_{cMFC}
M_O	η_{ohmic}
$[Cr_2O_7^{\ 2-}]$	ΔV_{rev}
$[Cr(VI)]$	ΔV_{MFC}
$[Cr(III)]$	$I_{\ MFC}$
	r_{int}
	r_{cta}
	r_{ctc}
Total = 8 DVs	Total = 11 AVs

The values in Table 6.1 are then used to determine the total number of unknowns calculated by using Equations (6.44)-(6.45):

$$Totalunknowns = DV + AV \tag{6.44}$$

$$Totalunknowns = 8 + 11 = 19 \tag{6.45}$$

The total number of linearly independent equations are then calculated from the total number of anode chamber linearly independent equations (ACLIE) (Equations (6.17)-(6.22), Equations (6.25)-(6.27)), cathode chamber linearly independent equations (CCLIE) (Equations (6.29)-(6.33)), ohmic loss linearly independent equations (OLLIE) (Equations (6.34)-(6.35)) and overall output potential difference linearly independent equations (OPDLIE) (Equations (6.36)-(6.38)):

$$Totallinearlyindependentequations = \mathrm{ACLIE} + \mathrm{CCLIE} + \mathrm{OLLIE} + \mathrm{OPDLIE} \tag{6.46}$$

$$Totallinear\ lyindependentequations = 9 + 5 + 2 + 3 = 19 \tag{6.47}$$

Finally, the total number of unknowns in Equation (6.45) and total number of linearly independent equations in Equation (6.47) are then used to determine the degrees of freedom (DOF) (Equation (6.49)):

$$DOF = Totalunknowns - Totallinearlyindependentequations \tag{6.48}$$

$$DOF = 19 - 19 = 0 \tag{6.49}$$

Since DOF = 0, this means that the Cr(VI)-reducing MFC model is correctly specified.

6.2 Parameter Determination

The parameters used in the Cr(VI)-reducing MFC model were measured and estimated. The estimated parameters were determined by using a Python-based minimize() function using the method SLSQP used for non-linear parameter estimation problems from a Python module scipy.optimize and minimising the objective function specified in Equation (6.41). The parameters were estimated using the complete data in Figure 6.2. Table 6.2 summarizes the parameter values used for the Cr(VI)-reducing MFC model.

Table 6.2 Model parameter values for the Cr(VI)-reducing MFC.

Param.	Values	Units	Ref.	Param.	Values	Units	Ref.
$K_{S,pr}$	18.8	mmol L^{-1}	Estimated	v_a	0.2	L	Measured
$K_{MO,pr}$	2.12	mmol L^{-1}	Estimated	v_c	0.2	L	Measured
$K_{S,se}$	19.3	mmol L^{-1}	Estimated	$\theta_{X_{pr},r_{int}}$	0.288	L mg^{-1}	Estimated
$\mu_{max,pr}$	2.21 x 10^{-4}	s^{-1}	Estimated	$\theta_{X_{pr},\Delta V_{rev}}$	0.036	L mg^{-1}	Estimated
$\mu_{max,se}$	3.32 x 10^{-19}	s^{-1}	Estimated	$\theta_{Cr(VI),r_{int}}$	0.023	L mmol^{-1}	Estimated
$Y_{Xpr/s}$	0.94	mg mg^{-1}	Estimated	$\theta_{Cr(VI),\Delta V_{rev}}$	4.8	L mmol^{-1}	Estimated
$Y_{Xse/s}$	0.23	mg mg^{-1}	Estimated	$\theta_{S,r_{int}}$	0.8	L mmol^{-1}	Estimated
$Y_{M_R/s}$	0.63	mg mg^{-1}	Estimated	$\theta_{S,\Delta V_{rev}}$	0.77	L mmol^{-1}	Estimated
MM_s	45.02	g mol^{-1}	Constant	E_{max}	0.54	V	Estimated
MM_{M_R}	665.12	g mol^{-1}	Constant	E_{min}	0.02	V	Measured
$k_{d,pr}$	1.49 x 10^{-5}	s^{-1}	Estimated	r_{max}	2100	Ω	Measured
$k_{d,se}$	2.55 x 10^{-4}	s^{-1}	Estimated	r_{min}	50	Ω	Measured
F	96485	A s mol^{-1}	Constant	r_{ext}	1000	Ω	Measured
R	8.314	J mol^{-1} K^{-1}	Constant	T_a	311	K	Measured
Io_a	7.48 x 10^{-4}	A	Estimated	T_c	298	K	Measured
Io_c	8.02 x 10^{-4}	A	Estimated				

The modelling results for Cr(VI) reduction and output potential difference in MFC are shown in Figure 6.2a and Figure 6.2b, respectively.

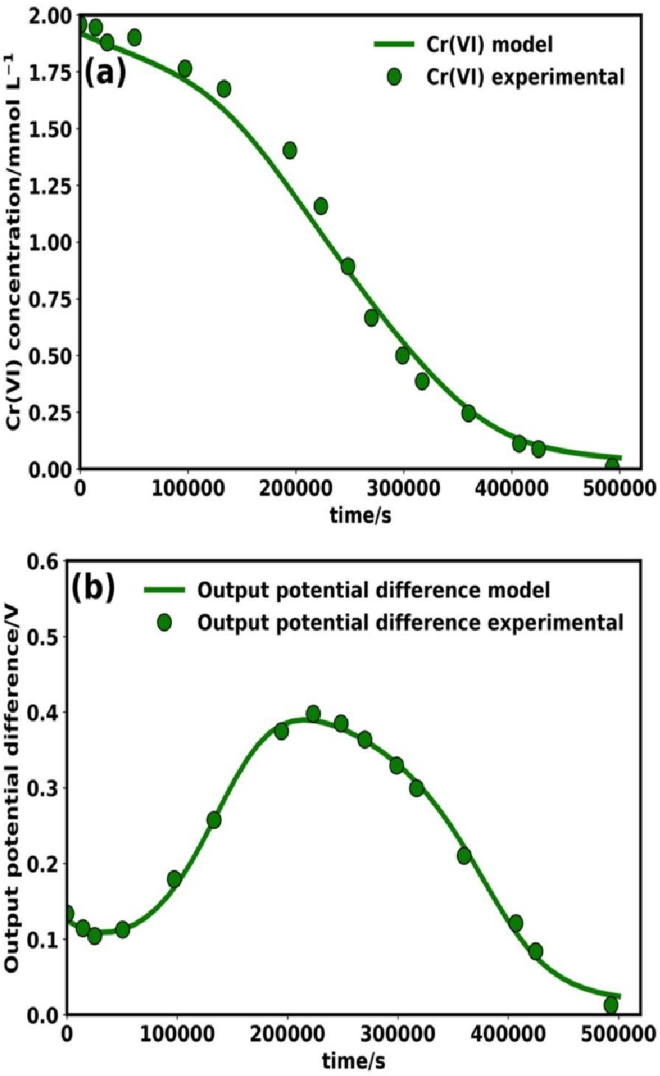

Figure 6.2 A comparison between predicted model values and experimental data for (a) Cr(VI) reduction and, (b) output potential difference.

A lag in Cr(VI) removal was observed in the first 150000 s (41.7 h) in Figure 6.2a. This was due to the microorganisms in the cells adapting to the electrical conditions which is a problem in MFCs that can be solved by using bioaugmentation (Pandit et al., 2015; Raghavulu et al., 2013). After the lag in removal of Cr(VI), an increase in the removal rate of Cr(VI) was seen due the consumption of the substrate by the electrogens which generates electrons and cause an increase in output potential difference (Sophia and Saikant, 2016). The decrease in Cr(VI) removal in the end was due to mass transfer losses caused by a decrease in bulk Cr(VI) concentration (Scott, 2016a). Therefore, as seen in Figure 6.2a, the profile of

Cr(VI) reduction was taken into account and successfully predicted using the determined parameters. The output potential difference was also predicted as shown in Figure 6.2b. The increase in output potential difference was caused by an increase in rate of Cr(VI) removal, and a decrease was due to the rate of Cr(VI) removal decreasing. In addition, the maximum of the output potential difference was located at the point where the Cr(VI) removal profile had reached an inflection point as shown in Figure 6.2a. This indicates that the output potential difference profile is related to the rate of Cr(VI) removal.

To ascertain that the model was a good fit to the experimental data, statistical analysis of the non-linear Cr(VI)-reducing MFC model was performed. The root mean squared error (RMSE) for each fit was calculated using Equations (6.50) and (6.51):

$$RMSE_{Cr(VI)} = \sqrt{\frac{\sum_{i=1}^{z_{Cr(VI)}} \left(Cr(VI)_{exp(i)} - Cr(VI)_{sim(i)}\right)^2}{z_{Cr(VI)}}} \tag{6.50}$$

$$RMSE_{\Delta V_{MFC}} = \sqrt{\frac{\sum_{i=1}^{z_{\Delta V_{MFC}}} \left(\Delta V_{MFC_{exp(i)}} - \Delta V_{MFC_{sim(i)}}\right)^2}{z_{\Delta V_{MFC}}}} \tag{6.51}$$

where $RMSE_{Cr(VI)}$ is the RSME for Cr(VI) and $RMSE_{\Delta V_{MFC}}$ is the RSME for output potential difference. Then both the RMSEs were normalized using Equations (6.52) and (6.53) to determine the normalized root mean squared error (NRMSE) (Jörnsten et al., 2007):

$$NRMSE_{Cr(VI)} = \frac{\sqrt{\frac{\sum_{i=1}^{z_{Cr(VI)}} \left(Cr(VI)_{exp(i)} - Cr(VI)_{sim(i)}\right)^2}{z_{Cr(VI)}}}}{\bar{\omega}_{Cr(VI)}} \tag{6.52}$$

$$NRMSE_{\Delta V_{MFC}} = \frac{\sqrt{\frac{\sum_{i=1}^{z_{\Delta V_{MFC}}} \left(\Delta V_{MFC_{exp(i)}} - \Delta V_{MFC_{sim(i)}}\right)^2}{z_{\Delta V_{MFC}}}}}{\bar{\omega}_{\Delta V_{MFC}}} \tag{6.53}$$

where $NRMSE_{Cr(VI)}$ is the NRMSE for Cr(VI) and $NRMSE_{\Delta V_{MFC}}$ is the NRMSE for output potential difference. A NRMSE value of less than 0.15 indicates that a model is a good fit, and a value between 0.15 to 0.2 is still acceptable (Didari and Zand-Parsa, 2017).

The results of RMSE and NRMSE for both Cr(VI) reduction and output potential difference (Figure 6.2) are summarized in Table 6.3. As it can be seen in Table 6.3, both the Cr(VI) reduction and output potential difference achieved NRMSE≤0.2. Therefore, the model fit for the experimental data was acceptable.

Table 6.3 RMSE and NRMSE values for both Cr(VI) reduction and output potential difference.

Variable	RMSE	NRMSE
Cr(VI)	0.072	0.069
Output potential difference	0.0079	0.037

6.3 Model Validation at Different Initial Cr(VI) Concentrations

Once all the parameters for the Cr(VI)-reducing MFC model were specified, the model was verified. This was done by simulating the fully specified Cr(VI)-reducing MFC model at varying Cr(VI) initial concentrations using an open source Python-based odeint() function which can be found from the Python-based scipy.integrate module, and comparing the results to experimental data. Figure 6.3 shows the experimental and simulated results at varying Cr(VI) initial concentrations.

As it can be seen in Figure 6.3, there is a satisfactory agreement between the experimental and simulated values. Furthermore, the relationships between initial Cr(VI) concentration and both the Cr(VI) reduction and output potential difference are maintained. Previous studies have shown that the initial concentration of Cr(VI) plays a significant role in the output potential difference of the MFC, and by increasing the initial Cr(VI) concentration, the output potential difference increases (Li et al., 2018; Wang et al., 2008). An increase in MFC performance as initial Cr(VI) concentration was being increased is attributed to the fact that the amount of Cr(VI) available to accept the electrons increases and this is elaborated in Section 6.4.

It should be noted that the model is able to predict the ohmic region of the polarization curve (Figure 6.3c), however, the activation region which is between 0-0.1 A/m^2 is not well predicted due to the assumption made that the activation overpotential is sufficiently small.

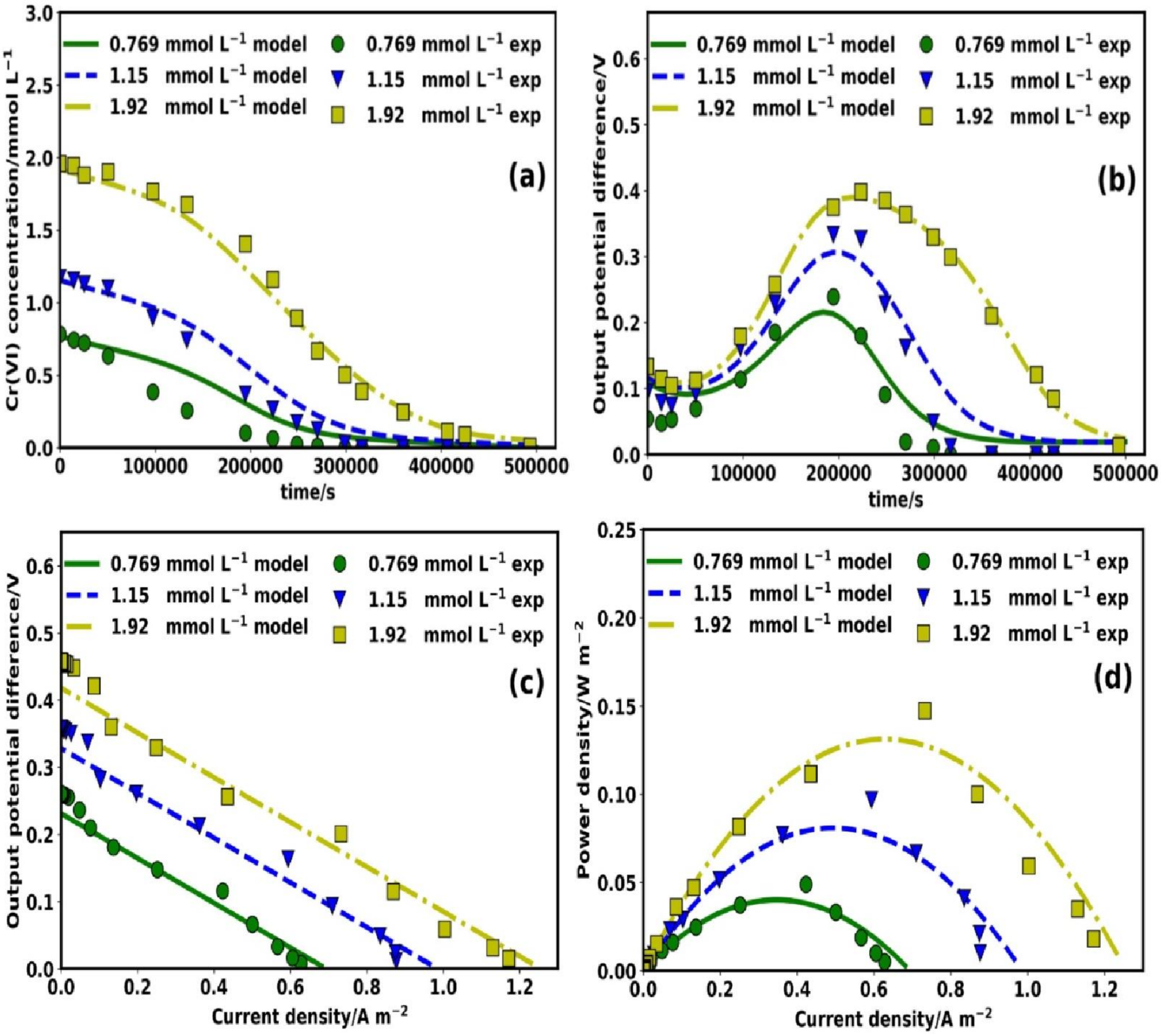

Figure 6.3 Model validation with experimental data at varying Cr(VI) initial concentrations.

6.4 Effect of Cr(VI) Initial Concentration on Coulombic Efficiency of Cr(VI)-Reducing MFC

To further explain the reason behind an increase in Cr(VI)-reducing MFC performance as Cr(VI) is increased, the Coulombic efficiency (CE) is used. CE will help in providing an explanation behind the improvement of electron transfer due to an increase in Cr(VI) initial concentration which leads to a rise in the amount of Cr(VI) available to accept electrons in the cathode chamber. This is because CE describes the charge efficiency in which electrons are being transferred in the MFC and its calculation is given by Equation (6.54).

CE is expressed as the ratio between the current generated to the theoretical current output as per Equation (6.54):

$$\mathrm{CE} = \frac{M\int_0^t Idt}{neFv\Delta C_{cr}} x100 \tag{6.54}$$

where I is output current (A), M is chromium molecular weight (52 g mol^{-1}), v is the cathodic chamber working volume (L), ne is exchanged number of electrons per mole of Cr(VI)=3, F is Faraday's constant (96485 A s mol^{-1}), ΔC_{cr} is the concentration of Cr(VI) (g L^{-1}).

Figure 6.4 was determined using data from Figure 6.3b and it shows the CE change with initial Cr(VI) concentration (0.769, 1.15, and 1.92 mmol L^{-1}) of the model compared with the one determined from experimental data.

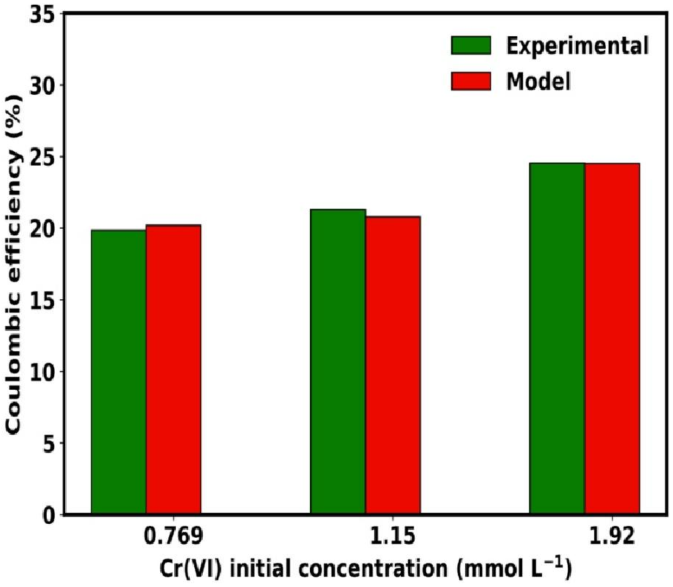

Figure 6.4 Model Coulombic efficiency (CE) change with initial Cr(VI) concentration (0.769, 1.15, and 1.92 mmol L^{-1}) compared with the one determined from experimental data.

As it can be seen in Figure 6.4, an increase in initial Cr(VI) concentration increased the CE, which means the efficiency in which electrons were being transferred in MFC so that they are accepted in the cathode chamber by Cr(VI) increased and was related to the amount of Cr(VI) available to accept electrons (Huang et al., 2010; Wang et al., 2008). Additionally, it can be seen from Figure 6.4 that the model was sufficiently able to predict the CE of the Cr(VI)-reducing MFC.

6.5 Effect of Primary Microbial Cell Concentration on Cr(VI)-Reducing MFC

The primary microbial cell concentration which relates to the concentration of electrogens in the anode chamber affects the performance of Cr(VI)-reducing MFC. When the concentration increases from 15 mg L^{-1} to 45 mg L^{-1}, the reduction rate of Cr(VI) in the cathode chamber increases (Figure 6.5a). This observation can be explained when the output potential difference is considered in Figure 6.5b.

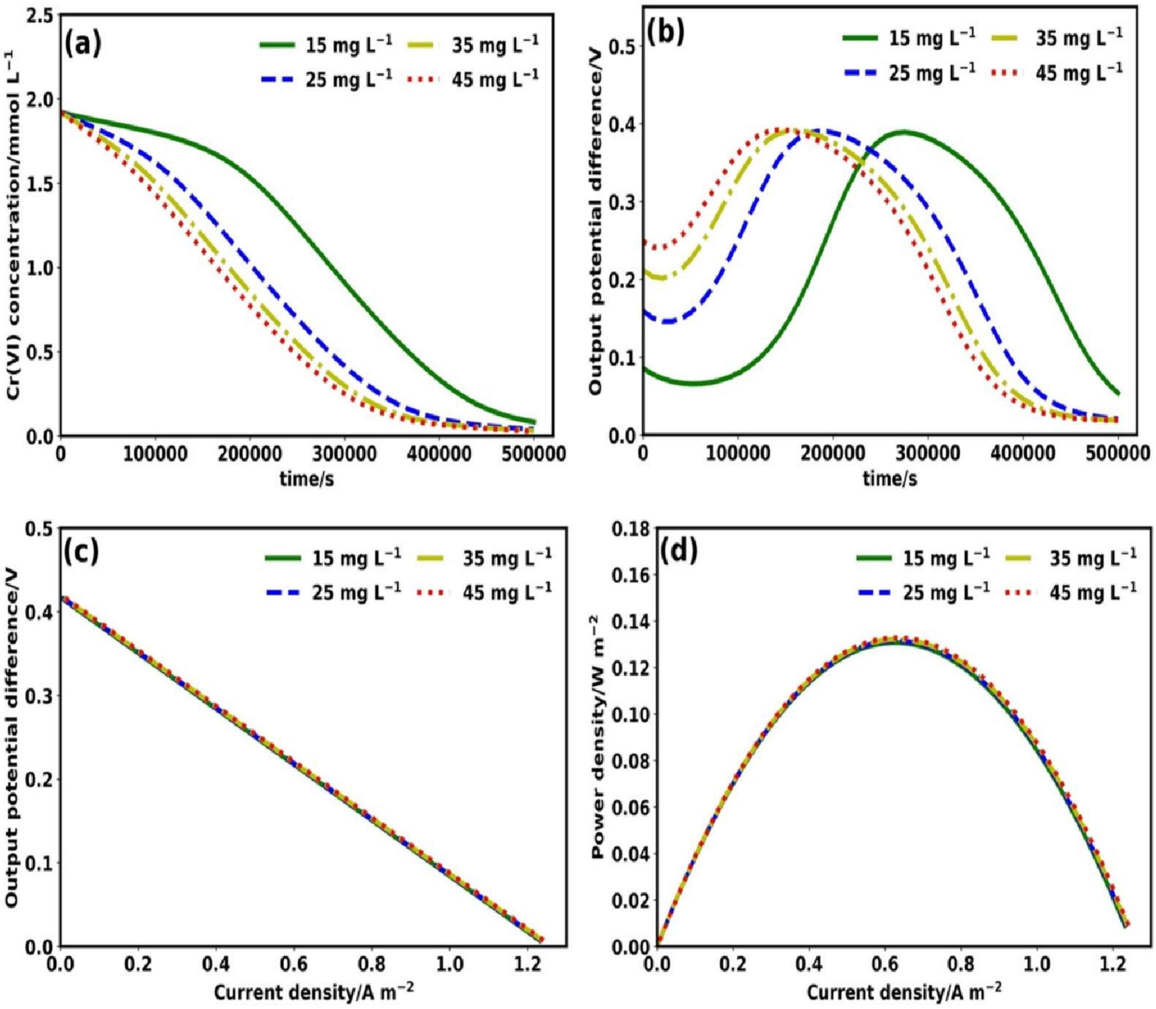

Figure 6.5 The effect of initial primary microbial cell concentration on (a) Cr(VI) reduction, (b) output potential difference, (c) polarization curve, and (d) power density.

As the primary microbial cell concentration increases, there is a decrease in the lag-time it takes for the output potential difference to begin to rise and also a decrease in the time it takes to reach the maximum output potential difference (Figure 6.5b). The reason behind this observation is related to the electrogens which do not only generate electrons but also influence the transfer of electrons to the anode through either DET (Cao et al., 2019), via a conductive pilus (Santoro et al., 2017), or MET mechanism (Cao et al., 2019). When the concentration is low, there are not enough electrogens to transfer the electrons to the anode, this leads to a lag-time until there is enough primary microbial cells to generate and transfer electrons. In addition, due to a decrease in the lag-time by increasing the concentration of primary microbial cells, the time it takes to reach maximum output potential difference decreases. Therefore, due to an improved transfer of electrons to the anode by increasing the primary microbial cell concentration, this leads to an improved rate of Cr(VI) reduction.

A simulation was conducted at a point where the maximum output potential difference was achieved in Figure 6.5b in order to construct the polarization curve and the power density curve. The polarization (Figure 6.5c) and the power density curve (Figure 6.5d) at maximum output potential difference is the same at varying primary microbial cell concentrations. This is because polarization and power density curves are normally determined at maximum output potential difference which remained similar as shown in Figure 6.5b. In addition, the ohmic region of the polarization curve (Figure 6.5c) is a function of internal resistance which depends on PEM type, temperature, type of microbes, ionic strength and reactor configuration. In simulating Figure 6.5, these were assumed to remain the same.

The reason maximum output potential difference remained similar is because although the low initial concentration of primary microbial cells leads to a lag-time, the concentration of the cells eventually increases until there are enough electrogens to transfer electrons and achieve the maximum output potential difference that can be delivered by MFC. In addition, since the maximum output potential difference is the same, this is an indication that the primary microbial cell concentration only influences the lag-time, and cannot improve the maximum achievable output potential difference of the MFC at specified initial substrate and Cr(VI) concentration.

The initial output potential difference in Figure 6.5b increased with an increase in the primary microbial cell concentration, this same observation was made by Park and Zeikus (2002) and it is related to the improved electron transfer.

6.6 Effect of Substrate Concentration on Cr(VI)-Reducing MFC

An increase in the substrate concentration improved the reduction rate of Cr(VI) as shown in Figure 6.6a. This is due to the substrate increasing the rate of production of electrons from the primary microbial cells which in turn improves the rate at which Cr(VI) is being reduced. Also, it has to be noted that although substrate concentration improves the rate of production of electrons, it does not improve the initial rate of transfer of electrons to the anode based on the initial output potential difference which did not change as shown in Figure 6.6b.

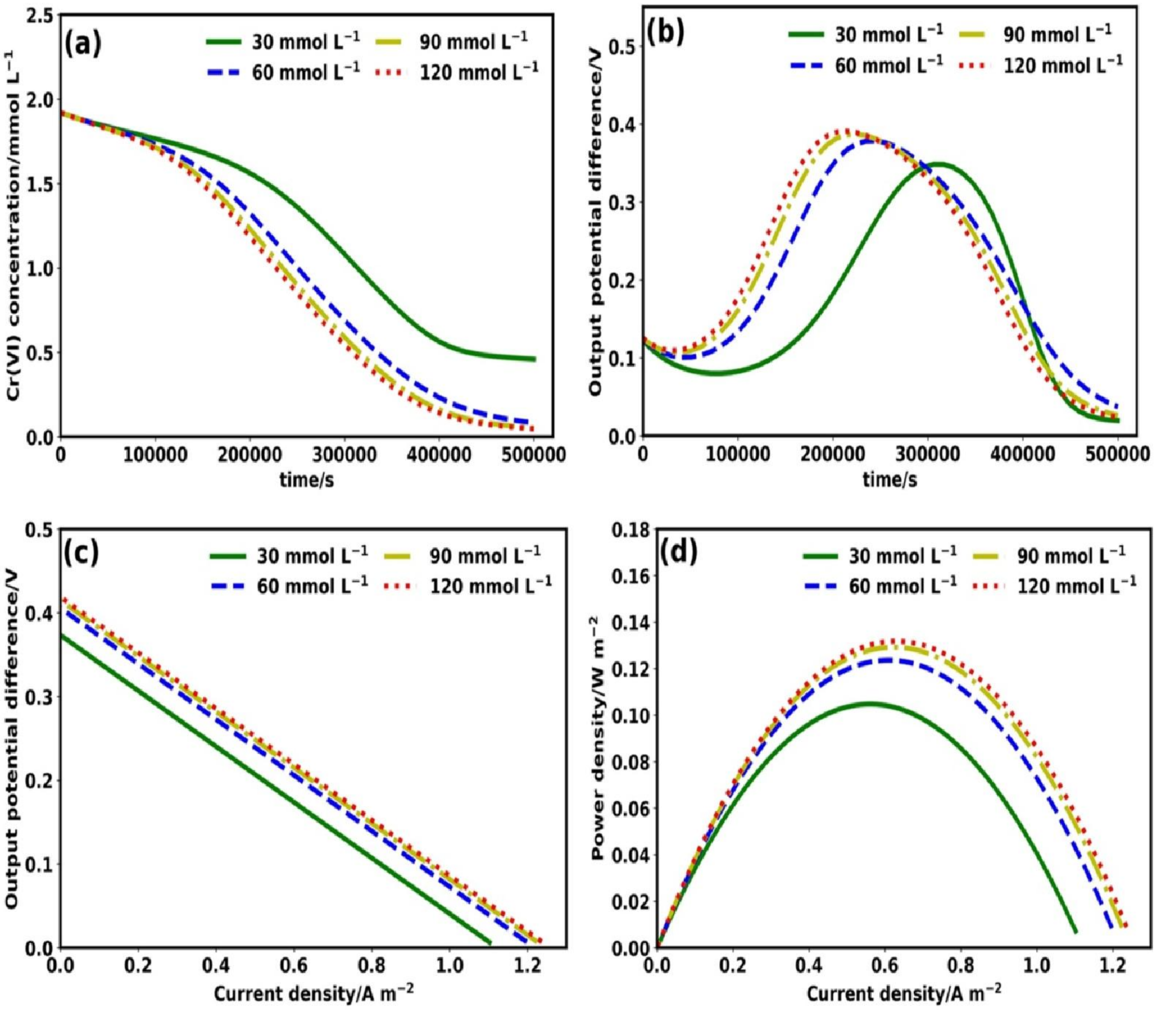

Figure 6.6 The effect of initial substrate concentration on (a) Cr(VI) reduction, (b) output potential difference, (c) polarization curve, and (d) power density.

However, substrate concentration does affect the rate of transfer of electrons as the MFC operation proceeds as shown in Figure 6.6b. When the substrate concentration is low, the rate of primary microbial cell growth is also low as indicated by Equation (6.17), and this increases the lag-time and lowers the rate of electron transfer (Igboamalu et al., 2019b). In addition, not only is the lag-time a problem at low substrate concentrations, but the maximum output potential difference is affected by the concentration of the substrate. This is because in addition to the rate of production of electrons being affected by the substrate, the amount of substrate available also influences the number of electrons that can be generated from the electrogens. Hence, the lower the substrate, the lower the amount of electrons generated which lowers the achievable maximum output potential difference. This observation was also reported by Tremouli et al. (2016).

Due to the maximum output potential difference being affected by the substrate concentration, both the polarization and power density curve are also affected. The polarization curve lowers as the substrate concentration is decreased and the linear curve indicates that the concentration overpotential is negligible and the activation overpotential is sufficiently small as per assumptions made in Equation (6.15) (Figure 6.6c). The maximum power density also decreases with a decrease in substrate concentration (Figure 6.6d) (Cheng and Logan, 2011). This is due to the less electrons generated by the electrogens at lower substrate concentration.

6.7 Optimization of Primary Microbial Cell and Substrate Concentrations

Due to the primary microbial cell concentration affecting the time it takes to achieve maximum output potential difference and the substrate concentration having an influence on the achieved maximum power density, it is important to optimize both variables to achieve the maximum power density at minimum time. The time it takes to achieve the maximum power density in Figure 6.7 was minimized by using a primary microbial cell concentration of 25 mg L^{-1} as opposed to a value determined from Figure 6.5a and Figure 6.5b of 45 mg L^{-1}. This is due to 25 mg L^{-1} reducing the maximum power density time of 671859 s (186.6 h) obtained at 5 mg L^{-1} by 72.3 % as shown in Figure 6.7a.

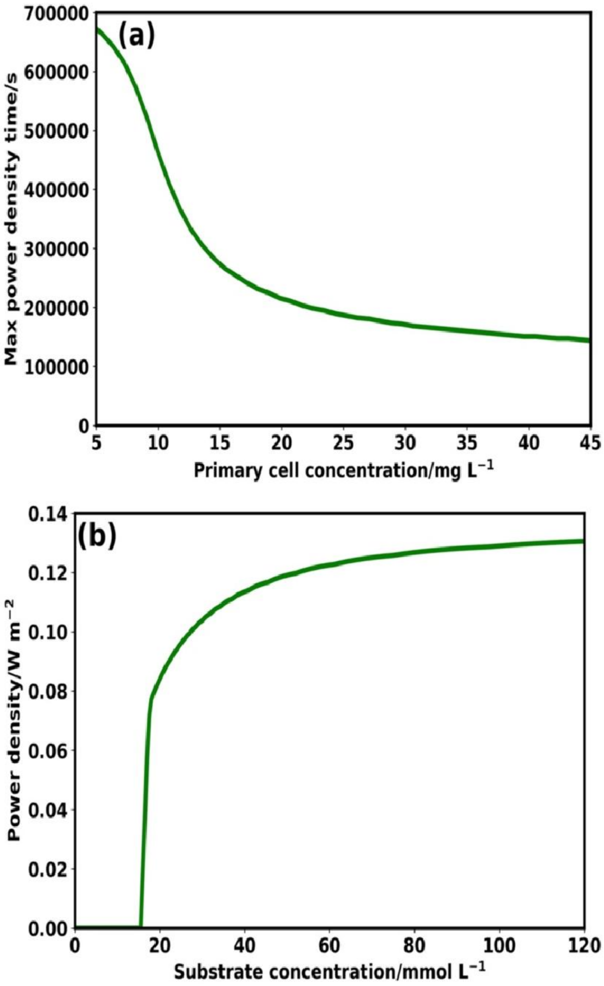

Figure 6.7 Optimization of (a) initial primary microbial cell concentration to reduce the time it takes to reach maximum power density, and (b) optimization of initial substrate concentration in order to maximise power density.

Furthermore, since 45 mg L^{-1} reduces the maximum power density time obtained at 5 mg L^{-1} by 78.5 %, this means that almost doubling the primary microbial cell concentration from 25 mg L^{-1} to 45 mg L^{-1} does not have much of impact as it reduces the time only by 6.2 %. In terms of the substrate concentration, the concentration was optimized to 60 mmol L^{-1} as opposed to a value determined from Figure 6.6 of 120 mmol L^{-1}. This is because doubling the substrate concentration from 60 mmol L^{-1} to 120 mmol L^{-1} only increases the maximum power density by 6.9 % from 0.122 W m^{-2} to 0.131 W m^{-2} as shown in Figure 6.7b. It should be noted that a minimum substrate concentration is required to begin generating substantial electricity (Figure 6.7b) (Amin et al., 2014).

CHAPTER 7: CONCLUSIONS AND RECOMMENDATIONS

7.1 Conclusions

The air-cathode MFC performance was improved by introduction of an optimized GAC particle size of 0.6-1.1 mm in carbon cloth. Furthermore, the optimized operational temperature of 35 °C, pH 8 and the usage of a Nafion 117 PEM proved to be suitable for the enhancement of the air-cathode MFC. The utilization of the GAC with the optimized particle size produced an output voltage of 507.5 mV and maximum power output of 1287.7 mW m^{-3} at a current output of 2537.5 mA m^{-3}. GAC particle size of 0.6-1.1 mm resulted in improved performance of air-cathode MFC as a result of enhanced available surface area for cell attachment based on the results of BET, and an increase in appropriate surface for attachment of cells which was rough based on the SEM results. On the other hand, although GAC size of particles of 0.45-0.6 mm had highest available surface area for cell attachment, it lacked the appropriate surface for the attachment of cells and reduced MFC performance. This means that particle size optimization of GAC is essential since there is a limit to which the particle diameter can be reduced. In addition, there is an economic benefit in modifying carbon cloth using GAC of optimized size of particles. Therefore, the simple low-cost modification method of the carbon cloth anode has the potential to improve air-cathode MFC performance.

The modification of GAC using Bio-PdNPs was also investigated based on its capability to improve the performance of Cr(VI)-reducing MFC. Upon successful optimization of GAC, the synthesized Bio-PdNPs were used in the GAC modification. The modified GAC demonstrated an ability to improve the performance of Cr(VI)-reducing MFC through the usage of Bio-PdNPs as electrocatalysts with Bio-PdNPs loading of 6 mg Bio-PdNPs g^{-1} GAC resulting in peak output potential difference of 393.1 mV, maximum power density of 1965.4 mW m^{-3}, and complete removal of 100 mg L^{-1} Cr(VI) in 25 h. Therefore, this study led to the development of an environmentally friendly and cost-effective method in the enhancement of the anode electrode for improved energy recovery and Cr(VI) reduction in MFC.

This study also presented a two population model for metal-reducing MFCs. The developed model incorporated Monod kinetics for substrate consumption and microbial cell growth. In addition, the Butler-Volmer equation was used to model the bioelectrochemical kinetics including Cr(VI) reduction. Accuracy of parameter estimation and capacity of prediction of the model was validated with usage of two independent data sets. The results of NRMSE for both reduction of Cr(VI) and output voltage achieved NRMSE$\leq$0.2. Therefore, model fit for the experimental data was acceptable.

Analysis of model demonstrated the effect of both the primary microbial cell concentration and substrate concentration on Cr(VI)-reducing MFC performance. An increase in primary microbial cell concentration and substrate concentration improves the reduction rate of Cr(VI) in the cathode chamber. Successful optimization of both concentrations was demonstrated during model analysis. The time it takes to achieve maximum power output was minimized by using a primary microbial cell concentration of 25 mg L^{-1} as opposed to a value of 45 mg L^{-1}. In addition, the substrate concentration was optimized to 60 mmol L^{-1} as opposed to a value of 120 mmol L^{-1}. Overall, the model provides an initial step into determining optimal MFC operational conditions without doing much lab-work.

7.2 Recommendations

In order to improve the performance of the Cr(VI)-reducing microbial fuel cell and improve the developed computational model, further research has to be conducted in the following areas:

- An investigation on the halophilic electrogens can help improve the performance instead of using wastewater sludge. Therefore the study can be expanded by collecting marine bacteria and investigating them for the improvement of Cr(VI)-reducing MFC.

- The batch reactor configuration has to be adapted to a continuous reactor set-up. Upflow MFCs are one of the reactor configurations that offer an advantage of improving performance through presenting an environment with a variable survivability range due to the biofilm thickness forming a dynamic concentration gradient.

- A cost effective proton exchange membrane as a replacement for Nafion 117 has to be developed to allow the possibility of the scale-up of the continuous reactor configuration.

CHAPTER 8: APPENDICES

8.1 Appendix A: Single Chamber (Air-Cathode) Reactor Configuration

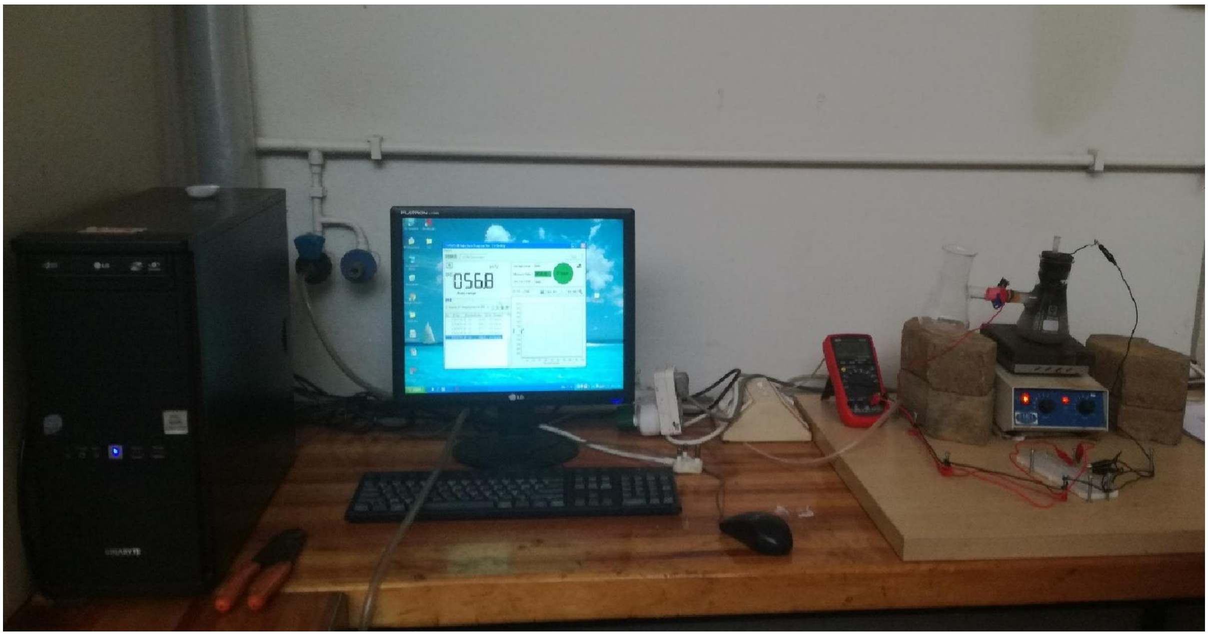

Figure 8.1 Experimental set-up.

Figure 8.2 Reactor set-up.

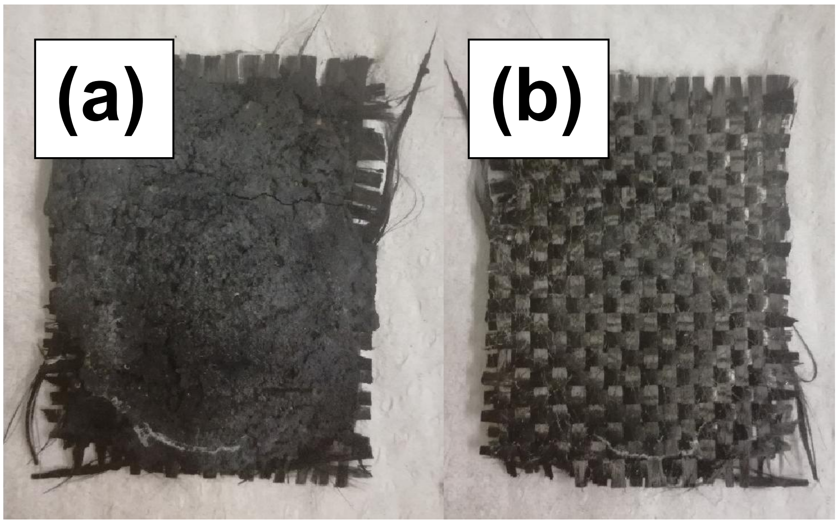

Figure 8.3 (a) The coated side of the cathode with a 10:30:3 ratio of PVDF solution:activated carbon powder:carbon black and (b) the uncoated side of the cathode.

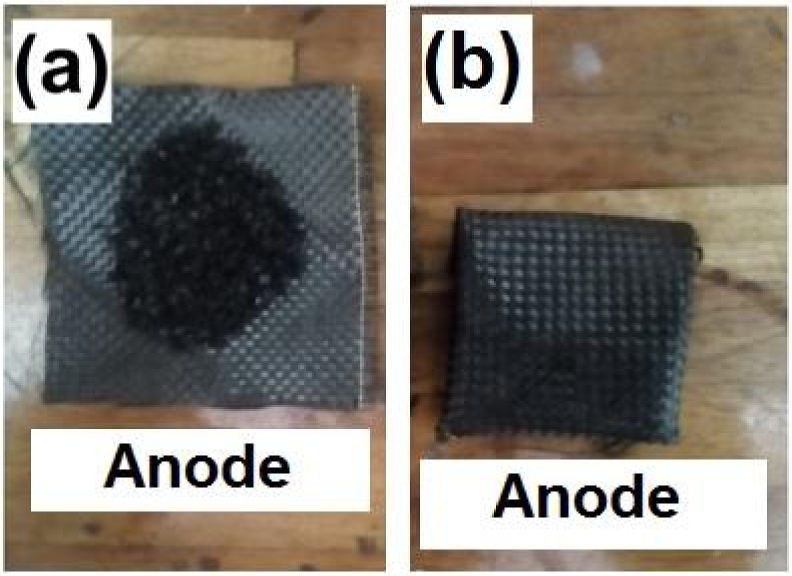

Figure 8.4 (a) The visual illustration of the anode with GAC placed inside the carbon cloth with area of an area of 49 cm^2 (b) The visual illustration anode carbon cloth with GAC inside folded over using a sewing thread.

8.2 Appendix B: Dual Chamber Reactor Configuration

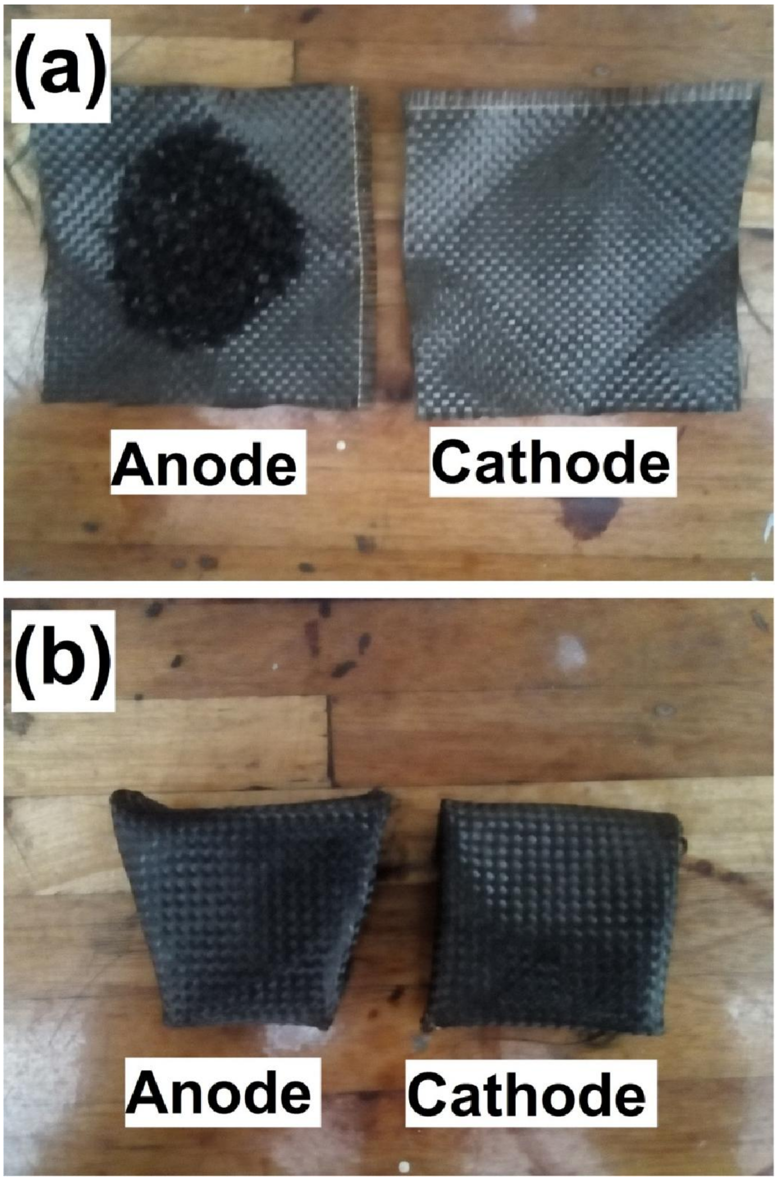

Figure 8.5 (a) The visual illustration of the anode with GAC placed inside the carbon cloth with area of an area of 49 cm^2 and cathode with carbon cloth of an area of 49 cm^2, (b) The visual illustration of both the carbon cloths folded over using a sewing thread.

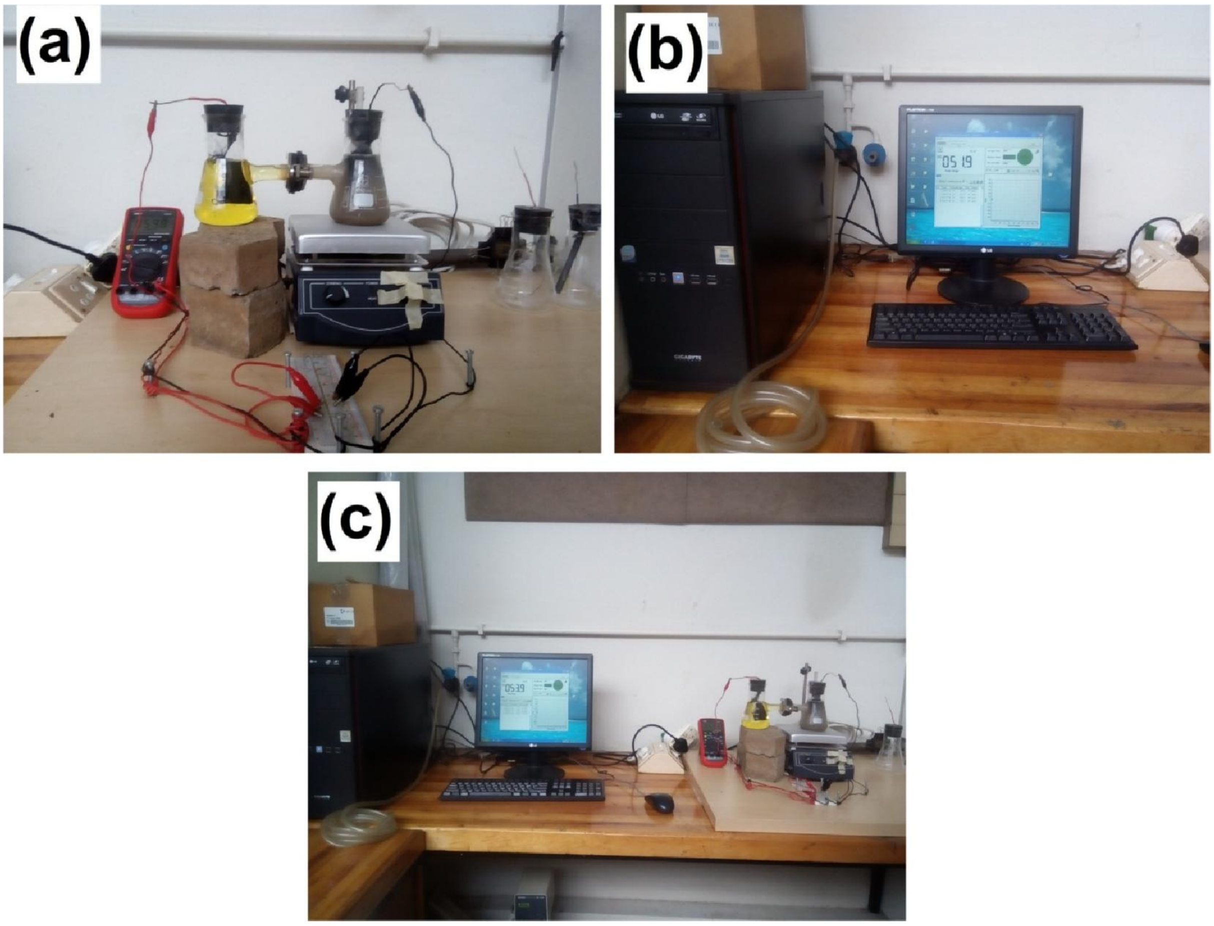

Figure 8.6 (a) Cr(VI)-reducing MFC set-up, (b) data logger, (c) The full MFC work station.

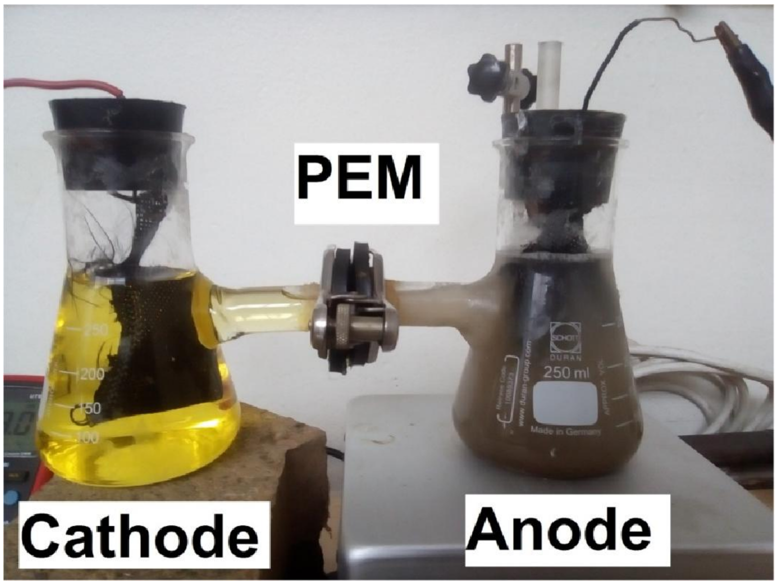

Figure 8.7 Illustration of the location of cathode, anode and proton exchange membrane (PEM).

8.3 Appendix C: Dual Chamber Model Python Code

1. Imported Modules

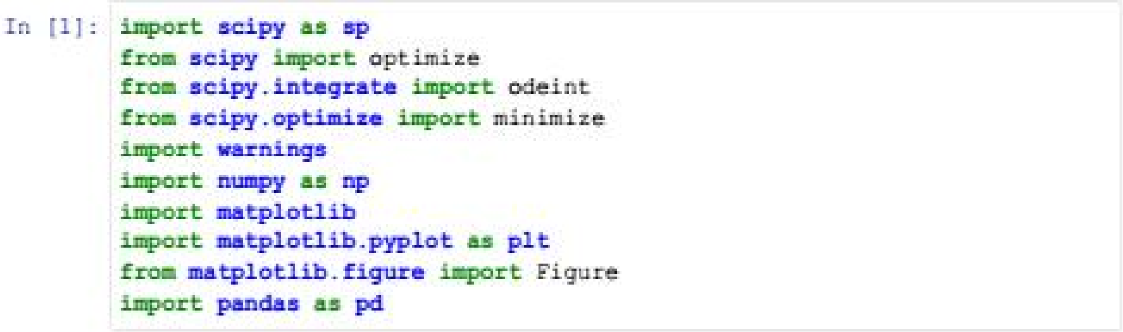

```
In [1]: import scipy as sp
        from scipy import optimize
        from scipy.integrate import odeint
        from scipy.optimize import minimize
        import warnings
        import numpy as np
        import matplotlib
        import matplotlib.pyplot as plt
        from matplotlib.figure import Figure
        import pandas as pd
```

2. Model Variable Descriptions

2.1. Differential variable descriptions

$x1$ - S $(mmolL^{-1})$
$x2$ - X_{pr} (mgL^{-1})
$x3$ - X_{se} (mgL^{-1})
$x4$ - M_R $(mmolL^{-1})$
$x5$ - M_O $(mmolL^{-1})$
$x6$ - $[Cr_2O_7^{2-}]$ $(mmolL^{-1})$
$x7$ - $[Cr(VI)]$ $(mmolL^{-1})$
$x8$ - $[Cr(III)]$ $(mmolL^{-1})$

2.2. Algebraic variable descriptions

$y1$ - μ_{pr} (s^{-1})

$y2$ - μ_{se} (s^{-1})

$y3$ - $r_{ct,a}$ (Ω)

$y4$ - $\eta_{a,MFC}$ (V)

$y5$ - $r_{ct,c}$ (Ω)

$y6$ - $\eta_{c,MFC}$ (V)

$y7$ - r_{int} (Ω)

$y8$ - η_{ohmic} (V)

$y9$ - ΔV_{rev} (V)

$y10$ - ΔV_{MFC} (V)

$y11$ - I_{MFC} (A)

2.3. Parameter descriptions

$p1$ - $K_{S,pr}$ (*Estimated; mmol* L^{-1})

$p2$ - $K_{M_O,pr}$ (*Estimated; mmol* L^{-1})

$p3$ - $K_{S,se}$ (*Estimated; mmol* L^{-1})

$p4$ - $\mu_{max,pr}$ (*Estimated;* s^{-1})

$p5$ - $\mu_{max,se}$ (*Estimated;* s^{-1})

$p6$ - $Y_{Xpr/s}$ (*Estimated; mg* mg^{-1})

$p7$ - $Y_{Xse/s}$ (*Estimated; mg* mg^{-1})

$p8$ - $Y_{M_g/s}$ (*Estimated; mg* mg^{-1})

$p9$ - MM_s (45.02 $g\ mol^{-1}$)

$p10$ - MM_{M_g} (665.12 $g\ mol^{-1}$)

$p11$ - $k_{d,pr}$ (*Estimated;* s^{-1})

$p12$ - $k_{d,se}$ (*Estimated;* s^{-1})

$p13$ - F (96485 $A\ s\ mol^{-1}$)

$p14$ - R (8.314 $J\ mol^{-1}\ K^{-1}$)

$p15$ - T_a (311 K)

$p16$ - T_c (298 K)

$p17$ - v_a (0.2 L)

$p18$ - v_c (0.2 L)

$p19$ - r_{ext} (1000 Ω)

$p20$ - Io_a (*Estimated; A*)

$p21$ - Io_c (*Estimated; A*)

$p22$ - E_{max} (*Estimated; V*)

$p23$ - E_{min} (0.02 V)

$p24$ - r_{max} (2100 Ω)

$p25$ - r_{min} (50 Ω)

$p26$ - $\theta_{X_{pr},r_{int}}$ (*Estimated; L* mg^{-1})

$p27$ - $\theta_{X_{pr},\Delta V_{MFC}}$ (*Estimated; L* mg^{-1})

$p28$ - $\theta_{Cr(VI),r_{int}}$ (*Estimated; L* $mmol^{-1}$)

$p29$ - $\theta_{Cr(VI),\Delta V_{MFC}}$ (*Estimated; L* $mmol^{-1}$)

$p30$ - $\theta_{S,r_{int}}$ (*Estimated; L* $mmol^{-1}$)

$p31$ - $\theta_{S,\Delta V_{MFC}}$ (*Estimated; L* $mmol^{-1}$)

3. Data Access

```
In [2]: #Parameter estimation data
        data=pd.read_excel('parameter_estimation.xlsx', index_col=0)

        t_data=[]
        for i in np.arange(len(data.index)):
            t_data.append(data.index[i])

        x7_data=[]
        for i in np.arange(len(data["x7_exp"])):
            x7_data.append(data["x7_exp"][data["x7_exp"].index[i]])
        y10_data=[]
        for i in np.arange(len(data["y10_exp"])):
            y10_data.append(data["y10_exp"][data["y10_exp"].index[i]])

        list_data=[x7_data,y10_data]

        #Initial Cr(VI) variation data
        data1=pd.read_excel('initial_crvi_conc.xlsx', index_col=0)

        t_data1=[]
        for i in np.arange(len(data1.index)):
            t_data1.append(data1.index[i])

        x7_data1=[]
        for i in np.arange(len(data1["x7_exp1"])):
            x7_data1.append(data1["x7_exp1"][data1["x7_exp1"].index[i]])
        x7_data2=[]
        for i in np.arange(len(data1["x7_exp2"])):
            x7_data2.append(data1["x7_exp2"][data1["x7_exp2"].index[i]])
        x7_data3=[]
        for i in np.arange(len(data1["x7_exp3"])):
            x7_data3.append(data1["x7_exp3"][data1["x7_exp3"].index[i]])

        y10_data1=[]
        for i in np.arange(len(data1["y10_exp1"])):
            y10_data1.append(data1["y10_exp1"][data1["y10_exp1"].index[i]])
        y10_data2=[]
        for i in np.arange(len(data1["y10_exp2"])):
            y10_data2.append(data1["y10_exp2"][data1["y10_exp2"].index[i]])
        y10_data3=[]
        for i in np.arange(len(data1["y10_exp3"])):
            y10_data3.append(data1["y10_exp3"][data1["y10_exp3"].index[i]])

        list_data1=[x7_data1,x7_data2,x7_data3,y10_data1,y10_data2,y10_data3]

        #Polarization curve data
        data2=pd.read_excel('polarization_curve.xlsx', index_col=0)

        V1_data=[]
        for i in np.arange(len(data2["V1"])):
            V1_data.append(data2["V1"][data2["V1"].index[i]])
        V2_data=[]
        for i in np.arange(len(data2["V2"])):
            V2_data.append(data2["V2"][data2["V2"].index[i]])
        V3_data=[]
        for i in np.arange(len(data2["V3"])):
```

4. Modelling Functions

4.1. Differential variables simulation

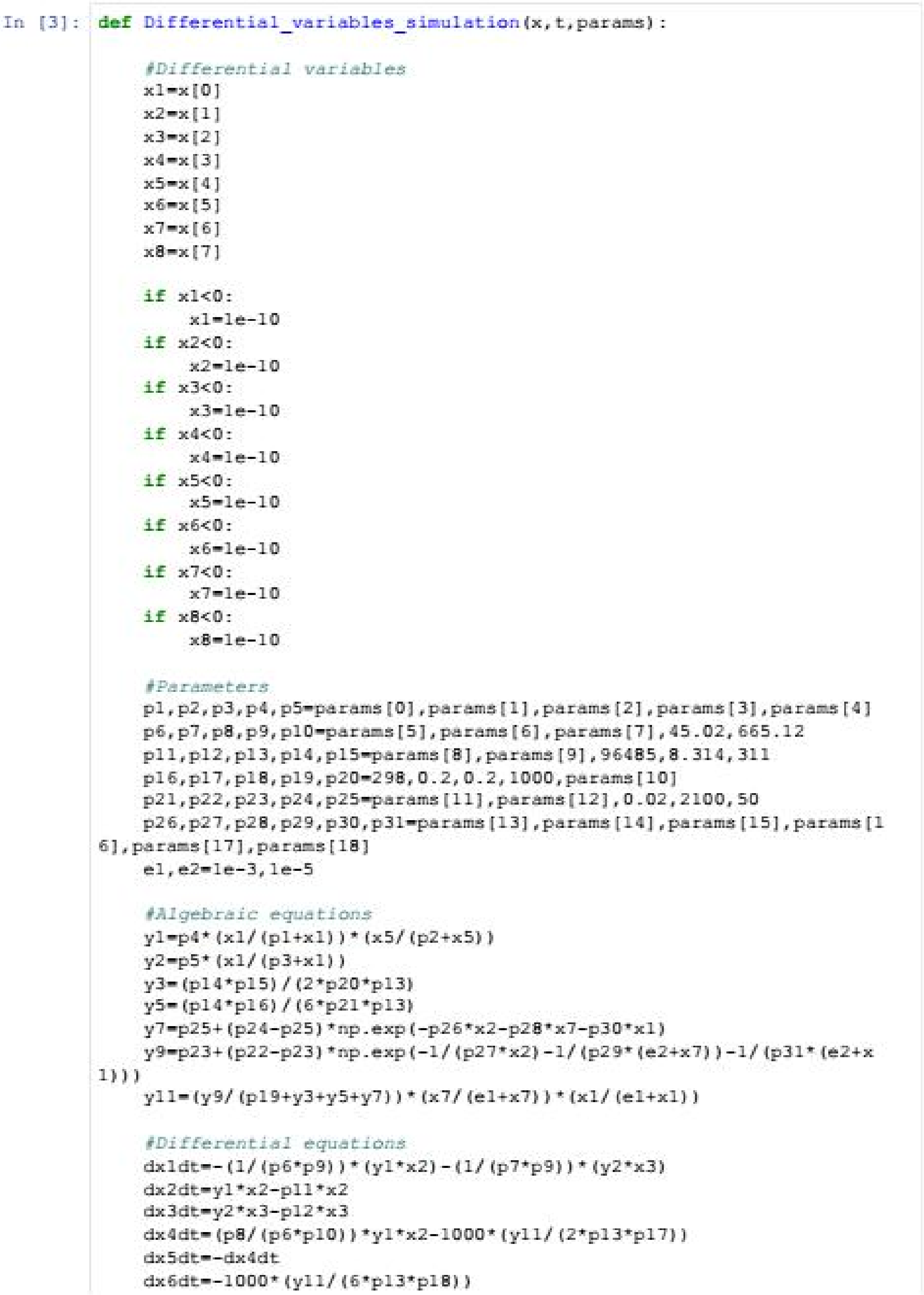

```
In [3]: def Differential_variables_simulation(x,t,params):

            #Differential variables
            x1=x[0]
            x2=x[1]
            x3=x[2]
            x4=x[3]
            x5=x[4]
            x6=x[5]
            x7=x[6]
            x8=x[7]

            if x1<0:
                x1=1e-10
            if x2<0:
                x2=1e-10
            if x3<0:
                x3=1e-10
            if x4<0:
                x4=1e-10
            if x5<0:
                x5=1e-10
            if x6<0:
                x6=1e-10
            if x7<0:
                x7=1e-10
            if x8<0:
                x8=1e-10

            #Parameters
            p1,p2,p3,p4,p5=params[0],params[1],params[2],params[3],params[4]
            p6,p7,p8,p9,p10=params[5],params[6],params[7],45.02,665.12
            p11,p12,p13,p14,p15=params[8],params[9],96485,8.314,311
            p16,p17,p18,p19,p20=298,0.2,0.2,1000,params[10]
            p21,p22,p23,p24,p25=params[11],params[12],0.02,2100,50
            p26,p27,p28,p29,p30,p31=params[13],params[14],params[15],params[1
        6],params[17],params[18]
            e1,e2=1e-3,1e-5

            #Algebraic equations
            y1=p4*(x1/(p1+x1))*(x5/(p2+x5))
            y2=p5*(x1/(p3+x1))
            y3=(p14*p15)/(2*p20*p13)
            y5=(p14*p16)/(6*p21*p13)
            y7=p25+(p24-p25)*np.exp(-p26*x2-p28*x7-p30*x1)
            y9=p23+(p22-p23)*np.exp(-1/(p27*x2)-1/(p29*(e2+x7))-1/(p31*(e2+x
        1)))
            y11=(y9/(p19+y3+y5+y7))*(x7/(e1+x7))*(x1/(e1+x1))

            #Differential equations
            dx1dt=-(1/(p6*p9))*(y1*x2)-(1/(p7*p9))*(y2*x3)
            dx2dt=y1*x2-p11*x2
            dx3dt=y2*x3-p12*x3
            dx4dt=(p8/(p6*p10))*y1*x2-1000*(y11/(2*p13*p17))
            dx5dt=-dx4dt
            dx6dt=-1000*(y11/(6*p13*p18))
```

4.2. Voltage and current simulation

```
In [4]: def y10_y11_simulation(params,Solution):

            #Parameters
            p1,p2,p3,p4,p5=params[0],params[1],params[2],params[3],params[4]
            p6,p7,p8,p9,p10=params[5],params[6],params[7],45.02,665.12
            p11,p12,p13,p14,p15=params[8],params[9],96485,8.314,311
            p16,p17,p18,p19,p20=298,0.2,0.2,1000,params[10]
            p21,p22,p23,p24,p25=params[11],params[12],0.02,2100,50
            p26,p27,p28,p29,p30,p31=params[13],params[14],params[15],params[1
        6],params[17],params[18]
            e1,e2=1e-3,1e-5

            x1=Solution[:,0]
            x2=Solution[:,1]
            x3=Solution[:,2]
            x4=Solution[:,3]
            x5=Solution[:,4]
            x6=Solution[:,5]
            x7=Solution[:,6]
            x8=Solution[:,7]

            #Algebraic equations
            y1=p4*(x1/(p1+x1))*(x5/(p2+x5))
            y2=p5*(x1/(p3+x1))
            y3=(p14*p15)/(2*p20*p13)
            y5=(p14*p16)/(6*p21*p13)
            y7=p25+(p24-p25)*np.exp(-p26*x2-p28*x7-p30*x1)
            y9=p23+(p22-p23)*np.exp(-1/(p27*x2)-1/(p29*(e2+x7))-1/(p31*(e2+x
        1)))
            y11=(y9/(p19+y3+y5+y7))*(x7/(e1+x7))*(x1/(e1+x1))
            y4=y11*y3
            y6=y11*y5
            y8=y11*y7
            y10=y9-y4-y6-y8

            y10_new=[]
            for i in y10:
                if np.isnan(i)==True:
                    y10_new.append(0)
                else:
                    y10_new.append(i)

            y11_new=[]
            for i in y11:
                if np.isinf(i)==True:
                    y11_new.append(0)
                else:
                    y11_new.append(i)

            return (np.array(y10_new),np.array(y11_new))
```

4.3. Model validation

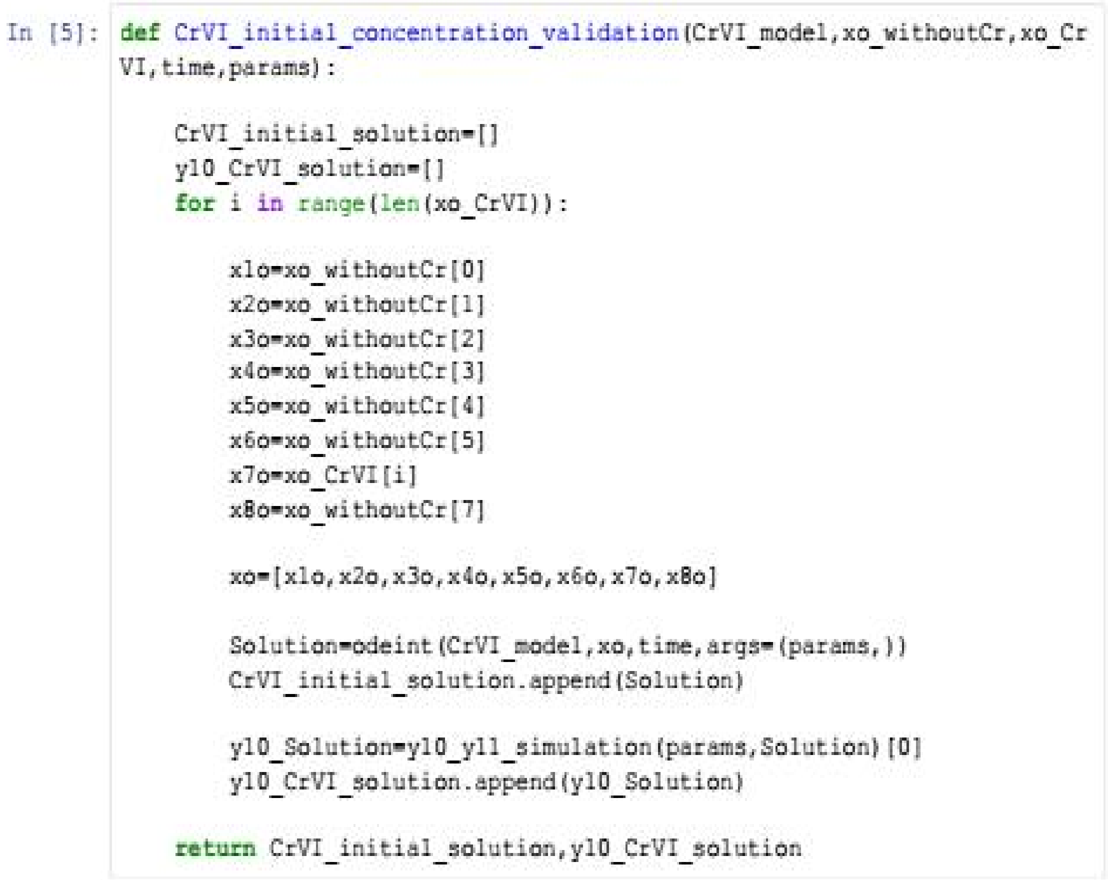

```
In [5]: def CrVI_initial_concentration_validation(CrVI_model,xo_withoutCr,xo_Cr
        VI,time,params):

            CrVI_initial_solution=[]
            y10_CrVI_solution=[]
            for i in range(len(xo_CrVI)):

                x1o=xo_withoutCr[0]
                x2o=xo_withoutCr[1]
                x3o=xo_withoutCr[2]
                x4o=xo_withoutCr[3]
                x5o=xo_withoutCr[4]
                x6o=xo_withoutCr[5]
                x7o=xo_CrVI[i]
                x8o=xo_withoutCr[7]

                xo=[x1o,x2o,x3o,x4o,x5o,x6o,x7o,x8o]

                Solution=odeint(CrVI_model,xo,time,args=(params,))
                CrVI_initial_solution.append(Solution)

                y10_Solution=y10_y11_simulation(params,Solution)[0]
                y10_CrVI_solution.append(y10_Solution)

            return CrVI_initial_solution,y10_CrVI_solution
```

4.4. Errors

In [6]:

```
def Error(paramso,Differential_variables_simulation,xo,time,list_data,p
ar_esti):

    try:

        cSolution=odeint(Differential_variables_simulation,xo,time,args
=(paramso,))

        #x7_simulated data
        x7_simulated=cSolution[:,6]

        #x7_experimental data
        x7_experimental=np.array(list_data[0])

        #y10_simulated data
        y10_simulated=y10_y11_simulation(paramso,cSolution)[0]

        #y10_experimental data
        y10_experimental=np.array(list_data[1])

        #residual
        resid1=x7_simulated-x7_experimental
        resid2=y10_simulated-y10_experimental

        #squared error
        SE_x7=np.sum(np.square(resid1))
        SE_y10=np.sum(np.square(resid2))

        #mean squared error
        MSE_x7=np.sum(np.square(resid1))/len(resid1)
        MSE_y10=np.sum(np.square(resid2))/len(resid2)

        #root mean squared error
        RMSE_x7=np.sqrt(MSE_x7)
        RMSE_y10=np.sqrt(MSE_y10)

        #normalized mean squared error
        NRMSE_x7=RMSE_x7/np.mean(list_data[0])
        NRMSE_y10=RMSE_y10/np.mean(list_data[1])

        x7_error_types=[SE_x7,MSE_x7,RMSE_x7,NRMSE_x7]
        y10_error_types=[SE_y10,MSE_y10,RMSE_y10,NRMSE_y10]

        simulation_error=[NRMSE_x7 + NRMSE_y10]

    except RuntimeError:

        error=[10,10]

    if par_esti=='yes':
        return simulation_error
    if par_esti=='no':
        return [x7_error_types,y10_error_types]
```

4.5. Figure plotter

In [7]:

```
def plotter1(figure,x,*series,**kwds):
    fig=plt.figure(figure)
    plt.rcParams["font.weight"] = "bold"
    plt.rcParams["axes.labelweight"] = "bold"
    ax = fig.add_subplot(111)
    for axis in ['top','bottom','left','right']:
          ax.spines[axis].set_linewidth(2.5)

    for i in range(len(series)):
        plt.plot(x[i],series[i][0], series[i][1],markersize=12,markeredgecolor='k',linewidth=4)
        plt.title(kwds.get('title',''))
        plt.xlabel(kwds.get('xlabel',''), fontsize=16)
        plt.ylabel(kwds.get('ylabel',''), fontsize=16)
        plt.tick_params(labelsize=16)
        labels=[kwds.get('label1',''),kwds.get('label2',''),kwds.get('label3',''),
                kwds.get('label4',''),kwds.get('label5',''),kwds.get('label6','')]
        size=kwds.get('size',)
        ncoll=kwds.get('ncol',)
        colsp=kwds.get('colsp',)
        if kwds.get('plot_legend',)=='yes':
            plt.legend(tuple(labels[:len(labels)-kwds.get('nrev_legend',)]),fontsize=size,ncol=ncoll,columnspacing=colsp,
                      frameon=False)

def plotter2(figure,*series,**kwds):
    fig=plt.figure(figure)
    plt.rcParams["font.weight"] = "bold"
    plt.rcParams["axes.labelweight"] = "bold"
    ax = fig.add_subplot(111)
    for axis in ['top','bottom','left','right']:
          ax.spines[axis].set_linewidth(2.5)

    br_list=[]
    for i in range(len(series)):

        barWidth=0.25
        if i==0:
            br= np.arange(len(series[i][0]))
            br_list.append(br)

        if i>0:
            br=[x + barWidth for x in br_list[i-1]]
            br_list.append(br)

        plt.bar(br,series[i][0], color=series[i][1],width = barWidth, edgecolor ='k')
        plt.title(kwds.get('title',''))
        plt.xlabel(kwds.get('xlabel',''), fontsize=16)
        plt.ylabel(kwds.get('ylabel',''), fontsize=16)
        plt.tick_params(labelsize=16)
        labels=[kwds.get('label1',''),kwds.get('label2',''),kwds.get('label3',''),
                kwds.get('label4',''),kwds.get('label5',''),kwds.get('l
```

4.6. Temporarily suppress warnings

```
In [8]: def fxn():
            warnings.warn("runtime", RuntimeWarning)
```

4.7. Simulation

4.7.1. Polarization and power curves

```
In [9]: def polarization_power(params,Solution,Rext):

            #Parameters
            p1,p2,p3,p4,p5=params[0],params[1],params[2],params[3],params[4]
            p6,p7,p8,p9,p10=params[5],params[6],params[7],45.02,665.12
            p11,p12,p13,p14,p15=params[8],params[9],96485,8.314,311
            p16,p17,p18,p19,p20=298,0.2,0.2,1000,params[10]
            p21,p22,p23,p24,p25=params[11],params[12],0.02,2100,50
            p26,p27,p28,p29,p30,p31=params[13],params[14],params[15],params[1
        6],params[17],params[18]
            e1,e2=1e-3,1e-5

            x1=Solution[:,0]
            x2=Solution[:,1]
            x3=Solution[:,2]
            x4=Solution[:,3]
            x5=Solution[:,4]
            x6=Solution[:,5]
            x7=Solution[:,6]
            x8=Solution[:,7]

            #Algebraic equations
            y1=p4*(x1/(p1+x1))*(x5/(p2+x5))
            y2=p5*(x1/(p3+x1))
            y3=(p14*p15)/(2*p20*p13)
            y5=(p14*p16)/(6*p21*p13)
            y7=p25+(p24-p25)*np.exp(-p26*x2-p28*x7-p30*x1)
            y9=p23+(p22-p23)*np.exp(-1/(p27*x2)-1/(p29*(e2+x7))-1/(p31*(e2+x
        1)))
            y11=(y9/(p19+y3+y5+y7))*(x7/(e1+x7))*(x1/(e1+x1))
            y4=y11*y3
            y6=y11*y5
            y8=y11*y7
            y10=y9-y4-y6-y8

            y10_new=[]
            for i in y10:
                if np.isnan(i)==True:
                    y10_new.append(0)
                else:
                    y10_new.append(i)

            y11_new=[]
            for i in y11:
                if np.isinf(i)==True:
                    y11_new.append(0)
                else:
                    y11_new.append(i)

            #index of maximum output potential difference
            max_output_potential_diff=max(y10)
            index=np.where(y10==max_output_potential_diff)

            #polarization curve at maximum output potential difference
            Area=49*1e-4
            current_density=((y9[index[0][0]]/(Rext+y3+y7[index[0][0]]))*
```

4.7.2. Primary cell concentration

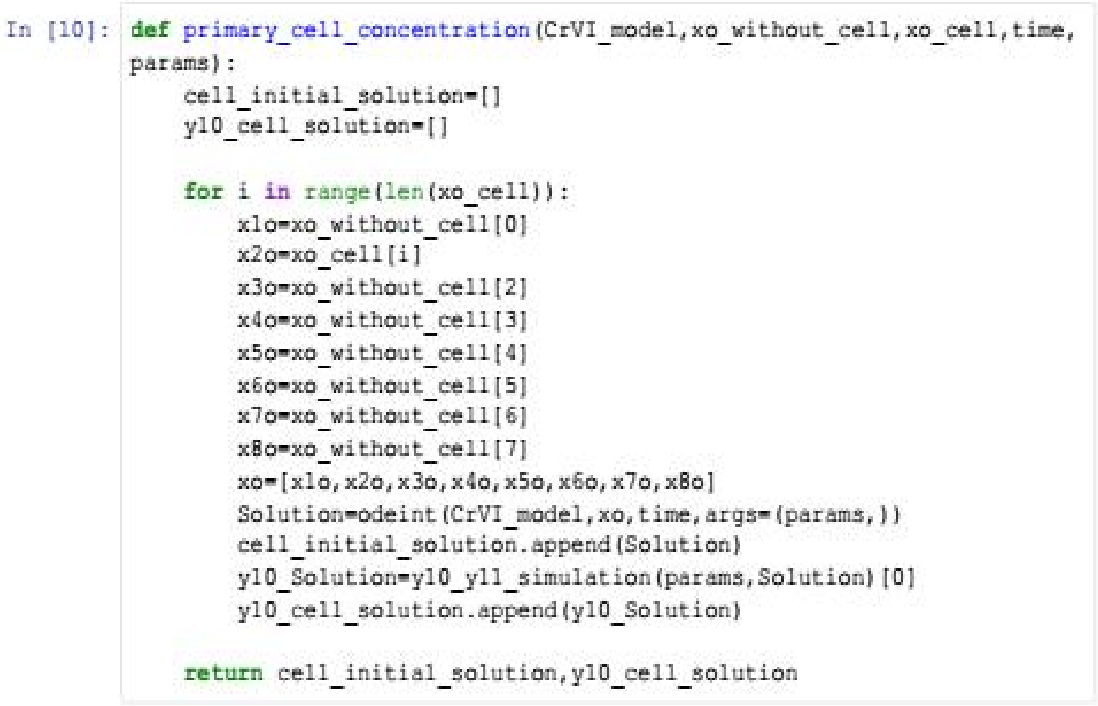

```
In [10]: def primary_cell_concentration(CrVI_model,xo_without_cell,xo_cell,time,params):
    cell_initial_solution=[]
    y10_cell_solution=[]

    for i in range(len(xo_cell)):
        x1o=xo_without_cell[0]
        x2o=xo_cell[i]
        x3o=xo_without_cell[2]
        x4o=xo_without_cell[3]
        x5o=xo_without_cell[4]
        x6o=xo_without_cell[5]
        x7o=xo_without_cell[6]
        x8o=xo_without_cell[7]
        xo=[x1o,x2o,x3o,x4o,x5o,x6o,x7o,x8o]
        Solution=odeint(CrVI_model,xo,time,args=(params,))
        cell_initial_solution.append(Solution)
        y10_Solution=y10_y11_simulation(params,Solution)[0]
        y10_cell_solution.append(y10_Solution)

    return cell_initial_solution,y10_cell_solution
```

4.7.3. Substrate concentration

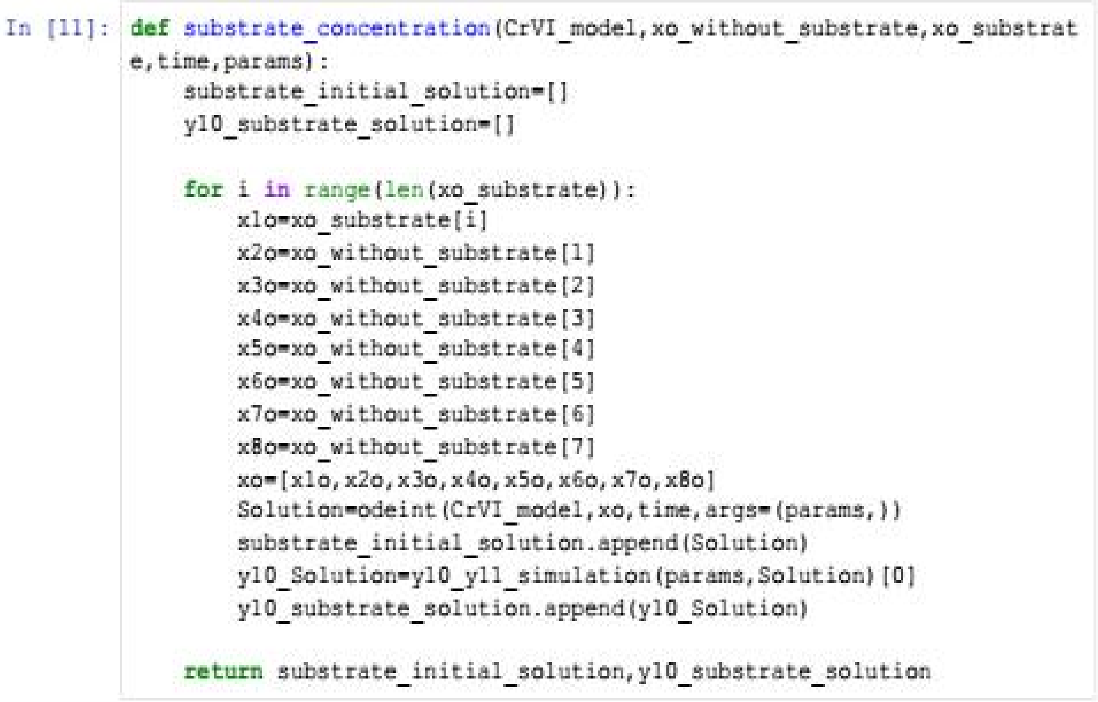

```
In [11]: def substrate_concentration(CrVI_model,xo_without_substrate,xo_substrate,time,params):
    substrate_initial_solution=[]
    y10_substrate_solution=[]

    for i in range(len(xo_substrate)):
        x1o=xo_substrate[i]
        x2o=xo_without_substrate[1]
        x3o=xo_without_substrate[2]
        x4o=xo_without_substrate[3]
        x5o=xo_without_substrate[4]
        x6o=xo_without_substrate[5]
        x7o=xo_without_substrate[6]
        x8o=xo_without_substrate[7]
        xo=[x1o,x2o,x3o,x4o,x5o,x6o,x7o,x8o]
        Solution=odeint(CrVI_model,xo,time,args=(params,))
        substrate_initial_solution.append(Solution)
        y10_Solution=y10_y11_simulation(params,Solution)[0]
        y10_substrate_solution.append(y10_Solution)

    return substrate_initial_solution,y10_substrate_solution
```

4.8. Optimization

4.8.1. Primary cell concentration optimization

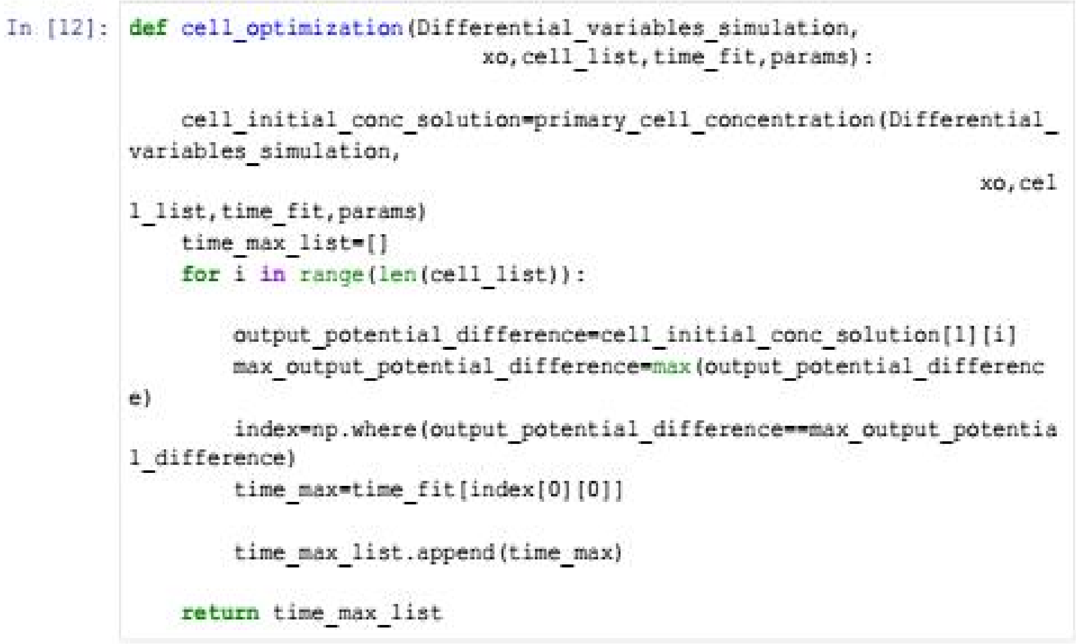

```
In [12]: def cell_optimization(Differential_variables_simulation,
                                   xo,cell_list,time_fit,params):

             cell_initial_conc_solution=primary_cell_concentration(Differential_
         variables_simulation,
                                                                               xo,cel
         l_list,time_fit,params)
             time_max_list=[]
             for i in range(len(cell_list)):

                 output_potential_difference=cell_initial_conc_solution[1][i]
                 max_output_potential_difference=max(output_potential_differenc
         e)

                 index=np.where(output_potential_difference==max_output_potentia
         l_difference)
                 time_max=time_fit[index[0][0]]

                 time_max_list.append(time_max)

             return time_max_list
```

4.8.2. Substrate concentration optimization

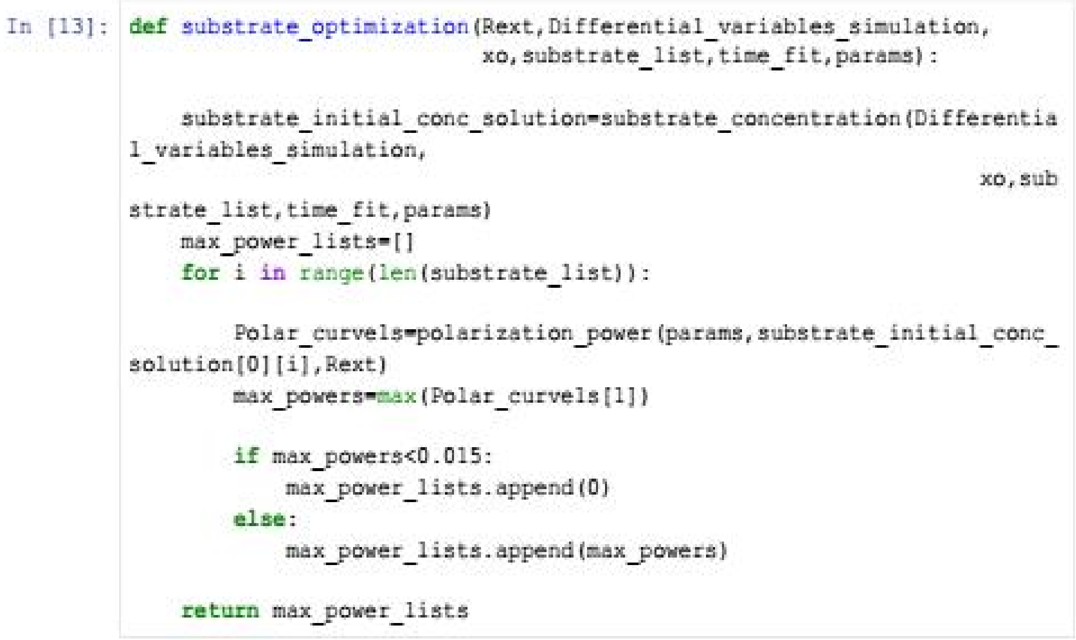

```
In [13]: def substrate_optimization(Rext,Differential_variables_simulation,
                                   xo,substrate_list,time_fit,params):

             substrate_initial_conc_solution=substrate_concentration(Differentia
         l_variables_simulation,
                                                                               xo,sub
         strate_list,time_fit,params)
             max_power_lists=[]
             for i in range(len(substrate_list)):

                 Polar_curvels=polarization_power(params,substrate_initial_conc_
         solution[0][i],Rext)
                 max_powers=max(Polar_curvels[1])

                 if max_powers<0.015:
                     max_power_lists.append(0)
                 else:
                     max_power_lists.append(max_powers)

             return max_power_lists
```

5. Parameter estimation

5.1. Initialization

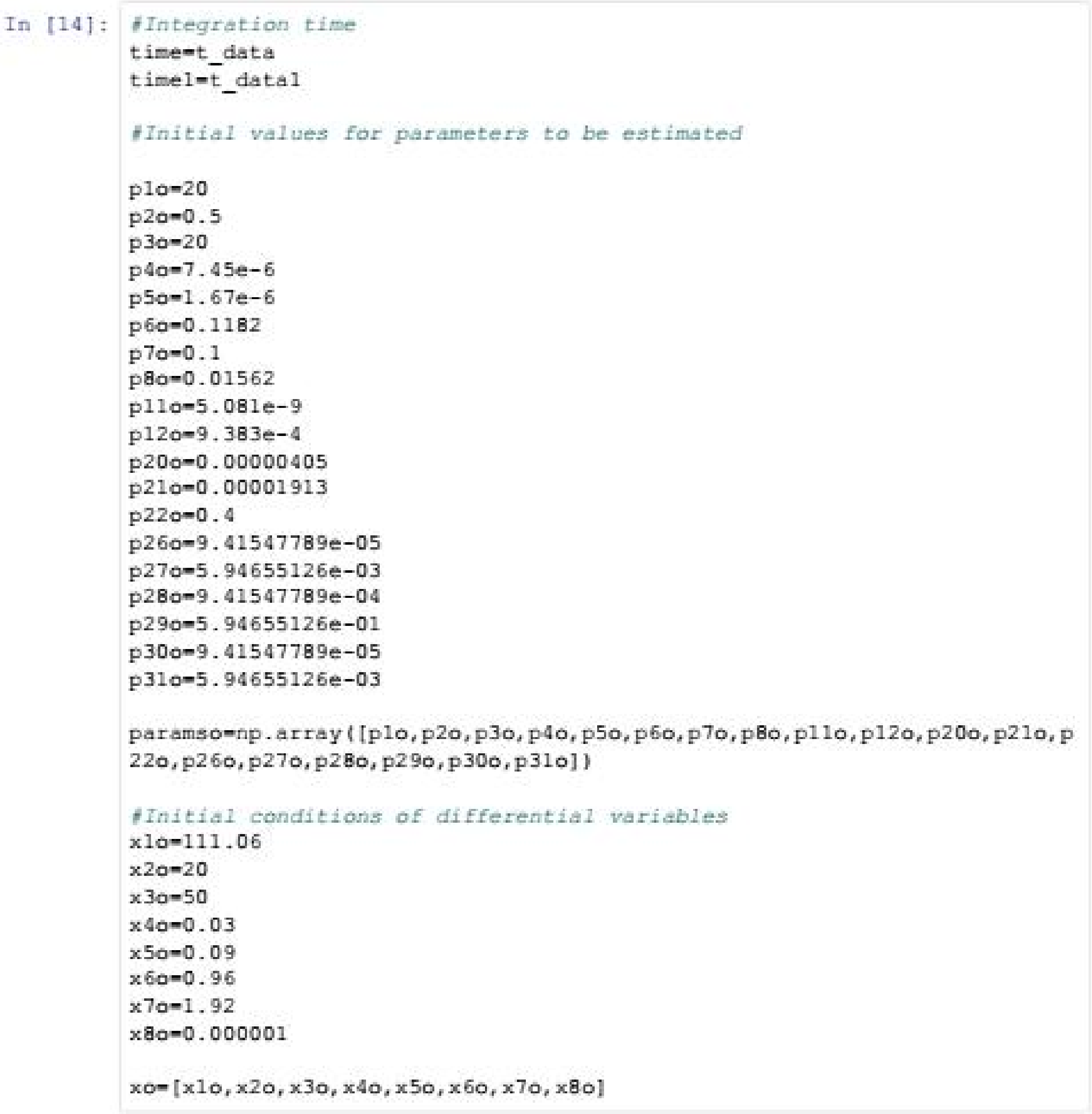

In [14]:

```
#Integration time
time=t_data
time1=t_data1

#Initial values for parameters to be estimated

p1o=20
p2o=0.5
p3o=20
p4o=7.45e-6
p5o=1.67e-6
p6o=0.1182
p7o=0.1
p8o=0.01562
p11o=5.081e-9
p12o=9.383e-4
p20o=0.00000405
p21o=0.00001913
p22o=0.4
p26o=9.41547789e-05
p27o=5.94655126e-03
p28o=9.41547789e-04
p29o=5.94655126e-01
p30o=9.41547789e-05
p31o=5.94655126e-03

paramso=np.array([p1o,p2o,p3o,p4o,p5o,p6o,p7o,p8o,p11o,p12o,p20o,p21o,p22o,p26o,p27o,p28o,p29o,p30o,p31o])

#Initial conditions of differential variables
x1o=111.06
x2o=20
x3o=50
x4o=0.03
x5o=0.09
x6o=0.96
x7o=1.92
x8o=0.000001

xo=[x1o,x2o,x3o,x4o,x5o,x6o,x7o,x8o]
```

5.2. Parameter estimation using Sequential Least SQuares Programming (SLSQP)

5.2.1. Bounds

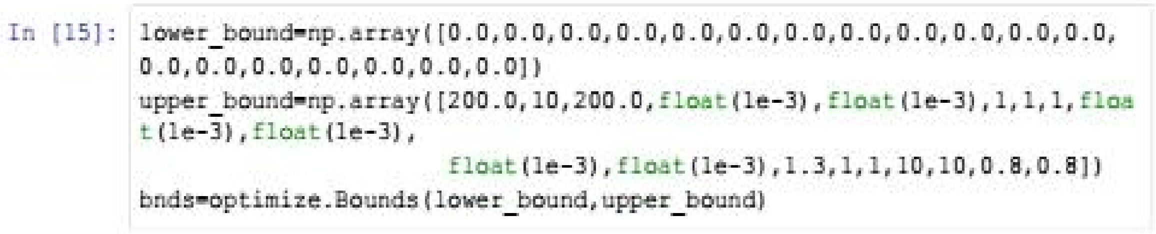

```
In [15]: lower_bound=np.array([0.0,0.0,0.0,0.0,0.0,0.0,0.0,0.0,0.0,0.0,0.0,0.0,
         0.0,0.0,0.0,0.0,0.0,0.0,0.0])
         upper_bound=np.array([200.0,10,200.0,float(1e-3),float(1e-3),1,1,1,floa
         t(1e-3),float(1e-3),
                                        float(1e-3),float(1e-3),1.3,1,1,10,10,0.8,0.8])
         bnds=optimize.Bounds(lower_bound,upper_bound)
```

5.2.2. Parameter estimation

```
In [16]: with warnings.catch_warnings():
             warnings.simplefilter("ignore")
             fxn()
             p_best=optimize.minimize(Error,
                 paramso,args=(Differential_variables_simulation,xo,time,list_da
         ta,'yes'),bounds=bnds,method='SLSQP')

         print('Estimated parameters:-',)
         print('p1:',p_best['x'][0])
         print('p2:',p_best['x'][1])
         print('p3:',p_best['x'][2])
         print('p4:',p_best['x'][3])
         print('p5:',p_best['x'][4])
         print('p6:',p_best['x'][5])
         print('p7:',p_best['x'][6])
         print('p8:',p_best['x'][7])
         print('p11:',p_best['x'][8])
         print('p12:',p_best['x'][9])
         print('p20:',p_best['x'][10])
         print('p21:',p_best['x'][11])
         print('p22:',p_best['x'][12])
         print('p26:',p_best['x'][13])
         print('p27:',p_best['x'][14])
         print('p28:',p_best['x'][15])
         print('p29:',p_best['x'][16])
         print('p30:',p_best['x'][17])
         print('p31:',p_best['x'][18])

         Estimated parameters:-
         p1: 18.773575914991238
         p2: 2.116300104274375
         p3: 19.332252976266105
         p4: 0.00022119978343642144
         p5: 3.3190681605600081e-19
         p6: 0.9418833867670316
         p7: 0.22540568463460114
         p8: 0.6319555112996377
         p11: 1.4853903207209211e-05
         p12: 0.00025533878879461572
         p20: 0.0007477192084868218
         p21: 0.0008017780692673 4
         p22: 0.5360844276530192
         p26: 0.288209628117437
         p27: 0.036055423265555462
         p28: 0.022978994176582 6
         p29: 4.797442925576977
         p30: 0.799692671978936 9
         p31: 0.772429781866567 9
```

5.3. Parameter estimation results simulation

```
In [17]: time_fit=np.linspace(0,500000,50)
         fit_results=odeint(Differential_variables_simulation,xo,time_fit,args=
         (p_best['x'],))
         y10_results=y10_y11_simulation(p_best['x'],fit_results)[0]
         y11_results=y10_y11_simulation(p_best['x'],fit_results)[1]
```

5.4. Parameter estimation results plots

```
In [18]: #Cr(VI) plot results
         with warnings.catch_warnings():
             warnings.simplefilter("ignore")
             fxn()
             fig1 = plt.figure(num=1, figsize=(9, 6), dpi=96, facecolor='w', edg
         ecolor='k')
             plt.text(3000, 1.70, "(a)", fontsize=25)
             plt.ylim(0, 2)
             plt.xlim(0,520000)
             plotter1(1, [time_fit,time], [fit_results[:,6],'g-'],[list_data
         [0],'go'],
                      xlabel=('time/s'),
                      ylabel='Cr(VI) concentration/mmol L$^{-1}$',
                      label1='Cr(VI) model',label2='Cr(VI) experimental',
                      size=16,
                      ncol=1,
                      colsp=1,
                      plot_legend='yes',
                      nrev_legend=2)

             plt.show()
```

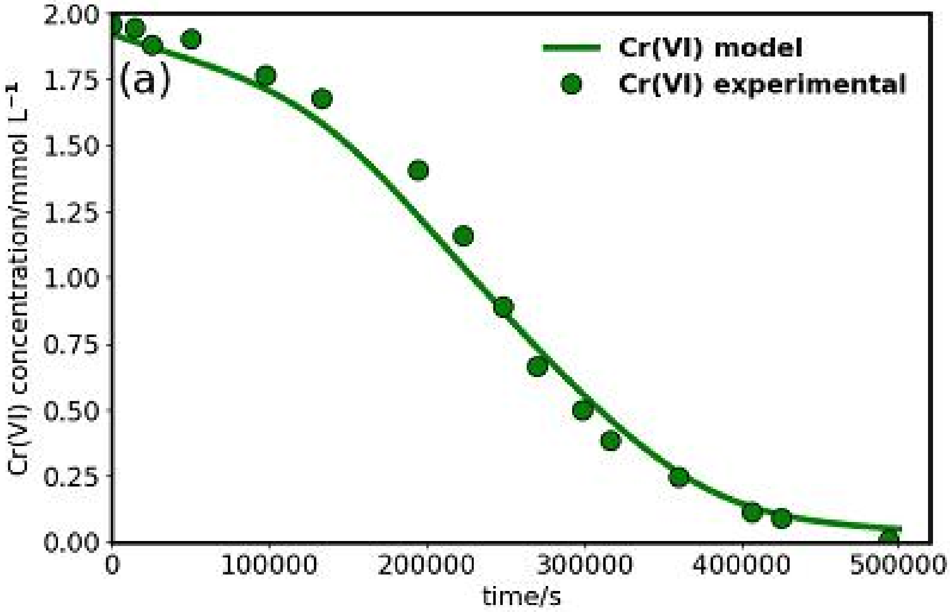

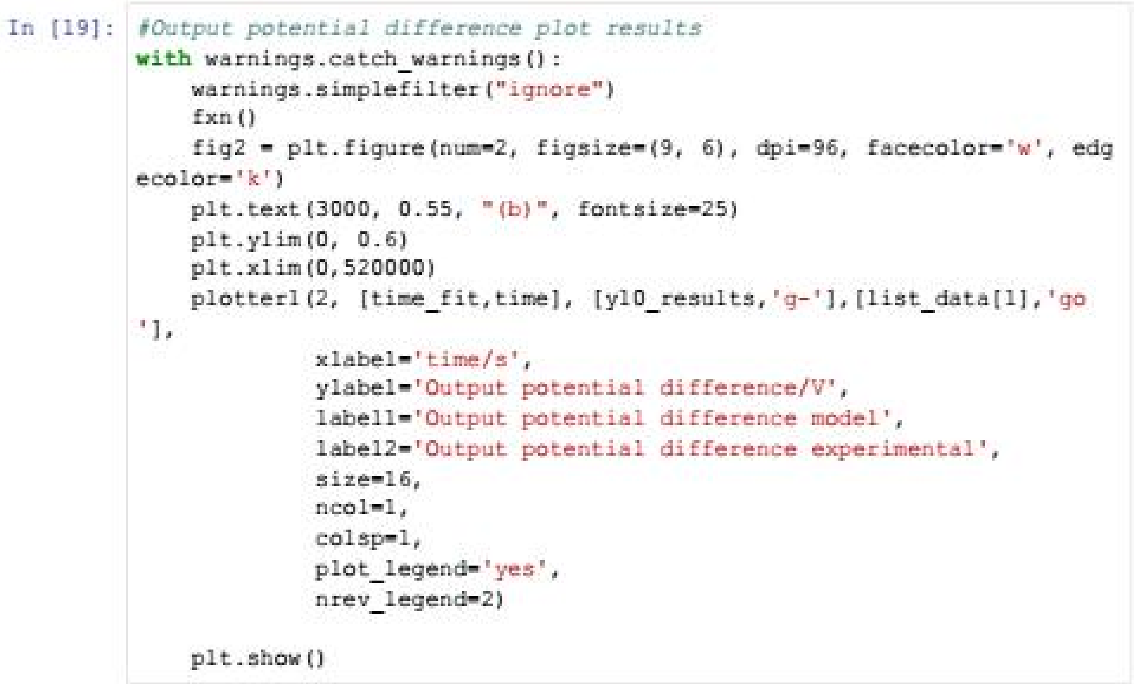

```
In [19]: #Output potential difference plot results
         with warnings.catch_warnings():
             warnings.simplefilter("ignore")
             fxn()
             fig2 = plt.figure(num=2, figsize=(9, 6), dpi=96, facecolor='w', edg
         ecolor='k')
             plt.text(3000, 0.55, "(b)", fontsize=25)
             plt.ylim(0, 0.6)
             plt.xlim(0,520000)
             plotter1(2, [time_fit,time], [y10_results,'g-'],[list_data[1],'go
         '],
                      xlabel='time/s',
                      ylabel='Output potential difference/V',
                      label1='Output potential difference model',
                      label2='Output potential difference experimental',
                      size=16,
                      ncol=1,
                      colsp=1,
                      plot_legend='yes',
                      nrev_legend=2)

             plt.show()
```

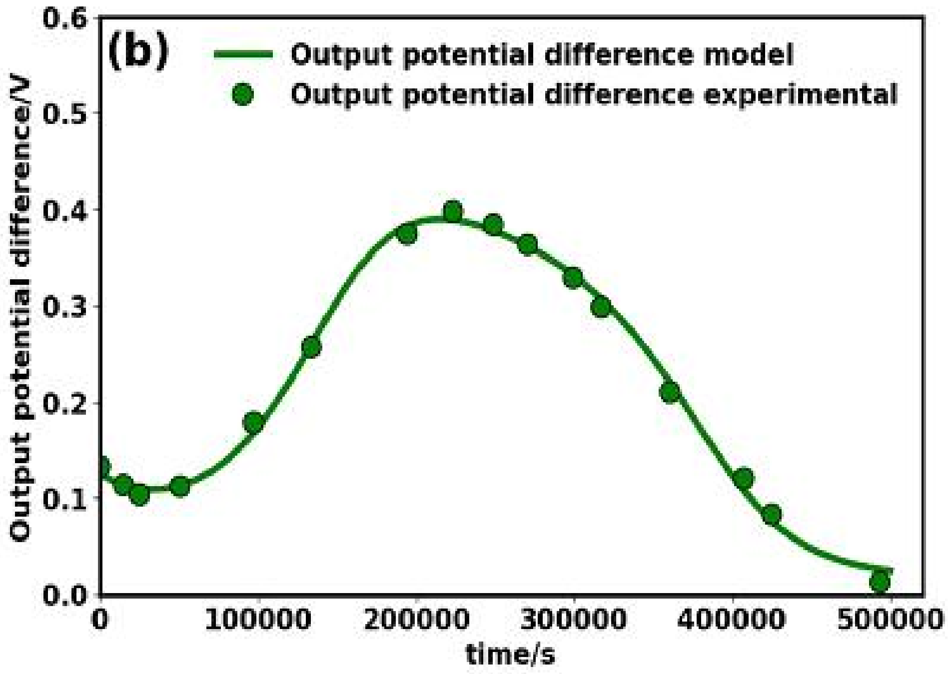

5.5. Parameter estimation errors

```
In [20]: Parameter_estimation_errors=Error(p_best['x'],Differential_variables_si
         mulation,xo,time,list_data,'no')

         SE_x7=Parameter_estimation_errors[0][0]
         MSE_x7=Parameter_estimation_errors[0][1]
         RMSE_x7=Parameter_estimation_errors[0][2]
         NRMSE_x7=Parameter_estimation_errors[0][3]

         SE_y10=Parameter_estimation_errors[1][0]
         MSE_y10=Parameter_estimation_errors[1][1]
         RMSE_y10=Parameter_estimation_errors[1][2]
         NRMSE_y10=Parameter_estimation_errors[1][3]

         print('Cr(VI) fit errors:-',)
         print('Cr(VI) squared error:',SE_x7)
         print('Cr(VI) mean squared error:',MSE_x7)
         print('Cr(VI) root mean squared error:',RMSE_x7)
         print('Cr(VI) normalized root mean squared error:',NRMSE_x7)
         print('')
         print('Output voltage fit errors:-')
         print('Output voltage squared error:',SE_y10)
         print('Output voltage mean squared error:',MSE_y10)
         print('Output voltage root mean squared error::',RMSE_y10)
         print('Output voltage normalized root mean squared error:',NRMSE_y10)
```

```
Cr(VI) fit errors:-
Cr(VI) squared error: 0.08230194201870898
Cr(VI) mean squared error: 0.005143871376169311
Cr(VI) root mean squared error: 0.0717207876153721
Cr(VI) normalized root mean squared error: 0.0691499751363125

Output voltage fit errors:-
Output voltage squared error: 0.0010100644843792537
Output voltage mean squared error: 6.312903027370336e-05
Output voltage root mean squared error:: 0.007945377918872289
Output voltage normalized root mean squared error: 0.0365208287529691
5
```

6. Model Validation

6.1. Change in Cr(VI) concentration model validation simulation

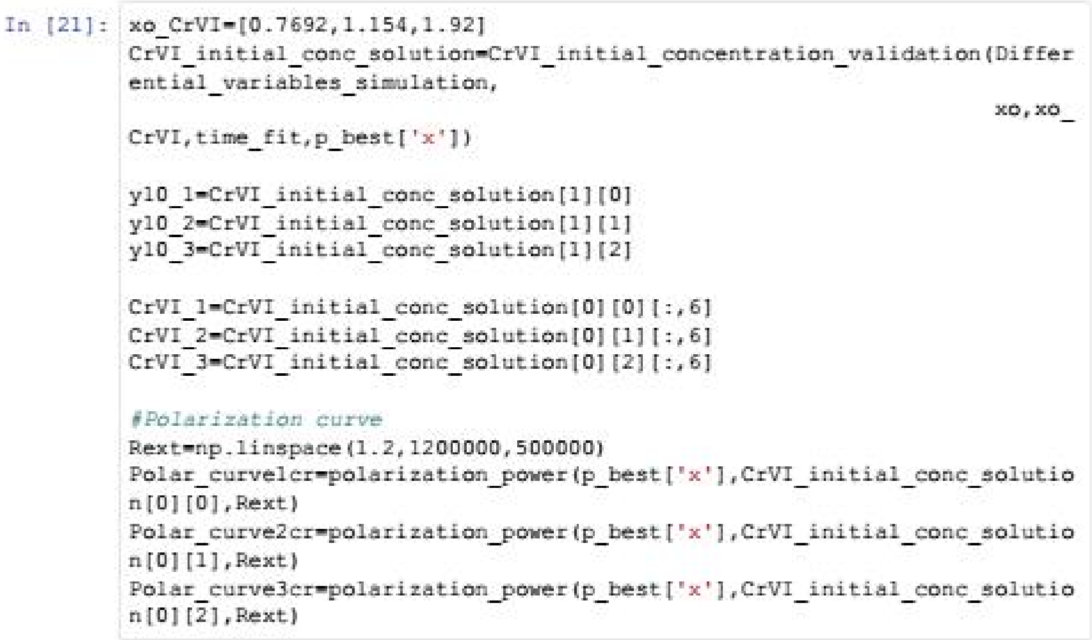

```
In [21]: xo_CrVI=[0.7692,1.154,1.92]
         CrVI_initial_conc_solution=CrVI_initial_concentration_validation(Differ
         ential_variables_simulation,
                                                                          xo,xo_
         CrVI,time_fit,p_best['x'])

         y10_1=CrVI_initial_conc_solution[1][0]
         y10_2=CrVI_initial_conc_solution[1][1]
         y10_3=CrVI_initial_conc_solution[1][2]

         CrVI_1=CrVI_initial_conc_solution[0][0][:,6]
         CrVI_2=CrVI_initial_conc_solution[0][1][:,6]
         CrVI_3=CrVI_initial_conc_solution[0][2][:,6]

         #Polarization curve
         Rext=np.linspace(1.2,1200000,500000)
         Polar_curve1cr=polarization_power(p_best['x'],CrVI_initial_conc_solutio
         n[0][0],Rext)
         Polar_curve2cr=polarization_power(p_best['x'],CrVI_initial_conc_solutio
         n[0][1],Rext)
         Polar_curve3cr=polarization_power(p_best['x'],CrVI_initial_conc_solutio
         n[0][2],Rext)
```

6.2. Model validation results plots

```
In [22]: #Cr(VI) plot results
         with warnings.catch_warnings():
             warnings.simplefilter("ignore")
             fxn()
             fig1 = plt.figure(num=1, figsize=(9, 6), dpi=96, facecolor='w', edg
         ecolor='k')
             plt.text(470000, 1.8, "(a)", fontsize=25)
             plt.ylim(0, 3)
             plt.xlim(0,520000)
             plotter1(1, [time_fit,time_fit,time_fit,time,time,time], [CrVI_1,'g
         -'],[CrVI_2,'b--'],[CrVI_3,'y-.'],
                       [list_data1[0],'go'],[list_data1[1],'bv'],[list_data1[2],'
         ys'],
                       xlabel='time/s',
                       ylabel='Cr(VI) concentration/mmol L$^{-1}$',
                       label1='0.769 mmol L$^{-1}$ model',label2='1.15   mmol L$^
         {-1}$ model',
                       label3='1.92   mmol L$^{-1}$ model',label4='0.769 mmol L$^
         {-1}$ exp',
                       label5='1.15   mmol L$^{-1}$ exp',label6='1.92   mmol L$^
         {-1}$ exp',
                       size=16,
                       ncol=2,
                       colsp=1,
                       plot_legend='yes',
                       nrev_legend=0)

             plt.show()
```

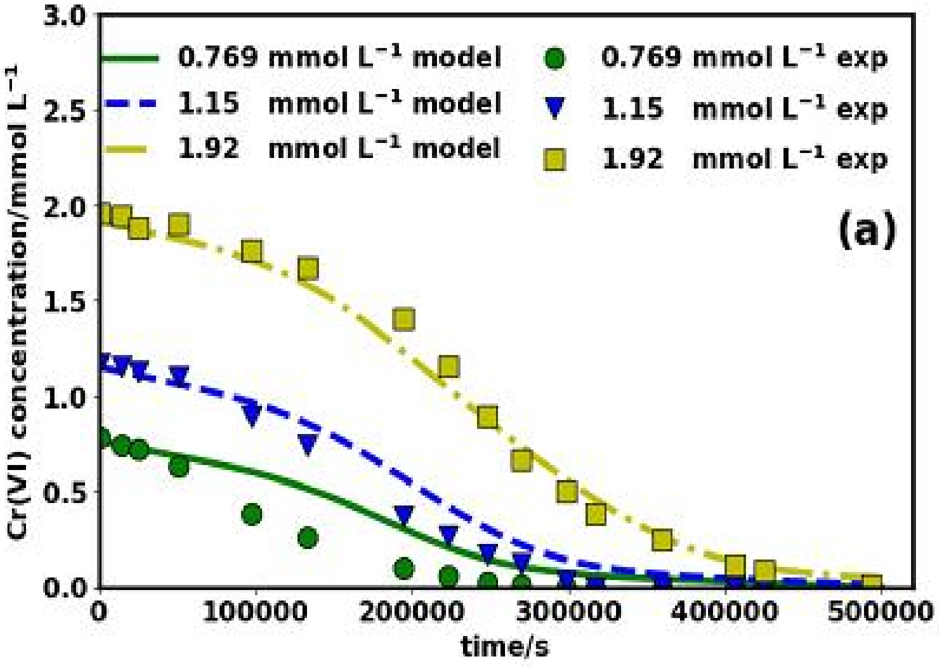

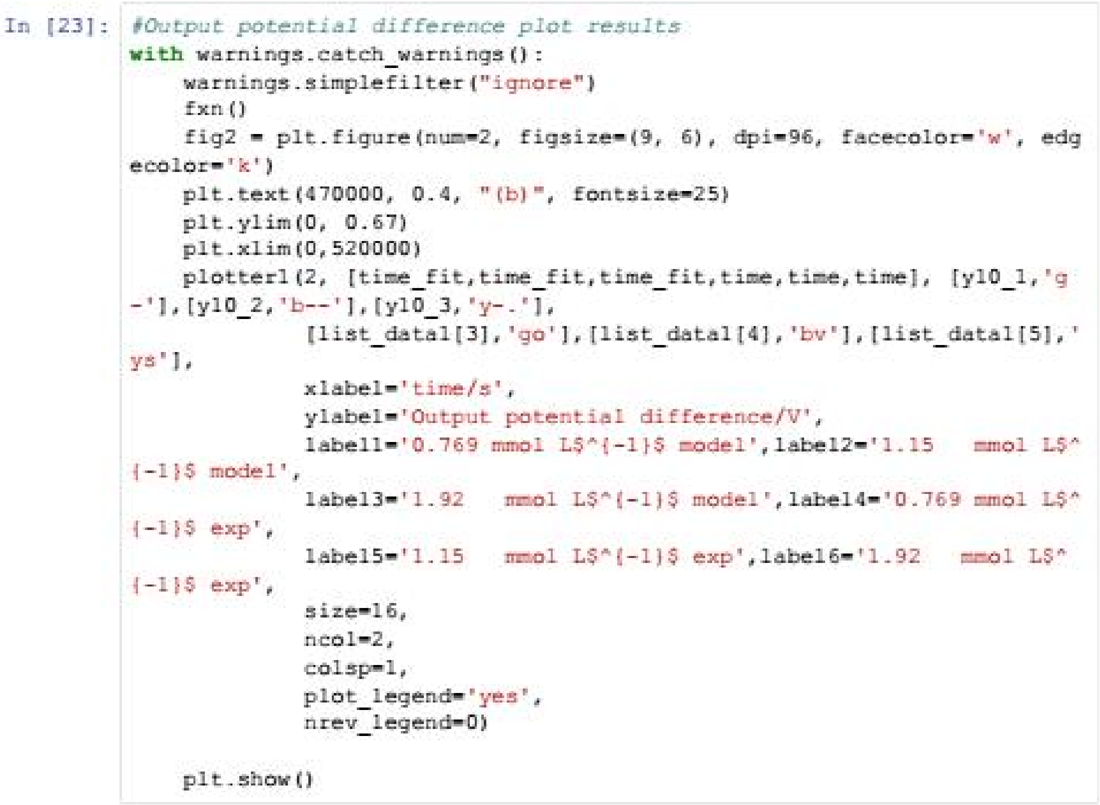

```
In [23]: #Output potential difference plot results
         with warnings.catch_warnings():
             warnings.simplefilter("ignore")
             fxn()
             fig2 = plt.figure(num=2, figsize=(9, 6), dpi=96, facecolor='w', edg
         ecolor='k')
             plt.text(470000, 0.4, "(b)", fontsize=25)
             plt.ylim(0, 0.67)
             plt.xlim(0,520000)
             plotter1(2, [time_fit,time_fit,time_fit,time,time,time], [y10_1,'g
         -'],[y10_2,'b--'],[y10_3,'y-.'],
                       [list_data1[3],'go'],[list_data1[4],'bv'],[list_data1[5],'
         ys'],
                       xlabel='time/s',
                       ylabel='Output potential difference/V',
                       label1='0.769 mmol L$^{-1}$ model',label2='1.15   mmol L$^
         {-1}$ model',
                       label3='1.92   mmol L$^{-1}$ model',label4='0.769 mmol L$^
         {-1}$ exp',
                       label5='1.15   mmol L$^{-1}$ exp',label6='1.92   mmol L$^
         {-1}$ exp',
                       size=16,
                       ncol=2,
                       colsp=1,
                       plot_legend='yes',
                       nrev_legend=0)

             plt.show()
```

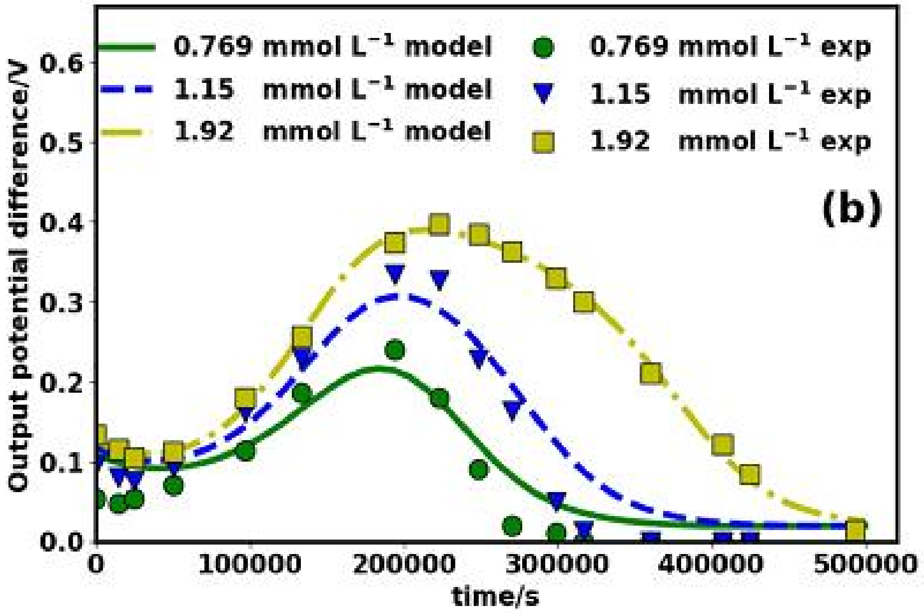

```
In [24]: #Polarization plot results
         with warnings.catch_warnings():
             warnings.simplefilter("ignore")
             fxn()
             fig1 = plt.figure(num=1, figsize=(9, 6), dpi=96, facecolor='w', edg
         ecolor='k')
             plt.text(1.17, 0.41, "(a)", fontsize=25)
             plt.ylim(0, 0.65)
             plt.xlim(0,1.3)
             plotter1(1, [Polar_curve1cr[2],Polar_curve2cr[2],Polar_curve3cr[2],
         C1_data,C2_data,C3_data],
                         [Polar_curve1cr[0],'g-'],[Polar_curve2cr[0],'b--'],[Polar_
         curve3cr[0],'y-.'],
                         [V1_data,'go'],[V2_data,'bv'],[V3_data,'ys'],
                         xlabel='Current density/A m$^{-2}$',
                         ylabel='Output potential difference/V',
                         label1='0.769 mmol L$^{-1}$ model',label2='1.15   mmol L$^
         {-1}$ model',
                         label3='1.92   mmol L$^{-1}$ model',label4='0.769 mmol L$^
         {-1}$ exp',
                         label5='1.15   mmol L$^{-1}$ exp',label6='1.92   mmol L$^
         {-1}$ exp',
                         size=16,
                         ncol=2,
                         colsp=1,
                         plot_legend='yes',
                         nrev_legend=0)

             plt.show()
```

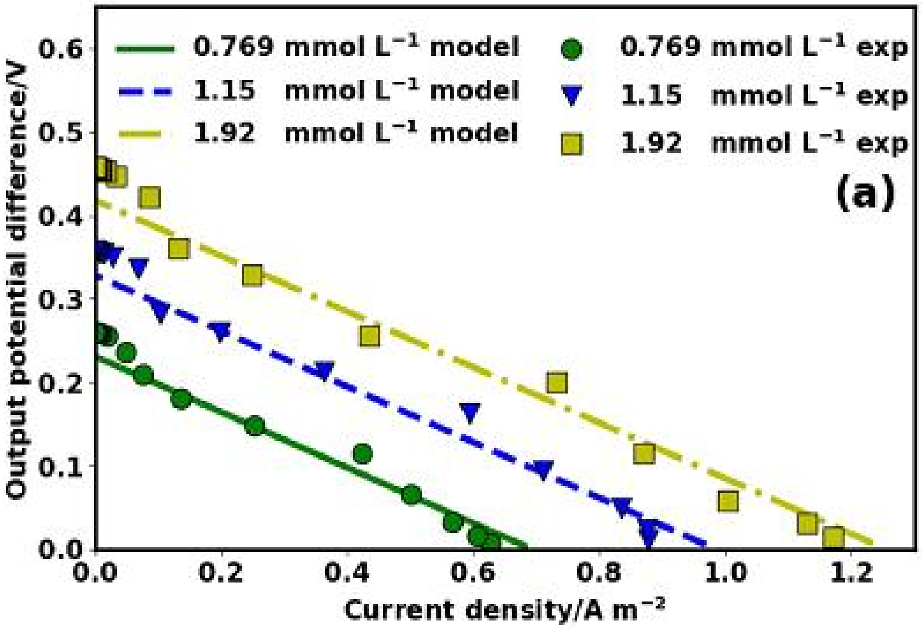

```
In [25]: #Power plot results
         with warnings.catch_warnings():
             warnings.simplefilter("ignore")
             fxn()
             fig2 = plt.figure(num=2, figsize=(9, 6), dpi=96, facecolor='w', edg
         ecolor='k')
             plt.text(1.17, 0.16, "(b)", fontsize=25)
             plt.ylim(0, 0.25)
             plt.xlim(0,1.3)
             plotter1(2, [Polar_curve1cr[2],Polar_curve2cr[2],Polar_curve3cr[2],
         C1_data,C2_data,C3_data],
                          [Polar_curve1cr[1],'g-'],[Polar_curve2cr[1],'b--'],[Polar_
         curve3cr[1],'y-.'],
                          [P1_data,'go'],[P2_data,'bv'],[P3_data,'ys'],
                          xlabel='Current density/A m$^{-2}$',
                          ylabel='Power density/W m$^{-2}$',
                          label1='0.769 mmol L$^{-1}$ model',label2='1.15   mmol L$^
         {-1}$ model',
                          label3='1.92   mmol L$^{-1}$ model',label4='0.769 mmol L$^
         {-1}$ exp',
                          label5='1.15   mmol L$^{-1}$ exp',label6='1.92   mmol L$^
         {-1}$ exp',
                          size=16,
                          ncol=2,
                          colsp=1,
                          plot_legend='yes',
                          nrev_legend=0)

             plt.show()
```

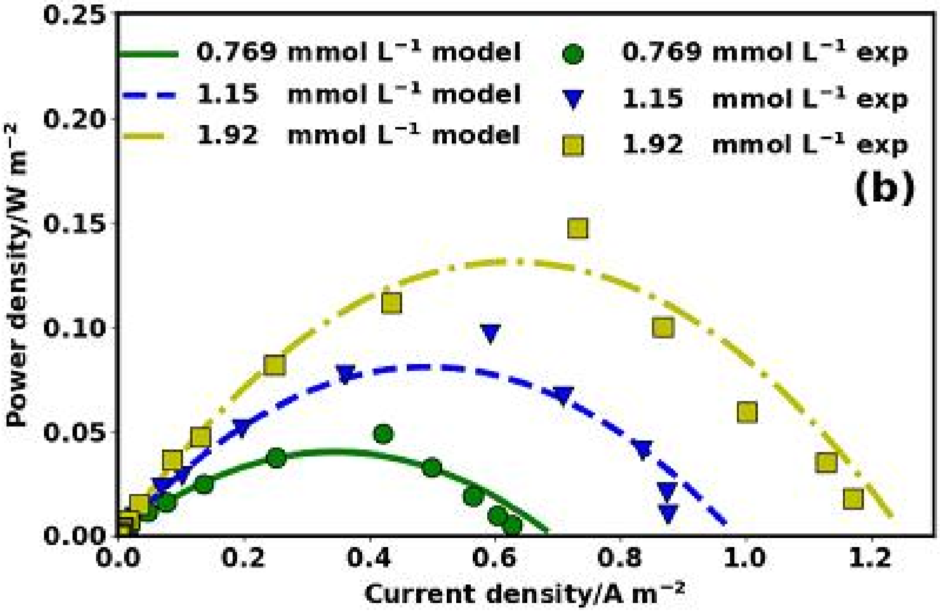

7. Coulombic efficiency

7.1. Coulombic efficiency simulation

```
In [26]: r=3200
Faradays_const=96845 #A s/mol
v_chamber=0.25 #L
C_Cr1o_exp=xo_CrVI[0]*52/1000 #g/L
C_Cr2o_exp=xo_CrVI[1]*52/1000 #g/L
C_Cr3o_exp=xo_CrVI[2]*52/1000 #g/L
C_Cr1o_model=CrVI_1[0]*52/1000 #g/L
C_Cr2o_model=CrVI_2[0]*52/1000 #g/L
C_Cr3o_model=CrVI_3[0]*52/1000 #g/L

def points(data):
    point=[]
    time=[]
    for i in range(len(data)):
        if i==0:
            point.append(data[i])
            time.append(time_fit[i])
        if i>0:
            if (i%2)==0:
                point.append(data[i])
                time.append(time_fit[i])
    return point,time

model1_points1=points(y10_1)[0]
model2_points2=points(y10_2)[0]
model3_points3=points(y10_3)[0]

time1_points1=points(y10_1)[1]
time2_points2=points(y10_2)[1]
time3_points3=points(y10_3)[1]

output_potential_exp1=np.array(list_data1[3]) #V
output_potential_model1=np.array(model1_points1) #V
output_potential_exp2=np.array(list_data1[4]) #V
output_potential_model2=np.array(model2_points2) #V
output_potential_exp3=np.array(list_data1[5]) #V
output_potential_model3=np.array(model3_points3) #V

current_output_exp1=output_potential_exp1/r #A
current_output_model1=output_potential_model1/r #A
current_output_exp2=output_potential_exp2/r #A
current_output_model2=output_potential_model2/r #A
current_output_exp3=output_potential_exp3/r #A
current_output_model3=output_potential_model3/r #A

def delta_times_current_list(current_output_list,time_list):
    delta_times_time_list=[]
    for i in range(len(current_output_list)-1):
        delta_times_time_list.append(current_output_list[i]*(time_list
[i+1]-time_list[i]))
    return delta_times_time_list

delta_times_time_list_exp1=delta_times_current_list(current_output_exp
1,time)
delta_times_time_list_exp2=delta_times_current_list(current_output_exp
2,time)
```

7.2. Coulombic efficiency plots

```
In [27]: with warnings.catch_warnings():
             warnings.simplefilter("ignore")
             fxn()
             fig1 = plt.figure(num=1, figsize=(9, 6), dpi=96, facecolor='w', edg
         ecolor='k')
             #plt.text(-0.2, 92, "(b)", fontsize=25)
             plt.ylim(0, 35)
             #plt.xlim(0,2)
             plotter2(1, [[Coulombic_efficiency_exp1,Coulombic_efficiency_exp2,C
         oulombic_efficiency_exp3],'g'],
                      [[Coulombic_efficiency_model1,Coulombic_efficiency_model2,
         Coulombic_efficiency_model3],'r'],
                      xlabel='Cr(VI) initial concentration (mmol L$^{-1}$)',
                      ylabel='Coulombic efficiency (%)',
                      label1='Experimental',
                      label2='Model',
                      tick_label=['0.769','1.15', '1.92'],
                      size=16,
                      ncol=1,
                      colsp=1,
                      plot_legend='yes',
                      nrev_legend=2)

             plt.show()
```

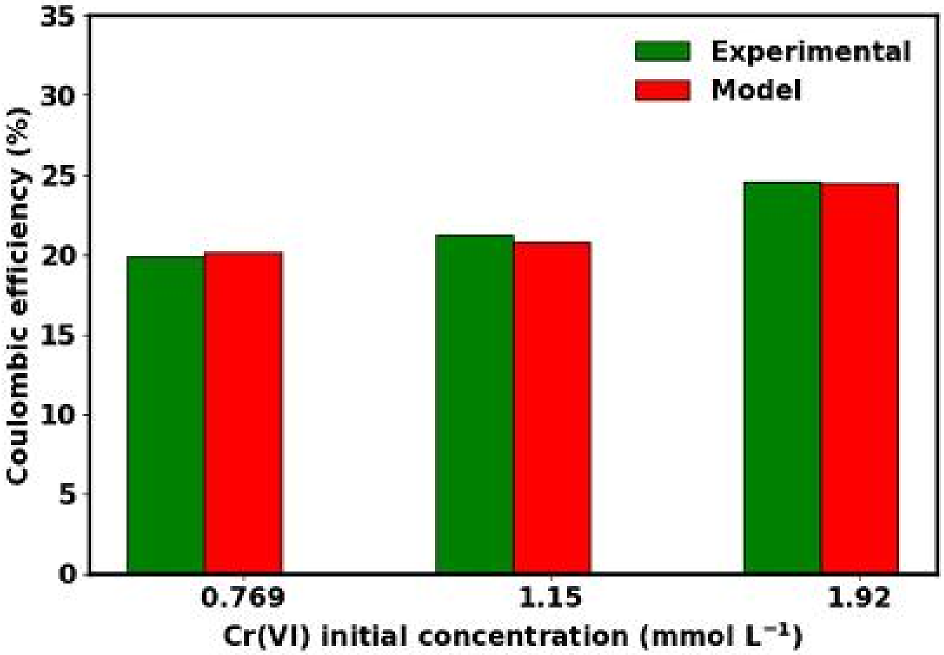

8. Simulation

8.1. The effect of primary cell concentration

8.1.1. Primary cell concentration results simulation

```
In [28]: #Profiles
         xo_cell=[15,25,35,45]
         cell_initial_conc_solution=primary_cell_concentration(Differential_vari
         ables_simulation,
                                                                                 xo,xo_
         cell,time_fit,p_best['x'])
         yl0_1c=cell_initial_conc_solution[1][0]
         yl0_2c=cell_initial_conc_solution[1][1]
         yl0_3c=cell_initial_conc_solution[1][2]
         yl0_4c=cell_initial_conc_solution[1][3]

         CrVI_cell_1=cell_initial_conc_solution[0][0][:,6]
         CrVI_cell_2=cell_initial_conc_solution[0][1][:,6]
         CrVI_cell_3=cell_initial_conc_solution[0][2][:,6]
         CrVI_cell_4=cell_initial_conc_solution[0][3][:,6]

         #Polarization curve
         Rext=np.linspace(1.2,1200000,500000)
         Polar_curve1c=polarization_power(p_best['x'],cell_initial_conc_solution
         [0][0],Rext)
         Polar_curve2c=polarization_power(p_best['x'],cell_initial_conc_solution
         [0][1],Rext)
         Polar_curve3c=polarization_power(p_best['x'],cell_initial_conc_solution
         [0][2],Rext)
         Polar_curve4c=polarization_power(p_best['x'],cell_initial_conc_solution
         [0][3],Rext)

         #Primary cell concentration optimization
         time_cell=np.linspace(0,700000,400)
         cell_list=np.linspace(1,45,50)
         time_max_cell_list=cell_optimization(Differential_variables_simulation,
                                              xo,cell_list,time_cell,p_best['x'])
```

8.1.2. Primary cell concentration results plots

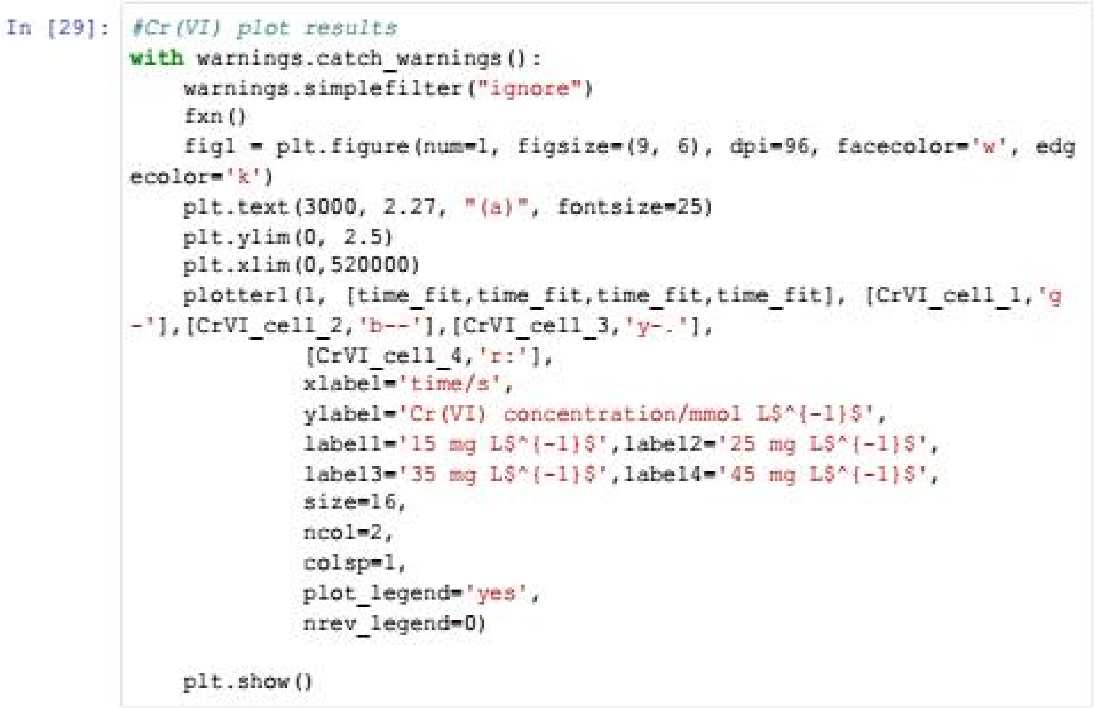

```
In [29]: #Cr(VI) plot results
         with warnings.catch_warnings():
             warnings.simplefilter("ignore")
             fxn()
             fig1 = plt.figure(num=1, figsize=(9, 6), dpi=96, facecolor='w', edg
         ecolor='k')
             plt.text(3000, 2.27, "(a)", fontsize=25)
             plt.ylim(0, 2.5)
             plt.xlim(0,520000)
             plotter1(1, [time_fit,time_fit,time_fit,time_fit], [CrVI_cell_1,'g
         -'],[CrVI_cell_2,'b--'],[CrVI_cell_3,'y-.'],
                      [CrVI_cell_4,'r:'],
                      xlabel='time/s',
                      ylabel='Cr(VI) concentration/mmol L$^{-1}$',
                      label1='15 mg L$^{-1}$',label2='25 mg L$^{-1}$',
                      label3='35 mg L$^{-1}$',label4='45 mg L$^{-1}$',
                      size=16,
                      ncol=2,
                      colsp=1,
                      plot_legend='yes',
                      nrev_legend=0)

             plt.show()
```

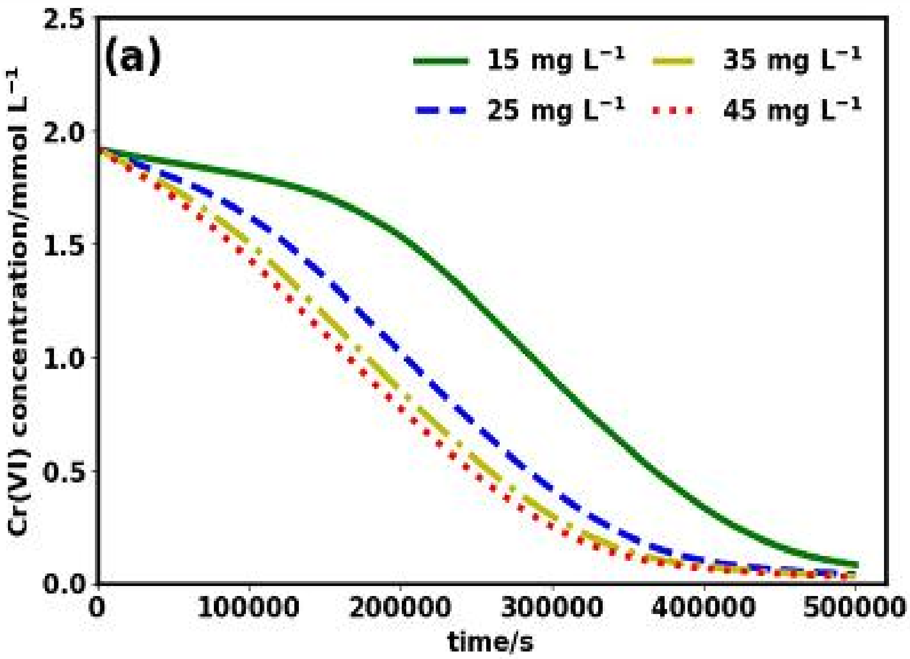

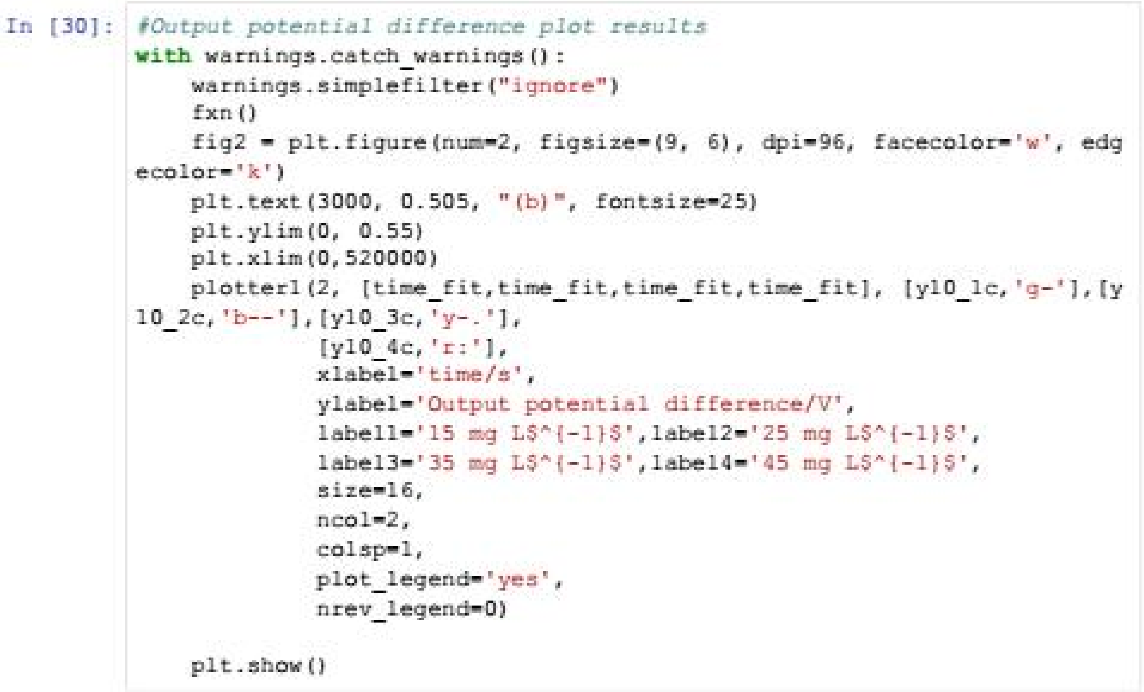

```
In [30]: #Output potential difference plot results
         with warnings.catch_warnings():
             warnings.simplefilter("ignore")
             fxn()
             fig2 = plt.figure(num=2, figsize=(9, 6), dpi=96, facecolor='w', edg
         ecolor='k')
             plt.text(3000, 0.505, "(b)", fontsize=25)
             plt.ylim(0, 0.55)
             plt.xlim(0,520000)
             plotter1(2, [time_fit,time_fit,time_fit,time_fit], [y10_1c,'g-'],[y
         10_2c,'b--'],[y10_3c,'y-.'],
                      [y10_4c,'r:'],
                      xlabel='time/s',
                      ylabel='Output potential difference/V',
                      label1='15 mg L$^{-1}$',label2='25 mg L$^{-1}$',
                      label3='35 mg L$^{-1}$',label4='45 mg L$^{-1}$',
                      size=16,
                      ncol=2,
                      colsp=1,
                      plot_legend='yes',
                      nrev_legend=0)

             plt.show()
```

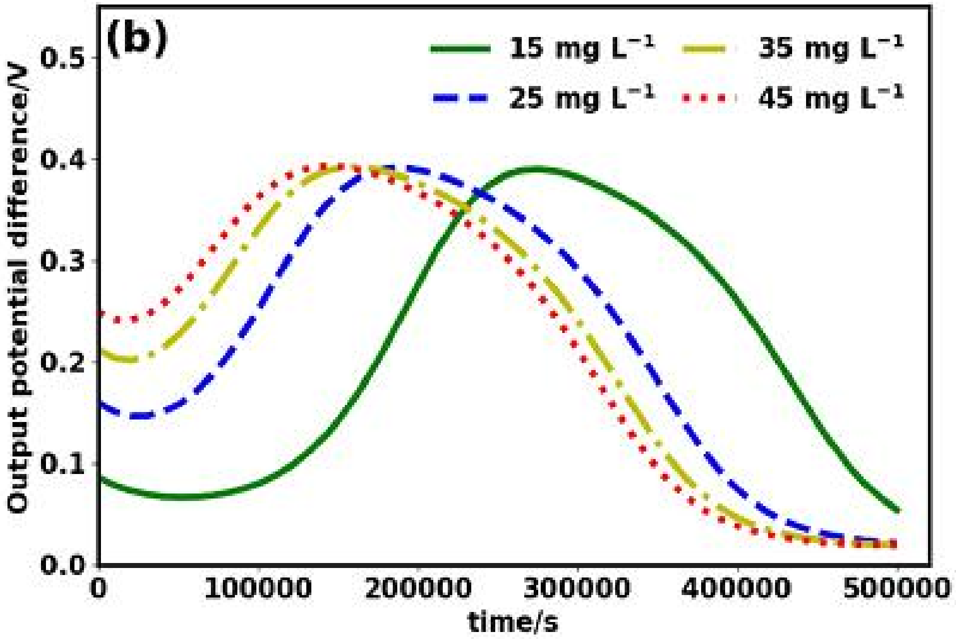

8.1.3. Primary cell concentration polarization and power curve

```
In [31]: #Polarization plot results
         with warnings.catch_warnings():
             warnings.simplefilter("ignore")
             fxn()
             fig1 = plt.figure(num=1, figsize=(9, 6), dpi=96, facecolor='w', edg
         ecolor='k')
             plt.text(0.005, 0.46, "(c)", fontsize=25)
             plt.ylim(0, 0.5)
             plt.xlim(0,1.3)
             plotter1(1, [Polar_curve1c[2],Polar_curve2c[2],Polar_curve3c[2],Pol
         ar_curve4c[2]],
                      [Polar_curve1c[0],'g-'],[Polar_curve2c[0],'b--'],[Polar_cu
         rve3c[0],'y-.'],[Polar_curve4c[0],'r:'],
                      xlabel='Current density/A m$^{-2}$',
                      ylabel='Output potential difference/V',
                      label1='15 mg L$^{-1}$',label2='25 mg L$^{-1}$',
                      label3='35 mg L$^{-1}$',label4='45 mg L$^{-1}$',
                      size=16,
                      ncol=2,
                      colsp=1,
                      plot_legend='yes',
                      nrev_legend=0)

             plt.show()
```

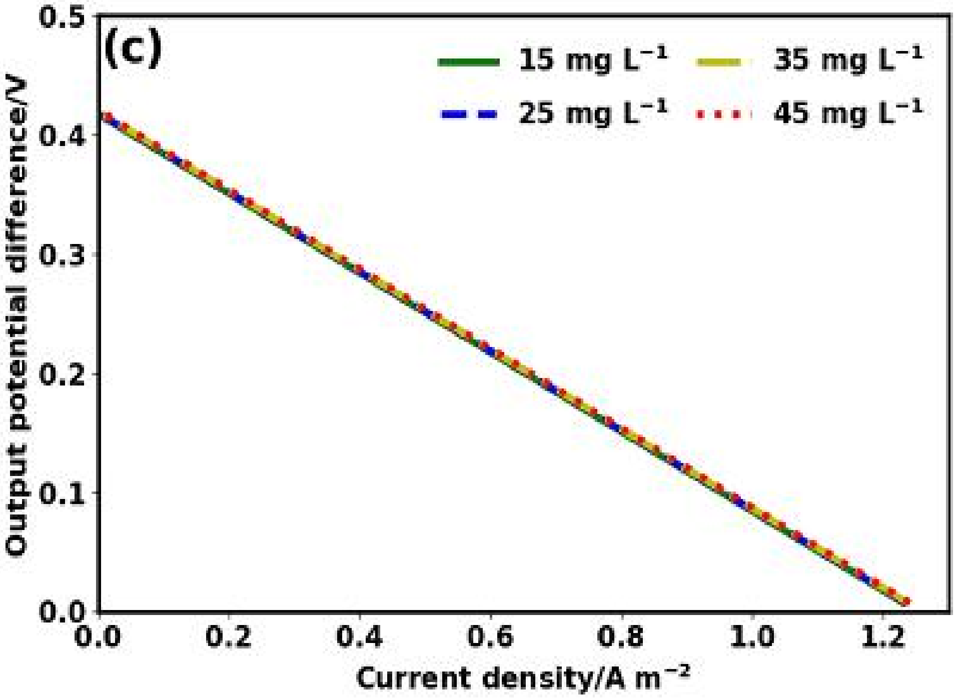

```
In [32]: #Power plot results
         with warnings.catch_warnings():
             warnings.simplefilter("ignore")
             fxn()
             fig2 = plt.figure(num=2, figsize=(9, 6), dpi=96, facecolor='w', edg
         ecolor='k')
             plt.text(0.005, 0.166, "(d)", fontsize=25)
             plt.ylim(0, 0.18)
             plt.xlim(0,1.3)
             plotter1(2, [Polar_curve1c[2],Polar_curve2c[2],Polar_curve3c[2],Pol
         ar_curve4c[2]],
                          [Polar_curve1c[1],'g-'],[Polar_curve2c[1],'b--'],[Polar_cu
         rve3c[1],'y-.'],[Polar_curve4c[1],'r:'],
                          xlabel='Current density/A m$^{-2}$',
                          ylabel='Power density/W m$^{-2}$',
                          label1='15 mg L$^{-1}$',label2='25 mg L$^{-1}$',
                          label3='35 mg L$^{-1}$',label4='45 mg L$^{-1}$',
                          size=16,
                          ncol=2,
                          colsp=1,
                          plot_legend='yes',
                          nrev_legend=0)

             plt.show()
```

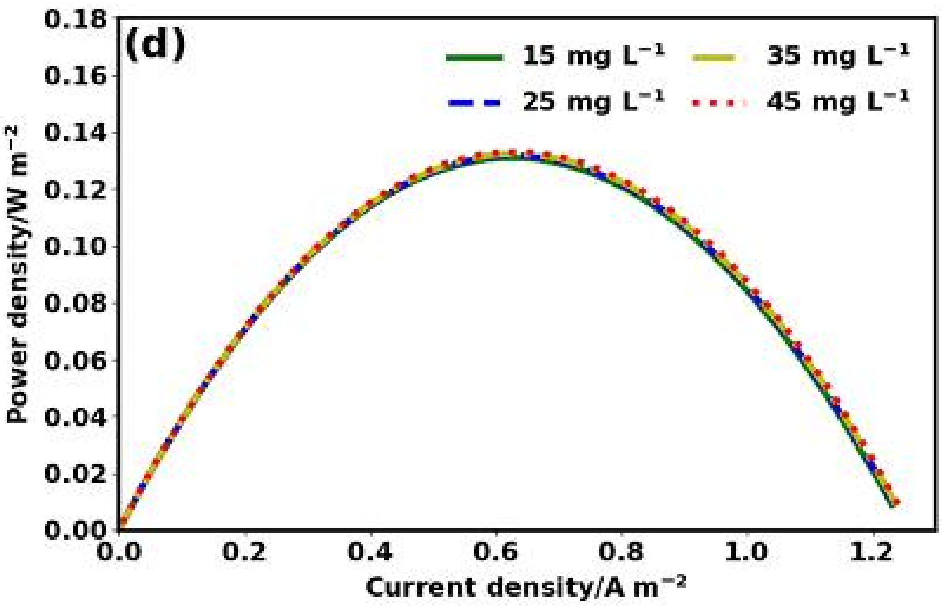

8.1.4. Primary cell concentration optimization plot

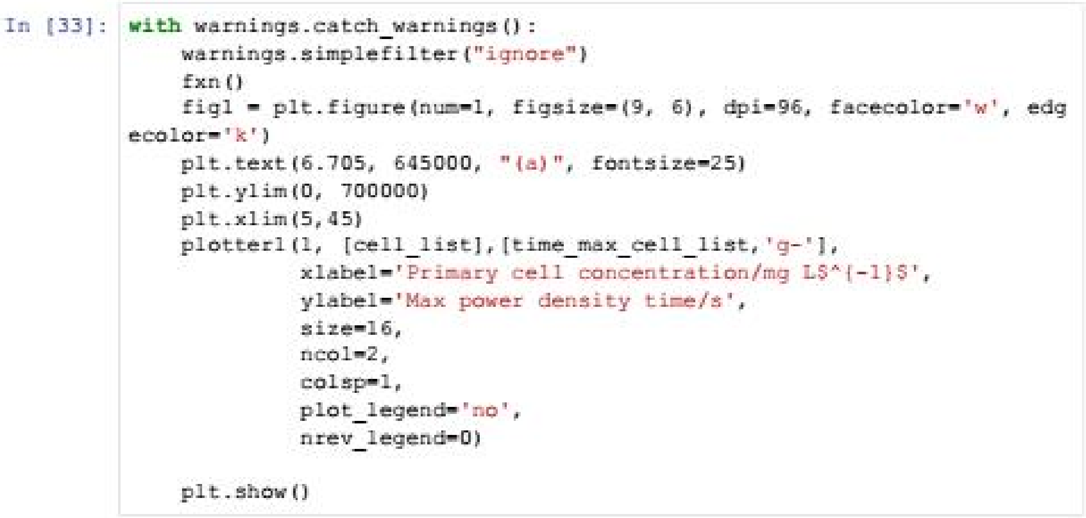

```
In [33]: with warnings.catch_warnings():
             warnings.simplefilter("ignore")
             fxn()
             fig1 = plt.figure(num=1, figsize=(9, 6), dpi=96, facecolor='w', edg
         ecolor='k')
             plt.text(6.705, 645000, "(a)", fontsize=25)
             plt.ylim(0, 700000)
             plt.xlim(5,45)
             plotter1(1, [cell_list],[time_max_cell_list,'g-'],
                      xlabel='Primary cell concentration/mg L$^{-1}$',
                      ylabel='Max power density time/s',
                      size=16,
                      ncol=2,
                      colsp=1,
                      plot_legend='no',
                      nrev_legend=0)

             plt.show()
```

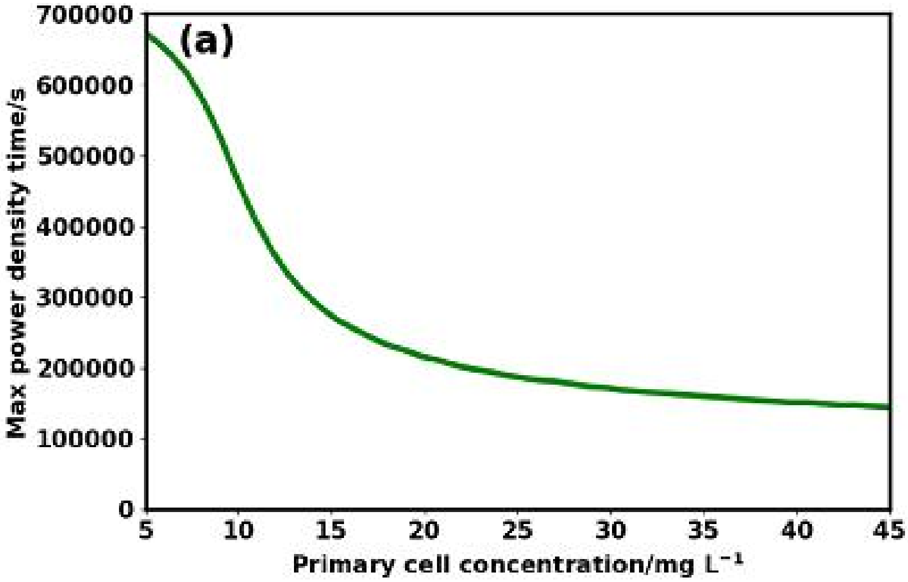

8.2. The effect of substrate concentration

8.2.1. Substrate concentration results simulation

```
In [34]: #Profiles
         xo_substrate=[30,60,90,120]
         substrate_initial_conc_solution=substrate_concentration(Differential_va
         riables_simulation,
                                                                          xo,xo_
         substrate,time_fit,p_best['x'])
         y10_1s=substrate_initial_conc_solution[1][0]
         y10_2s=substrate_initial_conc_solution[1][1]
         y10_3s=substrate_initial_conc_solution[1][2]
         y10_4s=substrate_initial_conc_solution[1][3]

         CrVI_substrate_1=substrate_initial_conc_solution[0][0][:,6]
         CrVI_substrate_2=substrate_initial_conc_solution[0][1][:,6]
         CrVI_substrate_3=substrate_initial_conc_solution[0][2][:,6]
         CrVI_substrate_4=substrate_initial_conc_solution[0][3][:,6]

         #Polarization curve
         Rext=np.linspace(1.2,1200000,500000)
         Polar_curve1s=polarization_power(p_best['x'],substrate_initial_conc_sol
         ution[0][0],Rext)
         Polar_curve2s=polarization_power(p_best['x'],substrate_initial_conc_sol
         ution[0][1],Rext)
         Polar_curve3s=polarization_power(p_best['x'],substrate_initial_conc_sol
         ution[0][2],Rext)
         Polar_curve4s=polarization_power(p_best['x'],substrate_initial_conc_sol
         ution[0][3],Rext)

         #Substrate concentration optimization
         substrate_list=np.linspace(0,120,241)
         Rext1=np.array([1.2,2.7,5.6,12,27,56,120,270,560,1000,2700,5600,
                        10000,12000,27000,56000,100000,120000,560000,1200000])
         max_power_substrate_list=substrate_optimization(Rext1,Differential_vari
         ables_simulation,
                                    xo,substrate_list,time_fit,p_best['x'])
```

8.2.2. Substrate concentration results plots

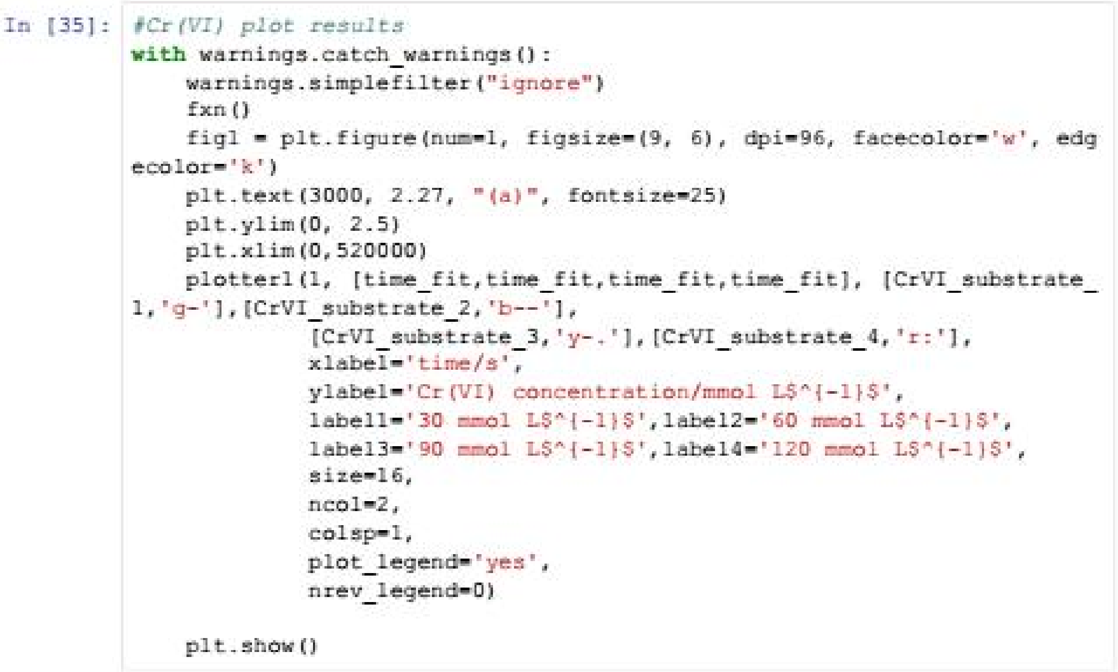

```
In [35]: #Cr(VI) plot results
         with warnings.catch_warnings():
             warnings.simplefilter("ignore")
             fxn()
             fig1 = plt.figure(num=1, figsize=(9, 6), dpi=96, facecolor='w', edg
         ecolor='k')
             plt.text(3000, 2.27, "(a)", fontsize=25)
             plt.ylim(0, 2.5)
             plt.xlim(0,520000)
             plotter1(1, [time_fit,time_fit,time_fit,time_fit], [CrVI_substrate_
         1,'g-'],[CrVI_substrate_2,'b--'],
                       [CrVI_substrate_3,'y-.'],[CrVI_substrate_4,'r:'],
                       xlabel='time/s',
                       ylabel='Cr(VI) concentration/mmol L$^{-1}$',
                       label1='30 mmol L$^{-1}$',label2='60 mmol L$^{-1}$',
                       label3='90 mmol L$^{-1}$',label4='120 mmol L$^{-1}$',
                       size=16,
                       ncol=2,
                       colsp=1,
                       plot_legend='yes',
                       nrev_legend=0)

             plt.show()
```

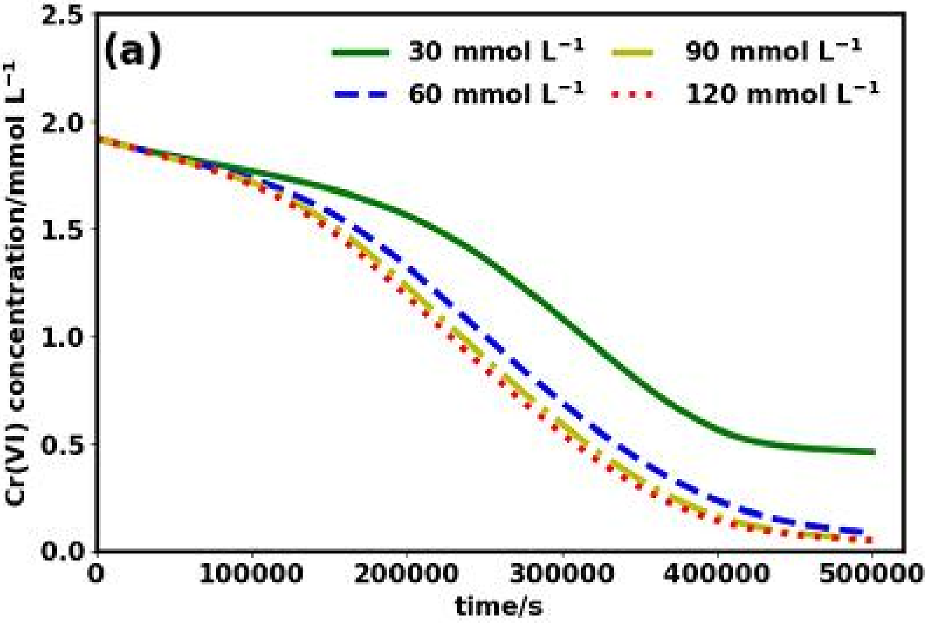

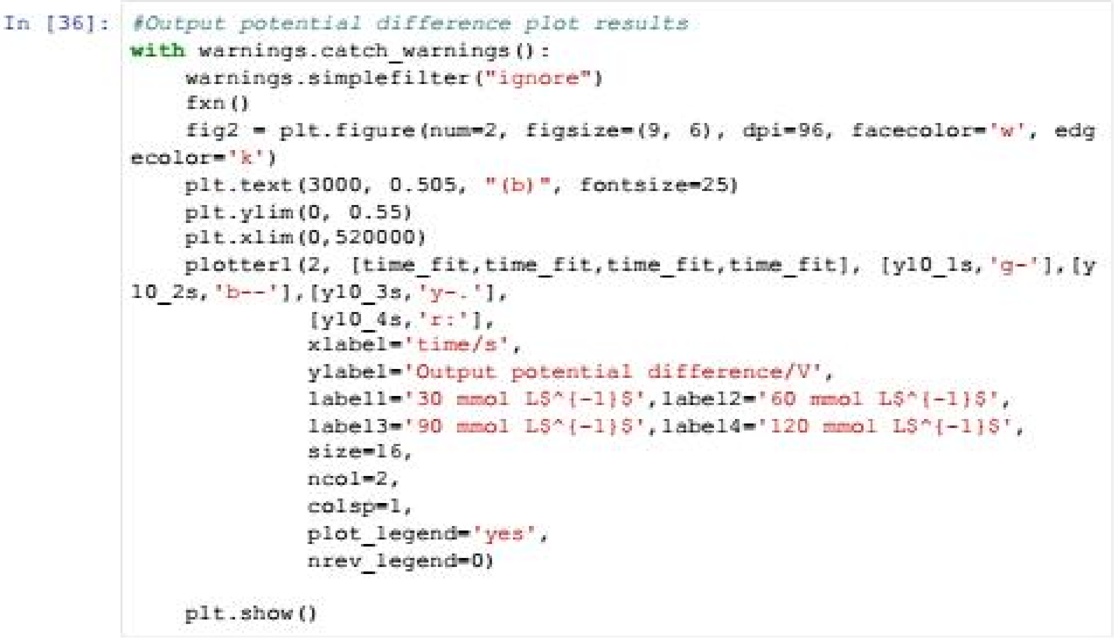

```
In [36]: #Output potential difference plot results
         with warnings.catch_warnings():
             warnings.simplefilter("ignore")
             fxn()
             fig2 = plt.figure(num=2, figsize=(9, 6), dpi=96, facecolor='w', edg
         ecolor='k')
             plt.text(3000, 0.505, "(b)", fontsize=25)
             plt.ylim(0, 0.55)
             plt.xlim(0,520000)
             plotter1(2, [time_fit,time_fit,time_fit,time_fit], [yl0_1s,'g-'],[y
         l0_2s,'b--'],[yl0_3s,'y-.'],
                       [yl0_4s,'r:'],
                       xlabel='time/s',
                       ylabel='Output potential difference/V',
                       label1='30 mmol L$^{-1}$',label2='60 mmol L$^{-1}$',
                       label3='90 mmol L$^{-1}$',label4='120 mmol L$^{-1}$',
                       size=16,
                       ncol=2,
                       colsp=1,
                       plot_legend='yes',
                       nrev_legend=0)

             plt.show()
```

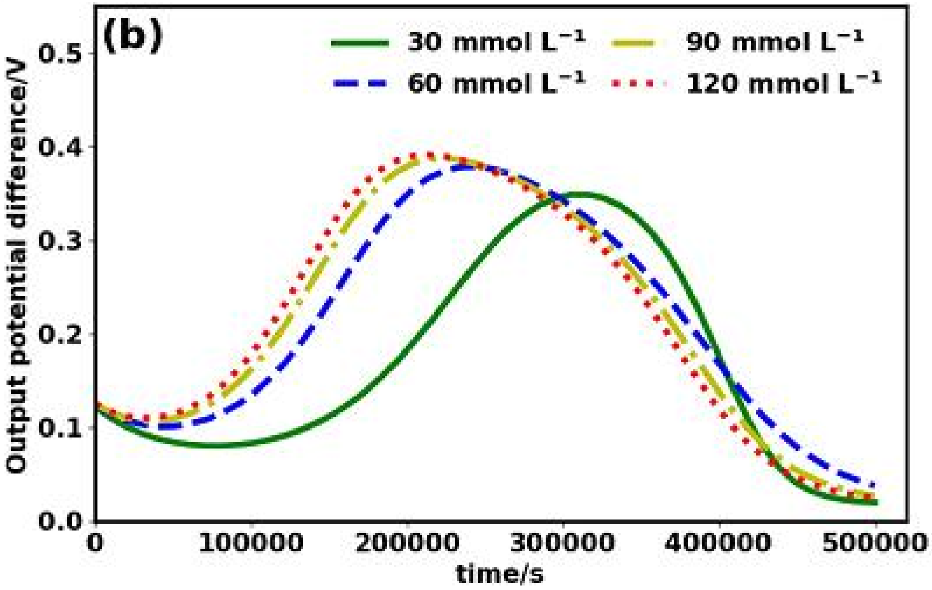

8.2.3. Substrate concentration polarization and power curve

```
In [37]: #Polarization plot results
         with warnings.catch_warnings():
             warnings.simplefilter("ignore")
             fxn()
             fig1 = plt.figure(num=1, figsize=(9, 6), dpi=96, facecolor='w', edg
         ecolor='k')
             plt.text(0.005, 0.46, "(c)", fontsize=25)
             plt.ylim(0, 0.5)
             plt.xlim(0,1.3)
             plotter1(1, [Polar_curve1s[2],Polar_curve2s[2],Polar_curve3s[2],Pol
         ar_curve4s[2]],
                      [Polar_curve1s[0],'g-'],[Polar_curve2s[0],'b--'],[Polar_cu
         rve3s[0],'y-.'],[Polar_curve4s[0],'r:'],
                      xlabel='Current density/A m$^{-2}$',
                      ylabel='Output potential difference/V',
                      label1='30 mmol L$^{-1}$',label2='60 mmol L$^{-1}$',
                      label3='90 mmol L$^{-1}$',label4='120 mmol L$^{-1}$',
                      size=16,
                      ncol=2,
                      colsp=1,
                      plot_legend='yes',
                      nrev_legend=0)

             plt.show()
```

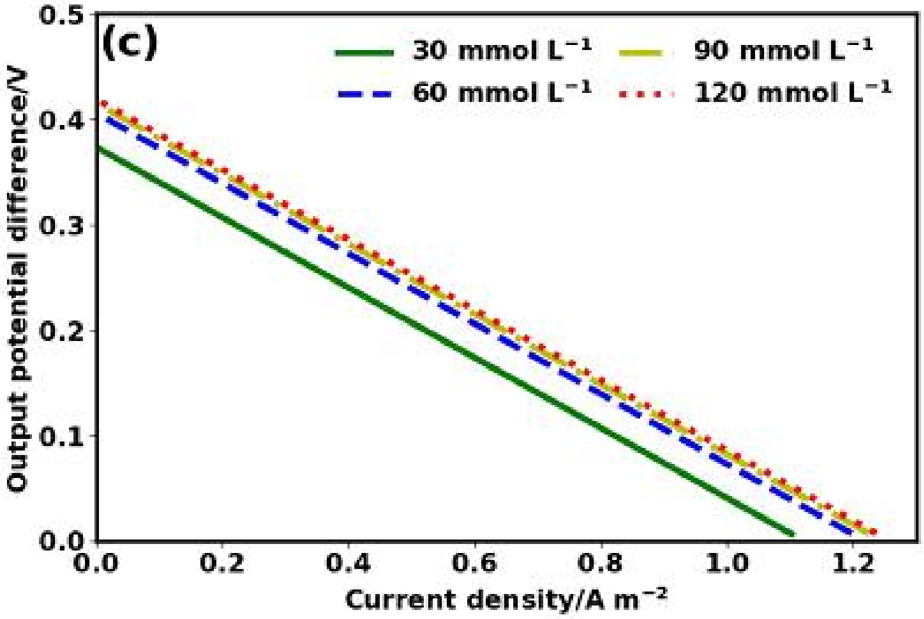

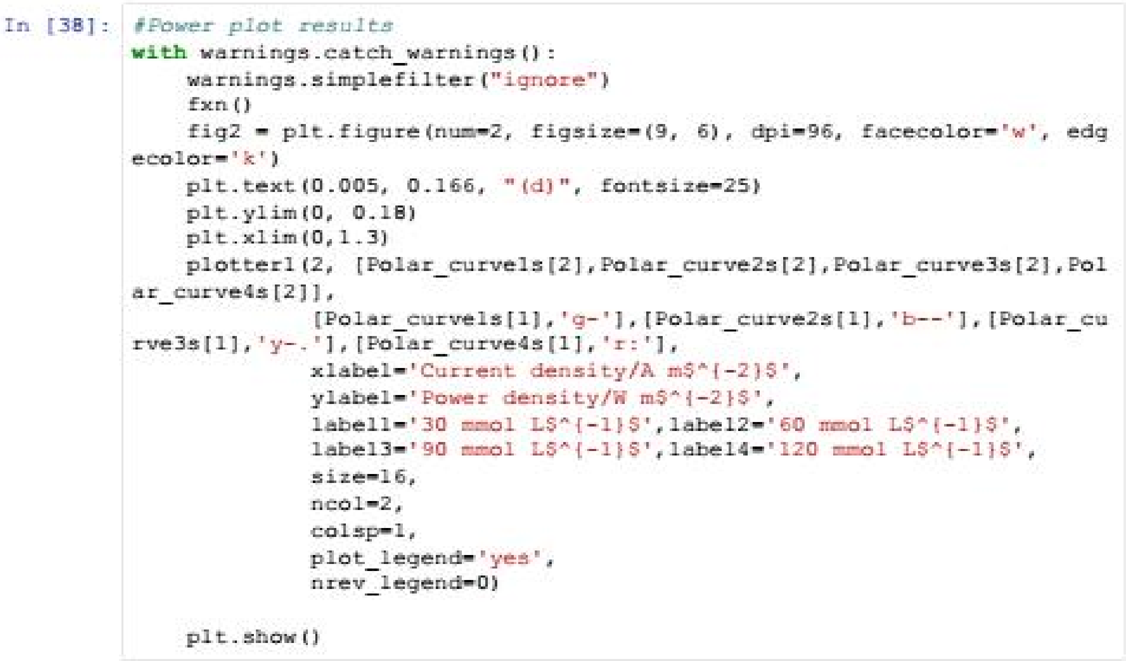

```
In [38]: #Power plot results
         with warnings.catch_warnings():
             warnings.simplefilter("ignore")
             fxn()
             fig2 = plt.figure(num=2, figsize=(9, 6), dpi=96, facecolor='w', edg
         ecolor='k')
             plt.text(0.005, 0.166, "(d)", fontsize=25)
             plt.ylim(0, 0.18)
             plt.xlim(0,1.3)
             plotter1(2, [Polar_curve1s[2],Polar_curve2s[2],Polar_curve3s[2],Pol
         ar_curve4s[2]],
                      [Polar_curve1s[1],'g-'],[Polar_curve2s[1],'b--'],[Polar_cu
         rve3s[1],'y-.'],[Polar_curve4s[1],'r:'],
                      xlabel='Current density/A m$^{-2}$',
                      ylabel='Power density/W m$^{-2}$',
                      label1='30 mmol L$^{-1}$',label2='60 mmol L$^{-1}$',
                      label3='90 mmol L$^{-1}$',label4='120 mmol L$^{-1}$',
                      size=16,
                      ncol=2,
                      colsp=1,
                      plot_legend='yes',
                      nrev_legend=0)

             plt.show()
```

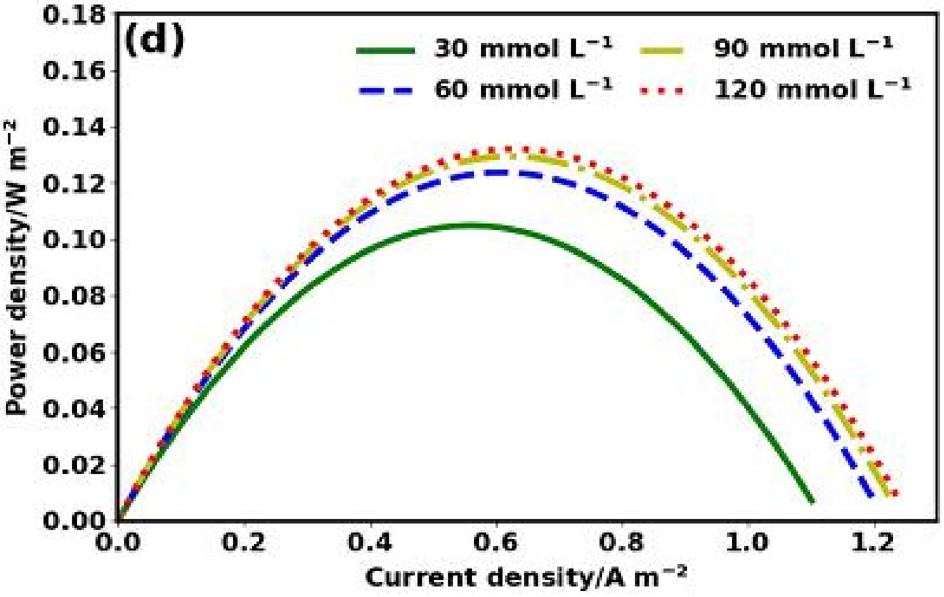

8.2.4. Substrate concentration optimization plot

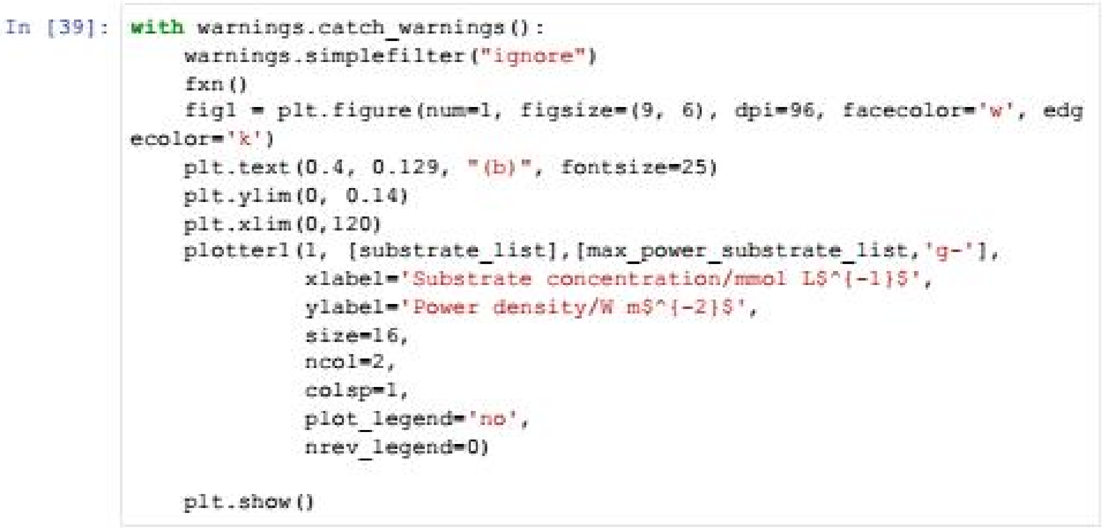

```
In [39]: with warnings.catch_warnings():
             warnings.simplefilter("ignore")
             fxn()
             fig1 = plt.figure(num=1, figsize=(9, 6), dpi=96, facecolor='w', edg
         ecolor='k')
             plt.text(0.4, 0.129, "(b)", fontsize=25)
             plt.ylim(0, 0.14)
             plt.xlim(0,120)
             plotter1(1, [substrate_list],[max_power_substrate_list,'g-'],
                      xlabel='Substrate concentration/mmol L$^{-1}$',
                      ylabel='Power density/W m$^{-2}$',
                      size=16,
                      ncol=2,
                      colsp=1,
                      plot_legend='no',
                      nrev_legend=0)

             plt.show()
```

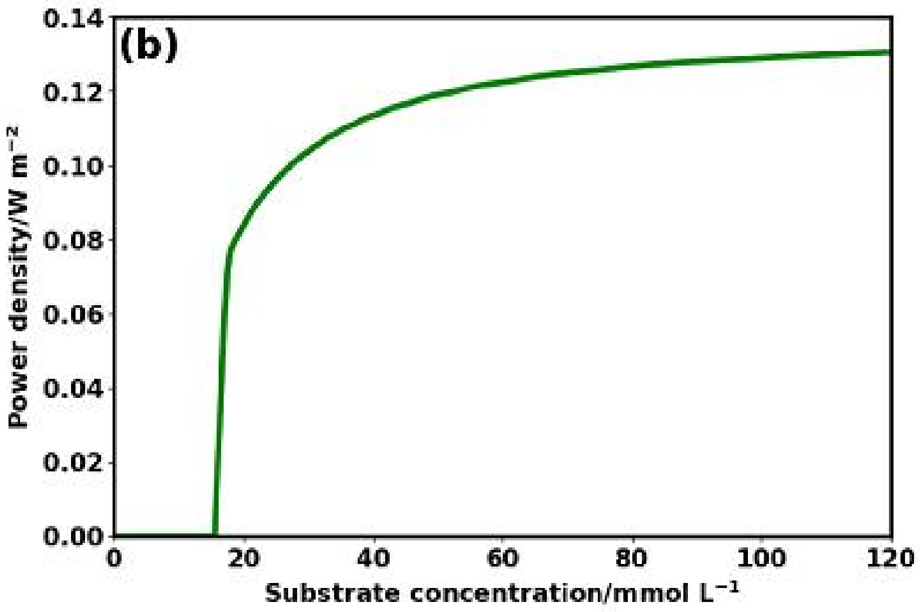

REFERENCES

Adekunle, A., Raghavan, V., Tartakovsky, B., 2017. Carbon source and energy harvesting optimization in solid anolyte microbial fuel cells. J. Power Sources 356, 324-330.

Aelterman, P., Rabaey, K., Pham, H.T., Boon, N., Verstraete, W., 2006. Continuous electricity generation at high voltages and currents using stacked microbial fuel cells. Environ. Sci. Technol. 40(10), 3388-3394.

Ahmed, S., Rozaik, E., Abdelhalim, H., 2015. Effect of configurations, bacterial adhesion, and anode surface area on performance of microbial fuel cells used for treatment of synthetic wastewater. Water Air Soil Pollut. 226(9), 300.

Aiyer, K.S., 2021. Synergistic effects in a microbial fuel cell between co-cultures and a photosynthetic alga Chlorella vulgaris improve performance. Heliyon 7(1), e05935.

American Public Health Association, 2005. Standard Methods for the Examination of Water and Wastewater. APHA, AWWA, WPCF, Washington.

Amin, M.S.A., Haque, T., Tarannum, R., Khan, M., 2014. Wastewater treatment and electricity generation by membrane less microbial fuel. Int. J. Environ. Eng. 6, 314.

Ascher, S., Li, W., You, S., 2020. Life cycle assessment and net present worth analysis of a community-based food waste treatment system. Bioresour. Technol. 305, 123076.

Badalamenti, J.P., Krajmalnik-Brown, R., Torres, C.I., 2013. Generation of high current densities by pure cultures of anode-respiring Geoalkalibacter spp. under alkaline and saline conditions in microbial electrochemical cells. mBio 4(3), e00144-00113.

Baranitharan, E., Khan, M.R., Prasad, D.M.R., Teo, W.F.A., Tan, G.Y.A., Jose, R., 2015. Effect of biofilm formation on the performance of microbial fuel cell for the treatment of palm oil mill effluent. Bioprocess Biosyst. Eng. 38(1), 15-24.

Bard, A.J., Faulkner, L.R., 2000. Electrochemical Methods: Fundamentals and Applications, 2nd Edition. Wiley Textbooks, New Jersey.

Basséguy, R., Délia, M.L., Erable, B., Bergel, A., 2014. Electroactive biofilms. In: Liengen, T., Féron, D., Basséguy, R., Beech, I.B. (Eds.), Understanding Biocorrosion. Woodhead Publishing, Oxford, pp. 107-143.

Behera, S.D., Kumari, U., Shankar, R., Mondal, P., 2018. Performance analysis of a double-chambered microbial fuel cell employing a low-cost sulfonated polystyrene proton exchange membrane. Ionics 24, 3573-3590.

Bennetto, H.P., Stirling, J.L., Tanaka, K., Vega, C.A., 1983. Anodic reactions in microbial fuel cells. Biotechnol. Bioeng. 25(2), 559-568.

Bian, B., Shi, D., Cai, X., Hu, M., Guo, Q., Zhang, C., et al., 2018. 3D printed porous carbon anode for enhanced power generation in microbial fuel cell. Nano Energy 44, 174-180.

Bockris, J.O.M., Nagy, Z., 1973. Symmetry factor and transfer coefficient. A source of confusion in electrode kinetics. J. Chem. Educ. 50(12), 839.

Bond, D.R., Lovley, D.R., 2003. Electricity production by Geobacter sulfurreducens attached to electrodes. Appl. Environ. Microbiol. 69(3), 1548-1555.

Bretschger, O., Obraztsova, A., Sturm, C.A., Chang, I.S., Gorby, Y.A., Reed, S.B., et al., 2007. Current production and metal oxide reduction by Shewanella oneidensis MR-1 wild type and mutants. Appl. Environ. Microbiol. 73(21), 7003-7012.

Cadirci, B.H., 2018. An electricity production study by Rhodobacter sphaeroides. Int. J. Hydrog. Energy 43(38), 18001-18006.

Cao, Y., Mu, H., Liu, W., Zhang, R., Guo, J., Xian, M., et al., 2019. Electricigens in the anode of microbial fuel cells: pure cultures versus mixed communities. Microb. Cell Factories 18, 39-52.

Chaudhuri, S.K., Lovley, D.R., 2003. Electricity generation by direct oxidation of glucose in mediatorless microbial fuel cells. Nat. Biotechnol. 21(10), 1229-1232.

Chen, W., Liu, Z., Hou, J., Zhou, Y., Lou, X., Li, Y., 2018. Enhancing performance of microbial fuel cells by using novel double-layer-capacitor-materials modified anodes. Int. J. Hydrog. Energy 43(3), 1816-1823.

Cheng, S., Logan, B.E., 2011. Increasing power generation for scaling up single-chamber air cathode microbial fuel cells. Bioresour. Technol. 102(6), 4468-4473.

Childers, S.E., Ciufo, S., Lovley, D.R., 2002. Geobacter metallireducens accesses insoluble Fe(III) oxide by chemotaxis. Nature 416(6882), 767-769.

Chirwa, E.M.N., Molokwane, P.E., 2011. Biological Cr(VI) reduction: microbial diversity, kinetics and biotechnological solutions to pollution. In: Sofo, A. (Ed.) Biodiversity. InTech, Croatia, pp. 75-100.

Choi, C., Cui, Y., 2012. Recovery of silver from wastewater coupled with power generation using a microbial fuel cell. Bioresour. Technol. 107, 522-525.

Choudhury, P., Ray, R.N., Bandyopadhyay, T.K., Basak, B., Muthuraj, M., Bhunia, B., 2021. Process engineering for stable power recovery from dairy wastewater using microbial fuel cell. Int. J. Hydrog. Energy 46(4), 3171-3182.

Coates, J.D., Cole, K.A., Chakraborty, R., O'Connor, S.M., Achenbach, L.A., 2002. Diversity and ubiquity of bacteria capable of utilizing humic substances as electron donors for anaerobic respiration. Appl. Environ. Microbiol. 68(5), 2445-2452.

Cohen, B., 1931. The bacterial culture as an electrical half-cell. J. Bacteriol. 21, 18-19.

Dan Pfenninger-Li, X., Dimroth, P., 1992. NADH formation by Na+-coupled reversed electron transfer in Klebsiella pneumoniae. Mol. Microbiol. 6(14), 1943-1948.

De Flora, S., 2000. Threshold mechanisms and site specificity in chromium(VI) carcinogenesis. Carcinogenesis 21(4), 533-541.

Debabov, V., 2008. Electricity from microorganisms. Microbiology 77(2), 123.

Deplanche, K., Caldelari, I., Mikheenko, I.P., Sargent, F., Macaskie, L.E., 2010. Involvement of hydrogenases in the formation of highly catalytic Pd(0) nanoparticles by bioreduction of Pd(II) using *escherichia coli* mutant strains. Microbiology 156(9), 2630-2640.

Dessì, P., Chatterjee, P., Mills, S., Kokko, M., Lakaniemi, A.-M., Collins, G., et al., 2019. Power production and microbial community composition in thermophilic acetate-fed up-flow and flow-through microbial fuel cells. Bioresour. Technol. 294, 122115.

Dicks, A.L., Rand, D.A.J., 2018. Introducing fuel cells. In: Dicks, A.L., Rand, D.A.J. (Eds.), Fuel Cell Systems Explained. John Wiley & Sons Ltd., New Jersey, pp. 1-26.

Didari, S., Zand-Parsa, S., 2017. Estimation of daily global solar irradiation under different sky conditions in central and southern Iran. Theor. Appl. Climatol. 127(3), 587-596.

Elangovan, M., Dharmalingam, S., 2017. Application of polysulphone based anion exchange membrane electrolyte for improved electricity generation in microbial fuel cell. Mater. Chem. Phys. 199, 528-536.

Elangovan, M., Dharmalingam, S., 2016. Preparation and performance evaluation of poly (ether-imide) based anion exchange polymer membrane electrolyte for microbial fuel cell. Int. J. Hydrog. Energy 41(20), 8595-8605.

Enerdata, 2020. Global energy statistical yearbook 2020. Available at: https://yearbook.enerdata.net/electricity/electricity-domestic-consumption-data.html. (Accessed 24 Apr 2020).

Erbay, C., Pu, X., Choi, W., Choi, M.-J., Ryu, Y., Hou, H., et al., 2015. Control of geometrical properties of carbon nanotube electrodes towards high-performance microbial fuel cells. J. Power Sources 280, 347-354.

Fang, D., Yang, L., Yang, G., Yi, G., Feng, Y., Shao, P., et al., 2020. Electrodeposited graphene hybridized graphitic carbon nitride anchoring ultrafine palladium nanoparticles for remarkable methanol electrooxidation. Int. J. Hydrog. Energy 45(41), 21483-21492.

Fazli, N., Mutamim, N.S.A., Shem, C.Y., Rahim, S.A., 2019. Bioelectrochemical cell (BeCC) integrated with Granular Activated Carbon (GAC) in treating spent caustic wastewater. J. Taiwan Inst. Chem. Eng. 104, 114-122.

Feng, G., Cheng, Y., Wang, S.-Y., Borca-Tasciuc, D.A., Worobo, R.W., Moraru, C.I., 2015. Bacterial attachment and biofilm formation on surfaces are reduced by small-diameter nanoscale pores: how small is small enough? npj Biofilms and Microbiomes 1(1), 15022.

Field, J.A., 2001. Recalcitrance as a catalyst for new developments. Water Sci. Technol. 44(8), 33-40.

Flimban, S.G.A., Ismail, I.M.I., Kim, T., Oh, S.-E., 2019. Overview of recent advancements in the microbial fuel cell from fundamentals to applications: design, major elements, and scalability. Energies 12(17).

Freguia, S., Tsujimura, S., Kano, K., 2010. Electron transfer pathways in microbial oxygen biocathodes. Electrochim. Acta. 55(3), 813-818.

Fu, L., You, S.-J., Yang, F.-l., Gao, M.-m., Fang, X.-h., Zhang, G.-q., 2010. Synthesis of hydrogen peroxide in microbial fuel cell. J. Chem. Technol. Biotechnol. 85(5), 715-719.

Fu, Q., Fukushima, N., Maeda, H., Sato, K., Kobayashi, H., 2015. Bioelectrochemical analysis of a hyperthermophilic microbial fuel cell generating electricity at temperatures above 80 °C. Biosci. Biotechnol. Biochem. 79(7), 1200-1206.

Fu, Q., Kobayashi, H., Kawaguchi, H., Wakayama, T., Maeda, H., Sato, K., 2013. A thermophilic gram-negative nitrate-reducing bacterium, calditerrivibrio nitroreducens, exhibiting electricity generation capability. Environ. Sci. Technol. 47(21), 12583-12590.

Gadkari, S., Shemfe, M., Sadhukhan, J., 2019. Microbial fuel cells: A fast converging dynamic model for assessing system performance based on bioanode kinetics. Int. J. Hydrog. Energy 44(29), 15377-15386.

Gambino, E., Toscanesi, M., Del Prete, F., Flagiello, F., Falcucci, G., Minutillo, M., et al., 2017. Polycyclic aromatic hydrocarbons (PAHs) degradation and detoxification of water environment in single-chamber air-cathode microbial fuel cells (MFCs). Fuel Cells 17(5), 618-626.

Geng, Y.-K., Yuan, L., Liu, T., Li, Z.-H., Zheng, X., Sheng, G.-P., 2020. Thermal/alkaline pretreatment of waste activated sludge combined with a microbial fuel cell operated at alkaline pH for efficient energy recovery. Appl. Energy 275, 115291.

Gorby, Y.A., Yanina, S., McLean, J.S., Rosso, K.M., Moyles, D., Dohnalkova, A., et al., 2006. Electrically conductive bacterial nanowires produced by Shewanella oneidensis strain MR-1 and other microorganisms. Proc. Natl. Acad. Sci. U.S.A 103(30), 11358-11363.

Gregory, K.B., Bond, D.R., Lovley, D.R., 2004. Graphite electrodes as electron donors for anaerobic respiration. Environ. Microbiol. 6(6), 596-604.

Grove, W.R., 1842. LXXII. On a gaseous voltaic battery. Lond. Edinb. Dubl. Phil. Mag. J. Sci. 21(140), 417-420.

Guertin, J., Jacobs, J.A., Avakian, C.P., 2004. Chromium(VI) Handbook. CRC Press, Florida.

Haan, J.L., Masel, R.I., 2009. The influence of solution pH on rates of an electrocatalytic reaction: formic acid electrooxidation on platinum and palladium. Electrochim. Acta 54(16), 4073-4078.

Habibul, N., Hu, Y., Wang, Y.-K., Chen, W., Yu, H.-Q., Sheng, G.-P., 2016. Bioelectrochemical Chromium(VI) Removal in Plant-Microbial Fuel Cells. Environ. Sci. Technol. 50(7), 3882-3889.

Hamelers, H.V.M., ter Heijne, A., Stein, N., Rozendal, R.A., Buisman, C.J.N., 2011. Butler–Volmer–Monod model for describing bio-anode polarization curves. Bioresour. Technol. 102(1), 381-387.

Harnisch, F., Schröder, U., Scholz, F., 2008. The suitability of monopolar and bipolar ion exchange membranes as separators for biological fuel cells. Environ. Sci. Technol. 42(5), 1740-1746.

He, Z., Wagner, N., Minteer, S.D., Angenent, L.T., 2006. An upflow microbial fuel cell with an interior cathode: Assessment of the internal resistance by impedance spectroscopy. Environ. Sci. Technol. 40(17), 5212-5217.

He, Z., Minteer, S.D., Angenent, L.T., 2005. Electricity generation from artificial wastewater using an upflow microbial fuel cell. Environ. Sci. Technol. 39(14), 5262-5267.

Heijne, A.T., Liu, F., Weijden, R.v.d., Weijma, J., Buisman, C.J.N., Hamelers, H.V.M., 2010. Copper recovery combined with electricity production in a microbial fuel cell. Environ. Sci. Technol. 44(11), 4376-4381.

Hejazi, F., Ghoreyshi, A.A., Rahimnejad, M., 2019. Simultaneous phenol removal and electricity generation using a hybrid granular activated carbon adsorption-biodegradation process in a batch recycled tubular microbial fuel cell. Biomass and Bioenergy 129, 105336.

Hernández-Flores, G., Andrio, A., Compañ, V., Solorza-Feria, O., Poggi-Varaldo, H.M., 2019. Synthesis and characterization of organic agar-based membranes for microbial fuel cells. J. Power Sources 435, 226772.

Holmes, D.E., Chaudhuri, S.K., Nevin, K.P., Mehta, T., Methé, B.A., Liu, A., et al., 2006. Microarray and genetic analysis of electron transfer to electrodes in Geobacter sulfurreducens. Environ. Microbiol. 8(10), 1805-1815.

Huang, L., Chen, J., Quan, X., Yang, F., 2010. Enhancement of hexavalent chromium reduction and electricity production from a biocathode microbial fuel cell. Bioprocess Biosyst. Eng. 33(8), 937-945.

Huang, X., 2009. Fabrication and Properties of Carbon Fibers. Materials 2(4).

Huggins, T.M., Haeger, A., Biffinger, J.C., Ren, Z.J., 2016. Granular biochar compared with activated carbon for wastewater treatment and resource recovery. Water Res. 94, 225-232.

IEA, 2017. Water-energy nexus. Available at: https://www.iea.org/reports/water-energy-nexus. (Accessed 23 Mar 2020).

Igboamalu, T.E., Nyakale, A., Matsena, M.T., Chirwa, E.M.N., 2020. Effect of oxidation reduction potential (Eh) on the biocatalytic oxidation of As 3+ to As 5+ in a mixed culture of chemoautotrophic bacteria. Chem. Eng. Trans. 79, 301-306.

Igboamalu, T.E., Chirwa, E.M.N., Bezuidenhout, N., Matsena, M.T., 2019a. Microbial fuel cell power output and growth: effect of substrate pH on anaerobic microbe consortium. Chem. Eng. Trans. 76, 1381-1386.

Igboamalu, T.E., Chirwa, E.M.N., Needham-Clark, B., Matsena, M.T., 2019b. Energy output from a dual chamber anoxic biofilm microbial fuel cell subjected to variation in substrate concentration. Chem. Eng. Trans. 76, 1387-1392.

Ishii, T., Kawaichi, S., Nakagawa, H., Hashimoto, K., Nakamura, R., 2015. From chemolithoautotrophs to electrolithoautotrophs: CO2 fixation by Fe(II)-oxidizing bacteria coupled with direct uptake of electrons from solid electron sources. Front. Microbiol. 6, 994.

Ismail, Z.Z., Jaeel, A.J., 2016. Modelling study of an upflow microbial fuel cell catalysed with anaerobic aged sludge. Int. J. Ambient. Energy 37(1), 85-93.

Jacobson, K.S., Drew, D.M., He, Z., 2011. Efficient salt removal in a continuously operated upflow microbial desalination cell with an air cathode. Bioresour. Technol. 102(1), 376-380.

Jay, Z.J., Hunt, K.A., Chou, K.J., Schut, G.J., Maness, P.-C., Adams, M.W.W., et al., 2020. Integrated thermodynamic analysis of electron bifurcating [FeFe]-hydrogenase to inform anaerobic metabolism and H2 production. Biochim. Biophys. Acta Biomembr. 1861(1), 148087.

Jiang, D., Li, B., 2009. Granular activated carbon single-chamber microbial fuel cells (GAC-SCMFCS): a design suitable for large-scale wastewater treatment processes. Biochem. Eng. J. 47, 31-37.

Jiang, R., Chu, D., 2003. Comparative studies of methanol crossover and cell performance for a DMFC. J. Electrochem. Soc. 151(1), A69.

Jong, B.C., Kim, B.H., Chang, I.S., Liew, P.W.Y., Choo, Y.F., Kang, G.S., 2006. Enrichment, performance, and microbial diversity of a thermophilic mediatorless microbial fuel cell. Environ. Sci. Technol. 40(20), 6449-6454.

Jörnsten, R., Ouyang, M., Wang, H.-Y., 2007. A meta-data based method for DNA microarray imputation. BMC Bioinform. 8(1), 109.

Kang, S., Wang, G., Zhao, H., Cai, W., 2017. Highly efficient removal of hexavalent chromium in aqueous solutions via chemical reduction of plate-like micro/nanostructured zero valent iron. RSC Adv. 7, 55905-55911.

Kato Marcus, A., Torres, C.I., Rittmann, B.E., 2007. Conduction-based modeling of the biofilm anode of a microbial fuel cell. Biotechnol. Bioeng. 98(6), 1171-1182.

Khan, M., Bhattacharjee, R., Amin, M.S.A., 2012. Performance of the salt bridge based microbial fuel cell. Int. J. Eng. Technol. 1, 115-123.

Kim, B., Hyun, M.S., Park, D.H., 1999. Direct electrode reaction of Fe(III)-reducing bacterium, Shewanella putrefaciens. J. Microbiol. Biotechnol. 9, 127-131.

Kim, C., Lee, C.R., Song, Y.E., Heo, J., Choi, S.M., Lim, D.-H., et al., 2017. Hexavalent chromium as a cathodic electron acceptor in a bipolar membrane microbial fuel cell with the simultaneous treatment of electroplating wastewater. Chem. Eng. J. 328, 703-707.

Kim, I.S., Kim, L.H., Kim, S.-J., Kim, K.-Y., 2015. Biofouling in osmotic membrane bioreactor. In: Shon, H.K., Phuntsho, S., Zhang, T.C., Surampalli, R.Y. (Eds.), Forward Osmosis: Fundamentals and Applications. American Society of Civil Engineers, Reston, pp. 241-275.

Kim, J., Kim, B., An, J., Lee, Y.S., Chang, I.S., 2016. Development of anode zone using dual-anode system to reduce organic matter crossover in membraneless microbial fuel cells. Bioresour. Technol. 213, 140-145.

Kim, J.R., Cheng, S., Oh, S.-E., Logan, B.E., 2007. Power generation using different cation, anion, and ultrafiltration membranes in microbial fuel cells. Environ. Sci. Technol. 41(3), 1004-1009.

Kipnis, N., 1987. Luigi Galvani and the debate on animal electricity, 1791–1800. Ann Sci. 44(2), 107-142.

Kondaveeti, S., Lee, S.-H., Park, H.-D., Min, B., 2020. Specific enrichment of different Geobacter sp. in anode biofilm by varying interspatial distance of electrodes in air-cathode microbial fuel cell (MFC). Electrochim. Acta 331, 135388.

Koók, L., Žitka, J., Bakonyi, P., Takács, P., Pavlovec, L., Otmar, M., et al., 2020. Electrochemical and microbiological insights into the use of 1,4-diazabicyclo[2.2.2]octane-functionalized anion exchange membrane in microbial fuel cell: a benchmarking study with Nafion. Sep. Purif. Technol. 237, 116478.

Kumar, S., Kumar, H.D., Gireesh Babu, K., 2012. A study on the electricity generation from the cow dung using microbial fuel cell. J. Biochem. Technol. 3(4).

Kundu, P.P., Dutta, K., 2018. Progress and Recent Trends in Microbial Fuel Cells. Elsevier Science, Amsterdam.

Lal, D., 2013. Microbes to generate electricity. Indian J Microbiol 53(1), 120-122.

Larrosa-Guerrero, A., Scott, K., Head, I.M., Mateo, F., Ginesta, A., Godinez, C., 2010. Effect of temperature on the performance of microbial fuel cells. Fuel 89(12), 3985-3994.

Li, A.Y.L., DiGiano, F.A., 1983. Availability of sorbed substrate for microbial degradation on granular activated carbon. J. Water Pollut. Control Fed. 55(4), 392-399.

Li, H., Xu, H., Yang, Y.-L., Yang, X.-L., Wu, Y., Zhang, S., et al., 2019. Effects of graphite and Mn ore media on electro-active bacteria enrichment and fate of antibiotic and corresponding resistance gene in up flow microbial fuel cell constructed wetland. Water Res. 165, 114988.

Li, L., Sun, Y., Yuan, Z.-H., Kong, X., Li, Y., 2013. Effect of temperature change on power generation of microbial fuel cell. Environ. Technol. 34, 1929-1934.

Li, M., Zhou, Y., Xu, Y., Liu, Z., Ma, F., Zhi, L., et al., 2018. Simultaneous Cr(VI) reduction and bioelectricity generation in a dual chamber microbial fuel cell. Chem. Eng. J. 334, 1621-1629.

Li, Y., Yang, W., Liu, X., Guan, W., Zhang, E., Shi, X., et al., 2020. Diffusion-layer-free air cathode based on ionic conductive hydrogel for microbial fuel cells. Sci. Total Environ. 743, 140836.

Li, Z., Zhang, X., Lei, L., 2008. Electricity production during the treatment of real electroplating wastewater containing Cr^{6+} using microbial fuel cell. Process Biochem. 43, 1352-1358.

Liang, B., Ren, C., Zhao, Y., Li, K., Lv, C., 2020. Nitrogenous mesoporous carbon coated with Co/Cu nanoparticles modified activated carbon as air cathode catalyst for microbial fuel cell. J. Electroanal. Chem. 860, 113904.

Liao, K., Hu, H., Ma, S., Ren, H., 2019. Effect of microbial activity and microbial community structure on the formation of dissolved organic nitrogen (DON) and bioavailable DON driven by low temperatures. Water Res. 159, 397-405.

Liengen, T., Basseguy, R., Feron, D., Beech, I., Birrien, V., 2014. Understanding Biocorrosion: Fundamentals and Applications. Elsevier Science, Amsterdam.

Lipczynska-Kochany, E., 2018. Humic substances, their microbial interactions and effects on biological transformations of organic pollutants in water and soil: A review. Chemosphere 202, 420-437.

Liu, H., Logan, B.E., 2004. Electricity generation using an air-cathode single chamber microbial fuel cell in the presence and absence of a proton exchange membrane. Environ. Sci. Technol. 38(14), 4040-4046.

Liu, J., Liu, Y., Feng, C., Wang, Z., Jia, T., Gong, L., et al., 2017. Enhanced performance of microbial fuel cell using carbon microspheres modified graphite anode. Energy Sci. Eng. 5(4), 217-225.

Liu, J., Zhang, F., He, W., Zhang, X., Feng, Y., Logan, B.E., 2014. Intermittent contact of fluidized anode particles containing exoelectrogenic biofilms for continuous power generation in microbial fuel cells. J. Power Sources 261, 278-284.

Liu, Y., Mallouk, K., Emamipour, H., Rood, M.J., Liu, X., Yan, Z., 2019. Isobutane adsorption with carrier gas recirculation at different relative humidities using activated carbon fiber cloth and electrothermal regeneration. Chem. Eng. J. 360, 1011-1019.

Lloyd, J.R., Yong, P., Macaskie, L.E., 1998. Enzymatic recovery of elemental palladium by using sulfate-reducing bacteria. Appl. Environ. Microbiol. 64(11), 4607-4609.

Logan, B.E., Rossi, R., Ragab, A.a., Saikaly, P.E., 2019. Electroactive microorganisms in bioelectrochemical systems. Nat. Rev. Microbiol. 17(5), 307-319.

Lovley, D.R., Walker, D.J.F., 2019. Geobacter protein nanowires. Front. Microbiol. 10(2078).

Lovley, D.R., 2017. Electrically conductive pili: Biological function and potential applications in electronics. Curr. Opin. Electrochem. 4(1), 190-198.

Lovley, D.R., Fraga, J.L., Coates, J.D., Blunt-Harris, E.L., 1999. Humics as an electron donor for anaerobic respiration. Environ. Microbiol. 1(1), 89-98.

Lovley, D.R., Coates, J.D., Blunt-Harris, E.L., Phillips, E.J.P., Woodward, J.C., 1996. Humic substances as electron acceptors for microbial respiration. Nature 382(6590), 445-448.

Luo, H., Xu, G., Lu, Y., Liu, G., Zhang, R., Li, X., et al., 2017. Electricity generation in a microbial fuel cell using yogurt wastewater under alkaline conditions. RSC Adv. 7(52), 32826-32832.

Luo, H., Liu, G., Zhang, R., Jin, S., 2009. Phenol degradation in microbial fuel cells. Chem. Eng. J. 147, 259-264.

Lv, C., Liang, B., Zhong, M., Li, K., Qi, Y., 2019. Activated carbon-supported multi-doped graphene as high-efficient catalyst to modify air cathode in microbial fuel cells. Electrochim. Acta. 304, 360-369.

Majidi, M.R., Shahbazi Farahani, F., Hosseini, M., Ahadzadeh, I., 2019. Low-cost nanowired α-MnO2/C as an ORR catalyst in air-cathode microbial fuel cell. Bioelectrochemistry 125, 38-45.

Malki, M., De Lacey, A.L., Rodríguez, N., Amils, R., Fernandez, V.M., 2008. Preferential use of an anode as an electron acceptor by an acidophilic bacterium in the presence of oxygen. Appl. Environ. Microbiol. 74(14), 4472-4476.

Malunga, K., Chirwa, E., 2019. Recovery of palladium (II) by biodeposition using a pure culture and a mixed culture. Chem. Eng. Trans. 74, 1519-1524.

Mann, R.F., Amphlett, J.C., Peppley, B.A., Thurgood, C.P., 2006. Application of Butler–Volmer equations in the modelling of activation polarization for PEM fuel cells. J. Power Sources 161(2), 775-781.

Martinez, C.M., Alvarez, L.H., Celis, L.B., Cervantes, F.J., 2013. Humus-reducing microorganisms and their valuable contribution in environmental processes. Appl. Microbiol. Biotechnol. 97(24), 10293-10308.

Matsena, M.T., Tichapondwa, S.M., Chirwa, E.M.N., 2020. Synthesis of biogenic palladium nanoparticles using *Citrobacter* sp. For application as anode electrocatalyst in a microbial fuel cell. Catalysts 10(8), 838.

Matsena, M.T., Igboamalu, T.E., Chirwa, E.M.N., 2018. Phenol degrading and chromium (VI) reducing biofilm system: effect of shock-loading. Chem. Eng. Trans. 70, 207.

McAnulty, M.J., G. Poosarla, V., Kim, K.-Y., Jasso-Chávez, R., Logan, B.E., Wood, T.K., 2017. Electricity from methane by reversing methanogenesis. Nat. Commun. 8(1), 15419.

Menictas, C., Skyllas-Kazacos, M., Lim, T.M., 2014. Advances in Batteries for Medium and Large-Scale Energy Storage: Types and Applications. Elsevier Science.

Merchant, S.S., Helmann, J.D., 2012. Elemental economy: microbial strategies for optimizing growth in the face of nutrient limitation. Adv Microb Physiol 60, 91-210.

Michie, I.S., Kim, J.R., Dinsdale, R.M., Guwyb, A.J., Premiera, G.C., 2011. The influence of psychrophilic and mesophilic start-up temperature on microbial fuel cell system performance. Energy Environ. Sci. 4, 1011-1019.

Min, B., Cheng, S., Logan, B.E., 2005. Electricity generation using membrane and salt bridge microbial fuel cells. Water Res. 39(9), 1675-1686.

Moon, J.-S., Lee, Y.-W., Han, S.-B., Park, K.-W., 2014. Pd nanoparticles on mesoporous tungsten carbide as a non-Pt electrocatalyst for methanol electrooxidation reaction in alkaline solution. Int. J. Hydrog. Energy 39(15), 7798-7804.

Mtimunye, P.J., 2011. A steady-state model for hexavalent chromium reduction in simulated biological reactive barrier: microcosm analysis. University of Pretoria, Pretoria, South Africa.

Niya, S.M.R., Hoorfar, M., 2014. Process modeling of the ohmic loss in proton exchange membrane fuel cells. Electrochim. Acta 120, 193-203.

Nunna, S., Blanchard, P., Buckmaster, D., Davis, S., Naebe, M., 2019. Development of a cost model for the production of carbon fibres. Heliyon 5(10), e02698.

Nunna, S., Naebe, M., Hameed, N., Fox, B.L., Creighton, C., 2017. Evolution of radial heterogeneity in polyacrylonitrile fibres during thermal stabilization: An overview. Polym. Degrad. Stab. 136, 20-30.

Occupational Safety and Health Administration., 2006. Occupational exposure to hexavalent chromium; final rule. Fed. Regist. 71(39), 10099-10385.

Oh, S.-E., Logan, B.E., 2006. Proton exchange membrane and electrode surface areas as factors that affect power generation in microbial fuel cells. Appl. Microbiol. Biotechnol. 70(2), 162-169.

Pandit, S., Khilari, S., Roy, S., Ghangrekar, M.M., Pradhan, D., Das, D., 2015. Reduction of start-up time through bioaugmentation process in microbial fuel cells using an isolate from dark fermentative spent media fed anode. Water Sci. Technol. 72(1), 106-115.

Park, D., Zeikus, J., 2002. Impact of electrode composition on electricity generation in a single-compartment fuel cell using Shewanella putrefaciens. Appl. Microbiol. Biotechnol. 59(1), 58-61.

Penteado, E.D., Fernandez-Marchante, C.M., Zaiat, M., Gonzalez, E.R., Rodrigo, M.A., 2018. Optimization of the performance of a microbial fuel cell using the ratio electrode-surface area/anode-compartment volume. Brazilian J. Chem. Eng 35(1), 141-146.

Picioreanu, C., Head, I.M., Katuri, K.P., van Loosdrecht, M.C.M., Scott, K., 2007. A computational model for biofilm-based microbial fuel cells. Water Res. 41(13), 2921-2940.

Pinto, R.P., Srinivasan, B., Manuel, M.F., Tartakovsky, B., 2010. A two-population bio-electrochemical model of a microbial fuel cell. Bioresour. Technol. 101(14), 5256-5265.

Potter, M.C., 1911. Electrical effects accompanying the decomposition of organic compounds. Proc. Royal Soc. Lond. B. Biol. Sci. 84(571), 260-276.

Potter, M.C., 1910. On the difference of potential due to the vital activity of microorganisms. Proc. Univ. Durham Phil. Soc. 3, 245-249.

Pramanick, B., Kumar, T., Halder, A., Siril, P.F., 2020. Engineering the morphology of palladium nanostructures to tune their electrocatalytic activity in formic acid oxidation reactions. Nanoscale Adv.

Puig, S., Serra, M., Coma, M., Cabré, M., Balaguer, M.D., Colprim, J., 2010. Effect of pH on nutrient dynamics and electricity production using microbial fuel cells. Bioresour. Technol. 101(24), 9594-9599.

Quaglio, M., Massaglia, G., Vasile, N., Margaria, V., Chiodoni, A., Salvador, G.P., et al., 2019. A fluid dynamics perspective on material selection in microbial fuel cell-based biosensors. Int. J. Hydrog. Energy 44(9), 4533-4542.

Quan, X., Zhang, X., Sun, Y., Zhao, J., 2018a. Iohexol degradation by biogenic palladium nanoparticles hosted in anaerobic granular sludge. Front. Microbiol. 9(1980).

Quan, X., Xu, H., Sun, B., Xiao, Z., 2018b. Anode modification with palladium nanoparticles enhanced evans blue removal and power generation in microbial fuel cells. Int. Biodeterior. Biodegradation 132, 94-101.

Quan, X., Sun, B., Xu, H., 2015. Anode decoration with biogenic Pd nanoparticles improved power generation in microbial fuel cells. Electrochim. Acta 182, 815-820.

Rabaey, K., Boon, N., Siciliano, S.D., Verhaege, M., Verstraete, W., 2004. Biofuel cells select for microbial consortia that self-mediate electron transfer. Appl. Environ. Microbiol. 70(9), 5373-5382.

Radeef, A.Y., Ismail, Z.Z., 2019. New application of microbial fuel cell-based biosensor for monitoring the quality of actual potato chips' processing wastewater. Waste Disposal Sustain. Energy 1(3), 227-235.

Raghavulu, S.V., Modestra, J.A., Amulya, K., Reddy, C.N., Venkata Mohan, S., 2013. Relative effect of bioaugmentation with electrochemically active and non-active bacteria on bioelectrogenesis in microbial fuel cell. Bioresour. Technol. 146, 696-703.

Rahimnejad, M., Adhami, A., Darvari, S., Zirepour, A., Oh, S.-E., 2015. Microbial fuel cell as new technology for bioelectricity generation: A review. Alexandria. Eng. J. 54(3), 745-756.

Reguera, G., Nevin, K.P., Nicoll, J.S., Covalla, S.F., Woodard, T.L., Lovley, D.R., 2006. Biofilm and nanowire production leads to increased current in Geobacter sulfurreducens fuel cells. Appl. Environ. Microbiol. 72(11), 7345-7348.

Reguera, G., McCarthy, K.D., Mehta, T., Nicoll, J.S., Tuominen, M.T., Lovley, D.R., 2005. Extracellular electron transfer via microbial nanowires. Nature 435(7045), 1098-1101.

Renslow, R., Babauta, J., Kuprat, A., Schenk, J., Ivory, C., Fredrickson, J., et al., 2013. Modeling biofilms with dual extracellular electron transfer mechanisms. Phys. Chem. Chem. Phys. 15(44), 19262-19283.

Rhoads, A., Beyenal, H., Lewandowski, Z., 2005. Microbial fuel cell using anaerobic respiration as an anodic reaction and biomineralized manganese as a cathodic reactant. Environ. Sci. Technol. 39(12), 4666-4671.

Rismani-Yazdi, H., Carver, S., Christy, A., Tuovinen, O., 2008. Cathodic limitations in microbial fuel cells: an overview. J. Power Sources 180, 683-694.

Santoro, C., Arbizzani, C., Erable, B., Ieropoulos, I., 2017. Microbial fuel cells: From fundamentals to applications. A review. J. Power Sources 356, 225-244.

Santoro, C., Soavi, F., Serov, A., Arbizzani, C., Atanassov, P., 2016. Self-powered supercapacitive microbial fuel cell: the ultimate way of boosting and harvesting power. Biosens. Bioelectron. 78, 229-235.

Santoro, C., Guilizzoni, M., Correa Baena, J.P., Pasaogullari, U., Casalegno, A., Li, B., et al., 2014. The effects of carbon electrode surface properties on bacteria attachment and start up time of microbial fuel cells. Carbon 67, 128-139.

Sarma, D., Barua, P.B., Dey, N., Nath, S., Thakuria, M., Mallick, S., 2019. Investigation and taguchi optimization of microbial fuel cell salt bridge dimensional parameters. J. Inst. Eng. India Ser. C. 100(1), 103-112.

Schiraldi, C., De Rosa, M., 2014. Mesophilic organisms. In: Drioli, E., Giorno, L. (Eds.), Encyclopedia of Membranes. Springer, Berlin, pp. 1-2.

Schönbein, C.F., 1839. X. On the voltaic polarization of certain solid and fluid substances. Lond. Edinb. Dubl. Phil. Mag. J. Sci. 14(85), 43-45.

Schröder, U., 2007. Anodic electron transfer mechanisms in microbial fuel cells and their energy efficiency. Phys. Chem. Chem. Phys. 9(21), 2619-2629.

Scott, D.T., McKnight, D.M., Blunt-Harris, E.L., Kolesar, S.E., Lovley, D.R., 1998. Quinone moieties act as electron acceptors in the reduction of humic substances by humics-reducing microorganisms. Environ. Sci. Technol. 32(19), 2984-2989.

Scott, K., 2016a. 1 - an introduction to microbial fuel cells. In: Scott, K., Yu, E.H. (Eds.), Microbial Electrochemical and Fuel Cells. Woodhead Publishing, Boston, pp. 3-27.

Scott, K., 2016b. 2 - Electrochemical principles and characterization of bioelectrochemical systems. In: Scott, K., Yu, E.H. (Eds.), Microbial Electrochemical and Fuel Cells. Woodhead Publishing, Boston, pp. 29-66.

Seeber, R., Zanardi, C., Inzelt, G., 2015. Links between electrochemical thermodynamics and kinetics. ChemTexts 1(4), 18.

Sevda, S., Sreekrishnan, T.R., 2012. Effect of salt concentration and mediators in salt bridge microbial fuel cell for electricity generation from synthetic wastewater. J. Environ. Sci. Health A 47(6), 878-886.

Sharma, Y., Li, B., 2010. The variation of power generation with organic substrates in single-chamber microbial fuel cells (SCMFCs). Bioresour. Technol. 101(6), 1844-1850.

Shelobolina, E.S., Walker, D.K., Parker, A.E., Lust, D.V., Schultz, J.M., Dickerman, G.E., 2018. Inactivation of *pseudomonas aeruginosa* biofilms formed under high shear stress on various hydrophilic and hydrophobic surfaces by a continuous flow of ozonated water. Biofouling 34(7), 826-834.

Shi, D., Guo, Z., Bedford, N., 2015. Carbon nanotubes. In: Shi, D., Guo, Z., Bedford, N. (Eds.), Nanomaterials and Devices. William Andrew Publishing, Oxford, pp. 49-82.

Shi, L., Dong, H., Reguera, G., Beyenal, H., Lu, A., Liu, J., et al., 2016. Extracellular electron transfer mechanisms between microorganisms and minerals. Nat. Rev. Microbiol. 14(10), 651-662.

Song, T.S., Jin, Y., Bao, J., Kang, D., Xie, J., 2016. Graphene/biofilm composites for enhancement of hexavalent chromium reduction and electricity production in a biocathode microbial fuel cell. J. Hazard. Mater. 317, 73-80.

Song, Y., An, J., Chae, K.-J., 2017. Effect of temperature variation on the performance of microbial fuel cells. Energy Technol. 5(12), 2163-2167.

Sophia, A.C., Sai, S., 2016. Modified microbial fuel cell for Cr(VI) reduction and simultaneous bio-electricity production. J. Environ. Chem. Eng. 4(2), 2402-2409.

Sophia, A.C., Saikant, S., 2016. Reduction of chromium(VI) with energy recovery using microbial fuel cell technology. J. Water Process. Eng. 11, 39-45.

Sriram, S., Nambi, I.M., Chetty, R., 2018. Electrochemical reduction of hexavalent chromium on titania nanotubes with urea as an anolyte additive. Electrochim. Acta 284, 427-435.

Stein, L.R., Imai, S.-i., 2012. The dynamic regulation of NAD metabolism in mitochondria. Trends Endocrinol. Metab. 23(9), 420-428.

Stirling, J.L., Bennetto, H.P., Delaney, G.M., Mason, J.R., Roller, S.D., Tanaka, K., et al., 1983. Microbial fuel cells. Biochem. Soc. Trans. 11(4), 451-453.

Su, S.-g., Cheng, H.-y., Zhu, T.-t., Wang, H.-c., Wang, A.-j., 2018. Kinetic competition between microbial anode respiration and nitrate respiration in a bioelectrochemical system. Bioelectrochemistry 123, 241-247.

Subha, C., Kavitha, S., Abisheka, S., Tamilarasan, K., Arulazhagan, P., Banu, J.R., 2019. Bioelectricity generation and effect studies from organic rich chocolaterie wastewater using continuous upflow anaerobic microbial fuel cell. Fuel 251, 224-232.

Sun, J., Li, W., Li, Y., Hu, Y., Zhang, Y., 2013. Redox mediator enhanced simultaneous decolorization of azo dye and bioelectricity generation in air-cathode microbial fuel cell. Bioresour. Technol. 142, 407-414.

ter Heijne, A., Hamelers, H.V.M., de Wilde, V., Rozendal, R.A., Buisman, C.J.N., 2006. A bipolar membrane combined with ferric iron reduction as an efficient cathode system in microbial fuel cells. Environ. Sci. Technol. 40(17), 5200-5205.

Tichapondwa, S.M., Tshemese, S., Mhike, W., 2018. Adsorption of phenol and chromium (VI) pollutants in wastewater using exfoliated graphite Chem. Eng. Trans. 70, 847-852.

Torres, C.I., Marcus, A.K., Parameswaran, P., Rittmann, B.E., 2008. Kinetic Experiments for Evaluating the Nernst−Monod Model for Anode-Respiring Bacteria (ARB) in a Biofilm Anode. Environ. Sci. Technol. 42(17), 6593-6597.

Tran, T.V., Lee, I.C., Kim, K., 2019. Electricity production characterization of a sediment microbial fuel cell using different thermo-treated flat carbon cloth electrodes. Int. J. Hydrog. Energy 44(60), 32192-32200.

Tremouli, A., Vlassis, T., Antonopoulou, G., Lyberatos, G., 2016. Anaerobic Degradation of Pure Glycerol for Electricity Generation using a MFC: The Effect of Substrate Concentration. Waste and Biomass Valorization 7(6), 1339-1347.

Tsai, H.-Y., Wu, C.-C., Lee, C.-Y., Shih, E.P., 2009. Microbial fuel cell performance of multiwall carbon nanotubes on carbon cloth as electrodes. J. Power Sources 194(1), 199-205.

Upton, D., de Groot, P., 2008. Planting and Establishment of Tropical Trees. Commonwealth Secretariat, London.

Vélez-Pérez, L.S., Ramirez-Nava, J., Hernández-Flores, G., Talavera-Mendoza, O., Escamilla-Alvarado, C., Poggi-Varaldo, H.M., et al., 2020. Industrial acid mine drainage and municipal wastewater co-treatment by dual-chamber microbial fuel cells. Int. J. Hydrog. Energy 45(26), 13757-13766.

Virdis, B., Rabaey, K., Rozendal, R.A., Yuan, Z., Keller, J., 2010. Simultaneous nitrification, denitrification and carbon removal in microbial fuel cells. Water Res. 44(9), 2970-2980.

Volta, A., 1800. XVII. On the electricity excited by the mere contact of conducting substances of different kinds. In a letter from Mr. Alexander Volta, F. R. S. Professor of Natural Philosophy in the University of Pavia, to the Rt. Hon. Sir Joseph Banks, Bart. K.B. P. R. S. Phil. Trans. Royal Soc. Lond. 90, 403-431.

Wang, A.-L., Xu, H., Feng, J.-X., Ding, L.-X., Tong, Y.-X., Li, G.-R., 2013. Design of Pd/PANI/Pd Sandwich-Structured Nanotube Array Catalysts with Special Shape Effects and Synergistic Effects for Ethanol Electrooxidation. J. Am. Chem. Soc. 135(29), 10703-10709.

Wang, C.T., Sangeetha, T., Ding, D.Q., Chong, W.T., Yan, W.M., 2018. Implementation of surface modified carbon cloth electrodes with biochar particles in microbial fuel cells. Int. J. Green Energy 15(13), 789-794.

Wang, F., Gu, Y., O'Brien, J.P., Yi, S.M., Yalcin, S.E., Srikanth, V., et al., 2019. Structure of microbial nanowires reveals stacked hemes that transport electrons over micrometers. Cell 177(2), 361-369.e310.

Wang, G., Huang, L., Zhang, Y., 2008. Cathodic reduction of hexavalent chromium [Cr(VI)] coupled with electricity generation in microbial fuel cells. Biotechnol. Lett. 30(11), 1959.

Wang, Q., Chen, F., Tang, Q., Guo, L., Gebremariam, T.T., Jin, T., et al., 2020. Transition from core-shell to janus segregation pattern in AgPd nanoalloy by Ni doping for the formate oxidation. Appl. Catal. B: Environ. 270, 118861.

Wang, W., Wei, X., Choi, D., Lu, X., Yang, G., Sun, C., 2015. Chapter 1 - electrochemical cells for medium- and large-scale energy storage: Fundamentals. In: Menictas, C., Skyllas-Kazacos, M., Lim, T.M. (Eds.), Advances in Batteries for Medium and Large-Scale Energy Storage. Woodhead Publishing, Cambridge, pp. 3-28.

Werner, C.M., Logan, B.E., Saikaly, P.E., Amy, G.L., 2013. Wastewater treatment, energy recovery and desalination using a forward osmosis membrane in an air-cathode microbial osmotic fuel cell. J. Membr. Sci. 428, 116-122.

Wisniak, J., 2015. Historical notes: electrochemistry and fuel cells: The contribution of William Robert Grove. Indian j. hist. sci. 50, 476-490.

Wu, L.C., Tsai, T.H., Liu, M.H., Kuo, J.L., Chang, Y.C., Chung, Y.C., 2017. A green microbial fuel cell-based biosensor for in situ chromium (VI) measurement in electroplating wastewater. Sensors 17, 2461-2474.

Xin, X., Pang, H., She, Y., Hong, J., 2020. Insights into redox mediators-resource harvest/application with power production from waste activated sludge through freezing/thawing-assisted anaerobic acidogenesis coupling microbial fuel cells. Bioresour. Technol. 311, 123469.

Xu, X., Zhao, Q.L., Wu, M.S., 2015. Improved biodegradation of total organic carbon and polychlorinated biphenyls for electricity generation by sediment microbial fuel cell and surfactant addition. RSC Adv. 5(77), 62534-62538.

Yamasaki, R., Maeda, T., Wood, T.K., 2018. Electron carriers increase electricity production in methane microbial fuel cells that reverse methanogenesis. Biotechnol. Biofuels 11(1), 211.

Yang, L., Deng, W., Zhang, Y., Tan, Y., Ma, M., Xie, Q., 2017. Boosting current generation in microbial fuel cells by an order of magnitude by coating an ionic liquid polymer on carbon anodes. Biosens. Bioelectron. 91, 644-649.

Yang, W., He, W., Zhang, F., Hickner, M.A., Logan, B.E., 2014. Single-step fabrication using a phase inversion method of poly(vinylidene fluoride) (PVDF) activated carbon air cathodes for microbial fuel cells. Environ. Sci. Technol. Lett. 1(10), 416-420.

Yang, Y., Yan, L., Song, J., Xu, M., 2018. Optimizing the electrode surface area of sediment microbial fuel cells. RSC Adv. 8(45), 25319-25324.

Yang, Y., Ding, Y., Hu, Y., Cao, B., Rice, S.A., Kjelleberg, S., et al., 2015. Enhancing bidirectional electron transfer of Shewanella oneidensis by a synthetic flavin pathway. ACS Synth. Biol. 4(7), 815-823.

Yao, L., Li, M., Hu, Y., Wang, Q., Liu, X., 2021. Comparative study of upgraded CO2 transcritical air source heat pump systems with different heat sinks. Appl. Therm. Eng. 184, 116289.

Yazdi, H., Alzate-Gaviria, L., Ren, Z.J., 2015. Pluggable microbial fuel cell stacks for septic wastewater treatment and electricity production. Bioresour. Technol. 180, 258-263.

Yong, P., Rowson, N.A., Farr, J.P.G., Harris, I.R., Macaskie, L.E., 2002. Bioreduction and biocrystallization of palladium by *Desulfovibrio desulfuricans* NCIMB 8307. Biotechnol. Bioeng. 80(4), 369-379.

Yu, X., Manthiram, A., 2015. Catalyst-selective, scalable membraneless alkaline direct formate fuel cells. Applied. Catal. B: Environ. 165, 63-67.

Zhang, B., Feng, C., Ni, J., Zhang, J., Huang, W., 2012. Simultaneous reduction of vanadium (V) and chromium (VI) with enhanced energy recovery based on microbial fuel cell technology. J. Power Sources 204, 34-39.

Zhang, F., Brastad, K.S., He, Z., 2011. Integrating forward osmosis into microbial fuel cells for wastewater treatment, water extraction and bioelectricity generation. Environ. Sci. Technol. 45(15), 6690-6696.

Zhang, L., Li, J., Zhu, X., Ye, D.-d., Fu, Q., Liao, Q., 2017. Response of stacked microbial fuel cells with serpentine flow fields to variable operating conditions. Int. J. Hydrog. Energy 42(45), 27641-27648.

Zhang, W., Hu, Y., Ma, L., Zhu, G., Wang, Y., Xue, X., et al., 2018. Progress and perspective of electrocatalytic CO2 reduction for renewable carbonaceous fuels and chemicals. Adv. Sci. 5(1), 1700275.

Zhang, X., Li, X., Zhao, X., Li, Y., 2019. Factors affecting the efficiency of a bioelectrochemical system: a review. RSC Adv. 9(34), 19748-19761.

Zhang, X., Shi, J., Liang, P., Wei, J., Huang, X., Zhang, C., et al., 2013. Power generation by packed-bed air-cathode microbial fuel cells. Bioresour. Technol. 142, 109-114.

Zhang, X.C., Halme, A., 1995. Modelling of a microbial fuel cell process. Biotechnol. Lett. 17(8), 809-814.

Zhao, X., Deng, W., Tan, Y., Xie, Q., 2020. Promoting electricity generation of shewanella putrefaciens in a microbial fuel cell by modification of porous poly(3-aminophenylboronic acid) film on carbon anode. Electrochim. Acta 354, 136715.

Zheng, W., Cai, T., Huang, M., Chen, D., 2017. Comparison of electrochemical performances and microbial community structures of two photosynthetic microbial fuel cells. J. Biosci. Bioeng. 124(5), 551-558.

Zou, L., Qiao, Y., Zhong, C., Li, C.M., 2017. Enabling fast electron transfer through both bacterial outer-membrane redox centers and endogenous electron mediators by polyaniline hybridized large-mesoporous carbon anode for high-performance microbial fuel cells. Electrochim. Acta. 229, 31-38.